

**Utilization of mswi bottom ash as a mineral resource for low-carbon construction materials  
Quality-upgrade treatments, mix design method, and microstructure analysis**

Chen, B.

**DOI**

[10.4233/uuid:0793986f-b875-4693-a0f9-568978f2d632](https://doi.org/10.4233/uuid:0793986f-b875-4693-a0f9-568978f2d632)

**Publication date**

2023

**Document Version**

Final published version

**Citation (APA)**

Chen, B. (2023). *Utilization of mswi bottom ash as a mineral resource for low-carbon construction materials: Quality-upgrade treatments, mix design method, and microstructure analysis*. [Dissertation (TU Delft), Delft University of Technology]. <https://doi.org/10.4233/uuid:0793986f-b875-4693-a0f9-568978f2d632>

**Important note**

To cite this publication, please use the final published version (if applicable).  
Please check the document version above.

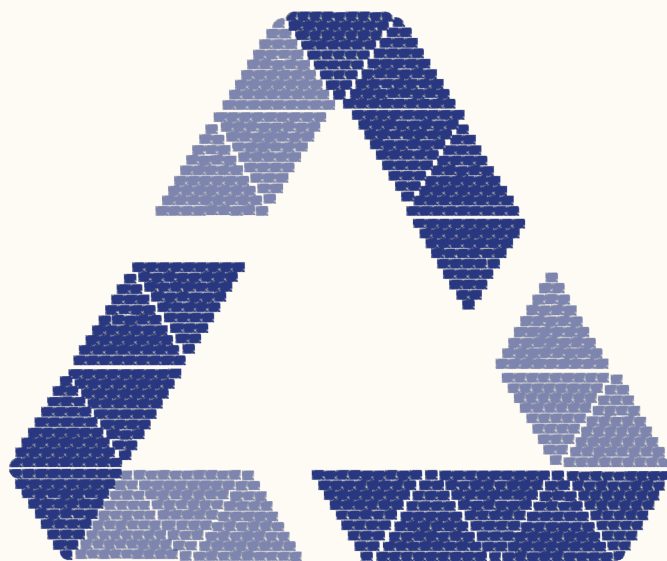
**Copyright**

Other than for strictly personal use, it is not permitted to download, forward or distribute the text or part of it, without the consent of the author(s) and/or copyright holder(s), unless the work is under an open content license such as Creative Commons.

**Takedown policy**

Please contact us and provide details if you believe this document breaches copyrights.  
We will remove access to the work immediately and investigate your claim.

# Utilization of MSWI bottom ash as a mineral resource for low-carbon construction materials



Boyu Chen

陈泊羽



**UTILIZATION OF MSWI BOTTOM ASH AS A MINERAL RESOURCE FOR  
LOW-CARBON CONSTRUCTION MATERIALS:**  
*QUALITY-UPGRADE TREATMENTS, MIX DESIGN METHOD, AND  
MICROSTRUCTURE ANALYSIS*

**Dissertation**

for the purpose of obtaining the degree of doctor  
at Delft University of Technology  
by the authority of the Rector Magnificus prof.dr.ir. T.H.J.J. van der Hagen  
chair of the Board for Doctorates  
to be defended publicly on  
Thursday 9 March 2023 at 12:30 o'clock

by

**Boyu CHEN**

Master of Science in Materials Engineering,  
Katholieke Universiteit Leuven, Belgium,  
born in Jingdezhen, P.R.China

This dissertation has been approved by the promotor.

Composition of the doctoral committee:

Rector Magnificus,  
Prof.dr.ir. K. van Breugel  
Dr. G. Ye

chairperson  
Delft University of Technology, promotor  
Delft University of Technology, promotor

Independent members:

Prof.dr. H.M. Jonkers  
Prof.dr. L.M. Ottosen  
Prof.dr. N. Štirmer  
Prof.dr. Y. Zhang  
Dr.ir. G.M.H. Meesters  
Prof.dr.ir. E. Schlangen

Delft University of Technology  
Technical University of Denmark, Denmark  
University of Zagreb, Croatia  
Southeast University, China  
Delft University of Technology  
Delft University of Technology, reserve member



*Keywords:* MSWI bottom ash; mechanical treatments; water treatment; NaOH solution treatment; supplementary cementitious material; precursor; reactivity; blended cement pastes; alkali-activated materials; alkali-activated pastes; thermodynamic modeling; microstructure; environmental impacts;

*Printed by:* Ipskamp Printing, the Netherlands

*Cover design by:* Boyu Chen

Copyright © 2023 by Boyu Chen

All rights reserved. This copy of the thesis has been supplied on condition that anyone who consults it is understood to recognize that its copyright rests with its author and that no quotation from the thesis and no information derived from it may be published without the author's prior consent.

ISBN 978-94-6366-667-1



To my beloved parents and grandparents

谨以此书献给我的父母和祖父母

# Table of Contents

Summary.....	I
Samenvatting.....	III
List of abbreviations.....	vi
Chapter 1 General introduction.....	1
1.1 Research background.....	2
1.2 Knowledge gaps .....	4
1.3 Research objectives .....	4
1.4 Research scope .....	5
1.5 Research strategy.....	5
1.6 Thesis outline .....	6
Chapter 2 Literature review.....	9
2.1 Introduction .....	10
2.2 Properties of fresh MSWI bottom ash.....	10
2.3 Plant-scale treatments of fresh MSWI bottom ash .....	10
2.4 Compositions of weathered MSWI bottom ash .....	12
2.4.1 Chemical composition.....	12
2.4.2 Mineralogical composition .....	15
2.5 Lab-scale treatments.....	18
2.5.1 Mechanical treatments.....	19
2.5.2 Chemical treatments .....	19
2.5.3 Thermal treatments.....	20
2.6 Utilization of MSWI bottom ash as supplementary cementitious material.....	21
2.6.1 Pozzolanic reactivity of MSWI bottom ash.....	22
2.6.2 Pozzolanic reaction products of MSWI bottom ash .....	23
2.6.3 Reaction of MSWI bottom ash in blended cement pastes .....	23
2.6.4 Effects of MSWI bottom ash on cement hydration.....	23
2.6.5 Mechanical properties of MSWI bottom ash blended cement pastes, mortars, and concretes.....	25
2.6.6 Leaching of contaminants from MSWI bottom ash blended cement pastes, mortars, and concretes .....	26
2.7 Utilization of MSWI bottom ash as precursor for AAM .....	27
2.7.1 Reactivity as AAM precursor .....	27

2.7.2	AAM prepared with MSWI bottom ash as precursor .....	28
2.7.2.1	Reaction products in alkali-activated MSWI bottom ash .....	28
2.7.2.2	Mechanical properties of alkali-activated MSWI bottom ash .....	30
2.7.2.3	Leaching of contaminants from alkali-activated MSWI bottom ash .....	32
2.7.3	AAM prepared with MSWI bottom ash and other industrial by-products as precursor.....	32
2.8	Environmental impacts of construction materials prepared with MSWI bottom ash .....	34
2.9	Summary of literature studies.....	35
2.10	Challenges of using MSWI bottom ash as SCM and AAM precursor .....	36
<b>Chapter 3 Characterization and mechanical treatments of as-received MSWI bottom ash ....</b>		<b>38</b>
3.1	Introduction .....	39
3.2	Materials and methods .....	41
3.2.1	Materials.....	41
3.2.2	Characterization techniques .....	41
3.2.2.1	Chemical composition .....	41
3.2.2.2	Mineralogical composition .....	41
3.2.2.3	Metallic Al content .....	42
3.2.2.4	Metallic Al embedded in MSWI bottom ash particles.....	43
3.3	Results and discussion of as-received MSWI bottom ash characterization.....	45
3.3.1	Particle size distribution of as-received MSWI bottom ash.....	45
3.3.2	Compositions of as-received MSWI bottom ash .....	46
3.3.2.1	Chemical composition .....	46
3.3.2.2	Mineralogical composition .....	47
3.3.3	Characterization of metallic Al in as-received MSWI bottom ash .....	50
3.3.3.1	Distribution of metallic Al among different size fractions .....	50
3.3.3.2	MSWI bottom ash particles containing metallic Al .....	50
3.4	Mechanical treatments of as-received MSWI bottom ash .....	56
3.4.1	Effects of mechanical treatments on the composition of MSWI bottom ash ..	57
3.4.2	Effectiveness of mechanical treatments on metallic Al removal .....	58
3.5	Conclusions .....	60
<b>Chapter 4 Reactivity and leaching potential of mechanically treated MSWI bottom ash .....</b>		<b>61</b>
4.1	Introduction .....	62
4.2	Materials and methods .....	64

4.2.1	Materials.....	64
4.2.2	Characterization techniques .....	65
4.2.2.1	Chemical and mineralogical compositions.....	65
4.2.2.2	Analysis of amorphous phase .....	65
4.2.2.3	Reactivity test for the application as SCMs.....	66
4.2.2.4	Reactivity test for the application as AAM precursors.....	66
4.2.3	Thermodynamic modeling .....	67
4.2.4	Assessment of leaching potential .....	69
4.3	Results and discussion .....	69
4.3.1	Compositions of MBA .....	69
4.3.1.1	Chemical composition .....	69
4.3.1.2	Mineralogical composition .....	71
4.3.1.3	Chemical composition of amorphous phase.....	74
4.3.2	Reactivity of MBA as SCM .....	77
4.3.3	Reactivity of MBA as AAM precursor .....	78
4.3.3.1	Concentrations of dissolved elements.....	78
4.3.3.2	Ratio of dissolved Si and Al .....	80
4.3.4	Thermodynamic modeling of the reactions in alkali-activated MBA paste .....	81
4.3.5	Leaching potential of MBA.....	86
4.3.6	Remarks on using MBA as SCM and AAM precursor.....	88
4.4	Conclusions .....	90
Chapter 5 Blended cement pastes prepared with mechanically treated MSWI bottom ash as supplementary cementitious material .....		91
5.1	Introduction .....	92
5.2	Materials and methods .....	93
5.2.1	Materials.....	93
5.2.2	Mix design.....	95
5.2.3	Samples preparation.....	95
5.2.4	Studies of reaction between MBA and water .....	97
5.2.5	Paste sample characterization .....	97
5.3	Results and discussion .....	101
5.3.1	Water treatment of MBA.....	101
5.3.2	Effectiveness of water treatment in improving compressive strength of blended cement pastes prepared with MBA.....	105

5.3.3	Effectiveness of water treatment in eliminating expansive cracks in blended cement pastes prepared with MBA.....	106
5.3.4	Formation and analysis of the microstructure of cement pastes.....	109
5.3.4.1	Effect of WMBA on cement hydration.....	109
5.3.4.2	Reaction products in hardened cement pastes .....	112
5.3.4.3	Morphology of hardened cement pastes .....	117
5.3.4.4	Chemical composition of C-S-H gel in hardened cement pastes.....	120
5.3.4.5	Porosity of hardened cement pastes .....	125
5.3.5	Strength development of hardened cement pastes .....	126
5.4	Conclusions .....	127
Chapter 6 Alkali-activated pastes prepared with mechanically treated MSWI bottom ash as precursor .....		128
6.1	Introduction .....	129
6.2	Materials and methods .....	131
6.2.1	Materials.....	131
6.2.2	Mix design.....	131
6.2.3	Sample preparation .....	132
6.2.4	Studies of reactions during NaOH solution treatment and pre-activation process .....	134
6.2.5	Paste sample characterization .....	135
6.3	Results and discussion .....	138
6.3.1	Reactions during NaOH solution treatment and pre-activation process.....	138
6.3.2	Effectiveness of NaOH solution treatment in eliminating volume expansion of alkali-activated pastes prepared with MBA and BFS .....	144
6.3.3	Comparison of compressive strength between CMBA-BFS AAM and FA-BFS AAM .....	146
6.3.4	Formation and analysis of the microstructure of alkali-activated pastes.....	147
6.3.4.1	Effects of CMBA on the reaction of BFS.....	147
6.3.4.2	Crystalline reaction products in hardened alkali-activated pastes .....	149
6.3.4.3	Chemical bonds in hardened alkali-activated pastes .....	154
6.3.4.4	Morphology of hardened alkali-activated pastes .....	156
6.3.4.5	Chemical composition of the gel phases in alkali-activated pastes .....	160
6.3.4.6	Porosity of hardened alkali-activated pastes.....	162
6.3.5	Strength development of hardened alkali-activated pastes .....	164
6.4	Conclusions .....	165

Chapter 7 Environmental impacts of blended cement pastes and alkali-activated pastes prepared with mechanically treated MSWI bottom ash .....	166
7.1 Introduction .....	167
7.2 Methodology .....	167
7.2.1 Definition of goal and scope .....	167
7.2.2 Inventory analysis .....	169
7.2.3 Impact analysis .....	172
7.3 Result interpretation.....	173
7.3.1 Environmental impacts of cement pastes.....	173
7.3.2 Environmental impacts of alkali-activated pastes.....	176
7.4 Conclusions .....	179
7.5 Limitations of this study .....	179
Chapter 8 Retrospection, conclusions, contributions, and outlooks .....	181
8.1 Retrospection.....	182
8.2 Conclusions .....	183
8.3 Contributions of this research to science and engineering .....	185
8.4 Outlooks.....	186
Appendix A.....	189
Appendix B.....	200
Appendix C.....	202
Appendix D .....	205
Appendix E.....	207
Appendix F .....	208
References .....	209
Acknowledgements .....	237
Curriculum vitae .....	240

# Summary

---

In recent years, considerable attention has been given to the utilization of municipal solid waste incineration (MSWI) bottom ash as a mineral resource for construction materials. MSWI bottom ash is the primary residue discharged after incinerating municipal solid waste. The generation of MSWI bottom ash is increasing dramatically with the wide application of waste incineration techniques. Different methods have been proposed to improve the quality of MSWI bottom ash and make it suitable as supplementary cementitious material (SCM) or precursor for alkali-activated materials (AAM). However, there is no systemic guidance on how to select quality-upgrade treatments for MSWI bottom ash. When using MSWI bottom ash to prepare blended cement pastes and alkali-activated pastes, the optimal mix design is usually found by trial and error. Very little information is available in the literature regarding the reaction of MSWI bottom ash as SCM and AAM precursor. The contribution of MSWI bottom ash to the microstructure formation and strength development of blended cement pastes and alkali-activated pastes is not very well understood.

The goal of this research is to develop knowledge that can be used to support the application of MSWI bottom ash as a mineral resource for construction materials. Based on this knowledge, a strategy for using MSWI bottom ash produced in the Netherlands (4-11 mm) as raw material to produce blended cement pastes and alkali-activated pastes is proposed. This research consists of the following parts:

## *Quality-upgrade treatments of as-received MSWI bottom ash*

As-received MSWI bottom ash cannot be used directly as SCM and AAM precursor due to its large particle size and presence of metallic aluminum (Al). Mechanical treatments consisting of grinding and sieving were studied and selected to reduce the particle size and the metallic Al content of as-received MSWI bottom ash. The effectiveness of the mechanical treatments used to reduce the metallic Al content of MSWI bottom ash is strongly influenced by the distribution of metallic Al in bottom ash particles. Most metallic Al separated during mechanical treatment comes from the coarse particles. The metallic Al embedded in the particles smaller than 0.5 mm is difficult to be removed via mechanical treatments (see *Chapter 3*).

## *Development and microstructure analysis of blended cement pastes and alkali-activated pastes*

The reactivity and leaching potential of *mechanically treated MSWI bottom ash (MBA)* are studied. This information is used in the development of blended cement pastes and alkali-activated pastes. A dissolution test is proposed to assess the reactivity of MBA as AAM precursor. The reactivity of MBA as SCM and AAM precursor is similar to that of Class F coal fly ash (FA), but much lower than that of blast furnace slag (BFS). The leaching of antimony (Sb) and sulfate from MBA is above the threshold value prescribed in Dutch Soil Quality Decree. The dosage of MBA in blended cement pasts and alkali-activated pastes should be

controlled to prevent excessive leaching of contaminants into the environment (see *Chapter 4*).

The reactivity of MBA is determined by the content and the chemical composition of its amorphous phase. The amorphous phase of MBA has a chemical composition within the same range as that of the amorphous phase of FA. Given that the reactivity of MBA is close to that of FA, previous experience with the mix design of Class F coal fly ash-based pastes is used as a reference for the mix design of MBA-based AAM. Additionally, thermodynamic modeling is used to predict the assemblage of reaction products and the composition of pore solution in alkali-activated MBA paste when changing the Na<sub>2</sub>O content in the activator. The modeling results are also used to guide the mix design of MBA-based AAM (see *Chapter 4*).

When water treatment and NaOH solution treatment are part of the mixture preparation procedure, the compressive strength of the blended cement pastes and alkali-activated pastes made from MBA is close to that of the pastes prepared with the same amount of FA (*Chapters 5 and 6*). The metallic Al that cannot be removed during mechanical treatments can be oxidized by treating MBA in water or NaOH solution at room temperature. Apart from reducing metallic Al content, water treatment and NaOH solution treatment also slightly change the mineralogical composition of MBA.

Blending *water-treated MBA (WMBA)* with Portland cement paste leads to changes in the reaction products and microstructure. WMBA delays clinker hydration on the first day but enhances clinker hydration at later ages. The reaction products of WMBA contribute to the strength development of blended cement pastes (see *Chapter 5*).

*NaOH solution-treated MBA (CMBA)* is used together with BFS to prepare alkali-activated pastes. CMBA retards the reaction of BFS during the first seven days but promotes the reaction of BFS at later ages. Adding CMBA into alkali-activated pastes changes the reaction products and microstructure. The reaction products of CMBA contribute to the strength development of alkali-activated pastes (see *Chapter 6*).

#### *Environmental impact assessment of blended cement pastes and alkali-activated pastes*

Compared with Portland cement paste, blended cement pastes and alkali-activated pastes prepared using MSWI bottom ash SCM and AAM precursor have lower environmental impacts, especially in the impact category of global warming (see *Chapter 7*).

*This research deepens the understanding of the reaction of MSWI bottom ash as SCM and AAM precursor. This study also demonstrates how to use MSWI bottom ash to prepare blended cement pastes and alkali-activated pastes by considering the chemical and physical properties of MSWI bottom ash. Since the MSWI bottom ash used in this research has chemical and mineralogical compositions within the same range as the MSWI bottom ash reported in the literature, the knowledge developed in this work stimulates the utilization of MSWI bottom ash produced in other regions as SCM and AAM precursor for construction materials.*



# Samenvatting

---

De laatste jaren is veel aandacht besteed aan het gebruik van bodemas uit de verbranding van vast stedelijk afval (AVI) als minerale grondstof voor bouwmaterialen. AVI-bodemas is het primaire residu dat vrijkomt na de verbranding van vast stedelijk afval. De aanvoer van AVI-bodemas neemt sterk toe door de brede toepassing van afvalverbrandingstechnieken. Er zijn verschillende methoden voorgesteld om de kwaliteit van AVI-bodemas te verbeteren en deze geschikt te maken als vulstof met bindmiddelfunctie in beton (SCM) of precursor voor alkali-geactiveerde materialen (AAM). Er bestaan echter geen systematische richtlijnen voor de selectie van bewerkingen ter verbetering van de kwaliteit van AVI-bodemas. Bij het gebruik van AVI-bodemas in cementpasta's en alkali-geactiveerde pasta's wordt het optimale mengselontwerp meestal proefondervindelijk vastgesteld. In de literatuur is zeer weinig informatie beschikbaar over de reactie van AVI-bodemas als SCM en AAM-precursor. De bijdrage van AVI-bodemas aan de microstructuurvorming en de sterkteontwikkeling van cementpasta's en alkali-geactiveerde pasta's is nog niet volledig duidelijk.

Het doel van dit onderzoek is kennis te ontwikkelen die kan worden gebruikt om de toepassing van AVI-bodemas als minerale grondstof voor bouwmaterialen te ondersteunen. Op basis van deze kennis wordt een strategie voorgesteld voor het gebruik van in Nederland geproduceerde AVI-bodemas (4-11 mm) als grondstof voor de productie van cementpasta's en alkali-geactiveerde pasta's. Dit onderzoek bestaat uit de volgende onderdelen:

## *Verbetering van de kwaliteit van ontvangen AVI-bodemas*

De ontvangen AVI-bodemas kan niet rechtstreeks worden gebruikt als SCM- en AAM-precursor vanwege de grote korrelgrootte en de aanwezigheid van metallisch aluminium (Al). Mechanische behandelingen, bestaande uit malen en zeven, worden bestudeerd en geselecteerd om de deeltjesgrootte en het metallisch Al-gehalte van de ontvangen AVI-bodemas te verminderen. De doeltreffendheid van de mechanische behandelingen, ter vermindering van het metallisch Al-gehalte van AVI-bodemas, wordt sterk beïnvloed door de verdeling van metallisch Al in de bodemaskorrels. Het meeste metallische Al dat tijdens de mechanische behandeling wordt afgescheiden, is afkomstig van de grove korrels. Het metallisch Al in de korrels kleiner dan 0,5 mm is moeilijk te verwijderen via mechanische bewerkingen (zie *hoofdstuk 3*).

## *Ontwikkeling en microstructuuranalyse van gemengde cementpasta's en alkali-geactiveerde pasta's*

De reactiviteit en het uitloogvermogen van *mechanisch behandeld AVI-bodemas (MBA)* worden bestudeerd. Deze informatie wordt gebruikt bij de ontwikkeling van cementpasta's en alkali-geactiveerde pasta's. Er wordt een oplossingstest voorgesteld om de reactiviteit van MBA als AAM-precursor te beoordelen. De reactiviteit van MBA als SCM en AAM-precursor is vergelijkbaar met die van klasse V (siliciumhoudend) poederkoolvliegas (FA), maar veel lager dan die van hoogovenslak (BFS). De uitloging van antimoon (Sb) en sulfaat uit MBA ligt boven de in het Besluit bodemkwaliteit voorgeschreven drempelwaarde. De dosering van MBA in

cementpasta's en alkali-geactiveerde pasta's moet worden gecontroleerd om overmatige uitloging van schadelijke stoffen naar het milieu te voorkomen (zie *hoofdstuk 4*).

De reactiviteit van MBA wordt bepaald door het gehalte en de chemische samenstelling van de amorfe fase ervan. De amorfe fase van MBA heeft eenzelfde chemische samenstelling als de amorfe fase van FA. Aangezien de reactiviteit van MBA dichtbij die van FA ligt, wordt eerdere ervaring met het mixontwerp van pasta's op basis van poederkoolvliegias (klasse V) gebruikt als referentie voor het mixontwerp van AAM op basis van MBA. Daarnaast worden thermodynamische modellen gebruikt om de samenstelling van reactieproducten en de samenstelling van de poriënwater in alkali-geactiveerde MBA-pasta te voorspellen bij wijzigen van het  $\text{Na}_2\text{O}$ -gehalte in de activator. De resultaten van de thermodynamische modellen worden gebruikt als leidraad voor het mengselontwerp van op MBA gebaseerde AAM's (zie *hoofdstuk 4*).

Wanneer waterbehandeling en behandeling met NaOH-oplossing deel uitmaken van de procedure voor de vervaardiging van het mengsel, ligt de druksterkte van de cementpasta's en alkali-geactiveerde pasta's gemaakt van MBA dicht bij die van de pasta's vervaardigd met dezelfde hoeveelheid FA (*hoofdstukken 5 en 6*). Het metallische Al dat niet kan worden verwijderd tijdens mechanische behandelingen kan worden geoxideerd door MBA te behandelen in water of een NaOH-oplossing bij kamertemperatuur. Naast de vermindering van het gehalte aan metallisch Al veranderen de waterbehandeling en de behandeling met de NaOH-oplossing ook enigszins de mineralogische samenstelling van MBA.

Het mengen van *met water behandeld MBA (WMBA)* in portlandcementpasta's leidt tot veranderingen in de reactieproducten en de microstructuur. WMBA vertraagt de hydratatie van het cement op de eerste dag, maar verbetert de hydratatie op latere leeftijden. De reactieproducten van WMBA dragen bij tot de sterkteontwikkeling van samengestelde cementpasta's (zie *hoofdstuk 5*).

*Met NaOH-oplossing behandeld MBA (CMBA)* wordt samen met BFS gebruikt om alkali-geactiveerde (AAM) pasta's te bereiden. CMBA vertraagt de reactie van BFS gedurende de eerste zeven dagen, maar bevordert de reactie van BFS op latere leeftijden. Toevoeging van CMBA aan alkali-geactiveerde pasta's verandert de reactieproducten en de microstructuur. De reactieproducten van CMBA dragen bij aan de sterkteontwikkeling van alkali-geactiveerde pasta's (zie *hoofdstuk 6*).

#### *Milieueffectbeoordeling van cementpasta's en alkali-geactiveerde pasta's met AVI bodemas*

Vergeleken met portlandcementpasta's hebben cementpasta's met SCM's en alkali-geactiveerde pasta's die AVI-bodemas bevatten lagere milieueffecten, vooral in de categorie opwarming van de aarde (zie *hoofdstuk 7*).

*Dit onderzoek verdiept het inzicht in de reactie van AVI-bodemas als SCM- en AAM-precursor. Dit onderzoek toont ook aan hoe AVI-bodemas kan worden gebruikt om cementpasta's en alkali-geactiveerde pasta's te vervaardigen door rekening te houden met de chemische en fysische eigenschappen van MSWI-bodemas. Aangezien de in dit onderzoek gebruikte AVI-bodemas chemische en mineralogische samenstellingen heeft die in hetzelfde bereik liggen als de in de literatuur vermelde AVI-bodemas, stimuleert de in dit werk ontwikkelde kennis het*

*gebruik van in andere regio's geproduceerde AVI-bodemas als SCM- en AAM-precursor voor bouwmaterialen.*

# List of abbreviations

---

(N,C)-A-S-H	Calcium-modified N-A-S-H
AACMBA	Alkali-activated CMBA
AAM	Alkali-activated materials
ASR	Alkali-silica reaction
ATR-FTIR	Attenuated total reflectance-Fourier transform infrared spectroscopy
BFS	Blast furnace slag
BSE	Backscattered electron
C-(N-)A-S-H	Sodium-incorporated calcium aluminosilicate hydrate
C-A-S-H	Calcium aluminosilicate hydrate
CMBA	NaOH solution-treated MBA
C-S-H	Calcium silicate hydrate
CT	X-ray computed tomography
EDS	Energy dispersive X-ray spectroscopy analysis
EPD	Environmental product declaration
FA	Class F coal fly ash
GBA	Ground MSWI bottom ash
IC	Ion chromatography
ICP-AES	Inductively coupled plasma-atomic emission spectroscopy
ICP-OES	Inductively coupled plasma-optical emission spectroscopy
ICSD	Inorganic crystal structure database
LCA	Life cycle assessment
LCI	Life cycle inventory
LCIA	Life cycle impact assessment
LOI	Loss on Ignition
MBA	Mechanically treated MSWI bottom ash
MSW	Municipal solid waste
MSWI	Municipal solid waste incineration
N-(C-)A-S-H	Sodium (calcium) aluminosilicate hydrate

---

N-A-S-H	Sodium aluminosilicate hydrate
PC	Portland cement
QXRD	Quantitative X-ray diffraction
RH	Relative humidity
SCM	Supplementary cementitious material
SCMs	Supplementary cementitious materials
SEM	Scanning electron microscopy
SI	Spectral imaging
TCLP	Toxicity characteristic leaching procedure
TGA	Thermogravimetric analysis
WMBA	Water-treated MBA
XRD	X-ray diffraction
XRF	X-ray fluorescence

# Chapter 1

---

## General introduction



MSWI bottom ash

*This chapter provides a general introduction to this thesis, regarding research background, knowledge gaps, research objectives, research scope, research strategy, and thesis outline.*

## 1.1 Research background

With the continuous growth of populations and economics, municipal solid waste (MSW) generated worldwide is predicted to reach 3.40 billion tonnes by 2050 [1]. This estimated waste generation almost doubles the MSW collected in 2016 (around 2.01 billion tonnes) [1]. At present, the practices used to deal with MSW include recycling, composting, open dump, landfill, and incineration [1]. Among all these waste disposal methods, recycling and composting are considered as the most sustainable solutions [1,2]. Open dump and landfill are unsustainable since they usually lead to pollution of surface water, underground water, soil, and air [3]. Incineration of MSW reduces the amount of waste entering landfills. However, when MSW is burned in the open air, toxic chemicals and pollutants are released, posing risks to the environment and human health. In comparison, modern waste incineration is regarded as sustainable disposal practice, as it has an effective air pollution control system and can generate a significant amount of thermal energy to produce electricity [1,4].

The modern waste incineration treatment is usually performed in waste-to-energy plants, where MSW can be converted into thermal energy at a temperature between 700 and 1100 °C [5–7]. Over the past decades, the amount of MSW incinerated in waste-to-energy plants increased dramatically in the world. For example, in the 27 European Union countries, the MSW treated by incineration rose from 15 % in 1995 to 27 % in 2020 [8]. In China, 62 % MSW was sent to incineration plants in 2020 (146 million tonnes), while only 3 % MSW was incinerated in 2004 (4.5 million tonnes) [9]. It is worth noting that waste incineration cannot reduce the mass of MSW to zero. The mass of the residue produced after MSW incineration can be around 20 % of the waste input [10–12]. The disposal of residues is one of the primary environmental concerns for the wide application of modern waste incineration techniques [13].

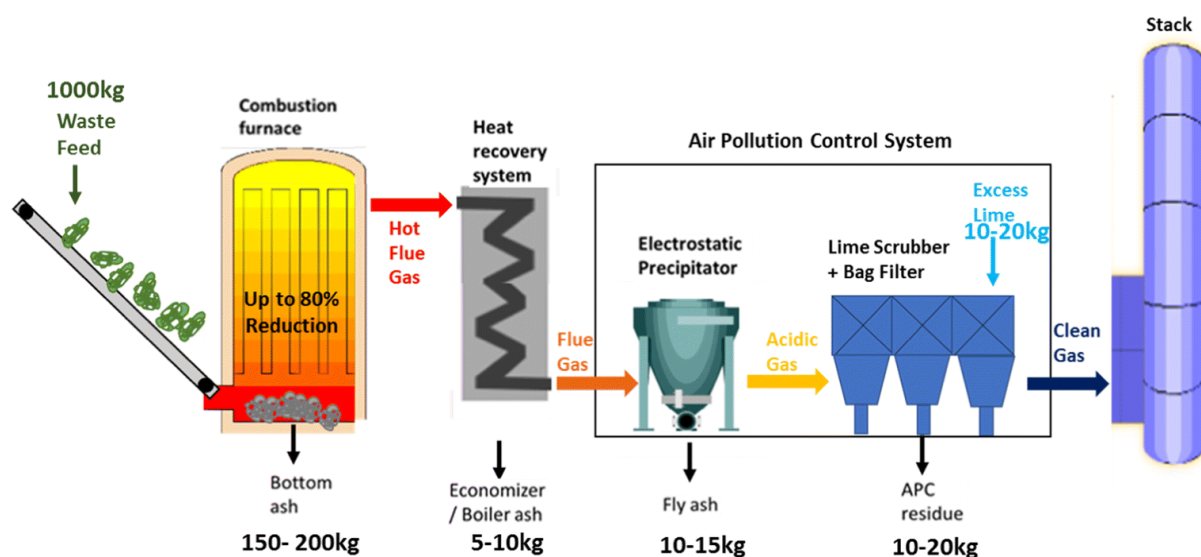


Figure 1.1 Mass balance of the input and output materials of the waste-to-energy plant [12].

As illustrated in Figure 1.1, the incineration of MSW generates three types of residues: bottom ash, fly ash (including the economizer/boiler ash), and air pollution residue [12]. Among these

residues, only bottom ash is generally considered as non-hazardous waste [14]. This municipal solid waste incineration (MSWI) bottom ash, which accounts for around 80 to 90 wt.% of the residues, is usually collected at the bottom of the combustion furnace [15,16]. It is worth exploring the technical feasibility of recycling MSWI bottom ash. One of the main reasons is that more and more MSW is treated with incineration, leading to an increase in the production of MSWI bottom ash [1,2].

The primary constituents in MSWI bottom ash are metals and minerals [17]. The metal scraps in MSWI bottom ash are recyclable and are usually recycled in metal recovery plants. Apart from metal recovery, recycling the minerals in MSWI bottom ash is also important. This action will help to mitigate the depletion of primary mineral resources in the world, as terrestrial mineral deposits are not renewable over human timescales [18]. The minerals in MSWI bottom ash can be used in the production of ceramics [19–24] and construction materials (including cement clinker, aggregates, and binders) [25–31].

It is estimated that the cement industry, in total, contributes around 8 % to the global carbon dioxide (CO<sub>2</sub>) emissions from human activities [32]. Reducing the proportion of clinker in cement can help to reduce the carbon footprints of cement production [33]. In blended cement, 10 to 90 wt.% clinker is substituted by supplementary cementitious materials, mainly blast furnace slag, coal fly ash, and limestone [33]. Replacing Portland cement with alkali-activated materials (AAM) can also reduce 40 to 80 % CO<sub>2</sub> emissions [34–42]. The alkali-activated materials do not contain clinker and are usually prepared by reacting aluminosilicate precursor under alkaline conditions.

At present, blast furnace slag and coal fly ash are the most used supplementary cementitious materials [33] and AAM precursors [43,44]. However, according to the World Business Council for Sustainable Development, the availability of blast furnace slag and coal fly ash is set to decrease in the coming 30 years [45]. A reduction in the supply of blast furnace slag and coal fly ash will inevitably hinder the low-carbon transition of cement industry, thereby increasing the need to explore alternative industrial by-products [46].

MSWI bottom ash is abundant worldwide, and its availability is in the range of massive cement production. The research on MSWI bottom ash as a mineral resource to produce blended cement pastes and alkali-activated pastes<sup>(1)</sup> has attracted increasing interest in recent years. The feasibility of using MSWI bottom ash as supplementary cementitious material (SCM) [27] and AAM precursor [47] has been proved. However, unlike coal fly ash and blast furnace slag, MSWI bottom ash usually contains metallic Al [48–52]. The metallic Al embedded in MSWI bottom ash particles can react in the alkaline environment of blended cement pastes and alkali-activated pastes. The hydrogen gas released after the redox reaction of metallic Al can result in significant volume expansion and strength reduction of the construction materials made from MSWI bottom ash [53,54].

Previous studies mainly focused on improving the engineering properties of the construction materials prepared with MSWI bottom ash. Methods, including mechanical treatments, chemical treatments, and thermal treatments, have been proposed to reduce the metallic Al content and improve the reactivity of MSWI bottom ash [53–57]. However, the intrinsic properties of MSWI bottom ash, such as the chemical composition of the reactive phases and

---

<sup>(1)</sup> Alkali-activated pastes, alkali-activated mortars, and alkali-activated concretes all belong to alkali-activated materials.



the distribution of metallic Al in MSWI bottom ash particles, are rarely considered in the selection of quality upgrade methods and mix design. Currently, the requirements of MSWI bottom ash being used as SCM and AAM precursor are not specified. The reaction of MSWI bottom ash in blended cement pastes and alkali-activated pastes has not been fully understood yet. Very few studies have assessed the environmental impacts of the construction materials prepared using MSWI bottom ash as a mineral resource.

## 1.2 Knowledge gaps

The following knowledge gaps need to be addressed to promote the utilization of MSWI bottom ash as a mineral resource for construction materials.

- The determination of acceptable metallic Al content in MSWI bottom ash as SCM and AAM precursor is necessary. The chemical properties of the reactive phases in MSWI bottom ash need to be fully understood. The quality-upgrade treatments of MSWI bottom ash should be selected according to the characteristics of received MSWI bottom ash and the requirements for the application in blended cement and AAM.
- The changes in the composition and the molecular structure of MSWI bottom ash during the quality-upgrade treatments need to be fully understood. The reaction products formed during the quality-upgrade treatments can affect the reaction of MSWI bottom ash in blended cement pastes and alkali-activated pastes.
- An in-depth understanding of the reaction of MSWI bottom ash in blended cement pastes and alkali-activated pastes is required to understand the contribution of MSWI bottom ash to the microstructure formation and strength development. The environmental impacts of the construction materials prepared with MSWI bottom ash as SCM and AAM precursor also need to be assessed. This information can help evaluate the value of using MSWI bottom ash as mineral additives.

## 1.3 Research objectives

The aim of this research is to provide a theoretical basis for the use of MSWI bottom ash as a mineral resource for construction materials. The MSWI bottom ash produced in the Netherlands with a particle size of 4 to 11 mm is studied in this work. According to the Dutch supplier of MSWI bottom ash, there will be more willingness to accept this size fraction as an ingredient for construction materials. This is because compared with the 4 - 11 mm size fraction, the size fraction below 4 mm contains more hazardous heavy metals and organics. The MSWI bottom ash particles larger than 11 mm are enriched with metals and un-burned organics. The specific objectives defined in this work are as follows:

- To develop knowledge that can be used to guide the selection of quality-upgrade treatments and the mix design when MSWI bottom ash is used to prepare blended cement pastes and alkali-activated pastes.
- To improve the quality of MSWI bottom ash and realize its utilization in blended cement pastes and alkali-activated pastes as an alternative to Class F coal fly ash.

- To provide insight into the reactive phases in MSWI bottom ash and assess the reactivity of MSWI bottom ash as SCM and AAM precursor.
- To understand the reaction kinetics and the microstructure formation of MSWI bottom ash blended Portland cement pastes and the alkali-activated pastes prepared with blends of MSWI bottom ash and blast furnace slag.
- To evaluate the advantages of producing blended Portland cement pastes and alkali-activated pastes with MSWI bottom ash in terms of environmental impacts.

## 1.4 Research scope

The primary goal of this research is to investigate the reaction of MSWI bottom ash as SCM and AAM precursor in pastes. It would be too complicated to introduce aggregates or additives into the cement or AAM system and to analyze all the influencing factors of microstructure formation. Therefore, the experimental work is restricted as follows:

1. Only paste samples are studied in this research.
2. No admixtures are used for the sample preparation.
3. All cement paste samples are prepared with water-to-binder ratio of 0.4.
4. All alkali-activated paste samples are prepared with water-to-binder ratio of 0.35.
5. All paste samples are sealed and cured in a fog room (20 °C, 99 % relative humidity (RH)) before the measurements.

## 1.5 Research strategy

The experiments and analyses performed in this work focus on the following aspects to achieve the goal of this research.

- Characterization and quality-upgrade treatments of as-received MSWI bottom ash

As-received MSWI bottom ash is characterized to identify the issues hindering its application as SCM and AAM precursor. Mechanical treatments are studied and selected to address the following issues: heterogeneous compositions, particle size in the range of fine aggregates, and incorporation of metallic Al.

- Characterization of *mechanically treated MSW bottom ash (MBA)*

Prior to the use of MBA in blended cement and AAM, the reactivity of MBA as SCM and AAM precursor is measured and compared with blast furnace slag (BFS) and Class F coal fly ash (FA). The leaching of contaminants from MBA is also assessed. The characterization results are used in the mix design of MSWI bottom ash blended cement pastes and alkali-activated pastes.

- Development of blended cement pastes and alkali-activated pastes with MBA

The target of sample preparation is to make the compressive strength of the pastes prepared with MBA close to that of the pastes made from FA. According to the application of MBA, different methods are used to reduce the metallic Al content in MBA during the sample

preparation process, like water treatment and NaOH solution treatment. Water treatment is performed when MBA is used as SCM. NaOH solution treatment is applied when MBA is used as AAM precursor. The reactions of MBA during water treatment or NaOH solution treatment are studied to detect the possible formation of reaction products.

- Characterization of the pastes prepared with MBA as SCM and AAM precursor

The reaction kinetics and microstructure formation of Portland cement pastes blended with *water-treated MBA (WMBA)* and alkali-activated pastes prepared with blends of *NaOH solution-treated MBA (CMBA)* and BFS are studied to reveal the contribution of MSWI bottom ash to the development of compressive strength.

- Life cycle assessment of the pastes prepared with MBA as SCM and AAM precursor

The environmental impacts of Portland cement pastes blended with WMBA (WMBA CEM) and alkali-activated pastes prepared with blends of CMBA and BFS (CMBA-BFS AAM) are compared with those of Portland cement paste with similar compressive strength. The life cycle assessment data can be used to evaluate whether the techniques proposed in this work for recycling MSWI bottom ash are eco-friendly.

## 1.6 Thesis outline

As illustrated in Figure 1.2, this thesis consists of eight chapters.

In **Chapter 1**, the background, objects, scope, and methodology of this research are introduced.

In **Chapter 2**, previous studies related to the utilization of MSWI bottom ash as SCM and AAM precursor are reviewed. The following aspects are covered for MSWI bottom ash: plant-scale and lab-scale treatments, chemical and mineralogical compositions, and reactivity as SCM and AAM precursor. Information about the mix design, microstructure, mechanical properties, risks of contaminant leaching, and environmental impacts of construction materials prepared with MSWI bottom ash as SCM and AAM precursor are also included in the literature study.

In **Chapter 3**, as-received MSWI bottom ash is characterized in terms of its particle size and composition. Special attention is given to the content and distribution of metallic Al in as-received MSWI bottom ash. The mechanical treatments are studied and selected to transform as-received MSWI bottom ash into fine powders that can be used as SCM and AAM precursor. The effectiveness of mechanical treatments in removing metallic Al from MSWI bottom ash is discussed.

In **Chapter 4**, the reactivity of MBA as SCM and AAM precursor is measured and compared with that of BFS and FA. Thermodynamic modeling is used to predict the assemblage of reaction products and the composition of pore solution in alkali-activated MBA paste when changing the Na<sub>2</sub>O content in the activator. The modeling results of alkali-activated MBA paste are compared with those of alkali-activated BFS paste and alkali-activated BFS paste. The leaching of contaminants from MBA is also discussed. Based on the experimental and modeling results, remarks are made regarding how to use MBA in blended cement pastes and alkali-activated pastes.

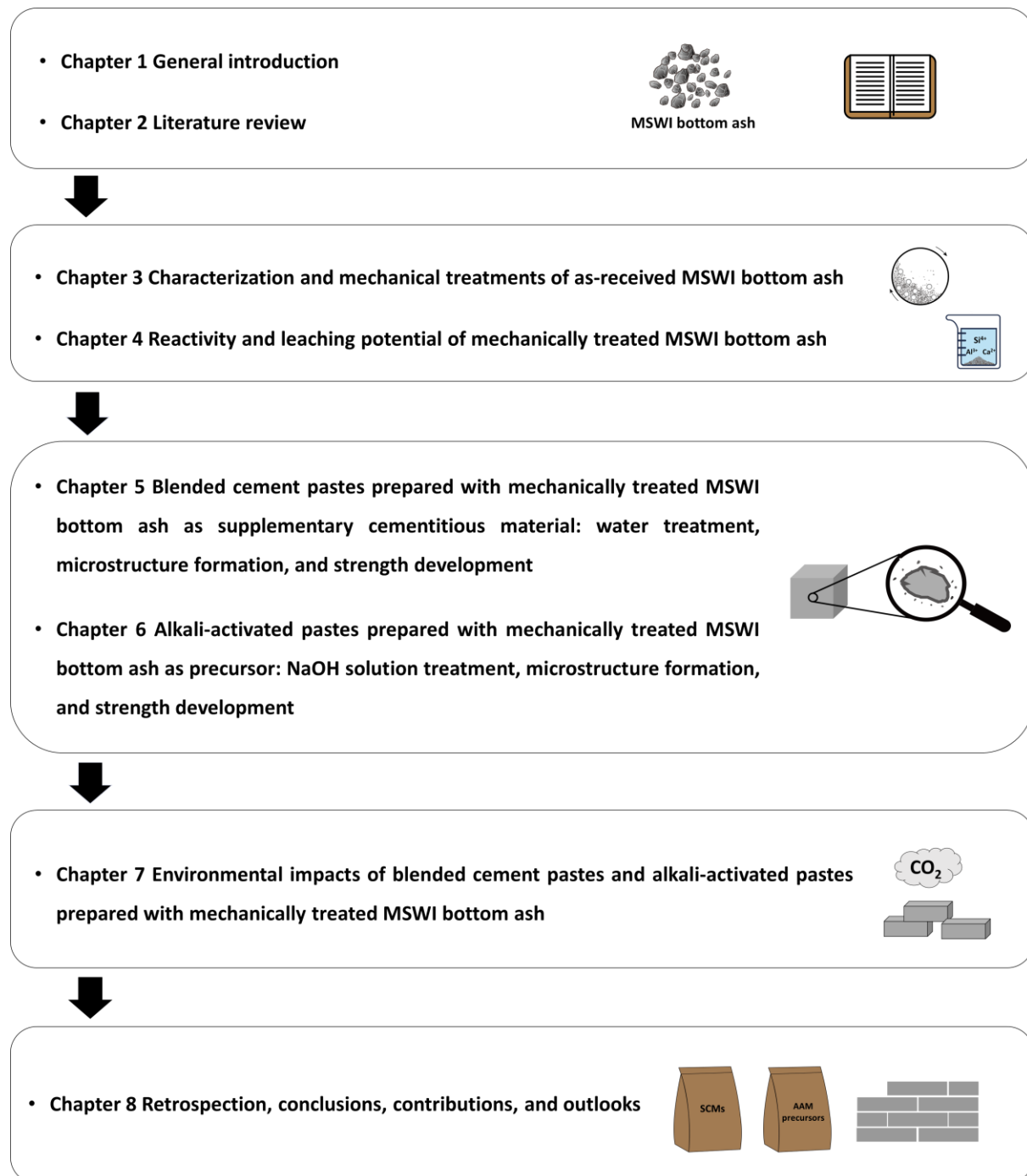


Figure 1.2 Thesis outline.

In **Chapter 5**, MBA after water treatment is used to prepare blended cement pastes. The effectiveness of water treatment in lowering the metallic Al content of MBA is examined. The reaction of MBA during water treatment is studied. Paste samples are prepared by blending *water-treated MBA* with Portland cement. The compressive strength of blended cement pastes prepared with *water-treated MBA* is compared with that of the blended cement made from the same amount of FA. The contribution of *water-treated MBA* to microstructure formation and strength development of blended cement pastes is investigated.

In **Chapter 6**, MBA after NaOH solution treatment is used to prepare alkali-activated pastes. The effectiveness of NaOH solution treatment in reducing the metallic Al content of MBA is demonstrated. The reaction of MBA during NaOH solution treatment is studied. The alkali-activated paste under investigation is a binary system composed of *NaOH solution-treated MBA* and blast furnace slag. The compressive strength of alkali-activated pastes prepared with *NaOH solution-treated MBA* is compared with that of the alkali-activated pastes made from the same amount of FA. The effects of *NaOH solution-treated MBA* on microstructure formation and strength development of alkali-activated pastes are analyzed.

In **Chapter 7**, the environmental impacts of MSWI bottom ash blended Portland cement pastes and alkali-activated pastes prepared with blends of MSWI bottom ash and BFS are assessed. The life cycle impact assessment results are compared with the environmental impacts of Portland cement paste and the pastes prepared with FA.

In **Chapter 8**, the main findings of Chapters 3 to 7 are summarized. Remarks about how to use MSWI bottom ash as SCM and AAM precursor are presented. Recommendations for further research in this field are proposed.

# Chapter 2

---

## Literature review



*This chapter reviews the literature on the use of MSWI bottom ash as supplementary cementitious material (SCM) and precursor for alkali-activated materials (AAM). The challenges of recycling MSWI bottom ash as SCM and AAM precursor are also discussed.*

## 2.1 Introduction

In this chapter, an overview of the literature is provided for using MSWI bottom ash as supplementary cementitious material (SCM) in blended cement and as precursor for alkali-activated materials (AAM). The plant- and lab-scale treatments used to improve the quality of municipal solid waste incineration (MSWI) bottom ash are introduced. The chemical and mineralogical compositions of treated MSWI bottom ash sourced from different regions are summarized. Information is collected on the reactivity of MSWI bottom ash, as well as on the mix design, reaction kinetics, and reaction products of hardened blended cement pastes and AAM. Based on the current state of the art, challenges concerning the use of MSWI bottom ash as SCM and AAM precursor are discussed.

## 2.2 Properties of fresh MSWI bottom ash

Fresh MSWI bottom ash is referred to as the ash collected upon its discharge from the bottom of the municipal solid waste incinerator. In most waste-to-energy plants worldwide, MSWI bottom ash is discharged wet, also known as water quenching [58]. The wet-discharged fresh MSWI bottom ash consists of moist granulates with typical particle sizes ranging from 0.1 to 100 mm [6,59,60]. The composition of wet-discharged fresh MSWI bottom ash shows considerable heterogeneity. The materials found in wet-discharged fresh MSWI bottom ash can be broadly classified as glass cullet, synthetic ceramic fragments, minerals (quartz, calcite, lime, feldspars), metals (both paramagnetic and diamagnetic), and unburned organic materials (paper, textiles, plastics) [15].

Apart from heterogeneous composition, wet-discharged fresh MSWI bottom ash also has unstable phase assemblage and high leaching of contaminants into the environment, making its application as an ingredient for construction materials challenging. The phase assemblage of wet-discharged fresh MSWI bottom ash is generally in the metastable state under natural environmental conditions [17]. The phase alteration process immediately starts after quenching the hot bottom ash and will continue if the bottom ash remains wet [61–63]. The wet-discharged fresh MSWI bottom ash has a pH close to that of saturated portlandite solution [64–66]. At a pH above 12, lead (Pb), zinc (Zn), and copper (Cu) are the primary heavy metals that leach out from fresh MSWI bottom ash [65].

## 2.3 Plant-scale treatments of fresh MSWI bottom ash

Fresh MSWI bottom ash is usually treated at the plant to recycle metal scraps and reduce the leaching of heavy metal ions into the environment. In this context, the treatments performed at the plant are referred to as “plant-scale treatments”. The plant-scale treatments of fresh MSWI bottom ash vary from plant to plant. Figure 2.1 summarizes the plant-scale treatments usually performed on fresh MSWI bottom ash. These treatments include particle size reduction, metal extraction, stabilization, cleaning, and classification. As illustrated in Figure 2.1, each plant-scale treatment is carried out through corresponding techniques.

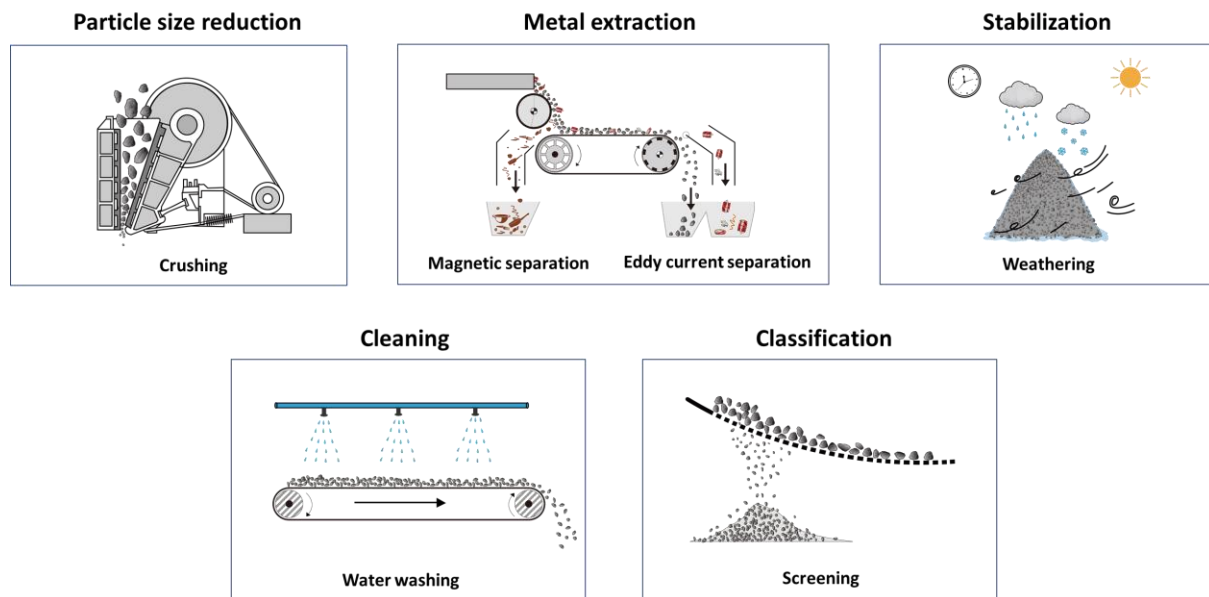


Figure 2.1 Plant-scale treatments and corresponding techniques.

### *Particle size reduction*

The particle size of fresh MSWI bottom ash is reduced by crushing. This treatment aims to liberate the constituents that bond together during the incineration process. After pulverization, the material separation and classification become viable.

### *Metal extraction*

The goal of metal extraction is to recover ferrous and non-ferrous metals. Magnetic separators are often used to extract Fe-enriched magnetic fractions [59,67]. Eddy current separators are developed to separate conductive metals, especially aluminum and copper [59,67].

### *Stabilization*

Fresh MSWI bottom ash is stabilized by weathering, which is also called aging. Weathering with a duration of one to three months [47,57,76–82,68–75] is regarded as the most economical treatment available to stabilize fresh MSWI bottom ash. This process can be conducted before or after metal extraction [60,83–85]. During weathering, fresh MSWI bottom ash is stacked in a heap of 5 to 10 meters high and is exposed to the wind and rain in the open air for months [60,83]. The fresh MSWI bottom ash stockpiles readily react with the oxygen, carbon dioxide, and water present in the environment. The reactions that can occur include dissolution and precipitation of salts, corrosion of the vitreous phases, and hydration and oxidation of the metal fragments [61].

The main purpose of stabilizing fresh MSWI bottom ash is to reduce the risk of heavy metal leaching. Fresh MSWI bottom ash usually has a pH ranging from 12.2 to 12.6 [64–66]. After one month of weathering, the pH drops to around 10.3 [64]. This pH decrease starts to slow down at the age of two months [64]. At 90 days, the pH falls within the range of 9.6 to 9.8 [65]. Within one and a half years, the pH can reach the lowest value, between 8 to 8.5. This value remains unchanged until the twelfth year [66]. The decrease of pH in fresh MSWI



bottom ash, from high alkaline ( $\geq 12$ ) to almost neutral ( $\approx 8 - 8.5$ ), could prevent the redissolution of metal hydroxides, one of the main causes of heavy metal leaching from fresh MSWI bottom ash [65]. After the weathering process, the leaching of heavy metals, such as Pb, Zn, Ba, and Mo, was significantly reduced [61,62,65,66,81,86–88].

### *Cleaning and classification*

Cleaning by water washing is to remove the fine contaminants attached to the coarse MSWI bottom ash particles. Classification is realized by mechanical screening, where MSWI bottom ash is separated into multiple grades according to particle size. By adjusting the sieving mesh size, the optimal particle size distribution similar to the natural aggregates can be obtained [84].

## **2.4 Compositions of weathered MSWI bottom ash**

Compared with fresh MSWI bottom ash, weathered MSWI bottom ash produced after plant-scale treatments shows greater potential for being used as an ingredient for construction materials due to its lower leaching of contaminants. The compositions of weathered MSWI bottom ash determine its reactivity as SCM and precursor for AAM. The chemical and mineralogical compositions of weathered MSWI bottom ash used in previous research are summarized in this section. The composition of weathered MSWI bottom ash is also compared with that of Portland cement clinker, blast furnace slag (BFS), and coal fly ash (both Class C and Class F). BFS and coal fly ash are the most commonly used supplementary cementitious materials [33] and AAM precursors [43,44].

### **2.4.1 Chemical composition**

The chemical compositions of weathered MSWI bottom ash were taken from the X-ray fluorescence (XRF) results. Figure 2.2 compares the contents of the main components in the weathered MSWI bottom ash sourced from different regions. The weathered MSWI bottom ash came from Belgium [48,89], China [90–92], France [93,94], the Netherlands [53,68–70,82,95,96], Spain [47,79], the United Kingdom (UK) [57,73–76], and the United States (US) [62]. The ranges of all the components in weathered MSWI bottom ash are given in Table 2.1, together with those of coal fly ash (both Class C and Class F), BFS, and Portland cement clinker.

### *Main components*

The main components in weathered MSWI bottom ash are  $\text{SiO}_2$ ,  $\text{CaO}$ ,  $\text{Al}_2\text{O}_3$ , and  $\text{Fe}_2\text{O}_3$ . These four components together account for more than 60 % of the total weight of weathered MSWI bottom ash (Figure 2.2 (a)). The weight percentages of  $\text{SiO}_2$ ,  $\text{CaO}$ ,  $\text{Al}_2\text{O}_3$ , and  $\text{Fe}_2\text{O}_3$  were plotted in the  $\text{SiO}_2$  -  $\text{CaO}$  -  $\text{Al}_2\text{O}_3$  and  $\text{SiO}_2$  -  $\text{CaO}$  -  $\text{Fe}_2\text{O}_3$  ternary diagrams after renormalization to 100 %. The ternary diagram graphically depicts the ratios of three components as positions in an equilateral triangle. As illustrated in Figure 2.2 (b) and (c), all the dots in the ternary diagrams are far from the vertex representing 100 %  $\text{Al}_2\text{O}_3$  and 100 %  $\text{Fe}_2\text{O}_3$ . This observation indicates that the percentage of  $\text{Al}_2\text{O}_3$  or  $\text{Fe}_2\text{O}_3$  is much lower than that of  $\text{SiO}_2$  or  $\text{CaO}$  in weathered MSWI bottom ash. Most of the dots in the ternary diagram are in the region where

the percentage of  $\text{SiO}_2$  is larger than that of  $\text{CaO}$ , indicating that most of the weathered MSWI bottom ash contains more  $\text{SiO}_2$  than  $\text{CaO}$ .

The contents of  $\text{SiO}_2$ ,  $\text{CaO}$ ,  $\text{Al}_2\text{O}_3$ , and  $\text{Fe}_2\text{O}_3$  in weathered MSWI bottom ash are within the same range as those in coal fly ash, especially the type of Class C (see Table 2.1). The  $\text{SiO}_2$  content of weathered bottom ash varies from 10.2 to 59.3 wt.%. This significant variation can also be observed in the  $\text{SiO}_2$  content of coal fly ash (both Class C and Class F) [97]. The weathered MSWI bottom ash contains 13.6 to 48.1 wt.%  $\text{CaO}$ , almost the same as Class C coal fly ash. The  $\text{Al}_2\text{O}_3$  content in weathered MSWI bottom ash ranges from 4.2 to 16.3 wt.%, which is close to that in Class C coal fly ash (between 2.6 and 20.5 wt.%), but much lower than that in Class F coal fly ash (between 16.6 and 35.6 wt.%) [97]. In weathered MSWI bottom ash, the  $\text{Fe}_2\text{O}_3$  content varies from 1.3 to 20.2 wt.%, similar to the situation in coal fly ash (both Class C and Class F).

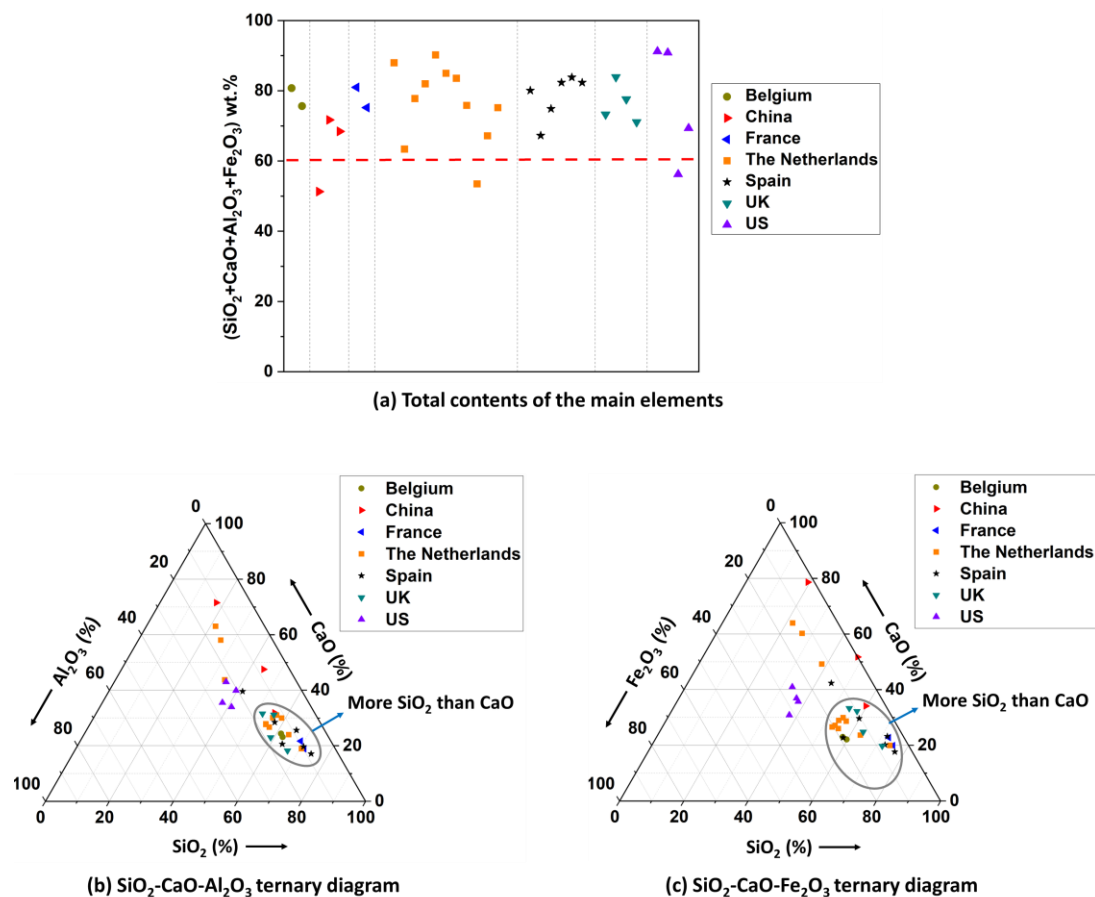


Figure 2.2 Comparison of the main components in weathered MSWI bottom ash produced in Belgium [48,89], China [90–92], France [93,94], the Netherlands [53,68–70,82,95,96], Spain [47,79], the UK [57,73–76], and the US [62]. The ternary diagram is plotted according to the weight percentages of the oxides.

Table 2.1 Ranges of the components present in weathered MSWI bottom ash [47,48,75,76,79,82,89–92,95,96,53,57,62,68–70,73,74], coal fly ash [97], granulated blast furnace slag [98], and Portland cement clinker [99].

Compound (wt.%)	Weathered MSWI bottom ash	Class C coal fly ash	Class F coal fly ash	Granulated blast furnace slag	Portland cement clinker
SiO <sub>2</sub>	10.2 - 59.3	11.8 - 46.4	37 - 62.1	30 - 40	21
CaO	13.6 - 48.1	15.1 - 54.8	0.5 - 14	30 - 50	67
Al <sub>2</sub> O <sub>3</sub>	4.2 - 16.3	2.6 - 20.5	16.6 - 35.6	7 - 20	6
Fe <sub>2</sub> O <sub>3</sub>	1.3 - 20.2	1.4 - 15.6	2.6 - 21.2	0 - 2.5	3
Na <sub>2</sub> O	0.0 - 8.1	0.2 - 2.8	0.1 - 3.6	-	-
Na <sub>2</sub> O <sub>e</sub>	0.8 - 9.0	-	-	-	0.7
MgO	1.6 - 3.3	0.1 - 6.7	0.3 - 5.2	0 - 21	1
SO <sub>3</sub>	0.6 - 6.8	1.4 - 12.9	0.2 - 4.7	-	≤ 3.5 - 4*
S	-	-	-	0 - 2	-
P <sub>2</sub> O <sub>5</sub>	0.3 - 3.5	0.2 - 0.4	0.1 - 1.7	-	-
TiO <sub>2</sub>	0.3 - 2.5	0.6 - 1.0	0.5 - 2.6	-	-
K <sub>2</sub> O	0.4 - 3.7	0.3 - 9.3	0.1 - 4.1	-	-
ZnO	0.2 - 1.3	-	-	-	-
CuO	0.1 - 0.9	-	-	-	-
Cl	0.1 - 9.5	-	-	-	≤ 0.1*
MnO	0.1 - 1.9	0.03 - 0.2	0.03 - 0.1	0.2 - 2.5	< 0.5
PbO	0.2 - 0.4	-	-	-	-
LOI	2.7 - 30	0.3 - 11.7	0.3 - 32.8	-	< 3

\*Value required by standard EN196-2 [100]

### Soluble salts

The contents of Cl, Na<sub>2</sub>O, K<sub>2</sub>O, and SO<sub>3</sub> are higher in weathered MSWI bottom ash than in Portland cement clinker (see Table 2.1), indicating that weathered MSWI bottom ash contains more soluble salts. The chloride content in weathered MSWI bottom ash is above the upper limit (0.1 wt.%) of Portland cement clinker, as set by the EN196-2 standard [100]. The equivalent sodium oxide (% Na<sub>2</sub>O<sub>e</sub> = % Na<sub>2</sub>O + 0.658 × % K<sub>2</sub>O) content of weathered MSWI bottom ash is between 0.8 and 9.0 wt.%, whereas this value changes within the range of 0.22 to 1.06 wt.% for Portland cement clinker [101]. The amount of SO<sub>3</sub> in weathered MSWI bottom ash is between 0.6 - 6.8 wt.%. Among available data, three types of weathered MSWI bottom ash exceed the upper limit of SO<sub>3</sub> content (3.5 - 4 wt.%) specified in the standard (EN196-2) [47,53,92].

The excessive soluble salts in weathered MSWI bottom ash may influence its application as SCM. Replacing Portland cement with weathered MSWI bottom ash could dramatically increase the contents of chloride, alkalis, and SO<sub>3</sub> in the binder of Portland cement concrete or mortar. An increase in chloride content can increase the risk of steel corrosion in Portland cement concrete [99]. Increasing the alkali content in binder could make the Portland cement concrete more susceptible to deterioration caused by alkali-silica reaction (ASR) [99]. The higher SO<sub>3</sub> content in the binder of Portland cement concrete may cause late formation of crystalline ettringite, resulting in expansion and cracking of hardened pastes [99].

The chloride content in weathered MSWI bottom ash is higher than in coal fly ash (both Class C and Class F) and BFS (see Table 2.1). Compared with coal fly ash and BFS, using weathered MSWI bottom ash to prepare AAM may increase the risk of steel corrosion in alkali-activated concrete. As shown in Table 2.1, the contents of  $\text{Na}_2\text{O}$  and  $\text{K}_2\text{O}$  are higher in weathered MSWI bottom ash than in BFS. Compared with coal fly ash (both Class C and Class F), the  $\text{Na}_2\text{O}$  content in weathered MSWI bottom ash changes within a wider range, indicating that the alkalinity of weathered MSWI bottom ash can be higher. In this case, replacing BFS or coal fly ash with weathered MSWI bottom ash in alkali-activated concrete and mortar may raise the risk of ASR-induced deterioration when reactive aggregates are used. The  $\text{SO}_2$  content in weathered MSWI bottom ash is close to that in Class F coal fly ash (see Table 2.1). The risk associated with late formation of ettringite may not be a problem when weathered MSWI bottom ash is used as AAM precursor. In previous studies, ettringite was not formed in the AAM prepared with weathered MSWI bottom ash [29,102].

#### *Heavy metal and organics*

As shown in Table 2.1, the content of components related to the heavy metals in weathered MSWI bottom ash is generally higher than that in Portland cement clinker, BFS, and coal fly ash (both Class C and Class F). Using weathered MSWI bottom ash as SCM or AAM precursor poses the risks of soil and underground water contamination due to excessive leaching of heavy metals [29,102,103].

The organics in MSWI bottom ash also contribute to heavy metal leaching from MSWI bottom ash, such as the leaching of Cu from humic acid-bound Cu and fulvic acid-bound Cu [104,105]. The content of organic matter in weathered MSWI bottom ash is usually determined by the LOI (Loss on Ignition) method at a temperature of 500-550 °C [106]. The organic matter detected by previous researchers varies from 2.7 to 30 wt.% [53,62,82,96].

The LOI value in weathered MSWI bottom ash is similar to Class F coal fly ash [97]. The polycyclic aromatic hydrocarbons (PAHs) adsorbed in coal fly ash are the main organic compounds harmful to the environment and human health, due to their toxicity, mutagenicity, and carcinogenicity [107]. This is different from the situation in MSWI bottom ash. Until now, there is no research indicating that organic compounds are responsible for heavy metal leaching from coal fly ash.

## **2.4.2 Mineralogical composition**

#### *Crystalline phases*

The mineralogical composition of weathered MSWI bottom ash is mainly determined by three factors: composition of the original waste feed, incineration techniques, and weathering strategies. Weathered MSWI bottom ash contains a wide variety of minerals, which can be classified into 11 categories (Table 2.2). These categories are silicon dioxide ( $\text{SiO}_2$ ), iron oxides ( $\text{FeOx}$ ), silicates, carbonates, sulfates, chloride salts, phosphates, non-ferrous metal oxides, hydroxides, sulfides, and other minerals. The minerals that belong to silicates are further divided into four sub-groups: melilite, feldspar, pyroxene, and other silicates. The group named "other minerals" includes minerals that are unique in specific kinds of bottom ash and

only present in rare cases. The detection of quartz, calcite, silicates, and iron oxides is most frequently reported in the literature (see Table 2.2).

Table 2.2 Classifications of minerals present in weathered MSWI bottom ash.

Categories		Typical minerals
1	Silicon dioxide ( $\text{SiO}_2$ )	Quartz [25,29,76,79,81,86,87,89,90,92,93,96,47,102,108–112,48,62,70–74] Cristobalite [17,47,81,108,109]
2	Iron oxides ( $\text{FeO}_x$ )	Magnetite and hematite [25,29,81,86,89,93,96,108,110–113,47,114,48,62,66,70,72,73,76] Wustite [47,48,66,72,81,93,110–112]
3	Melilite	Gehlenite and akermanite [25,29,86,87,89,93,96,102,108,110,114,47,48,62,70–73,81]
	Feldspar	Albite and anorthite [25,47,48,62,87,89,92,96,102,112]
	Pyroxene	Diopside and wollastonite [29,47,71,72,81,86,93,110]
	Other silicates	Mullite [47,90,115], zeolite [17,110]
4	Carbonates	Calcite [25,29,79,81,86,87,89,90,92,96,102,108,47,109–114,48,70–74,76] Dolomite [25,82,102,108]
5	Sulfates	Ettringite, gypsum, and anhydrite [48,62,96,102,108–111,71,72,81,86,87,89,92,93]
6	Chloride salts	Halite ( $\text{NaCl}$ ) and sylvite ( $\text{KCl}$ ) [25,48,71,86,87,92,96,116–118]
7	Phosphates	-
8	Non-ferrous metal oxides	Rutile [17,25,110], corundum [17], zincite [66]
9	Hydroxides	<ul style="list-style-type: none"> <li>Iron hydroxide</li> </ul> Goethite [62,111], lepidocrocite [17,111], ferrihydrite [119] <ul style="list-style-type: none"> <li>Aluminum hydroxide</li> </ul> Gibbsite [17,71,109,113]
10	Sulfides	Copper sulfides [17,120], iron sulfides [17]
11	Other minerals	-

Rietveld-based quantitative X-ray diffraction (QXRD) analysis is widely used to evaluate the abundance of individual crystalline phase and calculate the amount of amorphous phase in weathered MSWI bottom ash. Table A 1<sup>(2)</sup> summarizes the results of QXRD analyses of weathered MSWI bottom ash. The quartz content in weathered MSWI bottom ash can vary from 4.7 to 21 wt.%. The weight percentage of quartz is usually higher than that of other crystalline phases detected in weathered MSWI bottom ash. However, in the fine fraction (<

<sup>(2)</sup> Table A 1 is put in appendix A because it is a long table.

2 mm) of weathered MSWI bottom ash produced in the Netherlands [110] and Spain [112], calcite is the most abundant crystalline phase. There is a significant difference in the calcite content of weathered MSWI bottom ash collected from different regions. The weathered MSWI bottom ash can contain 0.9 to 22.7 wt.% calcite. The total silicate content in weathered MSWI bottom ash is generally below 15 wt.%. The silicates commonly found in MSWI bottom ash are gehlenite, akermanite of the melilite group, albite, anorthite of the feldspar group, and diopside, wollastonite of the pyroxene group. Weathered MSWI bottom ash usually contains less than 5 wt.% iron oxides, of which magnetite is the largest component.

### *Amorphous phase*

The amorphous phase makes up 30.8 to 81.3 wt.% of the weathered MSWI bottom ash used in previous research (see Table A 1). The amorphous content in weathered MSWI bottom ash can be similar to that in coal fly ash, as the amorphous content in coal fly ash ranges between 50 and 95 wt.% [121]. However, the amorphous phase in weathered MSWI bottom ash is less than that in BFS, which usually contains more than 90 wt.% amorphous phase [122,123]. The amorphous phase is the primary reactive phase in weathered MSWI bottom ash [28,54]. Given that the content of CaO, Al<sub>2</sub>O<sub>3</sub>, and SiO<sub>2</sub> in the amorphous phase determines the reactivity of coal fly ash and BFS [124], the reactivity of weathered MSWI bottom ash may also depend on the chemical composition of its amorphous phase. It is worth noting that previous studies mainly focused on quantifying the amorphous phase. The chemical composition of this phase was rarely examined.

### *Metallic Al and Zn*

Unlike coal fly ash and BFS, weathered MSWI bottom ash can contain metallic Al and Zn. The metals detected in weathered MSWI bottom ash are residues that cannot be removed during the metal extraction process of plant-scale treatments [85]. Metallic Al and Zn oxidize under the alkaline conditions in blended cement pastes and alkali-activated pastes. This redox reaction releases hydrogen gas, resulting in volume expansion and strength reduction of hardened pastes [53,54]. In previous research, metallic Zn is only detected in fresh MSWI bottom ash and is present in the form of Al-Zn alloy [55]. The detection of metallic Zn is not reported in the studies of weathered MSWI bottom ash. Only the metallic Al content of weathered MSWI bottom ash is mentioned in the literature (see Table 2.3).

The content of residual metallic Al is usually measured with the water displacement method [74]. In this test, weathered MSWI bottom ash is immersed in sodium hydroxide (NaOH) solution, and the hydrogen gas released after the oxidation of metallic Al is collected. The volume of hydrogen gas is measured and used to calculate the percentage of metallic Al by following the stoichiometry of the equation  $2\text{Al} + 2\text{NaOH} + 6\text{H}_2\text{O} \rightarrow 2\text{NaAl(OH)}_4 + 3\text{H}_2 \uparrow$ . As shown in Table 2.3, the metallic Al content is below 2 wt.% in weathered MSWI bottom ash used in previous research. There is a wide variation in the percentage of metallic Al in MSWI bottom ash produced in different countries. The variation in the content of metallic Al is mainly caused by the difference in the composition of municipal solid waste, the metal recovery process, and particle size.

Table 2.3 Metallic Al content in weathered MSWI bottom ash produced in different countries.

Countries	Particle size (mm)	Metallic Al content (wt.%)	References
Belgium	0 - 2	1.5	[56]
	2 - 6	0.64	
	6 - 15	0.24	
	< 8	1.1	[81]
Canada	unknown	0.06	[125]
China	< 2.36	0.048	[91]
Germany	2 - 8	1.22	[78]
	8 - 16	1.59	
	16 - 32	1.06	
Spain	0 - 1	0.38	[112]
	1 - 2	1.16	
The Netherlands	< 2	0.44	[53]
	0 - 2	0.8	[126]
	1 - 4	0.1	[96]
	0.25 - 1	0.13	
	< 0.25	0.12	

## 2.5 Lab-scale treatments

In contrast to the plant-scale treatments discussed in section 2.3, the treatments performed in the laboratory are referred to as “lab-scale treatments”. The goal of lab-scale treatments is to improve the quality of MSWI bottom ash and enable its application as SCM and AAM precursor. Previous work tailored the lab-scale treatments according to the chemical and physical properties of the fresh or weathered MSWI bottom ash. Most of the MSWI bottom ash sent to the laboratory is produced after the plant-scale treatments of fresh MSWI bottom ash.

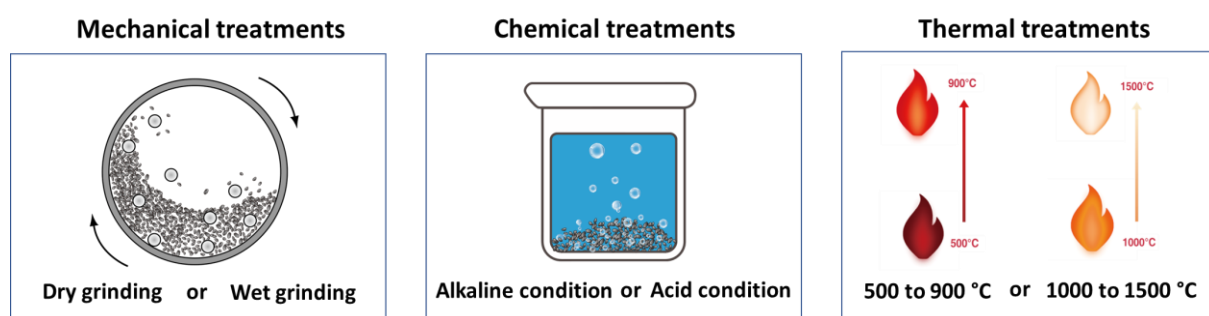


Figure 2.3 Lab-scale treatments proposed to improve the quality of MSWI bottom ash for the application as SCM and AAM precursor.

During lab-scale treatments, the following issues of MSWI bottom ash can be addressed: heterogeneous composition, presence of hazardous components (such as metallic Al, soluble salts, and heavy metals), and low reactivity. Lab-scale treatments can be classified into mechanical treatments, chemical treatments, and thermal treatments (see Figure 2.3). In the



following sections, the details of each method are introduced. The type of MSWI bottom ash (fresh or weathered) will only be mentioned when this information is included in the literature.

### 2.5.1 Mechanical treatments

Most of the mechanical treatments proposed in previous work consist of dry grinding and sieving. The goal of mechanical treatments is mainly to reduce particle size and obtain a homogeneous composition. Due to size reduction, the surface area of MSWI bottom ash is increased after grinding, resulting in improved reactivity. Sieving is performed after grinding to examine the particle size of ground MSWI bottom ash.

Metals embedded in MSWI bottom ash particles can also be removed during mechanical treatments. Current experience indicates that the effect of mechanical treatments on metal removal strongly depends on the parameter setting of the ball mill [127]. Short-time, low-speed dry milling of MSWI bottom ash is recommended, which can break brittle minerals into small fragments and meanwhile press ductile metals into plate-shaped scraps, making it easy to sieve out the metals [53,126]. Plate-shaped metal scraps sieved out from milled MSWI bottom ash are illustrated in Figure 2.4. Chen et al. [126] and Sun et al. [128] reported that this method could remove around 80 wt.% of the metallic Al present in weathered MSWI bottom ash.

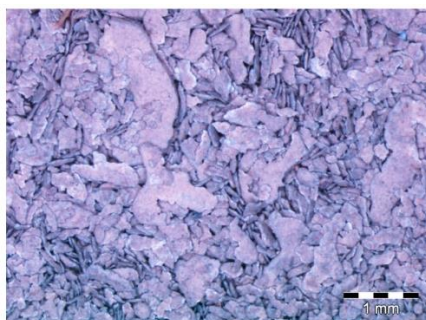


Figure 2.4 The plate-shaped metal scraps sieved out after the ball milling of MSWI bottom ash [53].

The content of metallic Al in MSWI bottom ash can also be reduced by adding water during the grinding process. Bertolini et al. [30] found that water added for grinding could dissolve the alkalis from MSWI bottom ash, creating an alkaline condition to promote the corrosion of metallic Al [30]. However, only part of the metallic Al would oxidize during the period of wet grinding. When the slurry obtained after wet grinding of MSWI bottom ash was stored at room temperature, the time required for metallic Al to oxidize entirely at room temperature could vary from 2 days to more than 3 months [30]. The amount of metallic Al that can oxidize depends on the alkalinity of MSWI bottom ash and the parameter setting of the wet milling process.

### 2.5.2 Chemical treatments

Chemical treatments of MSWI bottom ash can be alkaline solution treatment, water treatment, or acid solution treatment. The alkaline solution treatment is used to reduce the content of metallic Al and Zn in MSWI bottom ash to zero. The most commonly used alkaline solution is NaOH solution [55,126,129–131]. The factors that influence the reaction rate



between NaOH solution and metallic Al and Zn include the particle size of MSWI bottom ash, the concentration of NaOH solution, the liquid-to-solid ratio, and the heating temperature [55,130]. The MSWI bottom ash slurry obtained after NaOH solution treatment can be used directly to prepare alkali-activated materials [131]. However, for the application as SCM, the alkalis that remained in NaOH solution-treated MSWI bottom ash need to be removed by water washing [126,130]. According to Liu et al. [130], the pozzolanic reactivity of MSWI bottom ash was enhanced after the NaOH solution treatment and water washing, but the reasons for this reactivity enhancement were not explained.

The principle of water treatment is similar to alkaline solution treatment. Instead of adding an alkaline solution, water treatment is expected to create an alkaline environment by adding water to dissolve alkalis from MSWI bottom ash. The effectiveness and efficiency of water treatment depend on the particle size of MSWI bottom ash, the mass ratio between water and MSWI bottom ash, and the heating temperature. Joseph et al. [56] reduced the metallic Al content in fresh MSWI bottom ash via water treatment. After ground into powder, fresh MSWI bottom ash was immersed in water at the water-to-solid ratio of 5:1. The mixture was dried at 105 °C for 24 hours to accelerate the oxidation of metallic Al. However, the extent to which water treatment reduces the metallic Al content in MSWI bottom ash was not demonstrated [56].

Acid washing combined with water washing is used to reduce the chloride and sulfate content in MSWI bottom ash. Lo et al. [132] washed MSWI bottom ash with water and 0.1 M acetic acid, followed by calcination at 1100 °C. After all these three steps, the chloride content decreased dramatically, from 2.78 wt.% in the raw material to 0.09 wt.% in calcined MSWI bottom ash. Meanwhile, there is a tenfold reduction in the sulfate content. However, the effectiveness of acid treatment on chloride and sulfate content reduction is not specified. In addition, Saikia et al. [89] found that adding  $\text{Na}_2\text{CO}_3$  to water can promote the transformation of  $\text{CaSO}_4$  into more soluble  $\text{Na}_2\text{SO}_4$ , making it easy to remove the sulfate salt from MSWI bottom ash. After  $\text{Na}_2\text{CO}_3$  treatment, bottom ash particles were washed with deionized water and dried at about 100 °C.

### 2.5.3 Thermal treatments

Thermal treatment is usually applied to improve the quality of MSWI bottom ash by burning out the organic substances, promoting the formation of reactive phases, stabilizing heavy metals, and oxidizing metallic Al and Zn. The heating temperature determines the effectiveness of this treatment. In previous studies, the temperature ranges selected are 500 - 900 °C [53,54,57,74,76] and 1000 - 1500 °C [16,22,54,128,133,134].

When the heating temperature is between 500 and 900 °C, a substantial amount of harmful organic components can be removed [135]. Thermal decomposition of the dissolved organic carbon in MSWI bottom ash contributes to the decrease in the leaching of Cu [53,136]. The compressive strength of MSWI bottom ash blended cement pastes [53,89] and alkali-activated materials [131] increased significantly after removing organic substances. The retardation of MSWI bottom ash on cement hydration was mitigated after MSWI bottom ash was treated at 550 and 750 °C [53].

Moreover, heating MSWI bottom ash between 550 and 900 °C also promotes the transformation of crystalline phases [53,57,74] and the oxidation of metallic Al [53,54]. Qiao et al. [57,74] reported that heating weathered MSWI bottom ash at 700 °C promoted the formation of hydraulic minerals, such as lime (CaO), gehlenite ( $\text{Ca}_2\text{Al}_2\text{SiO}_7$ ), and mayenite ( $\text{Ca}_{12}\text{Al}_{14}\text{O}_{33}$ ). The formation of lime increased the pH of MSWI bottom ash, which would lead to a decrease in the leaching of Sb [53]. Tang et al. [53] indicated that low-temperature thermal treatment could oxidize the surface of aluminum particles present in weathered MSWI bottom ash. However, Chen et al. [54] found that heating weathered MSWI bottom ash at 500 °C for 2 hours only reduced the metallic Al content by 0.01 wt.%, which was insufficient for the complete oxidation of metallic Al.

The primary purpose of calcinating MSWI bottom ash at 1000 - 1500 °C is to solve the problem of leaching and increase the amount of amorphous phase. High-temperature thermal treatment of MSWI bottom ash facilitates the decomposition of organic substances (such as organochloride and dioxin) and the volatilization of heavy metals (such as Cu, Pb, and Zn) [134,137]. MSWI bottom ash with an amorphous structure can be obtained when high-temperature calcination is followed by rapid cooling. Lin et al. [16] found that vitrified MSWI bottom ash was highly resistant to leaching, as the glass melts formed at high temperature could immobilize heavy metals. Additionally, when vitrified MSWI bottom ash was used as cement substitute, it exhibited pozzolanic reactivity. In contrast, the combination of high-temperature calcination with slow cooling will reduce the amount of amorphous phase in MSWI bottom ash, leading to a decrease in reactivity [54].

Another advantage of high-temperature thermal treatment is that it helps to solve the problem of metallic Al and Zn. Increasing the calcination temperature to more than 1000 °C prolongs the reaction between metallic Al and Zn with air [54,131]. For example, Sun et al. [128] decreased the metallic Al content by 92.5 wt.% after heating weathered MSWI bottom ash at 1000 °C for 2 hours. Besides, calcinating bottom ash into molten state facilitates the agglomeration of MSWI bottom ash [54,57,76]. As a result, the metallic Al and Zn could be covered either by glass melts or newly formed crystalline phases, preventing their exposure to the alkaline solution [54]. Chen et al. [54] performed thermal treatment on weathered MSWI bottom ash at 1000 °C for 2 hours. The release of hydrogen gas was not detected after immersing thermally treated MSWI bottom ash in NaOH solution.

## 2.6 Utilization of MSWI bottom ash as supplementary cementitious material

Previous studies on the utilization of MSWI bottom ash as SCM are summarized in Table A 2<sup>(3)</sup> (see Appendix A). For the MSWI bottom ash used in previous research, its particle size, plant-scale and lab-scale treatments, and main components can be found in Table A 2. The information about mix design, curing condition, sample size, and compressive strength is also included in Table A 2. Based on the information presented in the literature, the pozzolanic reactivity and pozzolanic reaction products of MSWI bottom ash, the reaction of MSWI bottom ash in blended cement pastes, the effects of MSWI bottom ash on cement hydration,

---

<sup>(3)</sup> Table A 2 is put in appendix A because it is a long table.

and the mechanical properties and the leaching of contaminants from MSWI bottom ash blended cement pastes, mortars, and concretes are discussed in the following sections.

### 2.6.1 Pozzolanic reactivity of MSWI bottom ash

The pozzolanic reactivity of MSWI bottom ash is not always measured prior to its application as SCM. There is limited information about the pozzolanic reactivity of MSWI bottom ash. In previous work, pozzolanic reactivity was measured after grinding MSWI bottom ash into powder. The tested MSWI bottom ash was collected from Belgium [48,138], Italy [50], Portugal [49], Singapore [130], and the Netherlands [96].

The methods used to determine the pozzolanic reactivity of MSWI bottom ash include  $R^3$  test [138], saturated lime test [96,130], Frattini test [50], modified Chapelle test [49], and lime reactivity test [48]. Among all these methods, the  $R^3$  test is a newly developed standardized method (see ASTM C1897-20 [139]), and its result shows better correlations to the benchmark of 28-day relative strength than the other conventional standardized methods [140].

The  $R^3$  test was used by Joseph [138] to assess the pozzolanic reactivity of fresh MSWI bottom and weathered MSWI bottom ash produced in Belgium. The test results indicated that the pozzolanic reactivity of weathered MSWI bottom ash was similar to that of Class F coal fly ash and natural pozzolans. Weathered MSWI bottom ash exhibited slightly lower pozzolanic reactivity than fresh MSWI bottom ash.

The saturated lime test is a simplified Frattini test [141]. The saturated lime test was used by Caprai [96] to measure the pozzolanic reactivity of weathered MSWI bottom ash produced in the Netherlands. The weathered MSWI bottom ash sent for testing showed higher pozzolanic reactivity than quartz of the same particle size. The saturated lime test was also used by Liu et al. [130] to assess the pozzolanic reactivity of MSWI bottom ash produced in Singapore. The test result showed that MSWI bottom ash was less reactive than silica fume [130].

Like Liu et al. [130], detailed information about the plant-scale treatments of the MSWI bottom ash tested by Filipponi et al. [50], Simões et al. [49], and Saikia et al. [48] was not provided in their research. Filipponi et al. [50] determined the pozzolanic reactivity of MSWI bottom ash produced in Italy with the Frattini test. The test result indicated that MSWI bottom ash had weak pozzolanic reactivity. The strength gain resulting from the hydration of MSWI bottom could only be detected after 28 days of curing and in blended cement prepared with more than 50 wt.% MSWI bottom ash [50].

The modified Chapelle test and lime reactivity test were used by Simões et al. [49] and Saikia et al. [48], respectively, to examine the pozzolanic reactivity of MSWI bottom ash. Simões et al. [49] found that the pozzolanic reactivity of MSWI bottom ash was slightly lower than that of Class F coal fly ash. Saikia et al. [48] compared the lime reactivity of ground MSWI bottom ash with metakaolin. After 7 days, the  $\text{Ca}^{2+}$  ion consumed by MSWI bottom ash was almost half of that of metakaolin, indicating that the pozzolanic reactivity of MSWI bottom ash was much lower than metakaolin [48].

It should be noted that the CaO content is higher than the  $\text{SiO}_2$  content in the MSWI bottom ash used by Liu et al. [130] and Caprai [96]. In comparison, the MSWI bottom ash collected by

Joseph [138], Simões et al. [49], Saikia et al. [48], and Filipponi et al. [50] contains more  $\text{SiO}_2$  (> 40 wt.%) than  $\text{CaO}$  (< 26 wt.%). In previous studies, MSWI bottom ash with high  $\text{SiO}_2$ , but low  $\text{CaO}$  content, was commonly used as SCM to prepare blended cement pastes (see Table A 2).

### 2.6.2 Pozzolanic reaction products of MSWI bottom ash

Calcium silicate hydrate (C-S-H) gel is the main product formed after the pozzolanic reaction of MSWI bottom ash. The Ca/Si ratio of the gel derived from the pozzolanic reaction of MSWI bottom ash is much lower than that of the C-S-H detected in plain cement paste (between 1.5 and 2.0) [76,142]. Qiao et al. [76] studied the reaction between weathered MSWI bottom ash and commercially available hydrated lime ( $\text{Ca(OH)}_2$ ) and found that the amount of C-S-H formed was too small to be detected by X-ray diffraction (XRD) analysis. According to the energy dispersive X-ray spectroscopy analysis (EDS) under scanning electron microscopy (SEM), the C-S-H derived from MSWI bottom ash had a Ca/Si ratio of 1.11. After thermal treatment at 800 °C, MSWI bottom ash released more silicon during its reaction with  $\text{Ca(OH)}_2$ . As a result, the calculated Ca/Si ratio of the resultant C-S-H gel became lower, around 0.63.

### 2.6.3 Reaction of MSWI bottom ash in blended cement pastes

Very little information is available in the literature regarding the reaction of MSWI bottom ash in blended cement pastes. According to qualitative XRD analysis of MSWI bottom ash blended cement pastes, Li et al. [27] found that the  $\text{Ca(OH)}_2$  produced after cement hydration could be consumed by MSWI bottom ash. Zhang et al. [125] replaced 20 wt.% Portland cement with MSWI bottom ash in the binder of Portland cement concrete. The results of compressive strength measurements indicated that the reaction of MSWI bottom ash mainly contributed to the strength development in later stages. The 1-day compressive strength of the concrete made with the mixture of Portland cement and MSWI bottom ash was almost the same as that of Portland cement concrete. After 28 days of curing, the compressive strength of concrete containing MSWI bottom ash exceeded that of Portland cement concrete. The 90-day compressive strength of concrete containing MSWI bottom ash was 18.4 % higher than that of Portland cement concrete.

### 2.6.4 Effects of MSWI bottom ash on cement hydration

The effect of MSWI bottom ash on Portland cement hydration is usually studied via isothermal calorimetry. This method is generally used to monitor the early-age hydration of Portland cement by measuring the heat flow. Figure 2.5 shows the schematic representation of the heat evolution curves of Portland cement paste and MSWI bottom ash blended cement pastes during the first three days of reaction. These curves are derived from the calorimetry results reported in the literature [28,53,56,103,125,143].

As shown in Figure 2.5, replacing Portland cement with MSWI bottom ash usually results in a lower cumulative heat release. Like the hydration of pure cement, the hydration of MSWI bottom ash blended cement can be divided into five phases: initiation period (stage I), induction period (stage II), accelerating period (stage III), decelerating period (stage IV), and slow reaction period (stage V). The heat flow in MSWI bottom ash blended cement pastes is

lower than that of Portland cement paste in each stage. The decrease in the reaction heat could be owing to the fact that the reactivity of MSWI bottom ash is much lower than that of Portland cement [48–51].

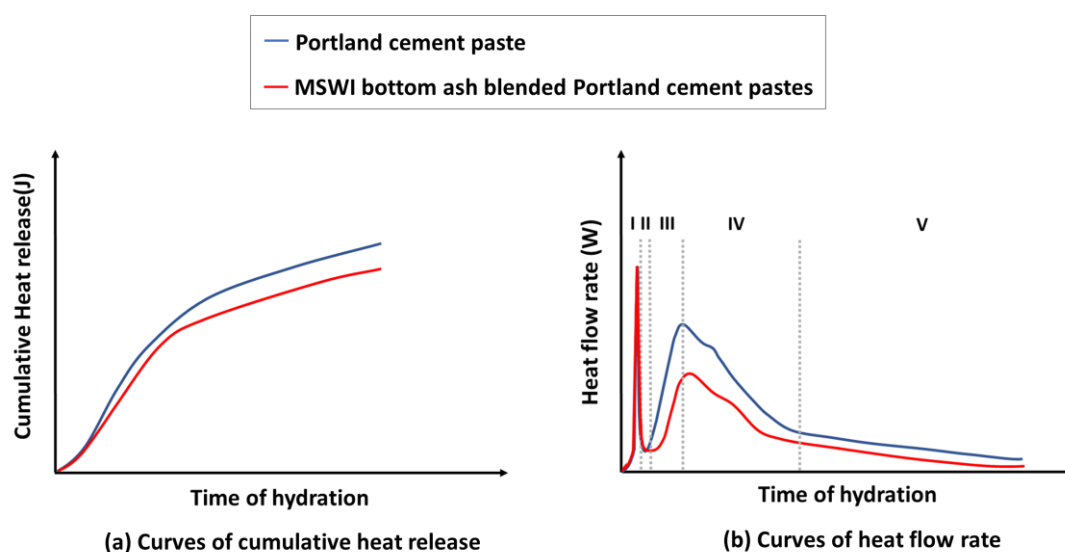


Figure 2.5 Schematic representation of the heat evolution curves that describe (a) cumulative heat release and (b) heat flow rate of Portland cement paste and MSWI bottom ash blended cement pastes during the first three days of reaction, derived from curves presented in the literature [28,53,56,103,125,143].

MSWI bottom ash is found to contribute to heat release in stage I and stage IV. Part of the reaction heat collected at the initiation period of MSWI bottom ash blended cement pastes could be attributed to the dissolution of soluble salts from MSWI bottom ash [143] or the oxidation of metallic Al present in MSWI bottom ash [56]. The shoulder peak in stage IV corresponds to the hydration of tricalcium aluminate ( $C_3A$ ) in cement pastes. This shoulder peak is broader and often observed in the calorimetric curve of MSWI bottom ash blended cement pastes [53,56,143]. This peak could be related to the anhydrite found in MSWI bottom ash, which can react with  $C_3A$  and promotes ettringite (AFt) and monosulfate (AFm) formation in stage IV [53,143,144].

The addition of MSWI bottom ash mainly influences the reaction rate by delaying cement hydration in stage II and stage III [16,27,53,103,143]. The delay already starts at a replacement level of 5 wt.%, but is often reported at replacement levels between 20 and 30 wt.% [28,53,56,103,125,143]. If the onset of stage III is delayed, the shoulder peak also appears late in stage IV. However, Tang et al. [28] observed that the incorporation of MSWI bottom ash could also accelerate AFm formation in stage IV. This is because the addition of MSWI bottom ash may change the ratio between calcium sulfate and  $C_3A$  in the mixture [28]. When this ratio is reduced, the formation of AFm can be accelerated [145].

The induction period is longer if MSWI bottom ash with a high amount of Ca-bearing substances and heavy metal is used to replace cement [143]. Upon contact with water, soluble Ca-bearing substances (such as anhydrite and lime) can release a large number of calcium ions, hydroxyl ions, and other complicated soluble ions into the pore solution of bottom ash

blended cement pastes. The existence of these ions in pore solution could inhibit the release of calcium ions, silicate ions, and hydroxyl ions from alite ( $C_3S$ ), which may partly explain the delay of cement hydration in an early stage [143].

The retarding effect on cement hydration can be reduced if heavy metals present in the form of organic matter are removed via thermal treatment of MSWI bottom ash [53]. The heavy metal ions, such as chromium, zinc, and lead, released from MSWI bottom ash tend to react with hydroxide ions in the pore solution of blended cement pastes. Metal hydroxides usually precipitate in the pore solution and could hinder cement hydration by precipitating on the surface of unhydrated cement particles [143]. Besides, some of the metal hydroxides formed are less soluble than portlandite. The formation of these metal hydroxides may delay the nucleation of portlandite [146–148], hindering the hydration of cement particles

### 2.6.5 Mechanical properties of MSWI bottom ash blended cement pastes, mortars, and concretes

As shown in Table A 2, there is a wide variety in the mix design and the type of MSWI bottom ash used in previous research. The compressive strength of MSWI bottom ash blended cement pastes, mortars, and concretes is mainly influenced by the properties of MSWI bottom ash, the percentage of cement replaced by MSWI bottom ash (replacement level), and water-to-binder (w/b) ratio. The properties of MSWI bottom ash refer to its metallic Al content, pozzolanic reactivity, and particle size.

#### *Metallic Al content*

The control of metallic Al and Zn content in MSWI bottom ash is critical for its application as SCM in concrete and mortar prepared with w/b ratio around 0.5. The detection of Zn has rarely been reported in previous studies. In the literature, recommendations can be found regarding the metallic Al content in MSWI bottom ash. Alderete et al. [149] recommend reducing the metallic Al content of MSWI bottom ash to less than 0.3 wt.% when 20 wt.% Portland cement was replaced by MSWI bottom ash in concrete. Tang et al. [53] reported that volume expansion and cracks were not observed with the naked eye in mortar samples after the metallic Al content of MSWI bottom ash was reduced to less than 0.2 wt.%. The replacement level of cement by MSWI bottom ash in mortar samples was 30 wt.%. Liu et al. [130] found that when the metallic Al content was reduced to zero, the 90-day compressive strength of the mortar with 20 wt.% MSWI bottom ash in its binder was close to that of Portland cement mortar. Zhang et al. [125] proposed that MSWI bottom ash containing 0.06 wt.% metallic Al was suitable for preparing zero-slump concrete (w/b ratio around 0.35). The generated hydrogen gas could easily escape from the channel pathways present in zero-slump concrete. As a result, cracks and volume expansion were not observed in the concrete with 20 wt.% MSWI bottom ash in its binder.

#### *Pozzolanic reactivity and replacement level*

The pozzolanic reactivity of MSWI bottom ash is much lower than that of Portland cement [48–51]. Therefore, the flexural and compressive strength of MSWI bottom ash blended cement pastes decrease with the addition of MSWI bottom ash. For example, Jurič et al. [150] found a linear decrease of flexural and compressive strength of concretes by 0.03 and 0.02



MPa per wt.% of MSWI bottom ash in the binder, respectively. As shown in Table A 2, the replacement level of MSWI bottom ash in blended cement was between 5 and 50 wt.% in previous research. In most cases, the percentage of MSWI bottom ash used for cement replacement did not exceed 30 wt.%. The main reason for choosing this replacement level is that the addition of MSWI bottom ash slows down the hydration of cement, leading to a dramatic decrease in strength at early ages (see section 2.6.4). Li et al. [27] reported that the 3-day compressive strength of mortars decreased by 54.7 % after replacing 50 wt.% cement with MSWI bottom ash.

#### *Water-to-binder ratio and particle size*

The compressive strength of MSWI bottom ash blended cement concrete can be higher than that of Portland cement concrete after reducing the w/b ratio and the particle size of MSWI bottom ash. Alderete et al. [149] reported that the 28-day and 90-day compressive strength of the MSWI bottom ash blended cement concrete prepared with w/b of 0.46 was higher than that of Portland cement concrete prepared with w/b ratio of 0.48. The particle size of MSWI bottom ash was similar to that of Portland cement, and the replacement level was 20 wt.%. The w/b ratio of MSWI bottom ash blended cement concrete was kept at 0.46 by adding superplasticizer.

Bertolini et al. [30] reported that compressive strength increased after replacing 30 wt.% Portland cement with wet ground MSWI bottom ash in Portland cement concrete. The average particle size of wet ground MSWI bottom ash was around 3 $\mu$ m, smaller than that of Portland cement. When the w/b ratio was kept at 0.5, the addition of superplasticizer was needed to improve the workability of MSWI bottom ash blended cement concrete. The 28-day compressive strength of this MSWI bottom ash blended cement concrete was 1.6 % higher than the Portland cement concrete prepared with the same w/b ratio [30]. Carsana et al. [151] used the same method as Bertolini et al. [30] to increase the compressive strength of self-compacting Portland cement concrete. The percentage of Portland cement replaced by wet ground MSWI bottom ash was 30 wt.%. The w/b ratio of MSWI bottom ash blended cement concrete was 0.43, the same as that of Portland cement concrete. Compared with Portland cement concrete, more superplasticizer was used to modify the workability of MSWI bottom ash blended cement concrete. The 180-day compressive strength of MSWI bottom ash blended cement concrete increased by around 20 % relative to Portland cement concrete [151].

#### **2.6.6 Leaching of contaminants from MSWI bottom ash blended cement pastes, mortars, and concretes**

The leaching of contaminants from MSWI bottom ash blended cement pastes, mortars, and concretes into the environment need to be assessed before applying these building materials. This environmental concern is related to the presence of heavy metals (such as Cu, Zn, Pb, and Cr) and soluble salts (including  $\text{Cl}^-$  and  $\text{SO}_4^{2-}$ ) in MSWI bottom ash. In most cases, the concentrations of these contaminants in leachates of MSWI bottom ash blended cement pastes, mortars, and concretes are lower than the allowable upper limits set by local government, when the replacement level of MSWI bottom ash is between 5 and 30 wt.% [16,27,53,103,132,152–154]. Whether the MSWI bottom ash has been weathered or not

during the plant-scale treatments is not always mentioned in the literature. The leaching test is usually carried out with deionized water, using the Toxicity Characteristic Leaching Procedure (TCLP) method, according to local standards.

The leaching of MSWI bottom ash blended cement pastes highly depends on the leaching resistance of MSWI bottom ash. The leaching resistance of MSWI bottom ash can be improved by introducing weathering and water-washing processes in plant-scale treatments [61,62,65,66,81,86–88] or by conducting lab-scale thermal treatments [16,134,137]. If the leaching of heavy metals from treated MSWI bottom ash is below the threshold value prescribed in the standard, there is no concern about heavy metal leaching when using this treated MSWI bottom ash as SCM [16,27,132,153,154].

For treated MSWI bottom ash with contaminants still above the legislative upper limit, it is necessary to control its replacement level to avoid the risk of excessive leaching. Loginova et al. [103] performed mechanical treatments on MSWI bottom ash (< 3 mm size fraction) and found that the leaching of chloride, sulfate, and antimony was beyond the regulatory threshold value. In this case, the recommended replacement level of this mechanically treated MSWI bottom ash would be 5 wt.%. Tang et al. [53] did mechanical and thermal treatments on MSWI bottom ash (< 2 mm size fraction) and found that the leaching of chloride, sulfate, and molybdenum still exceeded the upper limits. The replacement level was limited to 30 wt.%.

## 2.7 Utilization of MSWI bottom ash as precursor for AAM

Table A 3<sup>(4)</sup> summarizes the studies related to the utilization of MSWI bottom ash as precursor for AAM (see Appendix A). The particle size, plant-scale and lab-scale treatments, and main components of the MSWI bottom ash used by previous researchers can be found in Table A 3. The information about mix design, curing condition, sample size, and compressive strength is also provided in Table A 3. The reactivity of MSWI bottom ash as AAM precursor, the properties of the AAM prepared using MSWI bottom ash as precursor, and the properties of the AAM prepared with MSWI bottom ash and other industrial by-products as precursor are reviewed in the following sections.

### 2.7.1 Reactivity as AAM precursor

Very little information is available regarding the reactivity of MSWI bottom ash as AAM precursor. Currently, three methods are proposed in the literature to evaluate the reactivity of MSWI bottom ash as AAM precursor. These methods are the modified Chapelle test [155,156], chemical dissolution test [157], and the chemical attack test [47,158]. The modified Chapelle test is a standardized method designed to assess the pozzolanic reactivity of supplementary cementitious materials. In the research of Casanova et al. [155] and Carvalho et al. [156], the reactivity of MSWI bottom ash as AAM precursor was assessed by measuring the pozzolanic reactivity with the modified Chapelle test. The MSWI bottom ash used by Carvalho et al. [156] and Casanova et al. [155] is from the same plant in Portugal. Information about the plant-scale treatments was not provided. Their test results indicated that the pozzolanic reactivity of MSWI bottom ash was lower than that of Class F coal fly ash.

---

<sup>(4)</sup> Table A 3 is put in appendix A because it is a long table.



The chemical dissolution test is used to determine the content of reactive silica in cement and supplementary cementitious materials. This standardized testing method is not only used to determine the content of reactive  $\text{SiO}_2$ , but also used to quantify the content of reactive  $\text{Al}_2\text{O}_3$  and  $\text{CaO}$  in blast furnace slag [157] and coal fly ash [159]. Huang et al. [157] measured the content of reactive  $\text{SiO}_2$ ,  $\text{CaO}$ , and  $\text{Al}_2\text{O}_3$  in MSWI bottom ash according to the test procedure described in the standard for determining reactive silica content. The MSWI bottom ash tested by Huang et al. [157] was produced in China and had been water-washed at the recycling station. Prior to the reactivity test, the received MSWI bottom was ground into fine powder in the lab. Huang et al. [157] reported that the reactive  $\text{SiO}_2$  detected in MSWI bottom ash was 28.4 wt.%, higher than that in blast furnace slag (18.7 wt.%). In contrast, the reactive  $\text{CaO}$  in MSWI bottom ash was 12.7 wt.%, less than half of its content in blast furnace slag (33.6 wt.%). The MSWI bottom ash had 12.2 wt.% reactive  $\text{Al}_2\text{O}_3$ , slightly lower than that in blast furnace slag (18.4 wt.%).

The chemical attack test is proposed by previous researchers for determining the amount of reactive  $\text{SiO}_2$  and  $\text{Al}_2\text{O}_3$  in MSWI bottom ash that could participate in the AAM formation [47,158]. This test method has not been standardized yet. The chemical attack test is conducted by dissolving 1 g of MSWI bottom ash in 100 ml solution of hydrofluoric acid (HF) or NaOH. The attack with HF solution is usually performed at room temperature to quantify the amount of amorphous  $\text{SiO}_2$  in MSWI bottom ash. The attack with NaOH solution is conducted at 80 °C and is used to determine the amount of  $\text{SiO}_2$  and  $\text{Al}_2\text{O}_3$  released from MSWI bottom ash [47,158,160].

Maldonado-Alameda et al. [47] evaluated the potential of weathered MSWI bottom ash as AAM precursor using the chemical attack test. The MSWI bottom ash went through metal extraction and weathering treatments in a Spanish waste valorization plant. Before reactivity measurement, MSWI bottom ash was ground into fine powder. The results of the attack with HF solution showed that the attack with NaOH solution could only dissolve a small fraction of the amorphous  $\text{SiO}_2$ . The results of the attack with NaOH solution indicated that more  $\text{SiO}_2$  and  $\text{Al}_2\text{O}_3$  was dissolved from MSWI bottom ash when the concentration of NaOH solution increased from 2 M to 8 M. The molar ratio between dissolved Si and Al was much higher than two [47]. Given that the strength of alkali-activated metakaolin was maximized when the molar ratio between Si and Al in the mixture of metakaolin and activator was 1.9 [161], Maldonado-Alameda et al. [47] recommended introducing additional sources of reactive  $\text{Al}_2\text{O}_3$  or  $\text{SiO}_2$  to modify the Si/Al molar ratio when MSWI bottom ash was used for the preparation of AAM.

## 2.7.2 AAM prepared with MSWI bottom ash as precursor

### 2.7.2.1 Reaction products in alkali-activated MSWI bottom ash<sup>(5)</sup>

As shown in Table A 3, the activators, including NaOH solution, water glass solution, hydrated lime, and a mixture of water glass ( $\text{Na}_2\text{SiO}_3$ ) solution and NaOH solution, were used by previous researchers to prepare alkali-activated MSWI bottom ash. Among all these activators, a mixture of water glass solution and NaOH solution is the most commonly used. Although there is a wide variety in the concentration of NaOH solution and the types of water

---

<sup>(5)</sup> Alkali-activated MSWI bottom ash, which can be paste, mortar, or concrete, refers to the AAM prepared with MSWI bottom ash as precursor.

glass solution, the mass ratio between water glass solution and NaOH solution is usually set to be above one.

This section discusses the reaction products formed in alkali-activated MSWI bottom ash prepared using the mixture of water glass solution and NaOH solution as activator. Previous studies have shown that the alkali activation of MSWI bottom ash mainly leads to the formation of amorphous gel phases, including the C-S-H gel, the calcium aluminosilicate hydrate (C-A-S-H) gel, and the sodium aluminosilicate hydrate (N-A-S-H) gels. In addition to the amorphous reaction products, the detection of crystalline reaction products was also reported by previous researchers, such as tobermorite ( $\text{Ca}_5(\text{Si}_6\text{O}_{16})(\text{OH})_2$ ) [131], hillebrandite ( $\text{Ca}_2(\text{SiO}_3)(\text{OH})_2$ ) [131], pirssonite ( $\text{Na}_2\text{Ca}(\text{CO}_3)_2 \cdot 2\text{H}_2\text{O}$ ) [162], gehlenite ( $\text{Ca}_2\text{Al}(\text{AlSi})\text{O}_7$ ), albite ( $\text{NaAlSi}_3\text{O}_8$ ) [102,131], and gismondine ( $\text{CaAl}_2\text{Si}_2\text{O}_8 \cdot 4\text{H}_2\text{O}$ ) [29].

The C-S-H gel and N-A-S-H gel formed in alkali-activated MSWI bottom ash were found to be similar to the C-S-H gel generated after cement hydration and the N-A-S-H gel formed in alkali-activated Class F coal fly ash, respectively. Zhu et al. [162,163] selected the mixture of NaOH solution and  $\text{Na}_2\text{SiO}_3$  solution as activator to react with fresh MSWI bottom ash. The alkali-activated MSWI bottom ash paste samples were cured at 75 °C for 3 days. The MSWI bottom ash was collected from Singapore. According to the FTIR (Fourier transform infrared spectroscopy) analysis, the chemical structure of the C-S-H gel found in alkali-activated MSWI bottom ash paste was analogous to that of the C-S-H identified in 10-month Portland cement paste [162]. The main difference was that the C-S-H gel identified in alkali-activated MSWI bottom ash paste had a higher degree of polymerization of the silicate chains [162]. In the  $^{29}\text{Si}$  NMR spectrum of the N-A-S-H gel extracted from alkali-activated MSWI bottom ash paste, the main peak was observed at around -99 ppm, corresponding to Al-substituted Si units of  $\text{Q}^4(2\text{Al})$ . The same  $^{29}\text{Si}$  NMR resonance appeared in the measurement of 180-day alkali-activated Class F coal fly ash paste [164], indicating that the nanostructure of the N-A-S-H gel formed in alkali-activated MSWI bottom ash paste resembles that detected in alkali-activated Class F coal fly ash paste.

The formation of C-A-S-H gel in alkali-activated MSWI bottom ash can be influenced by the alkalinity of the activator. Maldonado-Alameda et al. [29,102] activated weathered MSWI bottom ash using a mixture of water glass solution and NaOH solution. The mass ratio between water glass solution and NaOH solution was fixed at four, while the concentration of NaOH solution was varied from 2 M to 8 M. Analysis of salicylic acid/methanol (SAM) extraction and hydrochloric acid (HCl) extraction indicated that both C-A-S-H gel and N-A-S-H gels were formed in alkali-activated MSWI bottom ash paste. When the NaOH concentration increased from 2 M to 6 M, the amount of C-A-S-H gel detected in alkali-activated MSWI bottom ash paste also increased. However, further increasing the NaOH molarity to 8 M did not increase the content of C-A-S-H gel [29].

Although the amorphous phase present in MSWI bottom ash mainly consists of waste glass particles, the gel formed in alkali-activated MSWI bottom ash is different from the gel obtained after the alkali activation of the glass fraction of MSWI bottom ash [165]. The chemical composition of these waste glass particles is almost the same as soda-lime silicate glass [165,166]. Zhu et al. [165] activated the glass fraction separated from fresh MSWI

bottom ash with the activator consisting of  $\text{Na}_2\text{SiO}_3$  solution and 14 M NaOH solution. The main reaction product detected in synthesized alkali-activated paste was the sodium silicate gel [165]. This gel is unstable under a moisture environment and may result in strength loss [167]. It is recommended to improve the hydrolytic stability of sodium silicate gel by providing supplementary Ca and Al to promote the formation of C-A-S-H and N-A-S-H gels [168].

### 2.7.2.2 Mechanical properties of alkali-activated MSWI bottom ash

The mechanical properties of alkali-activated MSWI bottom ash are mainly influenced by four factors: metallic Al content in MSWI bottom ash, reactivity of MSWI bottom ash, selection of activator, and selection of curing condition.

#### *Metallic Al content in MSWI bottom ash*

As illustrated in Table A 3, most of the MSWI bottom ash used for AAM preparation contains metallic Al. The metallic Al embedded in MSWI bottom ash particles usually works as the foaming agent, resulting in volume expansion and low compressive strength of alkali-activated MSWI bottom ash [29,131,155,156,169]. The volume expansion caused by the release of hydrogen gas is restrained by alkali-activated MSWI bottom ash paste, which would crack once the internal stress induced by volume expansion exceeds its strength [54]. Huang et al. [131] prepared alkali-activated mortars with MSWI bottom ash containing 1.92 wt.% metallic Al. After curing for three days at room temperature, the alkali-activated MSWI bottom ash mortars showed no strength, and severe defects, such as voids and interconnecting pores, were observed on the specimens. The 28-day compressive strength only reached 2.4 MPa.

In addition to the quality-upgrade treatment of MSWI bottom ash (see section 2.5.2), the following methods were also used by previous researchers to minimize the negative effects of metallic Al on the compressive strength of alkali-activated MSWI bottom ash:

- Method one is to prolong the mixing time of fresh pastes or cast freshly mixed pastes a few tens of minutes later during the preparation of alkali-activated MSWI bottom ash. The extension of mixing time accelerates the oxidation of metallic Al and facilitates the escape of hydrogen gas from fresh alkali-activated pastes [170]. A delay in the casting of fresh alkali-activated pastes provides sufficient time for the corrosion of metallic Al under alkaline conditions, making it possible to remove all the hydrogen gas released from the redox reaction of metallic Al via the vibration of fresh pastes [155,156]. Once entrained hydrogen gas is emitted from fresh pastes, the volume expansion of AAM can be dramatically reduced. It is worth noting that the feasibility of this method depends on the setting time of alkali-activated MSWI bottom ash.
- Method two is to reduce the amount of water used for the preparation of alkali-activated MSWI bottom ash. When MSWI bottom ash contains metallic Al, alkali-activated MSWI bottom ash prepared at a lower water-to-solid ratio exhibits higher compressive strength [76,170]. The adverse effect of metallic Al content on the compressive strength of alkali-activated MSWI bottom ash is smaller at a lower water-to-solid ratio. Qiao et al. [76] compared the alkali-activated MSWI bottom ash paste prepared at two different water-

to-solid ratios: 0.2 and 0.5. The voids caused by hydrogen gas release were only observed in alkali-activated MSWI bottom ash paste prepared with the water-to-solid ratio of 0.5.

- Method three is to separate MSWI bottom ash according to the metallic Al content and only use the fraction that contains the lowest amount of metallic Al to prepare AAM. Zhu et al. [168] separated the fresh MSWI bottom ash into non-ferrous, ferrous, and glass fractions. Among these three fractions, the metallic Al content in the glass fraction is the lowest, while the non-ferrous fraction has the highest metallic Al content. The 3-day compressive strength of the alkali-activated paste prepared with 100 % glass fraction reached up to 31.69 MPa.

#### *Reactivity of MSWI bottom ash*

Apart from metallic Al, the low reactivity of MSWI bottom ash is also responsible for the low compressive strength of alkali-activated MSWI bottom ash. Qiao et al. [57] used weathered MSWI bottom ash to prepare AAM and found that the 28-day compressive strength of alkali-activated MSWI bottom ash paste was very low. The compressive strength increased significantly after improving the reactivity of MSWI bottom ash via thermal treatment (at 700 °C). The 28-day compressive strength of the alkali-activated paste prepared with thermally treated MSWI bottom ash was around 2.9 MPa, much higher than that of the alkali-activated paste made from untreated MSWI bottom ash (about 0.6 MPa) [57].

#### *Selection of activator*

The alkalinity of the activator is an important factor that influences the compressive strength of alkali-activated MSWI bottom ash. Carvalho et al. [156] found that MSWI bottom ash dissolved more easily in NaOH solution than in  $\text{Na}_2\text{SiO}_3$  solution due to the higher alkalinity of NaOH solution. NaOH solution-activated MSWI bottom ash mortar had higher compressive strength than  $\text{Na}_2\text{SiO}_3$  solution-activated MSWI bottom ash mortar. The compressive strength of NaOH solution-activated MSWI bottom ash mortars increased as the concentration of NaOH solution increased from 4 to 10 mol/kg. Chen et al. [170] reported that the alkalinity of the activator prepared with  $\text{Na}_2\text{SiO}_3$  solution and 4 M NaOH solution was too low to activate MSWI bottom ash. When the concentration of NaOH solution increased from 4 M to 8 M, hardened paste samples were obtained as the result of an increased pH of the activator and the release of more monomers from the dissolution of MSWI bottom ash.

When MSWI bottom ash is activated with a mixture of water glass solution and NaOH solution, the alkalinity and the alkali modulus (Ms) of the activator (the molar ratio between  $\text{SiO}_2$  and  $\text{Na}_2\text{O}$ ) can both influence the compressive strength of alkali-activated MSWI bottom ash. Maldonado-Alameda et al. [102] activated weathered MSWI bottom ash using a mixture of water glass solution and NaOH solution. A dramatic increase in compressive strength was observed after increasing the concentration of NaOH solution from 2 M to 6 M. However, further increasing the concentration of NaOH solution to 8 M led to a strength reduction in synthesized alkali-activated MSWI bottom ash paste. Maldonado-Alameda et al. [102] found the optimum modulus of the activator to be in the range of 2.0 - 2.5.

### *Selection of curing condition*

The curing temperature strongly influences the early-age compressive strength of alkali-activated MSWI bottom ash. When alkali-activated MSWI bottom ash was cured at room temperature, the 1-day compressive strength could still be too low for demolding [29,57,76,102]. In this case, alkali-activated MSWI bottom ash was demolded after curing at room temperature for three days (see Table A 3). The early-age compressive strength of alkali-activated MSWI bottom ash can be increased by curing at an elevated temperature. In previous research, thermal curing was performed at a temperature between 70 and 90 °C, and the curing period varied from one to three days [155,156,165,168,170].

#### **2.7.2.3 Leaching of contaminants from alkali-activated MSWI bottom ash**

The leaching of contaminants from alkali-activated MSWI bottom ash into the environment can be higher than that from MSWI bottom ash. Maldonado-Alameda et al. [47] found that large quantities of heavy metals were detected in the leachate after dissolving weathered MSWI bottom ash in 8 M NaOH solution. Chen et al. [170] reported that alkali activation of MSWI bottom ash increased the leaching of chromium (Cr). Test results of Giro-Paloma et al. [79] also indicated that the amount of arsenic (As) leached from alkali-activated MSWI bottom ash paste was 30 to 40 times as much as that detected in the leachate of MSWI bottom ash powder. The antimony (Sb) and Zn in the leachate of alkali-activated MSWI bottom ash paste rose to more than 5 times their concentrations in the leachate of MSWI bottom ash powder [79]. It is worth mentioning that Chen et al. [170] and Giro-Paloma et al. [79] did not mention whether the MSWI bottom ash had been weathered or not during plant-scale treatments.

The leaching of heavy metals from alkali-activated MSWI bottom ash could exceed the regulatory limit. Maldonado-Alameda et al. [29,102] used weathered MSWI bottom ash to prepare AAM and found that the leaching of As and Sb from alkali-activated MSWI bottom ash paste exceeded the required limit of non-hazardous waste. The excessive leaching of these two metals can be related to the waste glass present in MSWI bottom ash, as  $\text{As}_2\text{O}_3$  and  $\text{Sb}_2\text{O}_3$  are usually used in the glass industry as fining agents to lighten glass and remove air bubbles [171]. When the pH of the activator became higher, more heavy metals would leach out from alkali-activated MSWI bottom ash paste, especially for the elements that were initially present in waste glass particles [29]. Zhu et al. [168] also found that alkali activation of the waste glass present in MSWI bottom ash promoted the leaching of Zn, Ni, Pb, and Cr, as compared with the leaching of unreacted waste glass.

#### **2.7.3 AAM prepared with MSWI bottom ash and other industrial by-products as precursor**

In previous studies, MSWI bottom ash was used together with other industrial by-products to prepare alkali-activated materials (see Table A 3). These industrial by-products include blast furnace slag [131,157,172–174], metakaolin [158,175], coal fly ash [176], waste glass [91], and secondary aluminum recycling by-product (PAVAL®) [177]. Compared with waste glass and PAVAL®, blast furnace slag, metakaolin, and coal fly ash are more commonly used AAM precursors [43,44]. Waste glass was used by Xuan et al. [91] to increase the content of reactive  $\text{SiO}_2$  in MSWI bottom ash-based AAM. The PAVAL® was used by Maldonado-Alameda et al.

[177] to compensate for the  $\text{Al}_2\text{O}_3$  deficiency in MSWI bottom ash-based AAM. Binary AAM systems, including MSWI bottom ash-BFS, MSWI bottom ash-metakaolin, and MSWI bottom ash-coal fly ash, are discussed in the following section.

#### *MSWI bottom ash and blast furnace slag*

Blast furnace slag was used to partially replace MSWI bottom ash to increase the compressive strength of alkali-activated MSWI bottom ash. Huang et al. [157] found that the content of active calcium in BFS was more than two times as much as that in MSWI bottom ash. Replacing MSWI bottom ash with BFS can increase the active CaO content in the precursor, which is beneficial to the strength development of AAM. However, the residual metallic Al in MSWI bottom ash always leads to a strength decrease. This risk can be eliminated by treating MSWI bottom ash in NaOH solution [131,157,172–174,178]. The MSWI bottom ash slurry obtained after NaOH solution treatment can be used directly to prepare AAM. Huang et al. [131] used thermally treated MSWI bottom ash as precursor to prepare alkali-activated mortars. NaOH solution treatment was used to reduce the metallic Al content in thermally treated MSWI bottom ash. In the end, the alkali-activated MSWI bottom ash mortar exhibited no volume expansion and had a 28-day compressive strength of 13.6 MPa. After replacing 40 wt.% MSWI bottom ash with BFS, the compressive strength of alkali-activated mortar increased by around 200 %.

The compressive strength of AAM prepared with blends of MSWI bottom ash and BFS not only depends on the metallic Al content of MSWI bottom ash and the mass ratios between MSWI bottom ash and BFS, but also on the type of activator and the curing conditions. Sealed curing at room temperature is found to be the optimal curing condition for the alkali-activated mortar prepared with MSWI bottom ash and BFS [172]. Compared with NaOH solution and water glass solution, a mixture of NaOH solution and water glass solution is more suitable for activating blends of MSWI bottom ash and BFS. More C-S-H and C-A-S-H gels are formed when the mixture of NaOH solution and  $\text{Na}_2\text{SiO}_3$  solution is used as activator, resulting in a higher compressive strength [157,174]. Besides, the compressive strength of alkali-activated mortar prepared with blends of MSWI bottom ash and BFS can be optimized by modifying the molar ratio between  $\text{SiO}_2$  and  $\text{Na}_2\text{O}$  in the mixture of NaOH solution and  $\text{Na}_2\text{SiO}_3$  solution. For the alkali-activate mortar prepared with 60 wt.% MSWI bottom ash and 40 wt.% BFS, the highest compressive strength can be obtained at the  $\text{SiO}_2$  to  $\text{Na}_2\text{O}$  molar ratio of 1.04 [157].

#### *MSWI bottom ash and metakaolin*

Lancellotti et al. [158] studied the possibility of using MSWI bottom ash as an alternative to metakaolin for the preparation of alkali-activated paste. The maximum replacement level of MSWI bottom ash was 70 wt.%. The sample failed upon demolding when more than 70 wt.% metakaolin was replaced by MSWI bottom ash. According to SEM-EDS analysis, the mass ratio of Si/Al in the gel phases formed in alkali-activated MSWI bottom ash-metakaolin paste increased from 2.5 to 3.36 when the replacement level of MSWI bottom ash increased from 50 wt.% to 70 wt. %. This test result indicated that the Si ions dissolved from MSWI bottom ash could participate in the formation of gel phases [158].



Zhu et al. [175] used the metallic Al-containing MSWI bottom ash as a gas-foaming agent to prepare aerated alkali-activated metakaolin paste. MSWI bottom ash was regarded as an alternative to Al powder rather than a replacement for metakaolin. The aeration capacity of MSWI bottom ash was about 1/250 that of Al powder. The rheological properties of alkali-activated metakaolin were almost independent of the incorporation of Al powder. In comparison, the addition of MSWI bottom ash delayed the setting and remarkably increased the yield stress and viscosity of the fresh paste. The porous alkali-activated metakaolin paste with MSWI bottom ash as a foaming agent showed similar compressive strength and thermal conductivity to that prepared with metallic Al.

#### *MSWI bottom ash and coal fly ash*

Wongsa et al. [176] used MSWI bottom ash to replace Class F coal fly ash for the preparation of alkali-activated mortar. This MSWI bottom ash was derived from the combustion of dry branches, paper, and dry leaves collected at a Thai university. The compressive strength of alkali-activated mortar decreased as the percentages of MSWI bottom ash increased from 20 to 40 wt. % in the precursor. The 28-day compressive strength of alkali-activated mortar increased by 26 % when 20 wt.% Class F coal fly ash was replaced by MSWI bottom ash. At a replacement level of 40 wt.%, the compressive strength of alkali-activated MSWI bottom ash-Class F coal fly ash mortar was still slightly higher than the alkali-activated coal fly ash mortar. The higher compressive strength of alkali-activated MSWI bottom ash-Class F coal fly ash mortar was attributed to the small particle size and high CaO content of MSWI bottom ash. The average particle size of MSWI bottom ash was 5.15  $\mu\text{m}$ , much smaller than that of Class F coal fly ash (32.58  $\mu\text{m}$ ). MSWI bottom ash contained 38.1 wt.% CaO, more than two times the CaO content in Class F coal fly ash (14.5 wt.%). Blending MSWI bottom ash with Class F coal fly ash increased the CaO content in the precursor, promoting the formation of C-S-H gel [176].

## **2.8 Environmental impacts of construction materials prepared with MSWI bottom ash**

Previous life cycle impact assessment (LCIA) results have indicated that using MSWI bottom ash to replace Portland cement [149] or to prepare AAM is environmentally beneficial [179]. There are, however, very few studies in this area [149,179], and life cycle assessment (LCA) is usually performed using the cradle-to-gate method according to ISO 14040 (2006) [180].

Alderete et al. [149] reported that replacing 20 wt.% Portland cement with MSWI bottom ash reduced the environmental impacts of Portland cement concrete in all categories, including global warming, abiotic resource depletion, ozone layer depletion, photochemical ozone creation, acidification of soil and water, eutrophication, human toxicity, and ecotoxicity. The compressive strength and durability of MSWI bottom ash blended cement concretes were similar to that of Portland cement concrete. It should be noted that (semi-)industrial-scale treatments were performed on MSWI bottom ash prior to its use as SCM, but the environmental impacts of these treatments were neglected during the life cycle assessments [149].

Torelli [179] assessed the environmental impacts of alkali-activated mortars with their precursor consisting of a blend of 40 wt.% MSWI bottom ash and 60 wt.% Class F coal fly ash [176] or a mixture of 60 wt.% MSWI bottom ash and 40 wt.% BFS [157,172]. The mix designs of the alkali-activated mortars were proposed by Wongsu et al. [176] and Huang et al. [157,172], respectively. For life cycle assessment, the MSWI bottom ash used by Wongsu et al. [176] and Huang et al. [157,172] were assumed to be the same. The life cycle inventory (LCI) data of MSWI bottom ash was obtained by assessing the environmental impacts of the plant-scale treatments required to transform freshly quenched MSWI bottom ash into fine powders suitable for being used as AAM precursor. The data about the plant-scale treatments was directly taken from the literature. The LCIA results showed that MSWI bottom ash blended alkali-activated mortars had a significantly lower impact on global warming than Portland cement mortar with the same compressive strength. However, the alkali-activated mortars had higher environmental footprints in other impact categories, including abiotic depletion, ozone layer depletion, photochemical oxidation, acidification, and eutrophication. Among all the constituents of alkali-activated mortars, Class F coal fly ash and BFS were the main contributors to these environmental impact categories [179].

## 2.9 Summary of literature studies

In this chapter, a comprehensive overview was given of studies related to the utilization of municipal solid waste incineration (MSWI) bottom ash as supplementary cementitious material (SCM) and precursor for alkali-activated materials (AAM). The summary of the literature studies is presented below.

- Due to its heterogeneous composition and high risk of heavy metal leaching, fresh bottom ash collected from MSWI plants cannot be directly used as an ingredient for building materials. Quality-upgrade treatments, such as plant-scale treatments and lab-scale treatments, are performed on fresh MSWI bottom ash to make it suitable to be used as SCM and AAM precursor.
- Compared with fresh MSWI bottom ash, weathered MSWI bottom ash obtained after plant-scale treatments usually has a more stable mineralogical composition and lower leaching of contaminants into the environment. Weathered MSWI bottom ash produced in different regions shows common features. The chemical composition of weathered MSWI bottom ash varies within the same range as that of coal fly ash. The crystalline phases fall within 11 mineral groups. Most weathered MSWI bottom ash has more than 50 wt.% amorphous phase.
- Most of the MSWI bottom ash sent to the laboratory is produced after plant-scale treatments of fresh MSWI bottom ash. The lab-scale treatments include mechanical treatments, chemical treatments, and thermal treatments. All these methods can be used to reduce the metallic Al content in MSWI bottom ash. In addition to metallic Al content reduction, mechanical treatments can also reduce the particle size of MSWI bottom ash. Thermal treatments can increase the reactivity of MSWI bottom ash and reduce the contents of organics.



- The reactivity of MSWI bottom ash as SCM and AAM precursor can be similar to that of Class F coal fly ash. Pozzolanic reaction products of MSWI bottom ash are C-S-H, similar to those formed during cement hydration. Alkali activation of MSWI bottom ash mainly leads to the formation of amorphous gel phases, including C-S-H, C-A-S-H, and N-A-S-H.
- Factors that influence the properties of MSWI bottom ash blended cement pastes, mortars, or concretes include the metallic Al content, pozzolanic reactivity, particle size, and replacement level of MSWI bottom ash and the water-to-binder ratio used in the mixture. For replacement levels ranging from 5-30 wt.%, the concentrations of heavy metals in the leachates of samples prepared with MSWI bottom ash as SCM are lower than the upper limits set by the government. The replacement of Portland cement with MSWI bottom ash will hinder cement hydration and strength development at early ages.
- Factors that influence the properties of alkali-activated MSWI bottom ash are the metallic Al content and reactivity of MSWI bottom ash, the type of activator, and the curing condition. In most cases, the leaching of heavy metals from alkali-activated MSWI bottom ash is more severe than from unreacted MSWI bottom ash. Leaching of some heavy metals from alkali-activated MSWI bottom ash could exceed the regulatory upper limit. In previous research, MSWI bottom ash was also blended with other types of precursors to prepare AAM, such as blast furnace slag, metakaolin, and coal fly ash.
- Previous studies indicated that construction materials prepared with MSWI bottom ash as SCM and AAM precursor had lower environmental impacts than Portland cement-based construction materials.

## 2.10 Challenges of using MSWI bottom ash as SCM and AAM precursor

Although a lot of research has been carried out to promote the use of MSWI bottom ash as SCM and AAM precursor, there are many challenges that need to be solved before the industrial application of MSWI bottom ash as a mineral resource for building materials can be realized.

- Previous studies were performed on locally produced MSWI bottom ash. Although different methods have been proposed to improve the quality of MSWI bottom ash, there is no systematic guidance for the quality-upgrade treatments of MSWI bottom ash. The reaction of MSWI bottom ash during the quality-upgrade treatments has rarely been studied in previous research.
- In previous research, the reactivity of MSWI bottom ash and the leaching of contaminants from MSWI bottom ash were not always measured before its application as SCM or AAM precursor. The link between the chemical composition of the amorphous phase and the reactivity of MSWI bottom ash remains unknown. When MSWI bottom ash was used to prepare blended cement pastes or alkali-activated pastes, the mix design was not based on the reactivity or the leaching potential <sup>(6)</sup> of MSWI bottom ash but on the mechanical properties of the construction materials. The mix design proposed for one type of MSWI bottom ash cannot be directly used to prepare blended cement pastes or alkali-activated pastes with another type of MSWI bottom ash.

---

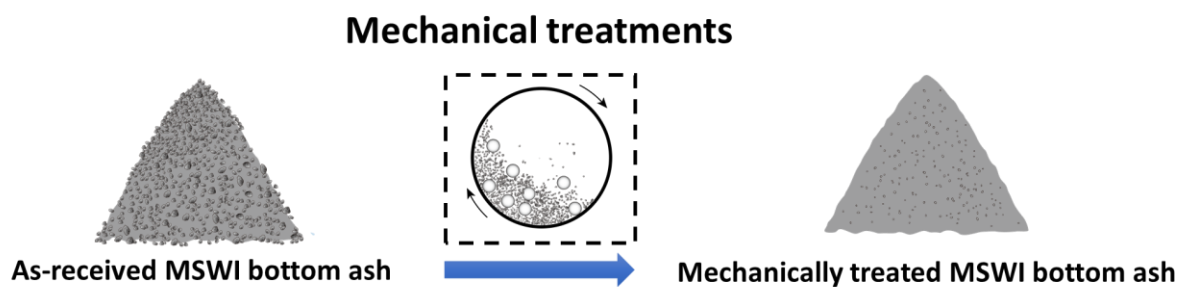
<sup>(6)</sup> Leaching potential refers to the likelihood of contaminants leaching from solids into the environment.

- Previous research mainly focused on the engineering properties of construction materials prepared with MSWI bottom ash as SCM and AAM precursor. The reaction kinetics and microstructure of blended cement paste and alkali-activated pastes determine the engineering properties of construction materials. A scientific understanding of the reaction of MSWI bottom ash in blended cement pastes and AAM is required to reveal the effects of MSWI bottom ash on the reaction kinetics and microstructure formation.
- Environmental impacts of the construction materials prepared with MSWI bottom ash as SCM and AAM precursor are strongly influenced by the quality-upgrade treatments of MSWI bottom ash and the mix design. It is always required to evaluate the environmental impacts of produced construction materials to check whether these products are environmentally friendly.

## Chapter 3

---

### Characterization and mechanical treatments of as-received MSWI bottom ash



#### Highlights

- As-received MSWI bottom ash cannot be directly used to prepare blended cement pastes or alkali-activated pastes, due to its large particle size and metallic Al content.
- Mechanical treatments can effectively reduce the particle size and metallic Al content of as-received MSWI bottom ash.
- The maximum amount of metallic Al that can be removed via mechanical treatments depends on the parameter settings and the distribution of metallic Al in different size fractions of as-received MSWI bottom ash.

### 3.1 Introduction

This chapter is about the characterization and mechanical treatments of as-received municipal solid waste incineration (MSWI) bottom ash. The goal is to identify and resolve the issues that hinder the application of as-received MSWI bottom ash as supplementary cementitious material (SCM) and precursor for alkali-activated materials (AAM). Previous research indicates that MSWI bottom ash usually has heterogeneous compositions and can contain metallic Al (see Chapter 2). When MSWI bottom ash was used as SCM or AAM precursor, the metallic Al embedded in MSWI bottom ash particles would oxidize. The hydrogen gas released from the oxidation of metallic Al would lead to volume expansion and strength reduction [53,54].

The particle size distribution, metallic Al content, and chemical and mineralogical compositions are usually measured for the characterization of weathered MSWI bottom ash (see Chapter 2). To the best of our knowledge, the distribution of metallic Al among different size fractions of weathered MSWI bottom ash particles has not been comprehensively studied yet. In previous research, only the metallic Al embedded in fresh MSWI bottom ash particles was studied [55,63]. However, the distribution of metallic Al in fresh MSWI bottom ash particles differs from that in weathered MSWI bottom ash particles. The weathered MSWI bottom ash is obtained after the weathering of fresh MSWI bottom ash (see Chapter 2). As a result of weathering, part of the metallic Al embedded in fresh MSWI bottom ash is oxidized. A significant reduction in metallic aluminum content was detected after weathering [56,85].

As summarized in Chapter 2, different methods have been proposed by previous researchers to improve the quality of MSWI bottom ash. The particle size of MSWI bottom ash is usually reduced via mechanical treatments consisting of grinding and sieving. Due to size reduction, the homogeneity in the compositions of MSWI bottom ash is also increased after mechanical treatments. Metallic Al can be separated from MSWI bottom ash by sieving during mechanical treatments. Other methods used to reduce the metallic Al content in MSWI bottom ash include chemical treatments (e.g., water treatment and NaOH solution treatment) and thermal treatments.

Mechanical treatments have advantages over chemical treatments. Mechanical treatments are usually performed at room temperature, and no wastewater is discharged during this process. In comparison, water treatment needs to combine with thermal treatments to accelerate the oxidation rate of metallic Al and, meanwhile, evaporate the water added for the treatments [56]. The residual alkalis in NaOH solution-treated MSWI bottom ash need to be removed for the application as SCM, leading to the discharge of wastewater [126,130].

The cost of thermal treatments can be higher than that of mechanical treatments. During thermal treatments, the heating temperature needs to reach 1000 °C to oxidize more than 90 wt.% of the metallic Al in MSWI bottom ash [54,128]. Due to the agglomeration of particles, additional mechanical treatments are employed to reduce the particle size and make thermally treated MSWI bottom ash suitable for the application of SCM and AAM precursor [54,128].

This chapter consists of three parts (Figure 3.1):

- Part 1 is to study the heterogeneity in the compositions of as-received MSWI bottom ash. The MSWI bottom ash particles of different sizes are compared regarding their chemical and mineralogical compositions.
- Part 2 is to study the metallic Al in as-received MSWI bottom ash. The distribution of metallic Al among different size fractions is measured. The particles that contain metallic Al are characterized to investigate the metallic Al embedded in MSWI bottom ash particles.
- In part 3, the mechanical treatments are selected to improve the quality of as-received MSWI bottom ash according to the information obtained in part 1 and part 2. The extent to which the metallic Al can be removed via mechanical treatments is discussed.

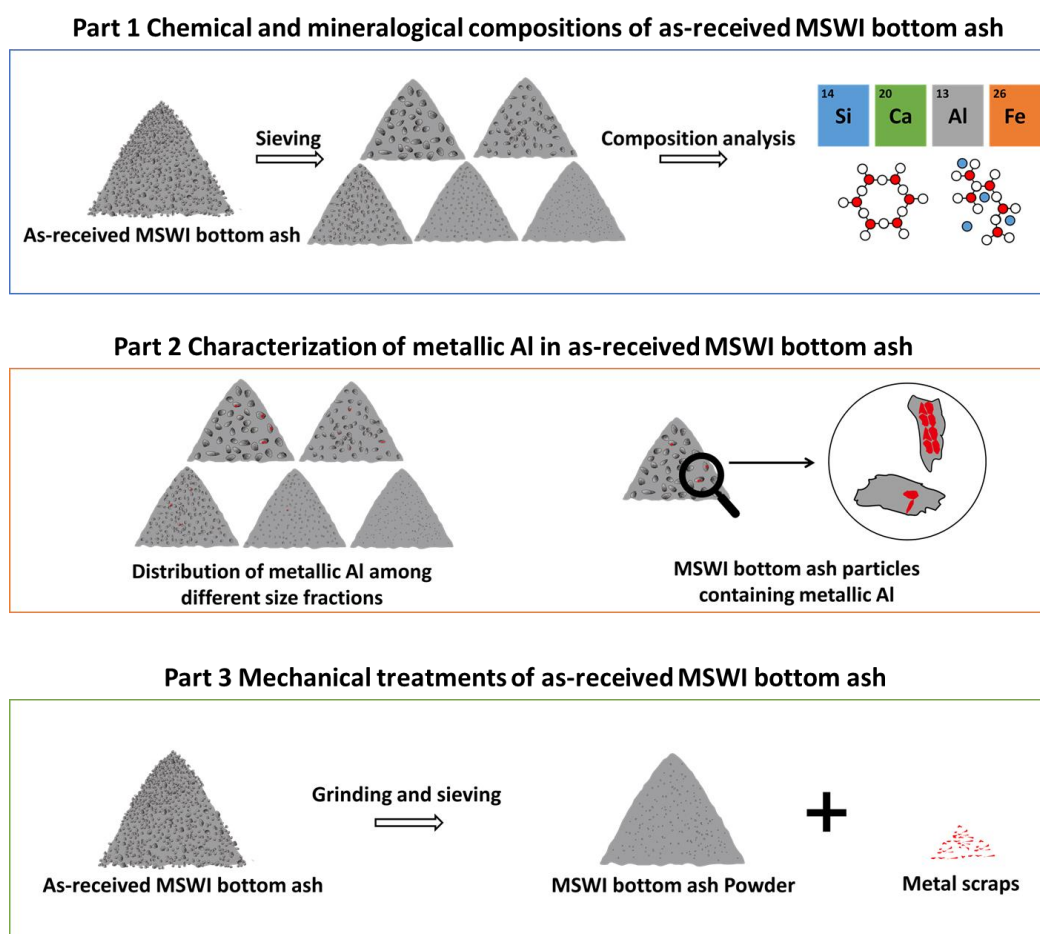
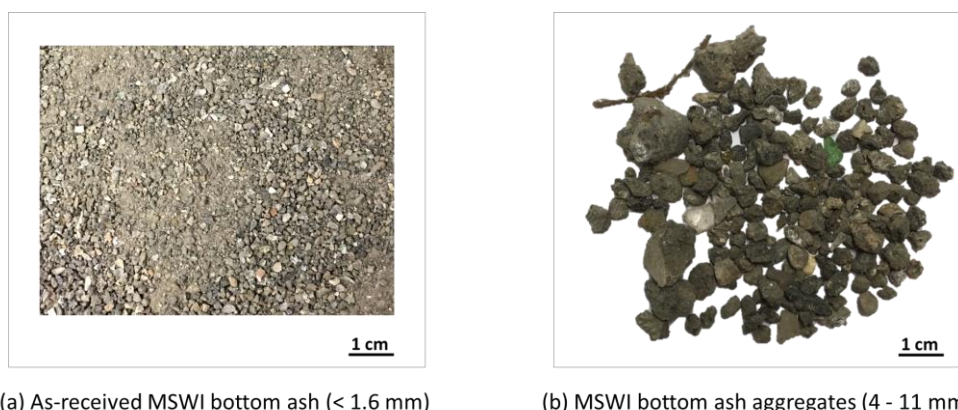


Figure 3.1 The content of this chapter.

## 3.2 Materials and methods

### 3.2.1 Materials

As-received MSWI bottom ash has a particle size below 1.6 mm (Figure 3.2 (a)). This raw material was obtained by crushing 4 - 11 mm MSWI bottom ash aggregates (Figure 3.2 (b)) with Retsch® BB100. The crushing process was performed in a way similar to that employed by Van de Wouw [181]. The MSWI bottom ash aggregates were produced in a Dutch waste-to-energy plant. The plant-scale treatments of MSWI bottom ash aggregates followed the strategy described by Keulen et al. [84], where the MSWI bottom ash was treated with dry separation, wet separation, and weathering. Most of the ferrous and non-ferrous metals were extracted during the dry separation process. The organic and inorganic leachable contaminants were removed in the wet separation process. The weathering process took around 3 months, and the goal was to immobilize heavy metals. After plant-scale treatments, the heavy metal leaching of MSWI bottom ash aggregates complied with the open (granular) application criteria of the Dutch Soil Quality Decree [84,182].



(a) As-received MSWI bottom ash (< 1.6 mm)

(b) MSWI bottom ash aggregates (4 - 11 mm)

Figure 3.2 Images of (a) as-received MSWI bottom ash and (b) MSWI bottom ash aggregates.

### 3.2.2 Characterization techniques

#### 3.2.2.1 Chemical composition

The Panalytical Axio Max WD-XRF spectrometer was used to measure the chemical composition of as-received and treated MSWI bottom ash. The test samples were ground to a size smaller than 63  $\mu\text{m}$  with planetary ball mill (Retsch® PM 100) before the X-ray fluorescence (XRF) measurements.

The unburned organic content in as-received MSWI bottom ash was also measured. This organic content, referred to as loss on ignition (LOI), was measured according to NEN-EN 1744-7 (2010) [183] at 550 °C.

#### 3.2.2.2 Mineralogical composition

The mineralogical composition of as-received and treated MSWI bottom ash was determined by X-ray diffraction (XRD) techniques using Bruker D8 Advance diffractometer. For the XRD

analysis, the samples were first ground to a particle size smaller than 63  $\mu\text{m}$ . Afterward, the ground samples were manually milled in agate mortar to ensure that their particle size was between 1 - 5  $\mu\text{m}$ . The mineral phases of the samples were identified with Bruker software Diffraction EVA 4.3. The mineralogical composition analysis of the metal scraps obtained after the treatments of as-received MSWI bottom ash (Figure 3.14) follows the same procedure as that of treated MSWI bottom ash.

For the quantitative XRD analysis (QXRD), ten percent (10 wt.%) of silicon powder was mixed with test samples during the sample preparation process. The content of each mineral phase was estimated by using the Rietveld method with the software Profex-BGMN [184]. The crystal structure models taken from the Inorganic Crystal Structure Database (ICSD) were used to fit the observed XRD pattern. The content of amorphous and crystal phases was determined by normalizing measured XRD patterns on an equal-silicon-intensity basis.

### 3.2.2.3 Metallic Al content

Figure 3.3 illustrates the set-up used for the measurement of metallic Al content in as-received MSWI bottom ash. The metallic Al content in the metal scraps separated from as-received MSWI bottom ash is determined in the same way. The water displacement method is used for the experimental design [74]. The MSWI bottom ash is immersed in the NaOH solution. The hydrogen gas released from the reaction between metallic Al and NaOH solution in the three-neck round-bottom flask is first led to a U-shaped drying tube to subtract the contribution of water vapor. Afterward, due to pressure increase, the hydrogen gas displaces the water inside the wide mouth stoppered glass bottle. The volume of yielded hydrogen gas equals the volume of water that goes up in the graduated cylinder.

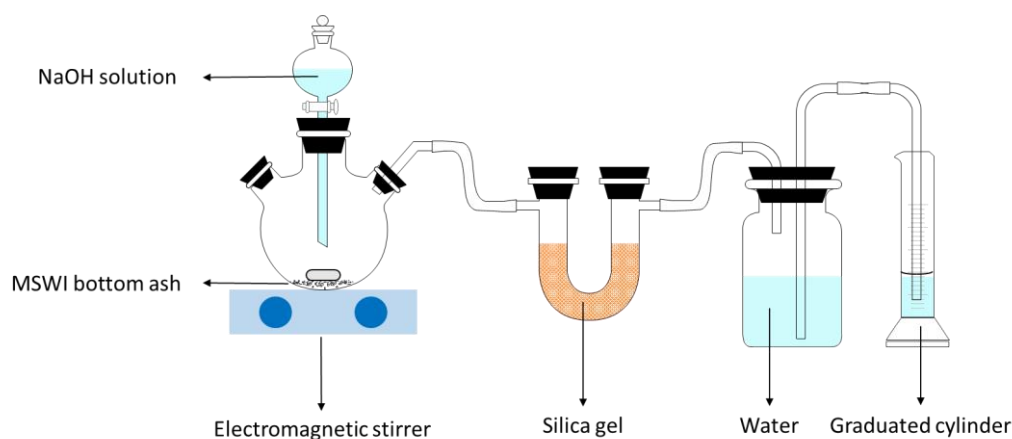
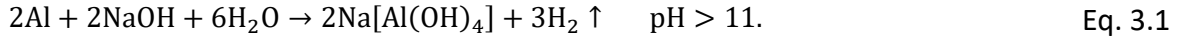


Figure 3.3 Set-up used for the measurement of metallic Al content in MSWI bottom ash.

The water displacement method cannot distinguish the hydrogen gas ( $\text{H}_2$  gas) released from the reaction of metallic Al and the reaction of metallic Zn. In our preliminary research, metallic Zn was hardly detected. A similar observation that the metallic Zn content was much less than metallic Al was reported in the literature for the MSWI bottom ash produced in the Netherlands [185,186]. Therefore, in the calculation, all the  $\text{H}_2$  gas collected was attributed to the reaction of metallic Al, and the contribution of metallic Zn to the release of the  $\text{H}_2$  gas was



neglected. The chemical reaction between metallic Al and NaOH solution is described in Eq. 3.1. The weight percentage of metallic Al in MSWI bottom ash ( $f_{Al}$ ) was calculated with Eq. 3.2. In Eq. 3.2,  $\Delta V$  corresponds to the volume of hydrogen gas measured at room temperature  $T$  in Celsius degree,  $V_0$  represents the molar gas volume at standard pressure and temperature ( $P_0 = 101.3\text{kPa}$ ,  $T_0 = 273\text{K}$ ),  $M_{Al}$  is the molar mass of aluminum, and  $m_{BA}$  stands for the mass of MSWI bottom ash.



$$f_{Al} = \frac{2\Delta V \left( \frac{273}{273+T} \right) \frac{M_{Al}}{3V_0}}{m_{BA}} \quad \text{Eq. 3.2}$$

### 3.2.2.4 Metallic Al embedded in MSWI bottom ash particles

The Energy Dispersive X-rays spectroscopy (EDS) combined with scanning electron microscopy (SEM) was used to measure the elemental distribution within MSWI bottom ash particles and find the particles that contain metallic Al. The size fraction of 0.5 - 1.6 mm was selected for this analysis because it has the highest metallic Al content. More explanations for this selection will be presented in section 3.3.3.1. As for SEM sample preparation, several hundred randomly selected MSWI bottom ash particles were mounted in epoxy resin (see Figure 3.4). The mold was a polyethylene bottle with a diameter of 35 mm. For the sake of avoiding metallic Al oxidation, mounted samples were ground and polished to a flat surface using isopropanol in a  $\text{N}_2$  - atmosphere glove box. Afterward, the polished samples were coated with a thin layer of carbon (around 10 nm) to improve their conductivity under a high vacuum. The samples were analyzed using FEI QUANTA FEG 650 ESEM. The accelerating voltage and working distance of the measurement were set as 15 kV and 10 mm, respectively.

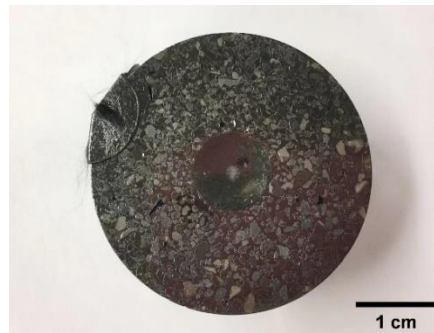


Figure 3.4 Image of SEM sample prepared for metallic Al analysis.

The optimal microscope settings for microanalysis were determined with Monte Carlo simulation in WinCasino v2.51 software. In the microanalysis, the phases of interest are metallic Al (including alloys of Al) and the oxidized Al ( $\text{Al}_2\text{O}_3$  and  $\text{Al}(\text{OH})_3$ ). Figure 3.5 provides visual depictions of the lateral extent of the X-ray interaction volume of metallic Al, aluminum oxides ( $\text{Al}_2\text{O}_3$ ), and aluminum hydroxides ( $\text{Al}(\text{OH})_3$ ). The pixel size ( $2\text{ }\mu\text{m}$ ) selected is close to the lateral dimension of the interaction volume of metallic Al. A pixel scan field of  $512 \times 340$  was selected for elemental mapping. The spectral imaging (SI) data sets (atomic percentage)



were acquired for the identification of metallic Al, aluminum oxide, and aluminum hydroxide in image analysis.

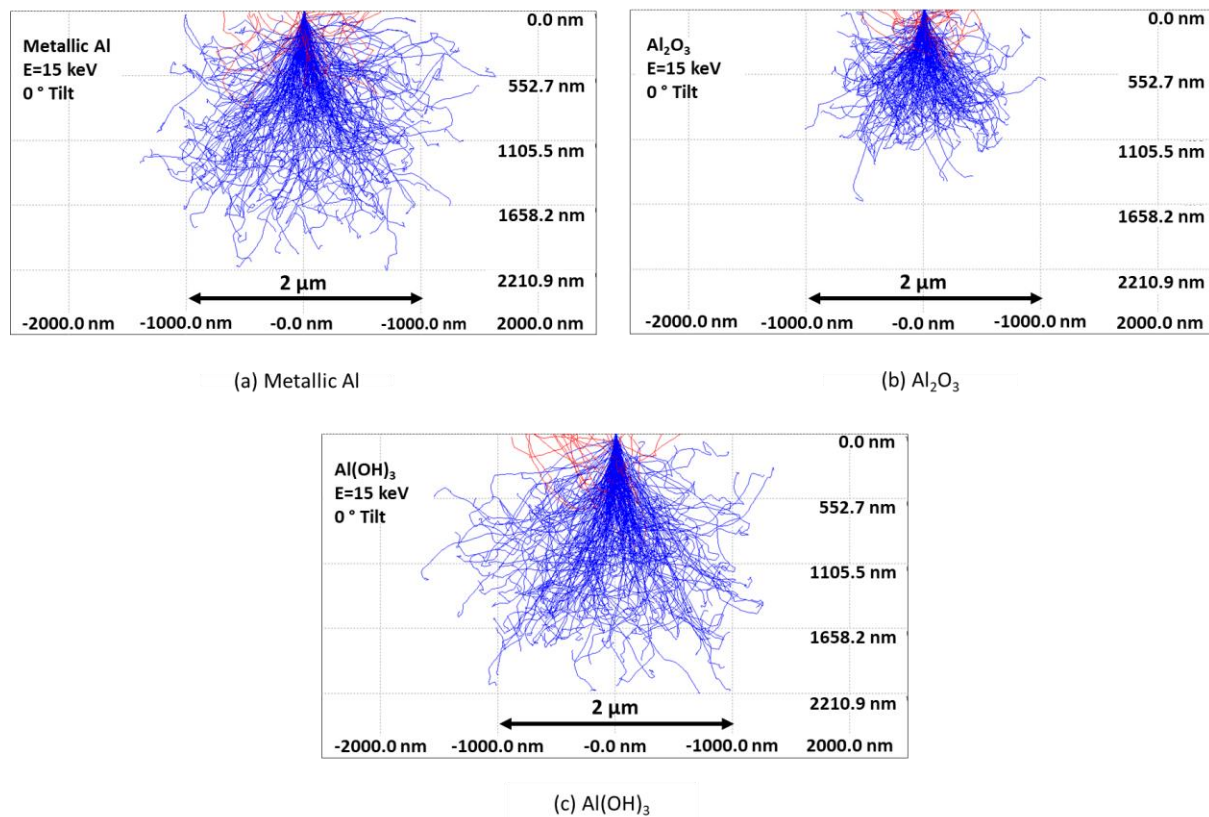


Figure 3.5 Monte Carlo simulation of the penetration of 1000 electrons accelerated at 15 keV in a beam of a radius of 10 nm into (a) metallic Al, (b) Al<sub>2</sub>O<sub>3</sub>, and (c) Al(OH)<sub>3</sub>, all shown at the same scale. (Red trajectories for Backscattered electrons, and blue trajectories for absorbed electrons).

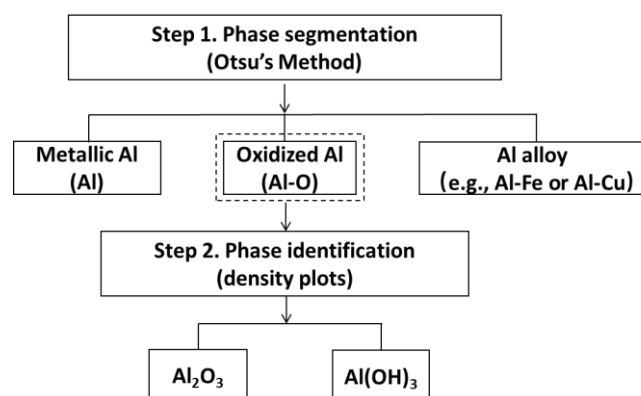


Figure 3.6 The process of image analysis for metallic Al containing MSWI bottom ash particles.

The process of image analysis used in this work is illustrated in Figure 3.6. The first step was phase segmentation, which was carried out following Otsu's method [187]. The image thresholding was performed on the atomic ratio between oxygen and aluminum (O/Al) at

each pixel location of the SEM images. The regions enriched with the phases, including metallic Al (Al), oxidized Al (Al-O), and Al alloy (e.g., Al-Fe or Al-Cu), were identified in the SEM images of MSWI bottom ash particles. For each segmented phase, their area percentage, average composition, and average O/Al ratio were calculated based on the information of corresponding pixels. In step two, the presence of  $\text{Al}_2\text{O}_3$  and  $\text{Al}(\text{OH})_3$  in segmented oxidized Al phase was demonstrated by creating density plots. Each point in the density plots represented the atomic percentages of Al and O at each pixel in the region of the Al-O phase. The density plots were colored according to the number of points in each area.

### 3.3 Results and discussion of as-received MSWI bottom ash characterization

#### 3.3.1 Particle size distribution of as-received MSWI bottom ash

As-received MSWI bottom ash was sieved into five size fractions to study the heterogeneity in its composition. These size fractions are 0.5 - 1.6 mm, 0.25 - 0.5 mm, 0.125 - 0.25 mm, 0.063 - 0.125 mm, and < 0.063 mm. The images of all these size fractions are illustrated in Figure 3.7, where the proportion of each size group in the MSWI bottom ash is also indicated. Regarding particle size distribution, the 0.5 - 1.6 mm size fraction constitutes around 50 wt.% of as-received MSWI bottom ash. The MSWI bottom ash with particle size between 0.063 mm and 0.125 mm accounts for the lowest proportion (less than 10 wt.%) among all the size fractions. For the remaining three size fractions, < 0.063 mm, 0.125 - 0.25 mm, and 0.25 - 0.5 mm, their percentages are all between 10 - 20 wt.%.

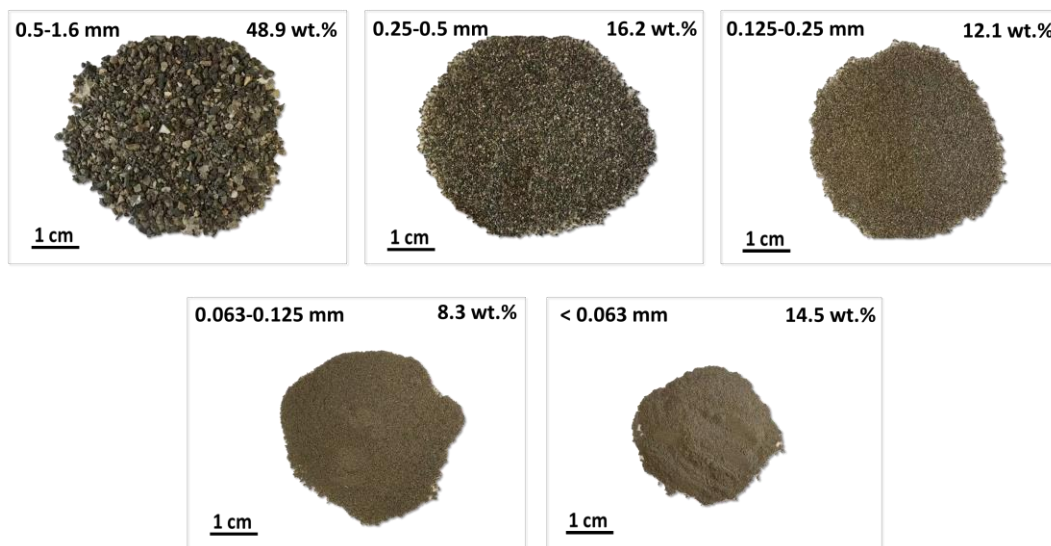


Figure 3.7 Different size fractions of as-received MSWI bottom ash (< 1.6 mm) and corresponding weight percentages.

### 3.3.2 Compositions of as-received MSWI bottom ash

#### 3.3.2.1 Chemical composition

The chemical composition of the coarse and fine particles in as-received MSWI bottom ash are compared in Figure 3.8. The detailed XRF results can be found in Table B 1. Overall, the chemical composition of as-received MSWI bottom ash falls within the same range as the weathered MSWI bottom ash used by previous researchers (see Chapter 2). Figure 3.8 (a) shows that the main components within all size groups of MSWI bottom ash are  $\text{SiO}_2$ ,  $\text{CaO}$ ,  $\text{Al}_2\text{O}_3$ , and  $\text{Fe}_2\text{O}_3$ . The  $\text{SiO}_2$  accounts for the highest proportion in each size fraction, ranging from 42.31 to 53.17 wt.% (see Table B 1).

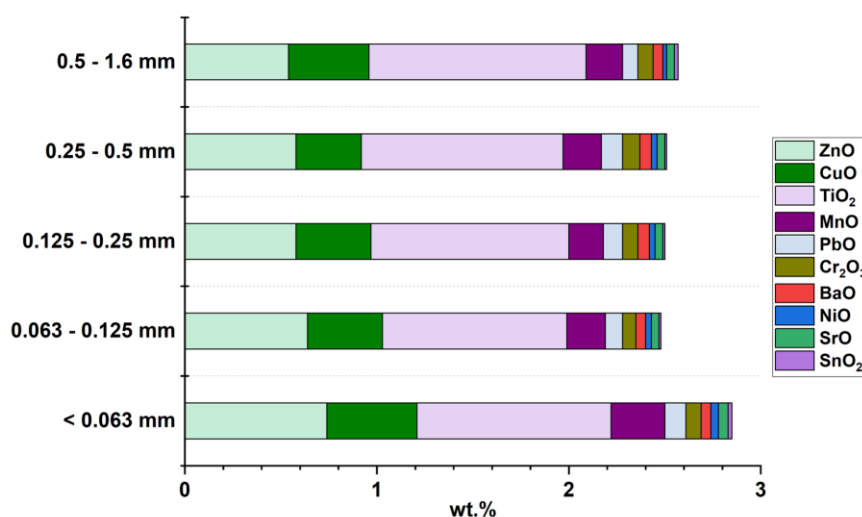
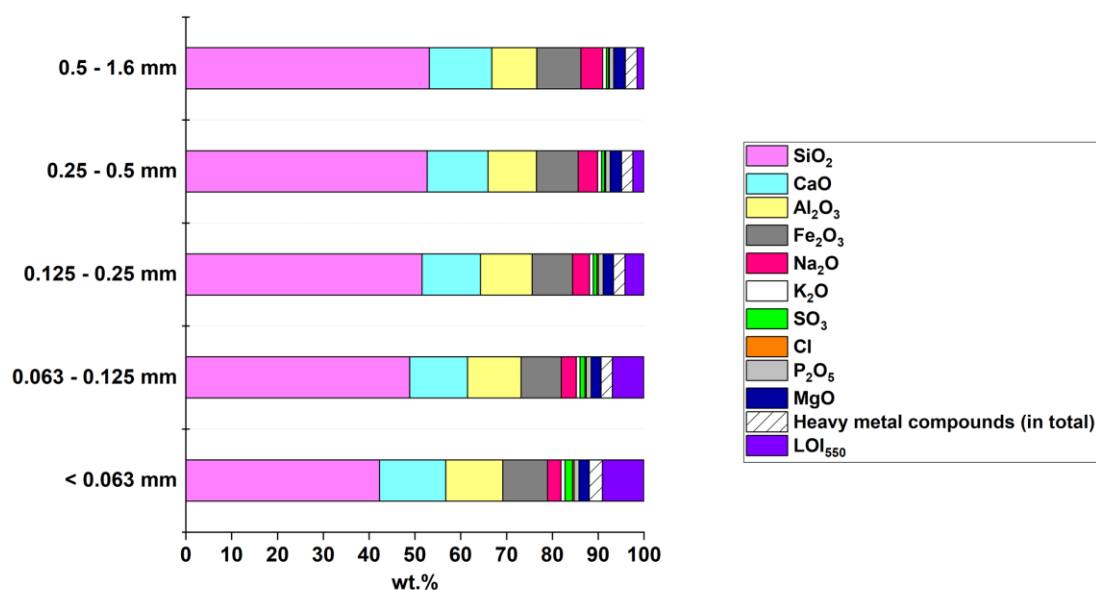


Figure 3.8 Comparison among the XRF results of different size fractions in as-received MSWI bottom ash.

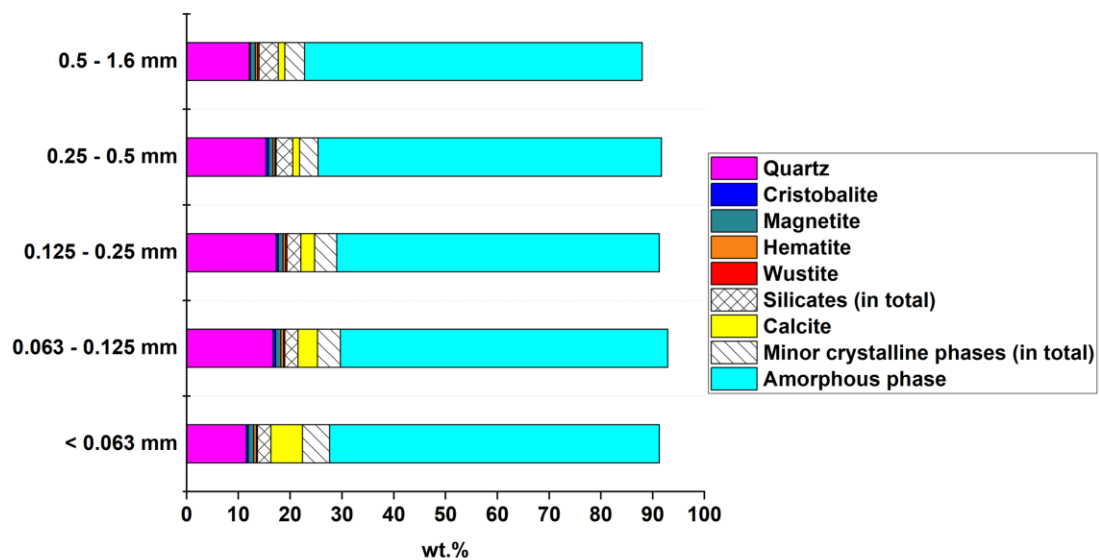
The content of CaO, Al<sub>2</sub>O<sub>3</sub>, or Fe<sub>2</sub>O<sub>3</sub> varies slightly among different size fractions (see Figure 3.8 (a)). As listed in Table B 1, the CaO content changes from 12.67 to 14.42 wt.%. The Al<sub>2</sub>O<sub>3</sub> content is within the range of 9 - 13 wt.%. The Fe<sub>2</sub>O<sub>3</sub> content is between 8 and 10 wt.%. Comparatively, Figure 3.8 (a) shows that the SiO<sub>2</sub> and Na<sub>2</sub>O contents tend to decrease from the large size fraction (0.5-1.6 mm) to the small size fraction (<0.063 mm). The SO<sub>3</sub> and Cl are concentrated in the smaller particles of MSWI bottom ash. The total amount of heavy metal compounds detected in the < 0.063 mm size fraction is much higher than in the coarser fractions. The content of each heavy metal compound can be found in Figure 3.8 (b). The fraction containing particles smaller than 0.063 mm has the highest unburned organic content (LOI), more than six times that detected in the 0.5 - 1.6 mm size fraction.

### 3.3.2.2 Mineralogical composition

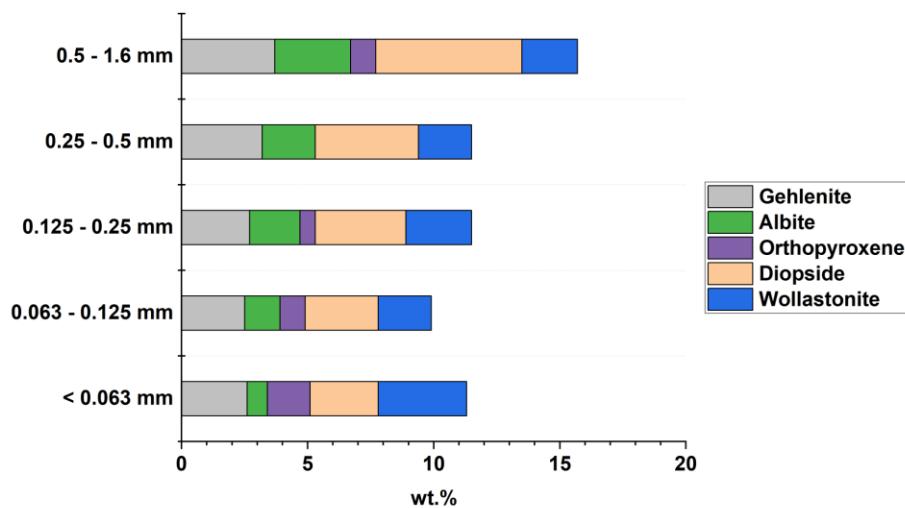
The mineral phases detected in as-received MSWI bottom ash, together with their formulae and ICSD codes, are listed in Table 3.1. The proportions of the mineral phases identified in the individual size fraction of as-received MSWI bottom ash are listed in Table B 2. Compared with the weathered MSWI bottom ash used by previous researchers, the mineralogical compositions of as-received MSWI bottom ash vary within the same range (see Chapter 2). The QXRD results of different size fractions are compared in Figure 3.9. This figure indicates that MSWI bottom ash with different particle sizes has almost the same phase assemblages. Regardless of the particle size, the amorphous phase accounts for the highest percentage (see Figure 3.9 (a)). The content of the amorphous phase fluctuates around 65 wt.% across all size fractions (Table B 2).

Table 3.1 Mineral phases present in MSWI bottom ash.

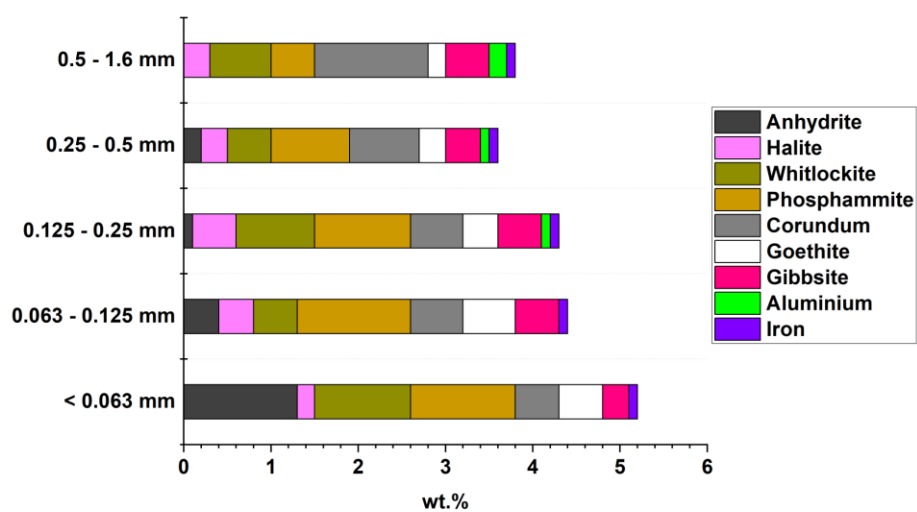
Classifications	Phases	Formulae	ICSD codes
Silicon dioxide	Quartz	SiO <sub>2</sub>	541929
	Cristobalite	SiO <sub>2</sub>	1251919
Iron oxides	Magnetite	Fe <sub>3</sub> O <sub>4</sub>	92356
	Hematite	Fe <sub>2</sub> O <sub>3</sub>	453828
	Wustite	FeO	309924
Silicates	Gehlenite	Ca <sub>2</sub> Al <sub>2</sub> Si O <sub>7</sub>	1411155
	Albite	NaAlSi <sub>3</sub> O <sub>8</sub>	1402109
	Orthopyroxene	Ca <sub>0.02</sub> Mg <sub>0.30</sub> Fe <sub>0.68</sub> Si O <sub>3</sub>	1615622
	Diopside	CaMg <sub>0.69</sub> Fe <sub>0.31</sub> Si <sub>2</sub> O <sub>6</sub>	77809
	Wollastonite	CaSiO <sub>3</sub>	1253098
Carbonates	Calcite	CaCO <sub>3</sub>	1611066
Minor crystalline phases	Anhydrite	CaSO <sub>4</sub>	16382
	Halite	NaCl	311644
	Whitlockite	Ca <sub>18.16</sub> Fe <sub>0.4</sub> H <sub>1.68</sub> Mg <sub>1.6</sub> ( P O <sub>4</sub> ) <sub>14</sub>	23598
	Phosphammite	H ( N H <sub>4</sub> ) <sub>2</sub> ( P O <sub>4</sub> )	1401715
	Corundum	Al <sub>2</sub> O <sub>3</sub>	527601
	Goethite	FeO(OH)	71810
	Gibbsite	Al(OH) <sub>3</sub>	1005040
	Aluminum	Al	251015
	Iron	Fe	1503158



(a) Mineralogical composition of the particles within different size fractions



(b) Content of each crystalline phase that belongs to silicates in different size fractions



(c) Content of each minor crystalline phase in different size fractions

Figure 3.9 Comparison among the QXRD results of different size fractions in as-received MSWI bottom ash.

As illustrated in Figure 3.9 (a), quartz, cristobalite, silicates (including gehlenite, albite, orthopyroxene, diopside, and wollastonite), calcites, and iron oxides (including magnetite, hematite, and wustite), are the primary crystalline phases in MSWI bottom ash. Quartz constitutes the highest proportion among all the crystals in each size fraction, ranging from 11.5 to 17.3 wt.%, while cristobalite is present in trace amounts. Silicates are the second major phase in as-received MSWI bottom ash. The total content of silicates is the highest in the 0.5 - 1.6 mm size fraction. The contents of the crystalline phases that belong to silicates are presented in Figure 3.9 (b). The calcite content increases with the decrease of particle size (see Figure 3.9 (a)). MSWI bottom ash with a particle size smaller than 0.063 mm has the highest percentage of calcite, up to 6.1 wt.%. Comparatively, the bottom ash with particle size between 0.5 and 1.6 mm has the smallest percentage of calcite, below 1.3 wt.%. The contents of iron oxides are very small ( $< 1.2$  wt.%) in all size fractions of as-received MSWI bottom ash (Table B 2)

Apart from the primary crystalline phases, other crystalline phases detected in as-received MSWI bottom ash are referred to as the minor crystalline phase, as shown in Figure 3.9 (a). The content of each minor crystalline phase can be found in Figure 3.9 (c). Figure 3.9 (c) indicates that the fraction of 0.5 - 1.6 mm has the highest percentage of metallic Al. The corundum content exceeds 1 wt.% only in the 0.5 - 1.6 mm size fraction (see Table B 2). In comparison, the content of gibbsite, the aluminum hydroxide, is around 0.5 wt.% in each size fraction. Corundum and gibbsite usually form due to the hydrolysis of metallic Al during the weathering process [17,71,109,113]. The metallic Al embedded in as-received MSWI bottom ash particles will be further studied in the following section.

### 3.3.3 Characterization of metallic Al in as-received MSWI bottom ash

#### 3.3.3.1 Distribution of metallic Al among different size fractions

The distribution of metallic Al was studied by measuring the metallic Al content in each size fraction and finding the size fraction with the highest percentage of metallic Al in as-received MSWI bottom ash. As shown in Figure 3.10 (a), the metallic Al content decreases from 0.71 wt.% in 0.5 - 1.6 mm size fraction to almost zero in the size fraction below 0.063 mm. Figure 3.10 (b) indicates that 73 wt.% of the metallic Al detected in as-received MSWI bottom ash is embedded in particles of 0.5 - 1.6 mm. The particles larger than 0.25 mm contain around 90 wt.% of the metallic Al in as-received MSWI bottom ash. Considering the distribution of metallic Al among different size fractions, removing metallic Al from the coarse particles (> 0.25 mm) is of high importance for the metallic Al content reduction in as-received MSWI bottom ash.

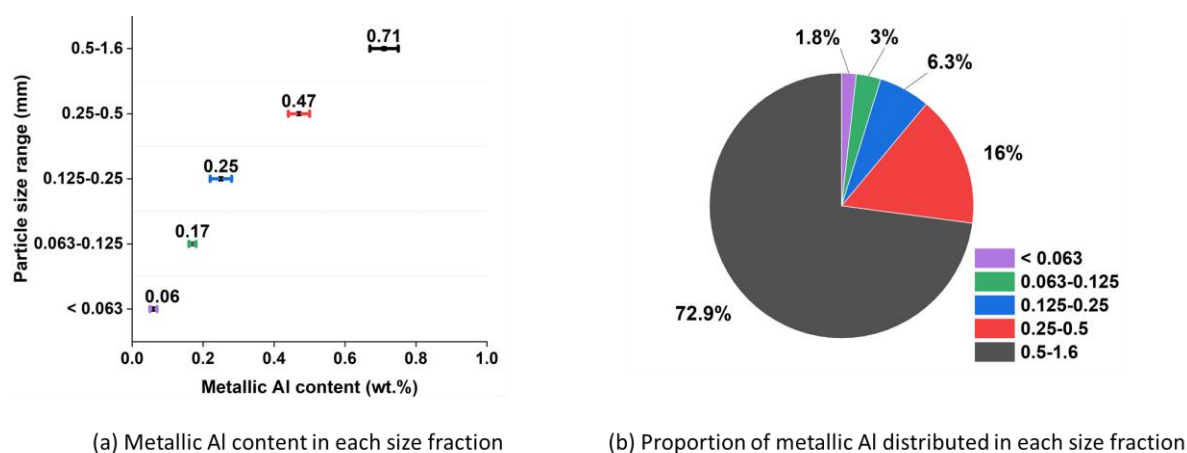


Figure 3.10 Distribution of metallic Al among different size fractions of as-received MSWI bottom ash.

#### 3.3.3.2 MSWI bottom ash particles containing metallic Al

As discussed in section 3.3.3.1, the 0.5 - 1.6 mm size fraction contains the highest percentage of metallic Al in as-received MSWI bottom ash. Therefore, the particles within this size fraction were chosen to investigate the metallic Al embedded in MSWI bottom ash particles. In our preliminary study, the large area phase mapping analysis was performed with SEM-EDS for all MSWI bottom ash particles mounted in the epoxy (see Figure 3.4). The analysis results indicated that *most* of the particles in the 0.5 - 1.6 mm size fraction *did not* contain metallic Al. The metallic Al was *only* found in a few MSWI bottom ash particles with characteristic features.

Two typical examples of the MSWI bottom ash particles containing metallic Al are illustrated in Figure 3.11 (particle 1) and Figure 3.12 (particle 2). Figure 3.11 (a) and Figure 3.12 (a) are the backscattered electron (BSE) images of these two particles. The element maps shown in Figure 3.11 (b)-(d) and Figure 3.12 (b)-(e) reveal the distribution of the major elements (Al, O, Fe, Mg) within MSWI bottom ash particles. After phase segmentation, the distribution of metallic Al in MSWI bottom ash particles is visualized in Figure 3.11 (e) and Figure 3.12 (f). The



area colored with blue, dark yellow, and purple corresponds to the phase identified as metallic Al (Al), oxidized Al (Al-O), and Al-Fe alloy (Al-Fe), respectively. The average O/Al atomic ratio and average composition of each phase are listed in Table 3.2. The average elemental composition is the mean value of the atomic percentages of each element measured at all pixel locations for each colored area labeled in Figure 3.11 (e) and Figure 3.12 (f).

Table 3.2 Quantification of segmented phases in particle 1 (Figure 3.11) and particle 2 (Figure 3.12).

Particle 1							
Phases	Area %	Average O/Al atomic ratio	Average elemental composition (at. %)				
			Al	O	Fe	Mg	Si
Al-O	35.22	2.9	29.80	48.84	0.48	0.00	0.51
Al	23.18	0.4	54.07	9.87	5.98	0.00	1.18
Al-Fe	0.18	0.0	29.21	0.28	63.31	0.00	0.00
Particle 2							
Phases	Area %	Average O/Al atomic ratio	Average elemental composition (at. %)				
			Al	O	Fe	Mg	Si
Al-O	9.96	2.8	27.19	42.83	0.07	5.73	0.83
Al	69.15	0.1	72.30	4.00	0.00	2.51	0.59
Al-Fe	0.02	0.1	48.85	2.15	20.23	0.97	5.84

#### *Phases classified as Metallic Al (Al)*

The phases in particle 1 show different shades of grey in the BSE image (Figure 3.11 (a)). The phases in the areas of bright grey (labeled 1) and light grey (labeled 2) were both classified as metallic Al and colored dark yellow (see Figure 3.11 (e)). According to the element maps of O and Al (Figure 3.11 (b) and (c)), the concentration of Al in the areas of bright grey and light grey is high, while the concentration of O is almost zero. However, only the area in light grey is composed of 100 % metallic Al. The area in bright grey consists of metallic Al with Fe impurities, as the weak signals of Fe are detected in this area (see Figure 3.11 (d)). The metallic Al that contains Fe impurities may come from the aluminum beverage cans in municipal solid waste [188].

For particle 2, the phases in the light grey area of the BSE image were categorized as metallic Al (Al) in phase segmentation (Figure 3.12 (f)). As illustrated in the element maps of O and Al (Figure 3.12 (b) and (c)), Al is highly concentrated in the light grey area, but the O content is nearly zero. However, the phase in the light grey area of particle 2 is metallic Al with Mg impurities rather than pure metallic Al. The element map of Mg (Figure 3.12 (e)) indicates that the phases in this area also incorporate Mg, but the signal of Mg is weak. The metallic Al that contains Mg impurities can be scrunched aluminum-magnesium foil initially used for food packing [189].

Quantitative analysis was performed on the recognized Al phase to validate the results of phase segmentation. As shown in Table 3.2, the mean value of the O/Al atomic ratio calculated at each pixel is close to zero. This result indicates that the recognized Al phase mainly consists of metallic Al. The Fe/Al ratio is 0.11 for the Al phase in particle 1, and the Mg/Al ratio is 0.03 for the Al phase in particle 2. The low value of these ratios indicates that the content of Fe or Mg is much smaller than that of Al in the recognized Al phase, and these



two metals are presented as impurities in metallic Al. It can be concluded that the image analysis used for the separation of metallic Al is reliable.

#### *Oxidized Al (Al-O) in the surroundings of metallic Al*

The images obtained after phase segmentation (Figure 3.11 (e) and Figure 3.12 (f)) show that metallic Al is surrounded by oxidized Al (colored blue) in MSWI bottom ash particles. In the phase segmentation, the phases in the areas mainly composed of Al and O were classified as oxidized Al (Al-O). The oxidized Al was found to concentrate in the dark grey area of the BSE image of particle 1 (labeled 3) and particle 2 (thin layers). The average of the O/Al atomic ratio of the pixels in the group of Al-O in particle 1 and particle 2 is 2.9 and 2.8, respectively (Table 3.2), which are close to the O/Al atomic ratio of  $\text{Al}(\text{OH})_3$ .

Since the MSWI bottom ash particles were ground and polished in a  $\text{N}_2$  atmosphere, the oxidation of metallic Al was prevented during the sample preparation process. The oxidized Al detected in MSWI bottom ash could be the oxidation product of aluminum cans, sheets, and foils in household wastes. During the process of metal recycling, the MSWI bottom ash particles are usually crushed into small pieces, resulting in the cracking of metallic Al scraps. The exposed surfaces of metallic Al easily react with oxygen and water during the weathering process. The oxidized Al can behave as a protective layer preventing the further oxidation of metallic Al.

The content of oxidized Al indicates the oxidation degree of the metallic Al initially embedded in MSWI bottom ash. In particle 1, the metallic Al was oxidized to a large extent as oxidized Al occupies a large area in the surroundings of metallic Al. The total area percentage of oxidized Al is 35.22 %, larger than the area covered by metallic Al (23.18 %). In comparison, only the surface of the metallic Al was oxidized in particle 2. The oxidized Al layers of 3 to 15  $\mu\text{m}$  are mainly found along the perimeter of the areas of metallic Al. The metallic Al occupies around 70 % of the area of particle 2, seven times the area of the Al-O phase.

The possible mineralogical composition of the Al-O phase recognized in phase segmentation can be determined with the help of density plots. In the density plots (Figure 3.13), the location of each point represents the atomic percentages of Al and O at each pixel location in the Al-O phase (Figure 3.11 (e) and Figure 3.12 (f)). The areas in the density plots were colored according to the number of points located in the area. The area without points was colored dark blue (the relative point density was set at 0). The area with the most densely distributed points was shown in bright yellow (the relative point density was set at 1). In the density plot of particle 1 and particle 2, the bright yellow region lies between the lines representing the O/Al ratio of  $\text{Al}_2\text{O}_3$  and  $\text{Al}(\text{OH})_3$ . This observation indicates that the Al-O phase in particle 1 and particle 2 could be a mixture of  $\text{Al}(\text{OH})_3$  and  $\text{Al}_2\text{O}_3$ . This inference is consistent with the results of the XRD analysis that both corundum and gibbsite are present in the bottom ash particles of 0.5 - 1.6 mm.

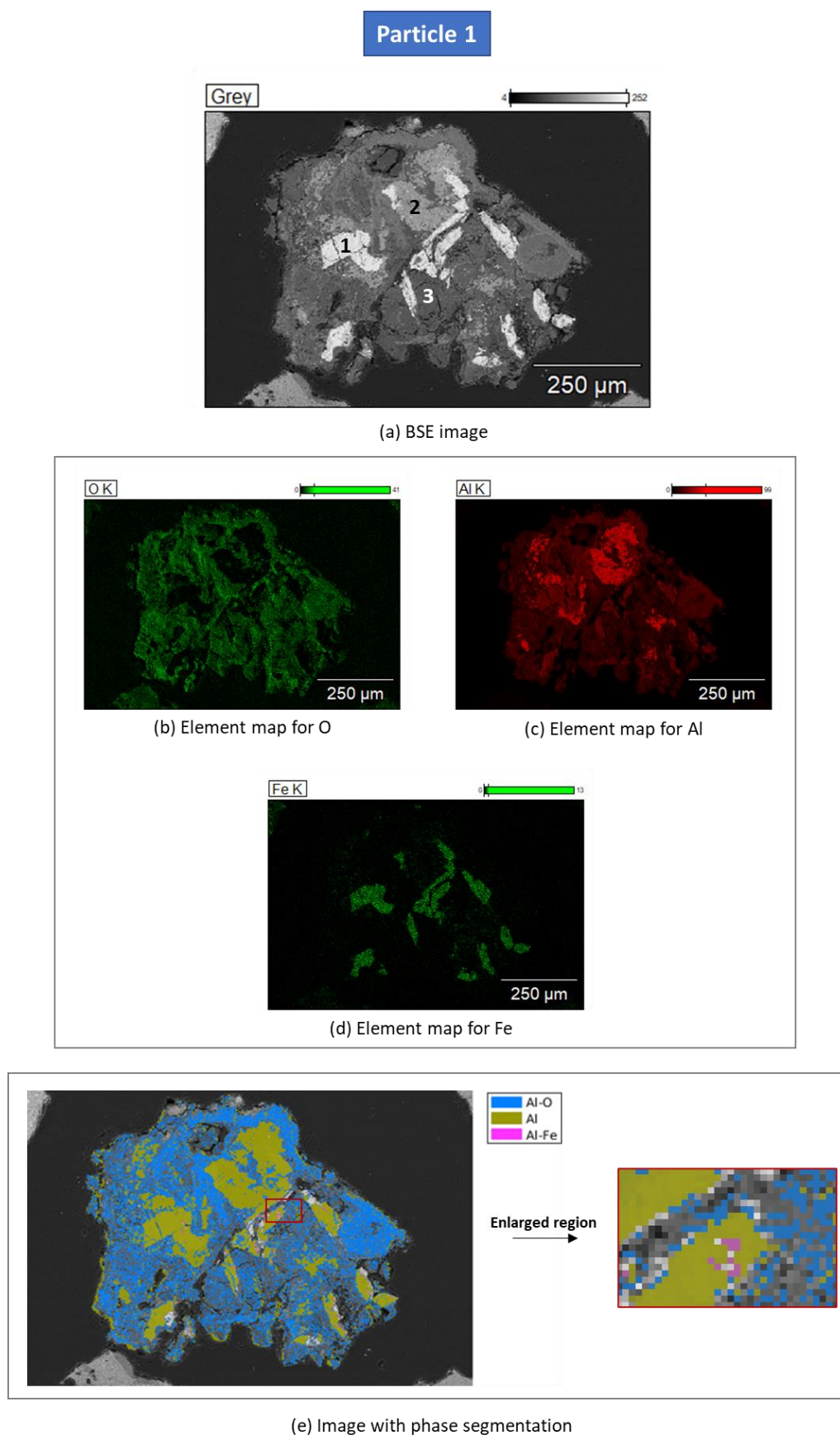


Figure 3.11. Typical morphology of MSWI bottom ash particle containing metallic Al (particle 1): (a) BSE image. (b)-(d) EDS element maps. (e) Image obtained after phase segmentation.

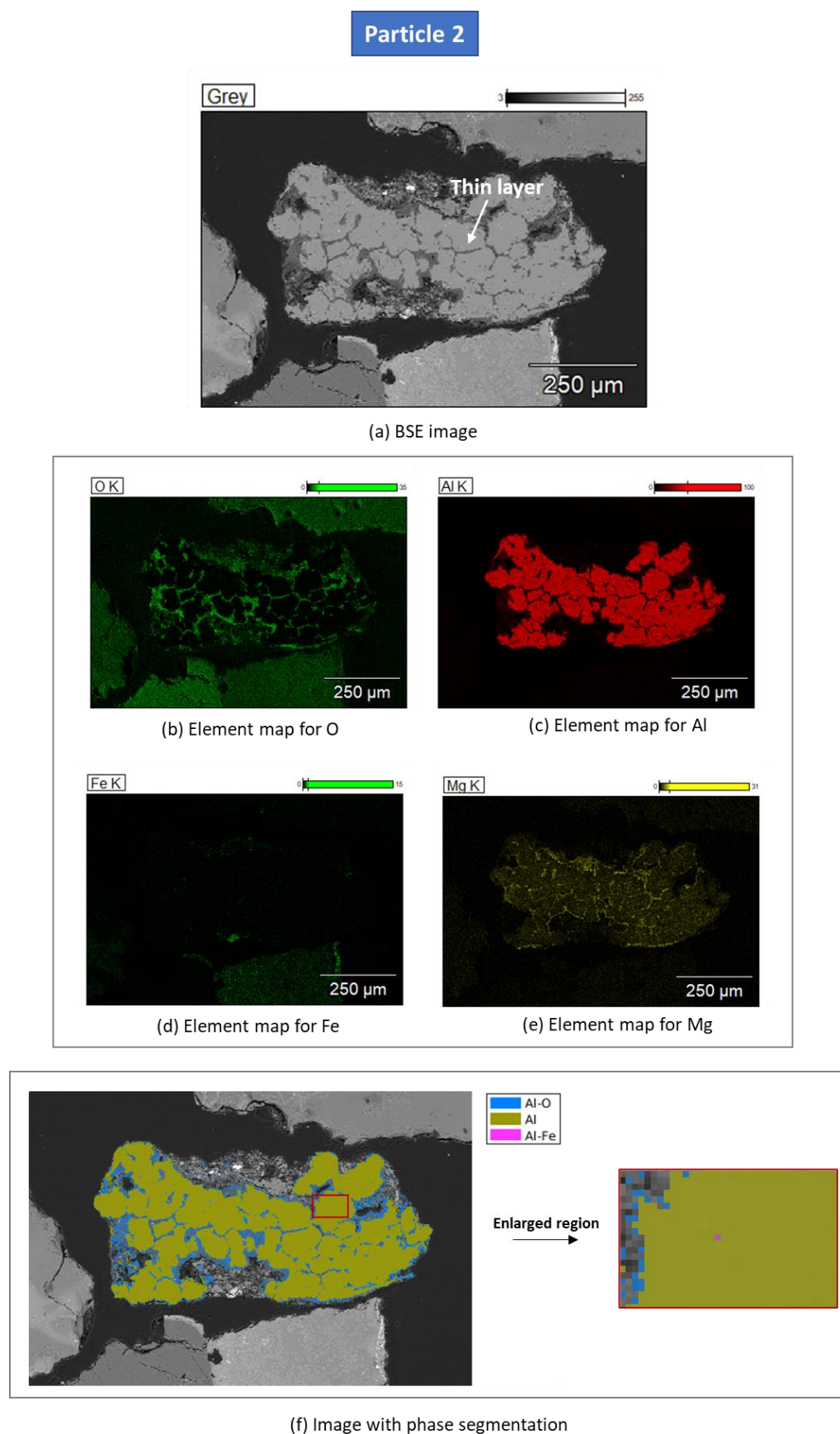


Figure 3.12 Typical morphology of MSWI bottom ash particle containing metallic Al (particle 2): (a) BSE image. (b)-(e) EDS element maps. (f) Image obtained after phase segmentation.

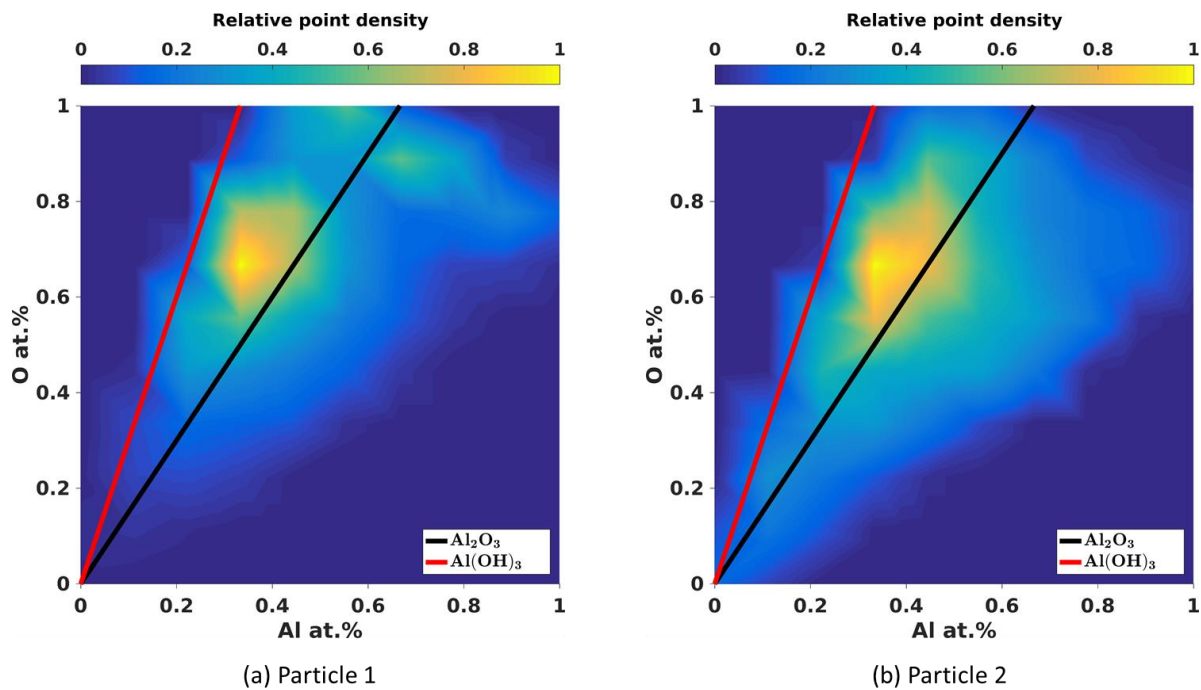


Figure 3.13 Density plot of the pixels representing Al-O phase in (a) particle 1 in Figure 3.11 and (b) particle 2 in Figure 3.12.

#### *Al alloy within metallic Al (Al)*

The phase segmentation results of particle 1 and particle 2 indicate that Al-Fe alloy (colored with purple) is scattered in the areas of metallic Al (Figure 3.11 (e) and Figure 3.12 (f)). According to the quantitative analysis, the Al-Fe alloy found in MSWI bottom ash particles also contains Si (Table 3.2). The detection of Al-Fe-Si alloy in MSWI bottom ash particles was also reported by Saffarzadeh et al. [63]. The formation of Al alloy can be induced by the melting of metallic Al during waste incineration. The melting point of pure metallic Al is around 660 °C [190], lower than the temperature in the waste incinerator (between 700 – 1100 °C) [6]. The metallic Al scraps of small size or the surface of large metallic Al scraps will melt during the waste incineration process. The formation of the liquidus metallic Al could lead to the adherence of the minerals on the surface of metallic Al scraps, as observed in particle 2 (Figure 3.12 (f)). The presence of Fe and Si could reduce the temperature when metallic Al becomes liquid, resulting in the formation of Al-Fe-Si alloy [63].

### 3.4 Mechanical treatments of as-received MSWI bottom ash

The characterization results of as-received MSWI bottom ash indicate that the large particle size and the incorporation of metallic Al are the main factors that inhibit its application as SCM and AAM precursor. These issues can be resolved by mechanical treatments, including ball milling and sieving (see Figure 3.14).

Considering the distribution of metallic Al in as-received MSWI bottom ash, the mechanical treatments are more suitable than chemical treatments and thermal treatments for the reduction of metallic Al content. As presented in section 3.3.3, around 90 wt.% of the metallic Al detected in as-received MSWI bottom ash are embedded in particles larger than 0.25 mm. The metallic Al in these particles is surrounded by oxidized Al (a mixture of  $\text{Al}_2\text{O}_3$  and  $\text{Al}(\text{OH})_3$ ), which usually functions as a protective layer and prevents the oxidation of metallic Al. The oxidation rate of metallic Al can be slow during chemical treatments and thermal treatments. It is worth noting that the efficiency of chemical treatments and thermal treatments on the oxidation of metallic Al can be improved after the mechanical treatments of as-received MSWI bottom ash [30,55]. This is because the grinding of as-received MSWI bottom ash can break the oxidized Al layers on the surface of metallic Al.

In this work, as-received MSWI bottom ash was loaded in the planetary ball mill (Retsch® PM 100). According to the performance of the ball mill, the grinding speed was set between 200 and 350 rpm. The milling duration was controlled between 20 and 30 min. Grinding as-received MSWI bottom ash into powder reduced its particle size, as well as the heterogeneity in its composition. The metallic Al was removed by passing ground MSWI bottom ash (GBA) through the sieve of 0.063 mm. The MSWI bottom ash powder obtained after sieving is named *mechanically treated MSWI bottom ash* (MBA), as shown in Figure 3.14.

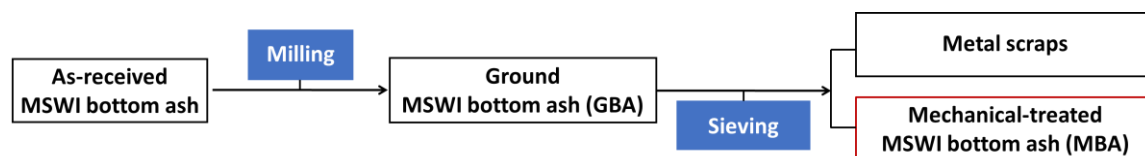


Figure 3.14 The process of mechanical treatments and material separation.

### 3.4.1 Effects of mechanical treatments on the composition of MSWI bottom ash

As illustrated in Figure 3.15, the XRD patterns of ground MSWI bottom ash and *mechanically treated MSWI bottom ash* are almost the same, indicating that these two have nearly the same mineralogical composition. The main difference between GBA and MBA lies in the peaks of metallic Al. The metallic Al peak at  $2\theta$  of  $38.5^\circ$  in the spectrum of GBA is not observed in the XRD spectrum of MBA. This change is mainly caused by the decrease in the metallic Al content.

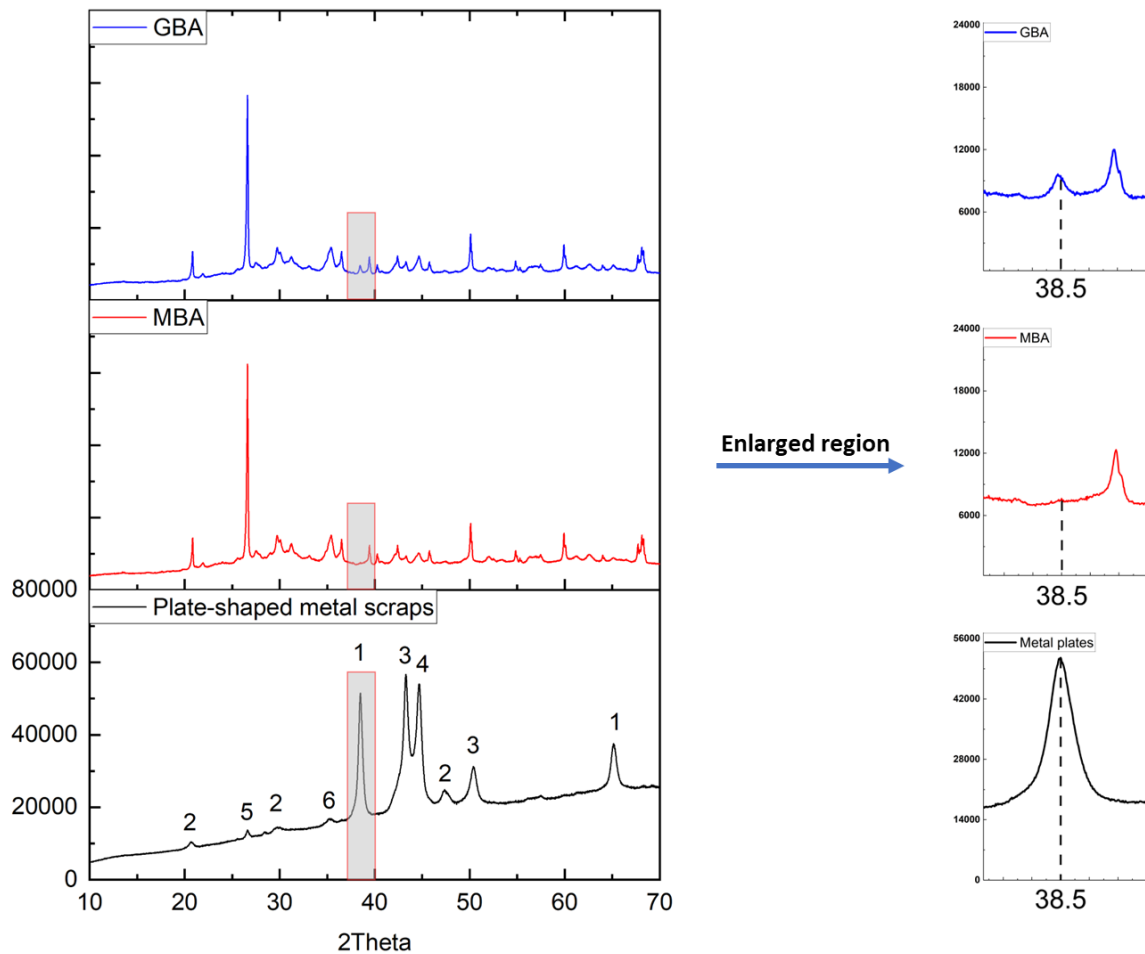


Figure 3.15 XRD spectra of GBA, MBA, and plate-shaped metal scraps. The labels in the spectrum of plate-shaped metal scraps: 1. Aluminum, 2. Khatyrkite, 3. Copper, 4. Iron, 5. Quartz, 6. Magnetite.



### 3.4.2 Effectiveness of mechanical treatments on metallic Al removal

Figure 3.16 (a) depicts the mechanical treatments of as-received MSWI bottom ash at optimal milling speed and duration. In the milling process, the brittle minerals were broken into small fragments while ductile metals were pressed into plate-shaped scraps. The images of separated metal scraps and MBA are shown in Figure 3.16 (a). The plate-shaped metal scraps separated from GBA has a diameter of up to 1 mm, much larger than the particle size of MBA. The size difference between MBA and metal scraps enables their separation by sieving.

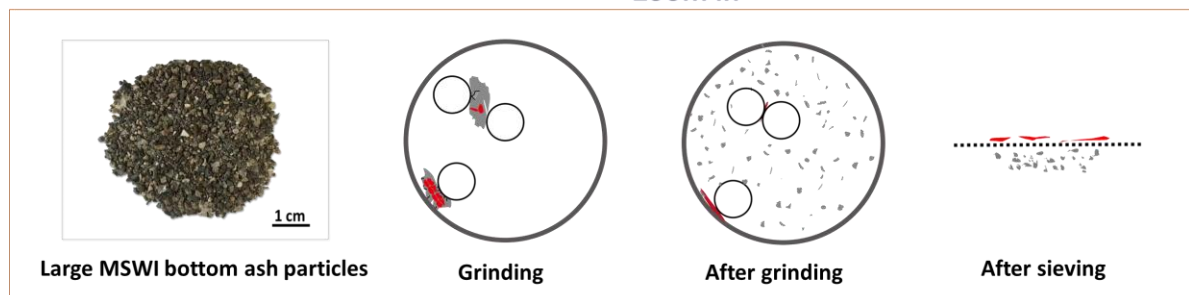
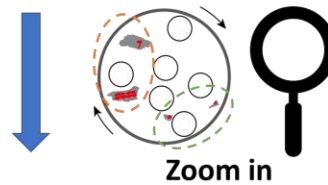
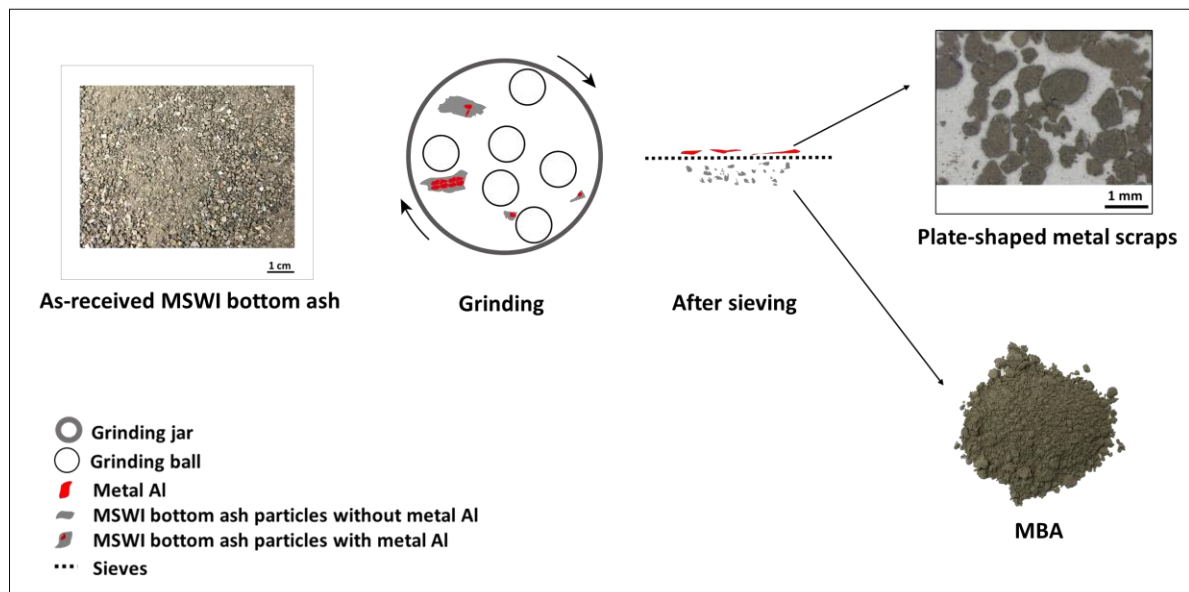
The metallic Al content in sieved metal scraps is only around 27.8 wt.%. Apart from metallic Al, other metals were also separated from as-received MSWI bottom ash during mechanical treatments. As shown in Figure 3.15, separated metal scraps consist of aluminum (Al, ICSD 251015), khatyrkite ( $\text{Al}_2\text{Cu}$ , ICSD 42517), copper (Cu, ICSD 261638), and iron (Fe, ICSD 1503158). In the XRD spectrum of the metal scraps, peaks of quartz ( $\text{SiO}_2$ , ICSD 541929) and magnetite ( $\text{Fe}_2\text{O}_3$ , ICSD 92356), albeit with low intensity, are also observed.

After mechanical treatments, the metallic Al content decreased from 0.56 wt.% in as-received MSWI bottom ash to 0.13 wt.% in MBA. The metallic Al content in MBA is close to that in the ground MSWI bottom ash used by Tang et al. [53], Caprai [96], and Alderete et al. [149] for the application as SCM, and Chen et al. [54] for the application as AAM precursor. Most metallic Al removed by the mechanical treatments is from the 0.5 - 1.6 mm size fraction. The metallic Al detected in the 0.5 - 1.6 mm size fraction accounts for 72.9 % of the total weight of the metallic Al in as-received MSWI bottom ash. This value is close to the percentage of the metallic Al content removed by the mechanical treatments (around 77 %).

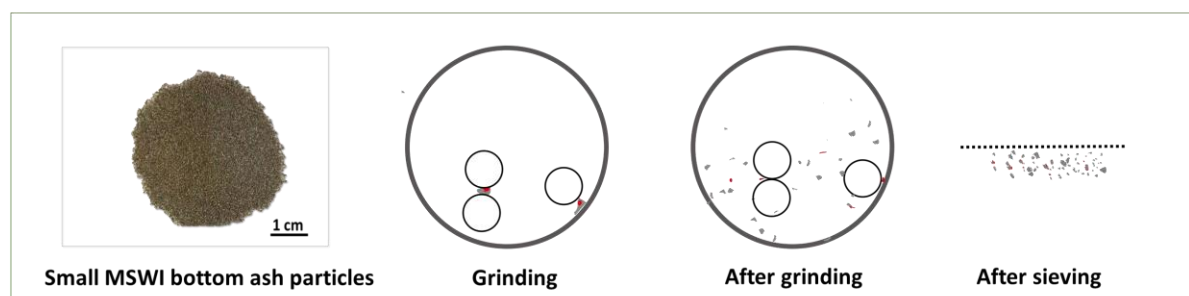
The effects of mechanical treatments on large and small particles of as-received MSWI bottom ash are different. During the milling process, the metallic Al embedded in the MSWI bottom ash particles of 0.5 - 1.6 mm is more likely to be pressed into plate-shaped scraps. This is because metallic Al can occupy up to 70 % of the area in the MSWI bottom ash particle (see section 3.3.3.2). As-received MSWI bottom ash mainly consists of mineral phases, while metals are only present in trace amounts (see Figure 3.9). As illustrated in Figure 3.16 (b), metals can be separated from ground MSWI bottom ash by sieving when the size of metal plate-shaped scraps is larger than the mineral particles.

Compared with metallic Al in the particles of 0.5 -1.6 mm, the size of metallic Al embedded in the MSWI bottom ash with particle size smaller than 0.5 mm is also smaller. After grinding, these metallic Al scraps easily fall in the same size range as the minerals derived from the pulverization of MSWI bottom ash in 0.5 - 1.6 mm size fraction. As shown in Figure 3.16 (c), the separation of the metallic Al from ground MSWI bottom ash is difficult when it has a particle size similar to that of the mineral particles. From this perspective, most of the residual metallic Al detected in MBA is originally embedded in the MSWI bottom ash particles smaller than 0.5 mm.

(a) Mechanical treatments of as-received MSWI bottom ash



(b) Effects of mechanical treatments on large particles in as-received MSWI bottom ash



(c) Effects of mechanical treatments on small particles in as-received MSWI bottom ash

Figure 3.16 Illustration of the mechanical removal process of metallic Al: (a) Mechanical treatments of as-received MSWI bottom ash particles (mix of all size fractions). (b) Effects of grinding and sieving on large MSWI bottom ash particles (c) Effects of grinding and sieving on small MSWI bottom ash particles.



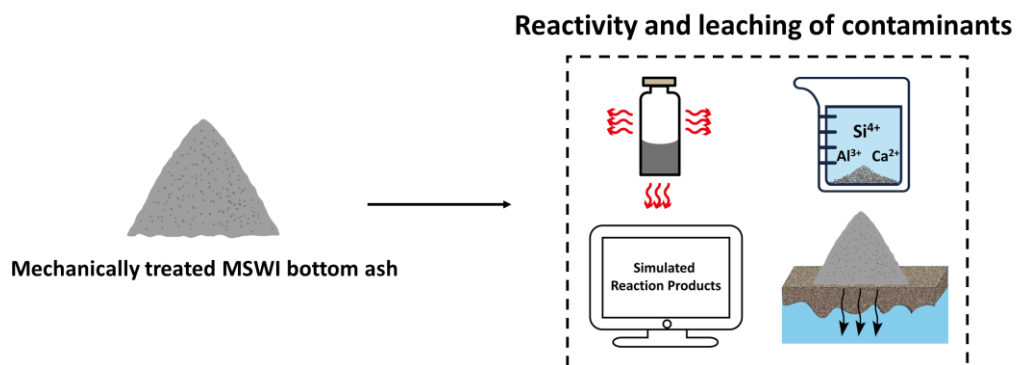
### 3.5 Conclusions

In this chapter, as-received municipal solid waste incineration (MSWI) bottom ash was characterized in terms of particle size distribution, chemical and mineralogical compositions, and distribution of metallic Al. The characterization results were used in the selection of quality-upgrade treatments of as-received MSWI bottom ash. Based on the experimental results and analysis, the following conclusions can be drawn:

- The composition analysis of as-received MSWI bottom ash indicates that the chemical and mineralogical composition varies slightly among different size fractions. Around 73 wt.% of the metallic Al detected in as-received MSWI bottom ash concentrates in the 0.5 - 1.6 mm size fraction.
- The MSWI bottom ash particles containing metallic Al have two typical morphologies. The main differences between these two types of particles are the thickness of the oxidized Al layers on the surface of metallic Al and the area percentage of metallic Al in the particle. The oxidized Al layers consist of  $\text{Al}_2\text{O}_3$  and  $\text{Al}(\text{OH})_3$ .
- The mechanical treatments effectively improved the quality of as-received MSWI bottom ash. After mechanical treatments, metallic Al content was reduced by 77 %, and the particle size was reduced to below 63  $\mu\text{m}$ . The *mechanically treated MSWI bottom ash (MBA)* with metallic Al content of 0.13 wt.% can be used as supplementary cementitious material (SCM) and precursor for alkali-activated materials.
- In addition to the settings of ball mill, the effectiveness of mechanical treatments on metallic Al content reduction is strongly influenced by the distribution of metallic Al in as-received MSWI bottom ash particles. The key to removing metallic Al by sieving lies in creating a size difference between metal scraps and mineral components of as-received MSWI bottom ash during the milling process.
- Most metallic Al removed by mechanical treatments is from 0.5 - 1.6 mm MSWI bottom ash particles. The metallic Al embedded in smaller MSWI bottom ash particles is difficult to be removed by mechanical treatments.

# Chapter 4

## Reactivity and leaching potential<sup>(6)</sup> of mechanically treated MSWI bottom ash



### Highlights

- The reactivity of *mechanically treated MSWI bottom ash (MBA)* as supplementary cementitious material (SCM) and precursor for alkali-activated materials (AAM) is determined by the content and chemical composition of its amorphous phase.
- The method of thermodynamic modeling is very useful for predicting the solid phase assemblages and pore solution in alkali-activated MBA paste. The modeling results can be used as references for the mix design of MBA-based AAM.
- Although the leaching of Sb and sulfate from MBA exceeds the allowable upper limits prescribed in the standard, this may not be an issue when using MBA as SCM and AAM precursor.
- This chapter provides recommendations for the reactivity assessments of MBA, the quality upgrade treatments of MBA, and the mix design of using MBA as SCM and AAM precursor.

<sup>(6)</sup> Leaching potential refers to the likelihood of contaminants leaching from solids into the environment.

## 4.1 Introduction

As a follow-up to the mechanical treatments presented in Chapter 3, this chapter deals with the reactivity of *mechanically treated MSWI bottom ash (MBA)* for its application as supplementary cementitious material (SCM) and precursor in alkali-activated materials (AAM). This chapter provides recommendations about the assessment of the reactivity of MBA as SCM and AAM precursor. The reactivity of MBA is compared with that of blast furnace slag and Class F coal fly ash. As introduced in Chapter 2, the leaching resistance of MSWI bottom ash influences its addition to blended cement and AAM. Therefore, the leaching of heavy metals from MBA is also assessed. The findings of this chapter provide a theoretical basis for the quality upgrade treatments performed on MBA and the mix design of using MBA to prepare the blended cement pastes (in Chapter 5) and alkali-activated materials (in Chapter 6).

As discussed in Chapter 2, the reactivity and leaching potential of MSWI bottom ash are determined by its chemical and mineralogical compositions. The presence of soluble salts and heavy metals in MSWI bottom ash is one of the main factors that inhibit its application as an ingredient for construction materials. The amorphous phase is usually regarded as the major reactive phase in blast furnace slag and Class F coal fly ash [191,192]. In MSWI bottom ash, the amorphous phase, which mainly consists of waste glass particles, is also the primary reactive phase [28,168]. Although the content of the amorphous phase was quantified in previous work, the chemical composition of the amorphous phase was not determined. Up till now, the contribution of the amorphous phase to the reactivity of MSWI bottom ash has not been very well understood.

The application of MSWI bottom ash as SCM and AAM precursor strongly depends on its reactivity. At present, different standardized methods have been used to measure the pozzolanic reactivity of MSWI bottom ash [48–51,130]. However, there is no standardized method for measuring the reactivity of MSWI bottom ash as AAM precursor. The alkali activation in AAM is generally considered as a series of reactions involving dissolutions of precursors and precipitation of products [193,194]. The dissolution of precursors in alkaline solution is the first step in the chemical reaction to form AAM [193,194]. Previous researchers assessed the reactivity of MSWI bottom ash as AAM precursor by measuring the amount of  $\text{SiO}_2$  and  $\text{Al}_2\text{O}_3$  that can dissolve from MSWI bottom ash in alkaline solutions [47,158]. However, this method neglects the contribution of other elements to the reaction product formation and thus provides limited information about the reactivity of MSWI bottom ash.

Thermodynamic modeling combined with accurate and complete thermodynamic databases can predict the phase formation in alkali-activated materials [195]. This method has been used to simulate the phase diagrams for alkali-activated blast furnace slag, when  $\text{NaOH}$ ,  $\text{Na}_2\text{SiO}_3$ ,  $\text{Na}_2\text{Si}_2\text{O}_5$ ,  $\text{Na}_2\text{CO}_3$ , or  $\text{Na}_2\text{SO}_4$  is used as activator [196]. The phase assemblages and pore solution predicted by thermodynamic modeling can be used to guide the mix design of alkali-activated materials [197]. It is meaningful to explore the possibility of using thermodynamic modeling to simulate the phase assemblages and pore solution in alkali-activated MSWI bottom ash. The simulation results may provide insight into the reactivity of MSWI bottom

ash as AAM precursor and can be used as references for the mix design of alkali-activated MSWI bottom ash.

As mentioned in Chapter 3, the heavy metal leaching of as-received MSWI bottom ash complies with the open (granular) application criteria of the Dutch Soil Quality Decree [84,182]. However, the mechanical treatments reduced the particle size of as-received MSWI bottom ash. The size reduction of MSWI bottom ash can facilitates the leaching of heavy metals. Giro-Paloma et al. [79] ground MSWI bottom ash aggregates (0 - 2 mm) into fine powder for the application of AAM precursor. The concentrations of As, Cr, Mo, and Sb in the leachate of MSWI bottom ash powder almost doubled that in the leachate of MSWI bottom ash aggregates. The leaching of contaminants from MSWI bottom ash determines its acceptable dosage in blended cement and AAM (see Chapter 2). Therefore, measuring the leaching potential of MBA is required prior to its application as SCM and AAM precursor.

This chapter consists of five parts (Figure 4.1):

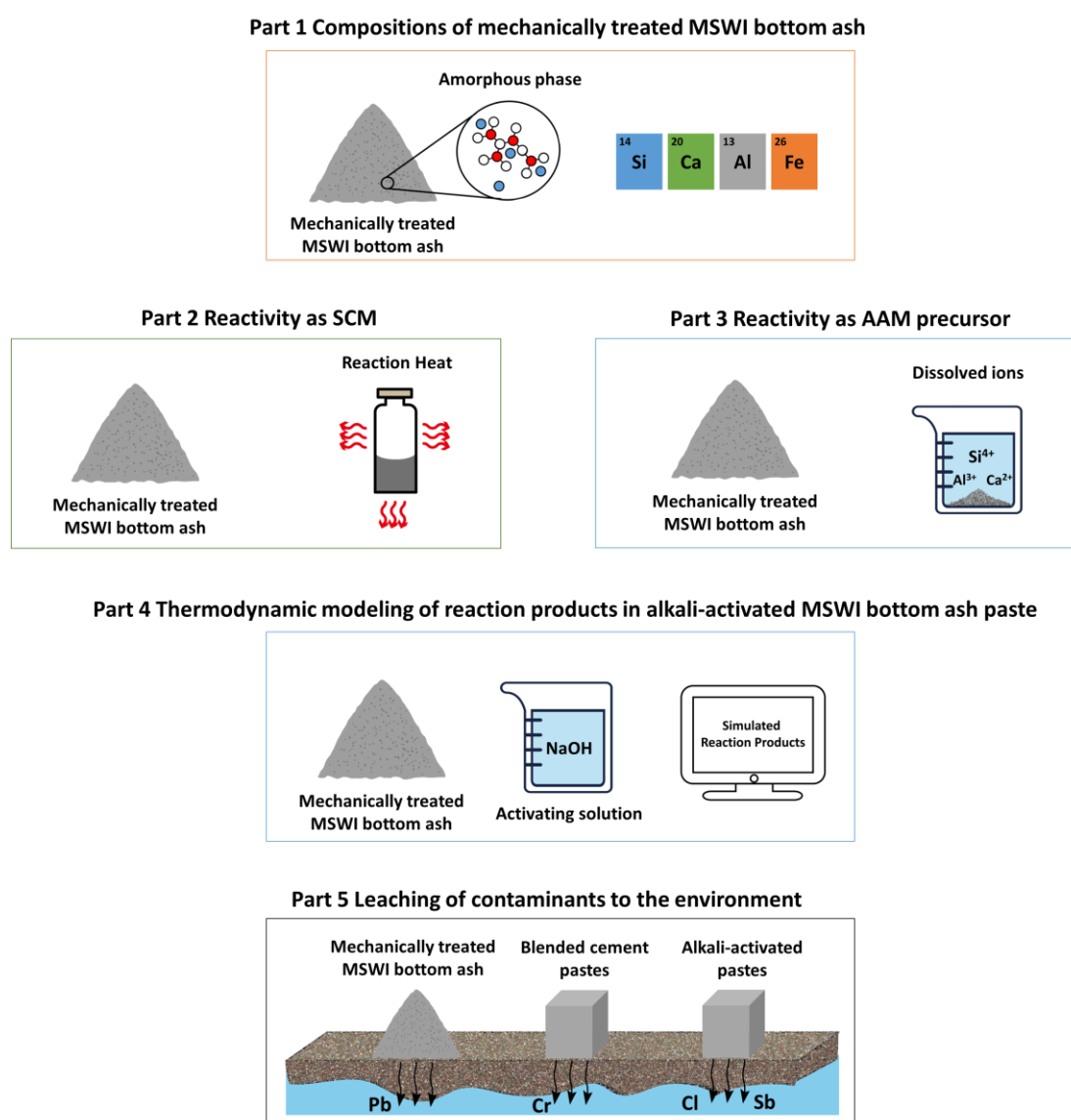


Figure 4.1 The content of this chapter.

- In part 1, the chemical composition of the amorphous phase in MBA is determined and compared with that of BFS and Class F coal fly ash.
- In part 2, the reactivity of MBA as SCM is studied by conducting calorimetry tests and following the rapid, relevant, and reliable ( $R^3$ ) methods. The pozzolanic reactivity of MBA is compared with that of blast furnace slag and Class F coal fly ash.
- In part 3, a dissolution test is proposed to measure the reactivity of MBA as AAM precursor. The reactivity of MBA is compared with that of blast furnace slag and Class F coal fly ash.
- In part 4, the solid phase assemblages and pore solution compositions of alkali-activated MBA paste are predicted with thermodynamic modeling. The modeling results are compared with experimental data reported in the literature to assess the reliability of the simulation. The modeling results provide references for the mix design of MBA-based AAM.
- In part 5, the leaching of contaminants from MBA is assessed, and the risks of environment contamination caused by the addition of MBA in blended cement pastes and alkali-activated pastes<sup>(1)</sup> are also discussed. Based on the information presented in these five parts, remarks about how to use MBA as SCM and AAM precursor are made.

## 4.2 Materials and methods

### 4.2.1 Materials

The MBA obtained after the mechanical treatments described in Chapter 3 was studied in this chapter. MBA has a particle size below  $63\ \mu\text{m}$  and contains around 0.13 wt.% residual metallic Al. The Class F coal fly ash (FA) and blast furnace slag (BFS) were used as reference materials. BFS met the specifications of NEN-EN 15167-1 [198] and was provided by Eco<sub>2</sub>cem Benelux B.V.. FA complied with the requirements of Class F coal fly ash and was supplied by Vliegasonie B.V.. The densities of MBA, FA, and BFS, as measured by pycnometer, are  $3.2\ \text{g/cm}^3$ ,  $2.7\ \text{g/cm}^3$ , and  $3.5\ \text{g/cm}^3$ , respectively.

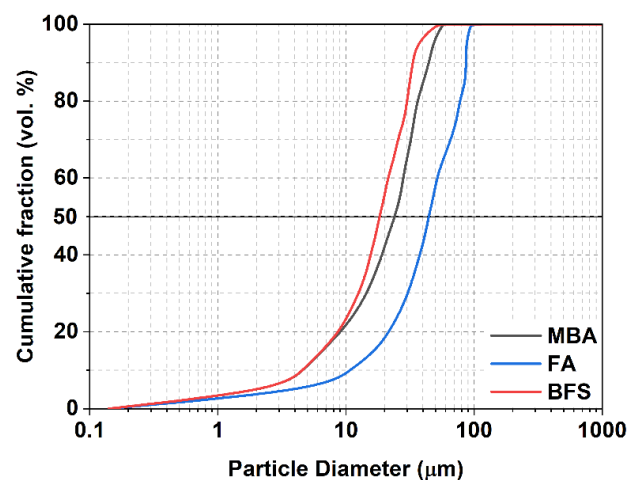


Figure 4.2 Particle size distribution of MBA, BFS, and FA determined by laser diffraction method.

<sup>(1)</sup> Alkali-activated paste, alkali-activated mortar, and alkali-activated concrete all belong to alkali-activated materials.

The particle size distribution of these materials was measured using the laser diffraction method (Malvern Mastersizer). As illustrated in Figure 4.2, FA with  $D_{50}$  of 44.2  $\mu\text{m}$  is coarser than MBA and BFS. The  $D_{50}$  of MBA is 24  $\mu\text{m}$ , larger than that of BFS (18.3  $\mu\text{m}$ ). The free lime content in MBA is zero, as measured by following the NEN-EN1744-1 [199].

## 4.2.2 Characterization techniques

### 4.2.2.1 Chemical and mineralogical compositions

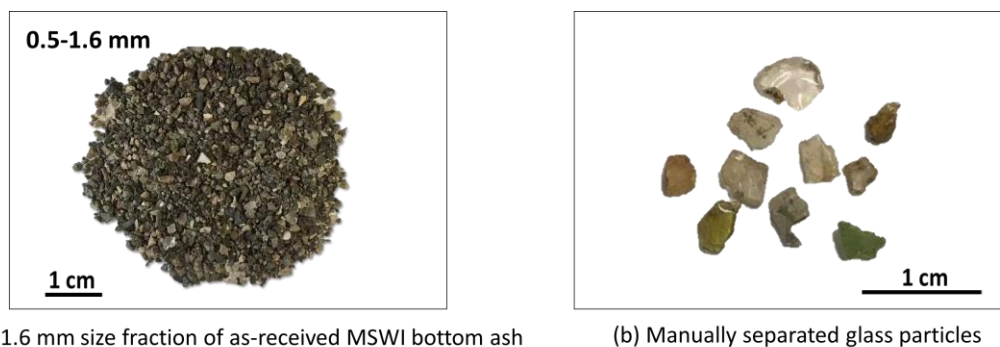
The chemical composition, mineralogical composition, and loss on ignition of MBA, FA, and BFS were determined in the same way as the methods used in Chapter 3.

### 4.2.2.2 Analysis of amorphous phase

The content of the amorphous phase in MBA was determined by quantitative XRD analysis (QXRD) analysis, the same method as that used in Chapter 3. The percentages of  $\text{SiO}_2$ ,  $\text{Al}_2\text{O}_3$ ,  $\text{CaO}$ ,  $\text{Fe}_2\text{O}_3$ ,  $\text{Na}_2\text{O}$ ,  $\text{K}_2\text{O}$ , and  $\text{MgO}$  present in the amorphous phase of MBA were obtained by subtracting the percentages of these oxides in crystalline phases from the bulk composition of MBA [184]. The proportions of  $\text{SiO}_2$ ,  $\text{Al}_2\text{O}_3$ ,  $\text{CaO}$ ,  $\text{Fe}_2\text{O}_3$ ,  $\text{Na}_2\text{O}$ ,  $\text{K}_2\text{O}$ , and  $\text{MgO}$  in the crystalline phases were calculated from the Rietveld refinement results with the software Profex-BGMN [184]. The bulk compositions refer to the chemical compositions determined by the XRF measurement. The methods used in the analysis of the amorphous phase MBA were also used to study the amorphous phase of FA and BFS.

The existence of the amorphous phase was further proved by performing chemical dissolution treatments on MBA. This method was also used by Ma [159] and Zhang et al. [200] to determine the contents of the amorphous phase and the reactive silica in Class F coal fly ash. According to NEN-EN 196-2 [201], the fraction of the  $\text{SiO}_2$  dissolved during the chemical dissolution treatments is defined as reactive silica content. The treatments were performed following the description in NEN-EN 196-2 [201]. MBA was successively treated with a hydrochloric acid solution and boiling potassium hydroxide solution. The insoluble residue of MBA was ignited at 950  $^{\circ}\text{C}$ . After all these steps, the amorphous phase, such as the glass and the organics, was removed from MBA. The insoluble residue was analyzed with XRD and XRF. The test results were compared with that of MBA to evaluate the composition changes.

Since waste glass is one of the primary sources of the amorphous phase in MBA, the chemical composition of the glass particles in MBA was compared with that of the amorphous phase of MBA. The glass particles in MBA were analyzed by measuring the chemical and mineralogical compositions of the waste glass particles initially present in as-received MSWI bottom ash. The glass particles were manually separated from the 0.5-1.6 mm size fraction of as-received MSWI bottom ash according to their transparent appearance. The images of the MSWI bottom ash particles within the 0.5-1.6 mm size fraction and the separated glass particles are illustrated in Figure 4.3. After grinding separated glass particles into fine powders, the compositions of glass particles were determined by XRF and XRD analysis, in the same way as that for MBA.



(a) 0.5- 1.6 mm size fraction of as-received MSWI bottom ash

(b) Manually separated glass particles

Figure 4.3 (a) Image of 0.5-1.6 mm size fraction of as-received MSWI bottom ash. (b) Image of glass particles separated from 0.5-1.6 mm size fraction.

It is worth mentioning that there are two reasons for choosing 0.5 -1.6 mm size fraction for glass composition analysis. First, the mineralogical composition of MBA is also the same as that of as-received MSWI bottom ash (see Chapter 3). The chemical and mineralogical composition varies slightly among different size fractions of as-received MSWI bottom ash (see Chapter 3). Second, the 0.5-1.6 mm size fraction accounts for around 50 wt.% of as-received MSWI bottom ash (see Chapter 3). Separating glass particles from 0.5-1.6 mm size fraction is much easier than the fraction with smaller particles.

#### 4.2.2.3 Reactivity test for the application as SCMs

The pozzolanic reactivity of MBA, which determines its application as SCM, was measured using isothermal calorimetry test. The experiment design followed the  $R^3$  method [139,140], where the reaction of SCM in blended cement pastes is mimicked. The test was conducted by following the procedures and protocols described in ASTM C1897-20 [139]. The test pastes (also called  $R^3$  pastes) were prepared by mixing 11.11 g SCM with 33.33 g  $\text{Ca}(\text{OH})_2$ , 5.56 g  $\text{CaCO}_3$ , 0.24 g KOH, 1.2 g  $\text{K}_2\text{SO}_4$ , and 60 g deionized water [140]. The supplementary cementitious materials (SCMs) measured in this work are MBA, BFS, and FA. The heat released during the hydration of the pastes at 40 °C until 7 days was recorded by isothermal conduction calorimeter (TAM-Air-314). The cumulative heat released by the pozzolanic reaction of 1 g of SCM was calculated after recording the heat release for 7 days. It is worth noting that the compressive strength was not used as an indicator for the pozzolanic reactivity of MBA. Since MBA contains metallic Al, the method of strength measurement will underestimate the pozzolanic reactivity of MBA. The metallic Al in MBA will react with  $\text{Ca}(\text{OH})_2$  and release hydrogen gas, causing a strength decrease [53].

#### 4.2.2.4 Reactivity test for the application as AAM precursors

The solubility of precursor in alkaline solution determines the amount of Si, Al, Ca, Fe and Mg that can participate in the formation of reaction products. The reactivity of MBA as AAM precursor was assessed by dissolution test, where the reaction of MBA in the alkaline environment of AAM was reproduced. The same test was performed on BFS and FA to compare with the test results of MBA.

The reactivity test was designed by adapting the dissolution test proposed for measuring the reactivity of synthesized blast furnace slag and coal fly ash in alkaline environment [202]. The



solid-to-liquid ratio was set as 1 g to 1 liter. At this ratio, the solution was in the undersaturated condition, preventing the precipitation of the reaction products to the largest possible extent [202,203]. To accelerate the dissolution of tested precursors, the pH of the NaOH solution used in the tests was slightly higher than that of the pore solution of alkali-activated slag (13.77 - 14.67) and alkali-activated fly ash (13.08 - 14.07) reported by Zuo et al. [204]. The sodium hydroxide solution with different molarity (4M, 5M, and 6 M) was selected to mimic the alkaline environment in the pore solution of AAM. The pH of 4 M, 5M, and 6M NaOH solutions is 14.6, 14.7, and 14.8, respectively.

In the experiment, 1 g of precursor (MBA, FA, or BFS) was dissolved in 1 L NaOH solution stored in a polypropylene container, and the solution was stirred continuously for 24 h. The whole setup was kept in a temperature-controlled room at 25 °C. After the dissolution test, the concentrations of dissolved Si, Al, Ca, Fe and Mg in the solution were determined. The filtered solutions were diluted with nitric acid (0.2 vol.%). The diluted solutions were analyzed through inductively coupled plasma-optical emission spectroscopy (ICP-OES), model PerkinElmer Optima 5300DV.

### 4.2.3 Thermodynamic modeling

Thermodynamic modeling was used to predict the solid phase assemblages and pore solution compositions of alkali-activated MBA paste, alkali-activated BFS paste, and alkali-activated FA paste. This information can be used to guide the application of MBA as AAM precursor. In the modeling, MBA was activated by NaOH solution. The reason for this mix design is to prevent the ions in the activator (especially  $\text{Si}^{4+}$ ) from affecting the reaction of the ions released by MBA. The NaOH solution was reacted with 100 g MBA, 100 g BFS, or 100 g FA. The water-to-precursor ratio in these three AAM systems was kept at 0.35. The alkalinity of NaOH was represented as the percentage of  $\text{Na}_2\text{O}$  relative to the mass of the precursor.

The changes in phase assemblages were simulated by changing the  $\text{Na}_2\text{O}$  content in the activator from 2 wt.% to 10 wt.%. It was assumed that only the  $\text{SiO}_2$ ,  $\text{CaO}$ ,  $\text{Al}_2\text{O}_3$ ,  $\text{Fe}_2\text{O}_3$ ,  $\text{Na}_2\text{O}$ ,  $\text{K}_2\text{O}$ , and  $\text{MgO}$  in the amorphous phase of MBA, FA, and BFS were reacted in alkali activation, and their reaction degree was 100 %. The remaining components in the amorphous phase, together with the crystalline phases, were considered as the un-reactive fraction. The AAM system was under (metastable) thermodynamic equilibrium conditions.

The thermodynamic calculations were performed using the Gibbs energy minimization software GEMS-Selektor v.3 (<https://gems.web.psi.ch/>) [205,206] and the Cemdata 18 database [195]. The ideal solid solution model (CNASH\_ss) derived by Myers et al. [207] for calcium (sodium) aluminosilicate hydrate (C-(N-)A-S-H) gel was used to simulate the gel phases in alkali-activated blast furnace slag. The hydrotalcite-like phases formed in alkali-activated blast furnace slag were simulated with the solid solution model, MA-OH-LDH\_ss [208]. The ideal solid solution model (N(C)ASH\_ss) proposed by Zuo [209] for sodium (calcium) aluminosilicate hydrate (N-(C-)A-S-H) gel was used for the simulation of gel phases formed in alkali-activated fly ash. The details of the end-members used in these three ideal solid solution models are listed in Table 4.1, Table 4.2, and Table 4.3.



Table 4.1 End-members in the CNASH<sub>ss</sub> model used to describe the C-(N)-A-S-H gel [207].

End-member groups	End-member names	Formulae	Molar ratios		
			Ca/Si	Al/Si	Na/Si
C-A-S-H	5CA	$(\text{CaO})_{1.25} \cdot (\text{Al}_2\text{O}_3)_{0.125} \cdot (\text{SiO}_2) \cdot (\text{H}_2\text{O})_{1.625}$	1.25	0.25	0
	INFCA	$(\text{CaO}) \cdot (\text{Al}_2\text{O}_3)_{0.15625} \cdot (\text{SiO}_2)_{1.1875} \cdot (\text{H}_2\text{O})_{1.65625}$	0.84	0.26	0
C-N-A-S-H	5CNA	$(\text{CaO})_{1.25} \cdot (\text{Na}_2\text{O})_{0.25} \cdot (\text{Al}_2\text{O}_3)_{0.125} \cdot (\text{SiO}_2) \cdot (\text{H}_2\text{O})_{1.25}$	1.25	0.25	0.50
	INFCNA	$(\text{CaO}) \cdot (\text{Na}_2\text{O})_{0.34375} \cdot (\text{Al}_2\text{O}_3)_{0.15625} \cdot (\text{SiO}_2)_{1.1875} \cdot (\text{H}_2\text{O})_{1.3}$	0.84	0.26	0.58
C-N-S-H	INFCN	$(\text{CaO}) \cdot (\text{Na}_2\text{O})_{0.3125} \cdot (\text{SiO}_2)_{1.5} \cdot (\text{H}_2\text{O})_{1.1875}$	0.67	0	0.42
	T2C	$(\text{CaO})_{1.5} \cdot (\text{SiO}_2) \cdot (\text{H}_2\text{O})_{2.5}$	1.50	0	0
C-S-H	T5C	$(\text{CaO})_{1.25} \cdot (\text{SiO}_2)_{1.25} \cdot (\text{H}_2\text{O})_{2.5}$	1.00	0	0
	TobH	$(\text{CaO}) \cdot (\text{SiO}_2)_{1.5} \cdot (\text{H}_2\text{O})_{2.5}$	0.67	0	0

Table 4.2 End-members in the MA-OH-LDH<sub>ss</sub> model used to describe the hydrotalcite-like phases [208].

End-member names	Formulae
M <sub>4</sub> AH <sub>10</sub>	$(\text{MgO})_4 \cdot (\text{Al}_2\text{O}_3) (\text{H}_2\text{O})_{10}$
M <sub>6</sub> AH <sub>12</sub>	$(\text{MgO})_6 \cdot (\text{Al}_2\text{O}_3) (\text{H}_2\text{O})_{12}$
M <sub>8</sub> AH <sub>14</sub>	$(\text{MgO})_8 \cdot (\text{Al}_2\text{O}_3) (\text{H}_2\text{O})_{14}$

Table 4.3 End-members in the N(C)ASH<sub>ss</sub> model used to describe the N-(C)-A-S-H gel [209].

End-member groups	End-member names	Formulae	Molar ratios		
			Ca/Si	Al/Si	Na/Al
N-C-A-S-H	NCASH_1-0.1	$(\text{Na}_2\text{O})_{0.05} \cdot (\text{CaO})_{0.45} \cdot (\text{Al}_2\text{O}_3)_{0.5} \cdot (\text{SiO}_2)_1 \cdot (\text{H}_2\text{O})_1$	0.45	1.00	0.1
	NCASH_2-0.1	$(\text{Na}_2\text{O})_{0.05} \cdot (\text{CaO})_{0.45} \cdot (\text{Al}_2\text{O}_3)_{0.5} \cdot (\text{SiO}_2)_2 \cdot (\text{H}_2\text{O})_1$	0.23	0.50	0.1
	NCASH_3-0.1	$(\text{Na}_2\text{O})_{0.05} \cdot (\text{CaO})_{0.45} \cdot (\text{Al}_2\text{O}_3)_{0.5} \cdot (\text{SiO}_2)_3 \cdot (\text{H}_2\text{O})_1$	0.15	0.33	0.1
	NCASH_4-0.1	$(\text{Na}_2\text{O})_{0.05} \cdot (\text{CaO})_{0.45} \cdot (\text{Al}_2\text{O}_3)_{0.5} \cdot (\text{SiO}_2)_4 \cdot (\text{H}_2\text{O})_1$	0.11	0.25	0.1
N-A-S-H	NASH_1-1	$(\text{Na}_2\text{O})_{0.5} \cdot (\text{Al}_2\text{O}_3)_{0.5} \cdot (\text{SiO}_2)_1 \cdot (\text{H}_2\text{O})_1$	0	1.00	1
	NASH_2-1	$(\text{Na}_2\text{O})_{0.5} \cdot (\text{Al}_2\text{O}_3)_{0.5} \cdot (\text{SiO}_2)_2 \cdot (\text{H}_2\text{O})_1$	0	0.50	1
	NASH_3-1	$(\text{Na}_2\text{O})_{0.5} \cdot (\text{Al}_2\text{O}_3)_{0.5} \cdot (\text{SiO}_2)_3 \cdot (\text{H}_2\text{O})_1$	0	0.33	1
	NASH_4-1	$(\text{Na}_2\text{O})_{0.5} \cdot (\text{Al}_2\text{O}_3)_{0.5} \cdot (\text{SiO}_2)_4 \cdot (\text{H}_2\text{O})_1$	0	0.25	1

For the simulation of the gel phases formed in alkali-activated MBA paste, the selection of the ideal solid solution model was based on the types of reaction products detected in alkali-activated MSWI bottom ash by previous researchers. The reaction products of the alkali activation of MSWI bottom ash were mainly amorphous phases, including calcium silicate hydrate (C-S-H) gel [29,131,162], calcium aluminosilicate hydrate (C-A-S-H) gel [29], and sodium aluminosilicate hydrate (N-A-S-H) gel [163]. Therefore, apart from CNASH<sub>ss</sub> model [207] and N(C)ASH<sub>ss</sub> model [209], the CSHQ model [195,210] usually used for Portland

cement simulation was also selected in the setting of the database. Table 4.4 provides the details of the end-members included in the CSHQ model.

Table 4.4 End-members in the CSHQ model used to describe the C-S-H gel [195,210].

End-member names	Formulae	Molar ratios
		Ca/Si
TobH	$(\text{CaO})_{2/3} (\text{SiO}_2) (\text{H}_2\text{O})_{1.5}$	0.67
TobD	$(\text{CaO})_{5/6} (\text{SiO}_2)_{2/3} (\text{H}_2\text{O})_{1.83}$	1.25
JenH	$(\text{CaO})_{1.33} (\text{SiO}_2) (\text{H}_2\text{O})_{2.17}$	1.33
JenD	$(\text{CaO})_{1.5} (\text{SiO}_2)_{0.67} (\text{H}_2\text{O})_{2.5}$	2.24

#### 4.2.4 Assessment of leaching potential

One stage batch test was used to assess the leaching of contaminants from MBA. The test was performed following the standard NEN-EN 12457-4 [211]. The leaching agent was mixed with MBA at the liquid-to-solid ratio of 10 L/kg. The mixture was agitated for 24 h. After the test, the eluate was filtered over a 0.45  $\mu\text{m}$  membrane filter. The concentrations of heavy metals were measured by inductively coupled plasma-atomic emission spectroscopy (ICP-AES). The chloride (Cl), bromide (Br), and sulfate ( $\text{SO}_4^{2-}$ ) in the filtered eluate were analyzed by ion chromatography (IC). The content of Fluoride (F) was determined by flow injection analysis with spectroscopic detection. The test results were compared with the limiting level described in the Dutch Soil Quality Decree, 2015 [212].

### 4.3 Results and discussion

#### 4.3.1 Compositions of MBA

##### 4.3.1.1 Chemical composition

The chemical composition of MBA provides information about the presence of major components and hazardous components (such as soluble salts and heavy metals). The chemical compositions of MBA, BFS, and FA are listed in Table 4.5. In MBA, the main constituents are  $\text{SiO}_2$ ,  $\text{CaO}$ ,  $\text{Al}_2\text{O}_3$ , and  $\text{Fe}_2\text{O}_3$ . The  $\text{SiO}_2$  content in MBA is 52.91 wt.%, close to that in FA but higher than in BFS. The  $\text{CaO}$  content in MBA is 13.44 wt.%, three times as much as that in FA but much lower than that detected in BFS. The amount of  $\text{Al}_2\text{O}_3$  in MBA is 10.18 wt.%, less than half of the  $\text{Al}_2\text{O}_3$  content in FA. The  $\text{Al}_2\text{O}_3$  content in MBA is around 4 wt.% less than that in BFS. Regarding  $\text{Fe}_2\text{O}_3$ , its content in MBA is higher than in FA and BFS. In addition to the major components, the contents of heavy metals, unburned organics, equivalent alkalis ( $\text{Na}_2\text{O}_e$ ),  $\text{SO}_3$ , and Cl are of concern when MBA is used as SCM or AAM precursor.

As illustrated in Table 4.5, MBA contains much more heavy metals, unburned organics, alkalis, and chloride than FA and BFS. Only the  $\text{SO}_3$  content in MBA is lower than that in FA and BFS. Although the toxic heavy metal components, such as  $\text{CuO}$ ,  $\text{PbO}$ , and  $\text{Cr}_2\text{O}_3$ , are present in trace amounts in MBA (< 1 wt.%), their contents are much higher in MBA than in FA and BFS. In MBA, the unburned organic content, referred to as  $\text{LOI}_{550}$ , is 2.17 wt.%, more than two times

as much as that in FA and BFS. The heavy metals and unburned organics in MSWI bottom ash were found to be the primary sources of the heavy metals leached from the building materials prepared with MSWI bottom ash [213].

Table 4.5 Chemical compositions of MBA, FA, and BFS, as determined by XRF analysis.

Compounds (wt.%)	MBA	FA	BFS
SiO <sub>2</sub>	52.91	55.29	34.99
CaO	13.44	4.43	36.33
Al <sub>2</sub> O <sub>3</sub>	10.18	25.03	14.32
Fe <sub>2</sub> O <sub>3</sub>	9.29	6.94	0.40
Na <sub>2</sub> O	4.24	0.91	0.24
K <sub>2</sub> O	0.84	1.66	0.46
SO <sub>3</sub>	0.70	0.73	1.36
Cl	0.27	0.01	0.02
P <sub>2</sub> O <sub>5</sub>	1.03	1.01	0.01
MgO	2.40	1.41	9.42
ZnO	0.55	0.03	-
CuO	0.31	0.01	0.18
TiO <sub>2</sub>	1.12	1.23	1.21
MnO	0.21	0.04	0.26
PbO	0.09	0.01	-
Cr <sub>2</sub> O <sub>3</sub>	0.07	0.02	-
BaO	0.09	0.07	0.04
NiO	0.03	0.01	-
ZrO <sub>2</sub>	-	0.06	0.04
SrO	0.04	0.12	0.05
SnO <sub>2</sub>	0.02	-	-
Rb <sub>2</sub> O	-	0.01	-
Nb <sub>2</sub> O <sub>5</sub>	-	-	-
Y <sub>2</sub> O <sub>3</sub>	-	0.01	0.01
V <sub>2</sub> O <sub>5</sub>	-	0.04	0.02
CeO <sub>2</sub>	-	-	0.08
LOI <sub>550</sub>	2.17	0.92	0.56
Sum	100	100	100

The Na<sub>2</sub>O<sub>e</sub> content in MBA is 4.79 wt.%, as calculated according to the equation: Na<sub>2</sub>O<sub>e</sub> = Na<sub>2</sub>O + 0.658 K<sub>2</sub>O. This value is 2.01 wt.% and 0.54 wt.% in FA and BFS, respectively. The Na<sub>2</sub>O present in the waste glass is responsible for this high Na<sub>2</sub>O<sub>e</sub> content in MBA, which will be confirmed in section 4.3.1.3. For Portland cement concrete prepared using MSWI bottom ash as aggregates, the products of alkali-silica reaction (ASR) were observed [214], and the cracks induced by the formation of ASR gel were also identified [55]. However, when using MSWI bottom ash as SCM and AAM precursor, it remains unclear whether adding MSWI bottom ash will induce alkali-silica reaction. More research is required in this area.

The chloride content in MBA is 0.27 wt.%. This value is much higher than that in FA or BFS. According to the European standard NEN-EN 206 [215], the chloride content in binder may not exceed 1 wt.% for concretes without steel reinforcement or other metal embedment. For reinforced and pre-stressed concretes, the maximum chloride content in binder is restricted to 0.2 wt.%. Given that the Cl content of MBA is slightly higher than 0.2 wt.%, it is suitable to use MBA as binder materials in non-reinforced concretes. For the application of reinforced concretes, the risk of steel reinforcement corrosion induced by the Cl in MBA can be mitigated by reducing the percentage of MBA in the binder.

#### 4.3.1.2 Mineralogical composition

The contents of the reactive crystalline phases and the amorphous phase determines the reactivity of MBA. Figure 4.4 (a) presents the XRD spectrum of MBA. This figure shows that quartz is the primary crystalline phase in MBA. Besides, the peaks of silicates and calcite are also identified in the spectrum of MBA. The silicates detected include gehlenite, albite, orthopyroxene, diopside, and wollastonite. Table 4.6 lists the formulae and the Inorganic Crystal Structure Database (ICSD) codes of all the crystalline phases found in MBA. The proportion of each phase, as determined by the QXRD analysis, is also presented in the same table. According to the QXRD analysis, quartz accounts for the largest proportion (12.1 wt.%) among all the crystalline phases. The second major crystalline phase in MBA is diopside, with its content of 4.4 wt.%. Except for diopside, the contents of other silicates are all below 3 wt.%. The content of calcite is around 2.1 wt.%. Phases like halite, corundum, goethite, gibbsite, and iron are present in trace amounts (< 1 wt.%).

The diffraction pattern of MBA also illustrates the “hump” feature. By enlarging the area marked in Figure 4.4 (a), a broad hump centered at a  $2\theta$  angle of  $32.5^\circ$  between  $25^\circ$  and  $40^\circ$  can be observed in Figure 4.4 (b). As presented in Table 4.6, the amorphous phase in MBA reaches 68.1 wt.%. The quantity of the amorphous phase in MBA is slightly lower than in FA, but much lower than in BFS. As illustrated in Figure 4.5 (a) and (b), the broad amorphous hump can be easily recognized in the spectra of FA and BFS. In the XRD patterns of FA and BFS, the hump centered at  $2\theta$  of  $22.5^\circ$  and  $30^\circ$ , respectively. Unlike entirely amorphous BFS, FA contains crystal phases, mainly quartz and mullite. The QXRD analysis results indicate that FA has 11.5 wt.% quartz and 11.7 wt.% mullite (Table 4.7). The amorphous phase makes up 74 % of the total weight of FA.

Figure 4.4 (c) shows the XRD spectrum of the insoluble residue obtained after the dissolution treatments of MBA. The hump representing the amorphous phase is not found in Figure 4.4 (c), indicating that the amorphous phase in MBA was dissolved during the chemical dissolution treatments. This observation further confirms the presence of amorphous phase in MBA. According to the results of XRF analysis, the insoluble residue mainly consists of  $\text{SiO}_2$  (70.5 wt.%),  $\text{Al}_2\text{O}_3$  (12.5 wt.%),  $\text{CaO}$  (5.5 wt.%),  $\text{Fe}_2\text{O}_3$  (3.8 wt.%), and  $\text{MgO}$  (2.5 wt.%). In the XRD pattern of the insoluble residue, mainly the peaks of quartz, augite, and wollastonite are observed. Quartz and wollastonite are the phases of MBA that remained undissolved after the chemical dissolution tests, while augite ( $\text{CaMg}_{0.6}\text{Fe}_{0.2}\text{Al}_{0.7}\text{Si}_{1.5}\text{O}_6$ , ICSD 16905) is the newly formed crystalline phase. The mass of MBA decreased by 78.5 % due to dissolution treatments, higher than the amorphous phase content calculated by the QXRD analysis (68.1 wt.%). This

is because part of the mass loss is caused by the dissolution of the crystalline phases during the chemical dissolution treatments of MBA.

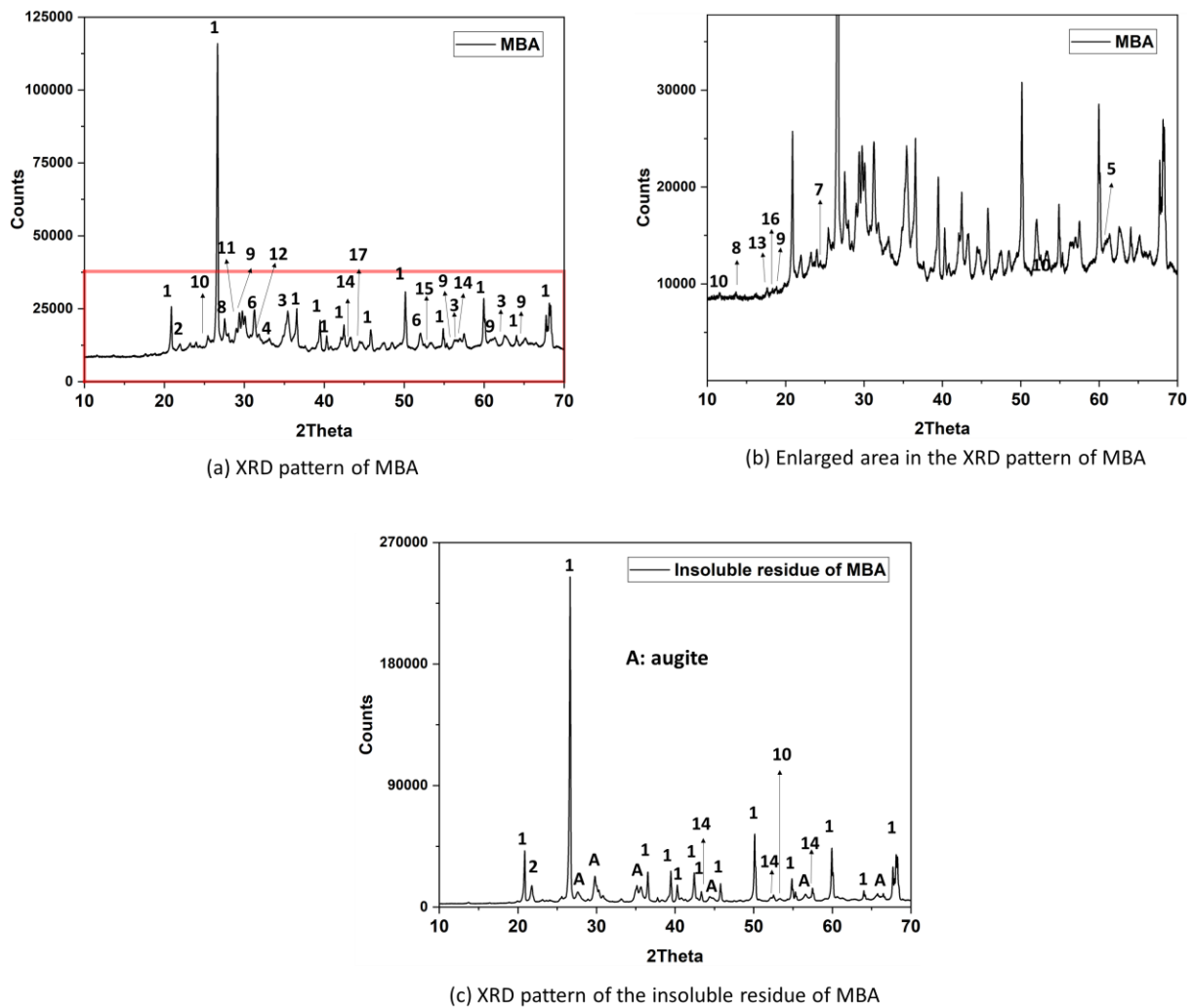


Figure 4.4 (a) XRD spectrum of MBA. (b) Enlarged image of the area labeled in the XRD spectrum of MBA. (c) XRD spectrum of the insoluble residue of MBA obtained after chemical dissolution treatments. The peak labels follow the labels described in Table 4.6.

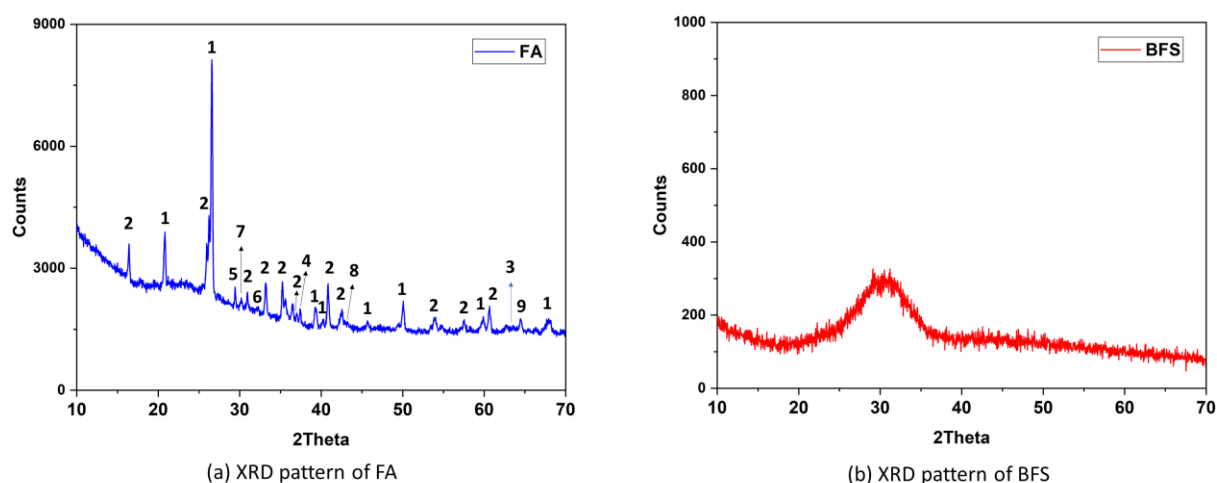


Figure 4.5 (a) XRD spectrum of FA. The peak labels follow the labels defined in Table 4.7. (b) XRD spectrum of BFS.

Table 4.6 Mineral phases present in MBA and QXRD analysis results of MBA

Phases	Proportions (wt.%)	Labels	Formulae	ICSD codes
Quartz	12.1	1	SiO <sub>2</sub>	541929
Cristobalite	0.4	2	SiO <sub>2</sub>	1251919
Magnetite	0.9	3	Fe <sub>3</sub> O <sub>4</sub>	92356
Hematite	0.4	4	Fe <sub>2</sub> O <sub>3</sub>	453828
Wustite	0.2	5	FeO	309924
Gehlenite	2.8	6	Ca <sub>2</sub> Al <sub>2</sub> SiO <sub>7</sub>	1411155
Albite	1.9	7	NaAlSi <sub>3</sub> O <sub>8</sub>	1402109
Orthopyroxene	1.4	8	Ca <sub>0.02</sub> Mg <sub>0.30</sub> Fe <sub>0.68</sub> SiO <sub>3</sub>	1615622
Diopside	4.4	9	CaMg <sub>0.69</sub> Fe <sub>0.31</sub> Si <sub>2</sub> O <sub>6</sub>	77809
Wollastonite	2.6	10	CaSiO <sub>3</sub>	1253098
Calcite	2.1	11	CaCO <sub>3</sub>	1611066
Halite	0.4	12	NaCl	311644
Phosphammite	1.1	13	H(NH <sub>4</sub> ) <sub>2</sub> (PO <sub>4</sub> )	1401715
Corundum	0.7	14	Al <sub>2</sub> O <sub>3</sub>	527601
Goethite	0.4	15	FeO(OH)	71810
Gibbsite	0.2	16	Al(OH) <sub>3</sub>	1005040
Iron	0.1	17	Fe	1503158
Amorphous phase	68.1	-	-	-
Sum	100	-	-	-

Table 4.7 Mineral phases present in FA and QXRD analysis results of FA

Phases	Proportions (wt.%)	Labels	Formulae	ICSD codes
Quartz	11.5	1	SiO <sub>2</sub>	156198
Mullite	11.7	2	Al <sub>2.24</sub> Si <sub>0.76</sub> O <sub>4.88</sub>	313794
Hematite	0.5	3	Fe <sub>2</sub> O <sub>3</sub>	2070090
Lime	0.1	4	CaO	1503123
Calcite	0.2	5	CaCO <sub>3</sub>	1611066
Hexapotassium hexaoxodiferrate	0.1	6	K <sub>6</sub> (Fe <sub>2</sub> O <sub>6</sub> )	16534
Iron(III) oxide hydroxide	1.3	7	FeO(OH)	94874
Periclase	0.3	8	MgO	1110749
Wadsleyite	0.3	9	Mg <sub>1.84</sub> Fe <sub>0.16</sub> SiO <sub>4</sub>	66491
Amorphous phase	74.0	-	-	-
Sum	100	-	-	-

#### 4.3.1.3 Chemical composition of amorphous phase

When MBA is used as SCM and AAM precursor, it is necessary to determine the chemical composition of the amorphous phase in MBA. The amorphous phase is the primary reactive phase in MBA, and its chemical composition can influence the reaction product formation. Table 4.8 lists the chemical composition of the amorphous phase in MBA, FA, and BFS. The percentages are absolute values and are presented without normalization. As shown in Table 4.8, SiO<sub>2</sub> is the primary component (34.2 wt.%) in the amorphous phase of MBA. In terms of CaO, Al<sub>2</sub>O<sub>3</sub>, Na<sub>2</sub>O, Fe<sub>2</sub>O<sub>3</sub>, and MgO, the content of each is lower than 10 wt.%. It is worth noting that the SiO<sub>2</sub> content calculated for the amorphous phase of MBA in the QXRD analysis is slightly lower than the reactive silica content (37.77 wt.%) determined by the chemical dissolution treatments. One possible explanation is that the chemical dissolution treatments overestimate the content of the amorphous phase in MBA, resulting in a higher value of the reactive silica content.

Table 4.8 Chemical composition of amorphous phase in MBA, FA, and BFS, calculated by subtracting the percentages of the elements in crystalline phases from the chemical compositions of MBA, FA, and BFS.

Compounds	Percentages in amorphous phase (wt.%)		
	MBA	FA	BFS
SiO <sub>2</sub>	34.2	41.3	35.0
CaO	8.8	4.3	36.3
Al <sub>2</sub> O <sub>3</sub>	7.9	15.7	14.3
Fe <sub>2</sub> O <sub>3</sub>	6.2	5.1	0.4
Na <sub>2</sub> O	3.8	0.9	0.2
K <sub>2</sub> O	0.8	1.6	0.5
MgO	1.7	0.9	9.42
Others	4.7	4.2	3.9
Sum	68.1	74.0	100

Compared with FA, MBA contains less  $\text{SiO}_2$  in the amorphous phase. The  $\text{SiO}_2$  content in the amorphous phase of MBA is almost equal to that in BFS. The  $\text{CaO}$  content in the amorphous phase of MBA (8.8 wt.%) is about one-quarter of that in BFS, but twofold the  $\text{CaO}$  content in FA. The  $\text{Al}_2\text{O}_3$  content in the amorphous phase of MBA is 7.9 wt.%, only around half of that in the amorphous phase of FA or BFS. Besides, much more  $\text{Na}_2\text{O}$  was found in the amorphous phase of MBA (3.8 wt.%) than in FA or BFS (lower than 1 wt.%). The amount of  $\text{Fe}_2\text{O}_3$  in the amorphous phase of MBA is also higher than that in FA and BFS. In terms of the  $\text{MgO}$  content, MBA has 1.7 wt.%  $\text{MgO}$ , much lower than BFS.

#### *Composition difference between the amorphous phase and the glass in MBA*

Given that waste glass is one of the major sources of the amorphous phase in MBA, it is necessary to examine whether the amorphous phase of MBA and the glass particles in MBA have the same composition. The XRD spectrum in Figure 4.6 (a) proves that these manually selected glass particles are almost 100 % amorphous. The QXRD analysis results indicate that these glass particles only contain 1 wt.% quartz. The hump representing the amorphous phase appeared in the XRD spectrum of the glass particles at the same location as that observed in the XRD spectrum of MBA (Figure 4.4 (a)).

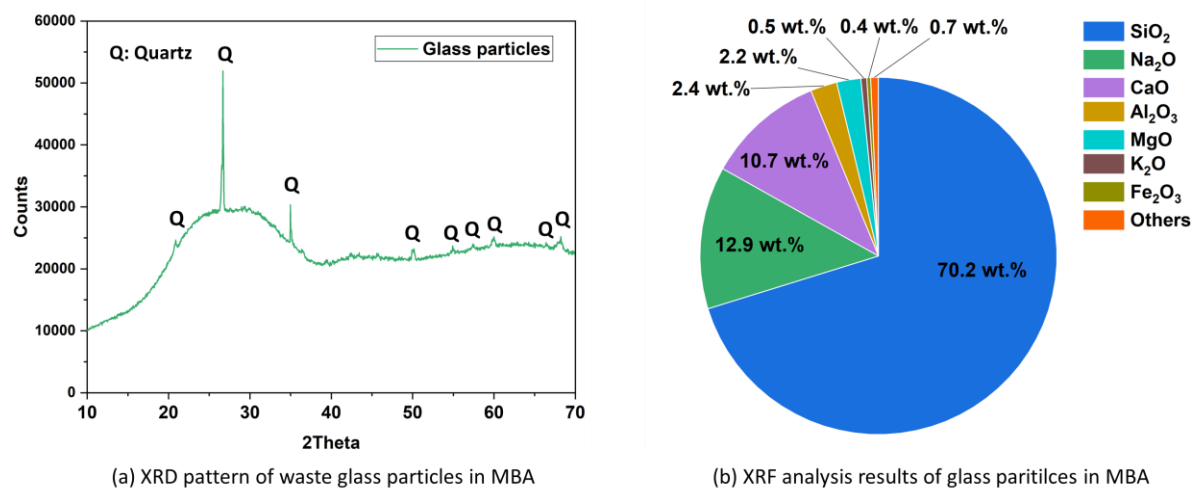


Figure 4.6 (a) mineralogical composition (determined by XRD analysis) and (b) chemical composition (determined by XRF analysis) of the glass particles shown in Figure 4.3 (b).

The chemical composition of the glass particles in MBA is illustrated in Figure 4.6 (b). The main components in the glass particles are  $\text{SiO}_2$  (70.2 wt.%),  $\text{Na}_2\text{O}$  (12.9 wt.%), and  $\text{CaO}$  (10.7 wt.%). This chemical composition is almost the same as that of the soda-lime glass used in the production of glass containers and glass windows [216]. In the  $\text{SiO}_2$ - $\text{CaO}$ - $\text{Al}_2\text{O}_3$  and the  $\text{SiO}_2$ - $\text{Na}_2\text{O}$ - $\text{Fe}_2\text{O}_3$  ternary diagram, the location of the dot representing the composition of glass particles does not overlap with the dot of the amorphous phase in MBA (see Figure 4.7 (a) and (b)). This observation indicates that the chemical composition of the glass particles is quite different from the chemical composition determined in the amorphous phase in MBA. In addition to soda-lime glass, other amorphous phases containing  $\text{CaO}$ ,  $\text{Al}_2\text{O}_3$ , and  $\text{Fe}_2\text{O}_3$  are also present in MBA.



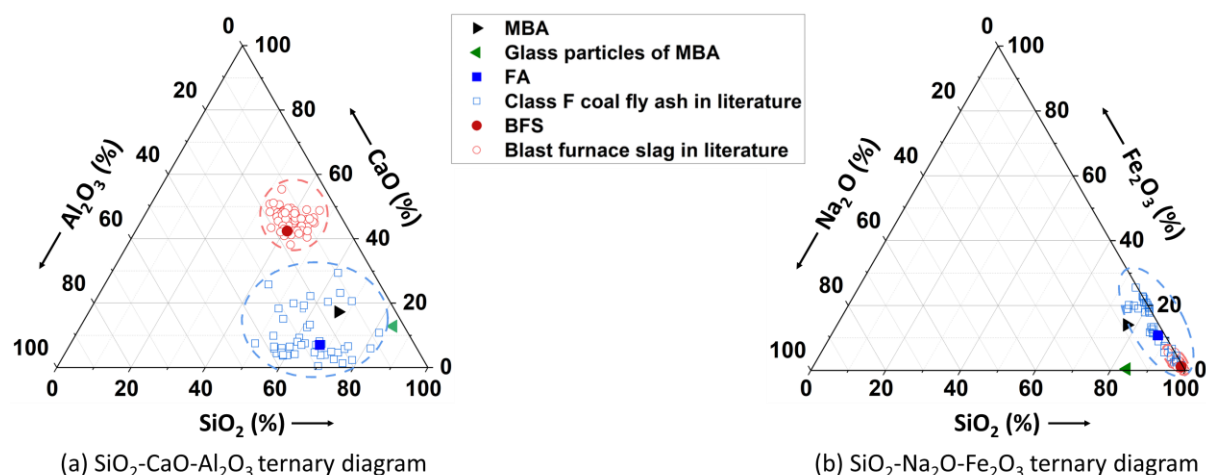


Figure 4.7 (a) Ternary diagram showing the relative content of SiO<sub>2</sub>, CaO, and Al<sub>2</sub>O<sub>3</sub> in the amorphous phase of MBA, BFS, FA, and glass particles of MBA (b) Ternary diagram showing the relative content of SiO<sub>2</sub>, Na<sub>2</sub>O, and Fe<sub>2</sub>O<sub>3</sub> in the amorphous phase of MBA, BFS, FA, and glass particles of MBA. The data of the amorphous phase of Class F coal fly ash are collected from the literature [217–224]. The composition information of blast furnace slag is from the literature [225,226,235–244,227,245–254,228,255–264,229,265–274,230,275–279,231–234]. The ternary diagrams are plotted according to the weight percentages of the oxides.

#### *Relative contents of SiO<sub>2</sub>, CaO, and Al<sub>2</sub>O<sub>3</sub> in the amorphous phase of MBA*

The chemical composition of the amorphous phase in MBA was compared with the chemical composition of the amorphous phase in Class F coal fly ash and blast furnace slag reported in the literature. The reference data collected for Class F coal fly ash are the chemical composition of the amorphous phase [217–224]. The reference data collected for blast furnace slag are the XRF results [49–103]. There are two reasons for this choice. First, the information about the composition of the amorphous phase is very limited in the literature. Second, blast furnace slag usually contains more than 90 % amorphous phase [122,123]. The XRF results of blast furnace slag can largely reflect the composition of the amorphous phase. As shown in the SiO<sub>2</sub>-CaO-Al<sub>2</sub>O<sub>3</sub> ternary diagram (Figure 4.7 (a)), the chemical compositions of the amorphous phase in FA and BFS used in this work are typical for Class F coal fly ash [217–224] and blast furnace slag [49–103]. The dot representing the relative contents of SiO<sub>2</sub>, CaO, and Al<sub>2</sub>O<sub>3</sub> in the amorphous phase of MBA is within the same region as that in the amorphous phase of Class F coal fly ash reported in the literature [217–224].

The mass ratio of CaO/SiO<sub>2</sub> in the amorphous phase of blast furnace slag is usually used as an indicator to assess its reactivity as AAM precursor [123]. As demonstrated in Figure 4.8, the CaO/SiO<sub>2</sub> ratio of MBA is 0.3, much lower than that of BFS (1.0). BFS with higher CaO/SiO<sub>2</sub> usually has a more depolymerized and disordered structure, resulting in a higher reactivity for the application of AAM precursor [280–282]. In the case of coal fly ash, the mass ratio between SiO<sub>2</sub>/Al<sub>2</sub>O<sub>3</sub> in the amorphous phase can be used to indicate its reactivity as AAM precursor [123]. As shown in Figure 4.8, the SiO<sub>2</sub>/Al<sub>2</sub>O<sub>3</sub> ratio for the amorphous phase of MBA is 4.3, almost two times that in the amorphous phase of FA. The aluminosilicate glass with its SiO<sub>2</sub>/Al<sub>2</sub>O<sub>3</sub> ratio within the range of 2 to 4 was found to be a suitable precursor for alkali-

activated materials [161,283–288]. Unlike FA, the  $\text{SiO}_2/\text{Al}_2\text{O}_3$  ratio of the amorphous phase in MBA is not within the desirable range.

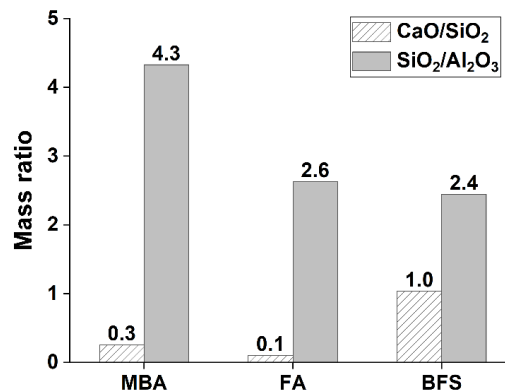


Figure 4.8 Mass ratio of  $\text{CaO}/\text{SiO}_2$  and  $\text{SiO}_2/\text{Al}_2\text{O}_3$  calculated for the amorphous phase in MBA, BFS, and FA.

### 4.3.2 Reactivity of MBA as SCM

The information about the pozzolanic reactivity of MBA can be used in the mix design of blended cement pastes. The reactivity of MBA as SCM was studied by measuring the hydration heat evolution of  $\text{R}^3$  pastes. The calorimetry test results of the  $\text{R}^3$  pastes prepared with MBA, FA, or BFS are presented in Figure 4.9 (a). The cumulative heat collected after different time intervals is shown in Figure 4.9 (b). After 7 days of reaction, the cumulative heat generated by MBA is only one-third of that by BFS, but slightly more than that of FA. These results indicate that MBA is much less reactive than BFS but could be as reactive as FA.

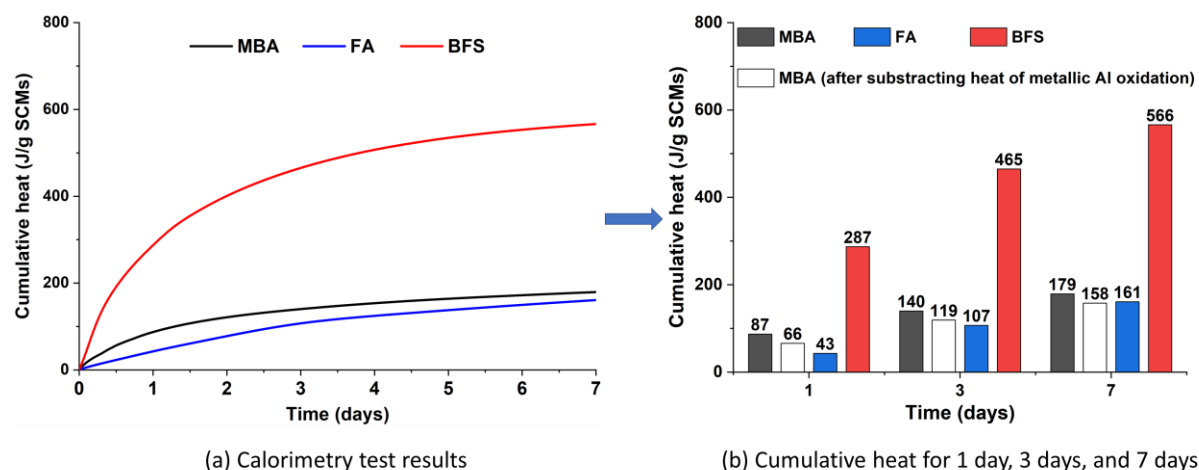


Figure 4.9 (a) Calorimetry test results of the  $\text{R}^3$  pastes prepared with MBA, FA, or BFS, the results are expressed as J/g of SCMs. The details of the  $\text{R}^3$  pastes can be found in section 4.2.2.3. (b) Cumulative heat collected after different time intervals.

The difference in the heat release between MBA and FA is significant during the first 3 days (Figure 4.9 (a)). Afterward, this heat release difference decreased, reaching the lowest value at 7 days. The big difference observed at early ages ( $< 3$  days) can be attributed to the

intensive oxidation of the residual metallic Al in MBA. The residual metallic Al in MBA reacts readily with  $\text{Ca(OH)}_2$ , which is introduced excessively in the  $\text{R}^3$  pastes [140]. The oxidation of the metallic Al is expected to finish within 1 day [56].

At room temperature, in the alkaline solution, metallic Al first reacts with water to form  $\text{Al(OH)}_3$  and  $\text{H}_2$ , then  $\text{Al(OH)}_3$  reacts with  $\text{OH}^-$ . Theoretically, the reaction of 1 g of metallic Al with water generates 16.3 kJ of heat ( $2\text{Al} + 6\text{H}_2\text{O} \rightarrow 2\text{Al(OH)}_3 + 3\text{H}_2$ ) [289]. The mass of metallic Al in 1 g of MBA is 0.0013 g. In this case, the reaction heat contributed by the reaction between metallic Al and water in the calorimetry test of MBA would be 21 J. As shown in Figure 4.9 (b), after subtracting the reaction heat of metallic Al, the heat released by the reaction of the reactive minerals in MBA is around 158 J, almost the same as the 7-day heat of FA (161 J). It can be concluded that as SCM, the reactivity of MBA is similar to FA.

### 4.3.3 Reactivity of MBA as AAM precursor

The reactivity of MBA as AAM precursor was assessed via dissolution tests. The dissolution tests mimic the dissolution of precursors in the pore solution. Analysis of the dissolution behavior of MBA provides information about the elements that participate in the formation of reaction products and delivers a fundamental understanding of the early-age reaction. The concentrations of Si, Al, Ca, Fe, and Mg (hereafter denoted as [Si], [Al], [Ca], [Fe], and [Mg], respectively) in the filtrated solution are shown in Figure 4.10. This solution was obtained after dissolving MBA, FA, or BFS in NaOH solution for 24 hours.

#### 4.3.3.1 Concentrations of dissolved elements

##### [Si], [Al], and [Ca]

As shown in Figure 4.10, the filtrate of MBA, FA, and BFS is enriched with Si and Al. Regardless of the concentration of the NaOH solution, MBA and FA released much less Si and Al than BFS. Compared with MBA and FA, the amorphous phase of BFS with higher  $\text{CaO/SiO}_2$  has a more depolymerized and disordered structure [280] and dissolves more easily in alkaline solution. Accordingly, the reactivity of MBA and FA is much lower than that of BFS. The high [Si] and [Al] in the filtrate of BFS indicates that a large amount of BFS has been dissolved.

Given that the mass ratio between  $\text{SiO}_2$  and CaO in the amorphous phase of BFS is one, the [Ca] in the filtrate of BFS is expected to be in the same range as [Si]. However, the [Ca] in the filtrate of BFS is much lower than [Si]. When 4M NaOH solution was used in the dissolution test, the [Ca] in the filtrate of BFS was higher than that in the filtrate of MBA and FA. Further increasing the concentration of NaOH solution to 5 M or 6 M, the [Ca] in the filtrate of BFS decreased and was similar to that in the filtrate of MBA and FA.

The low [Ca] in the filtrate of BFS can be attributed to the formation of Ca-bearing phases, such as  $\text{Ca(OH)}_2$ , C-S-H gel, and C-A-S-H gel. Although a large liquid-to-solid ratio is used to prevent the precipitation of reaction products, there exists a concentration gradient in the vicinity of the surface of BFS particles [290]. The [Ca] in the region close to the surface of BFS particles is higher than the bulk solution [290]. As a result, the  $\text{Ca}^{2+}$  ions in this region could combine with  $\text{OH}^-$  and form  $\text{Ca(OH)}_2$  precipitates. In the NaOH solution with a pH higher than 11.5,  $\text{Ca(OH)}_2$  is thermodynamically more stable than  $\text{Ca}^{2+}$  ions [291]. Compared with  $\text{Ca(OH)}_2$ ,

the  $\text{Ca}^{2+}$  ions are less likely to interact with the silicate and aluminate species to form a C-S-H or C-A-S-H layer on the surface of BFS particles. This is because if  $\text{Ca}^{2+}$  ions are consumed due to the formation of C-S-H or C-A-S-H gel, the decline of [Si], [Al], and [Ca] in the filtrate should be in the same order of magnitude. In reality, [Ca] is much smaller than [Si] and [Al] in the filtrate of BFS.

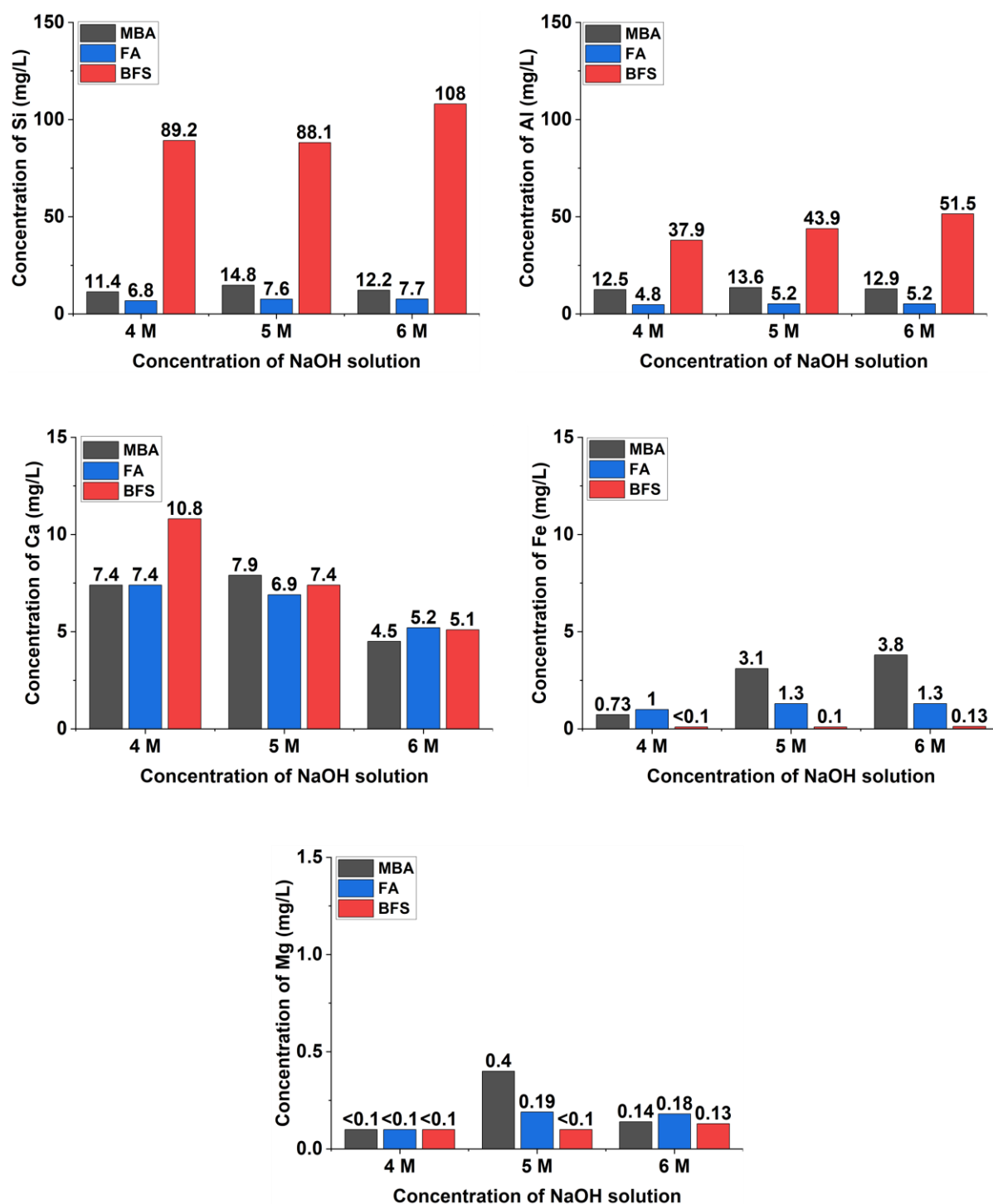


Figure 4.10 Element concentrations in the filtrated solution obtained after the dissolution tests of MBA, FA, and BFS in the NaOH solution of 4M, 5M, and 6M (M: molarity).

The [Si] and [Al] in the filtrate of MBA are higher than in the filtrate of FA, indicating that MBA is more soluble than FA. Considering that the CaO content in the amorphous phase of MBA is around two times that in FA, MBA with higher solubility is expected to release more  $\text{Ca}^{2+}$  than FA during the dissolution tests. However, the [Ca] in the filtrate of MBA appeared to be in the same range as that in the filtrate of FA. As discussed above, precipitation of  $\text{Ca}^{2+}$  ions cannot be avoided during the dissolution test. The precipitate formed is more likely to be  $\text{Ca}(\text{OH})_2$  than the C-S-H gel or C-A-S-H gel. It is possible that the  $\text{Ca}^{2+}$  ions released by MBA also react with  $\text{OH}^-$  to form  $\text{Ca}(\text{OH})_2$ , resulting in a low [Ca] in its filtrate.

#### [Fe] and [Mg]

The [Fe] in the filtrate of MBA is only around one-quarter of [Si]. The [Fe] in the filtrate of MBA is higher than that of FA and BFS. This higher Fe concentration in MBA can be due to the higher  $\text{Fe}_2\text{O}_3$  content in the amorphous phase of MBA compared with FA and BFS. In the filtrate of MBA, the [Mg] is the lowest ( $< 0.5 \text{ mg/l}$ ) among the measured element ([Si], [Al], [Ca], [Fe], and [Mg]). The concentration of Mg remained at a very low level regardless of the molarity of NaOH. Similar phenomena can also be observed for the Mg dissolved from BFS and FA.

#### 4.3.3.2 Ratio of dissolved Si and Al

The compressive strength of AAM can be used as an indicator of the reactivity of precursors. The AAM prepared with a more reactive precursor usually has a higher compressive strength. Duxson et al. [292] indicated a correlation between the compressive strength of AAM and the Si/Al molar ratio in the mixture of precursor and alkaline activator. When increasing the Si/Al molar ratio from 1.15 to 1.9, the compressive strength of the AAM became higher due to the formation of a more homogeneous and denser microstructure. The optimal Si/Al molar ratio was 1.9 for preparing AAM with aluminosilicate materials [292]. Therefore, the Si/Al molar ratio in the filtrate of MBA, FA, or BFS was calculated to provide additional insight into the reactivity of these precursors and the mix design of AAM.

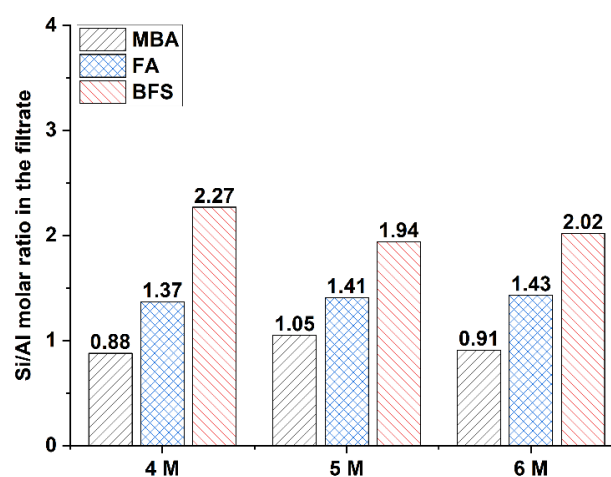


Figure 4.11 Si/Al molar ratio in the filtrate, calculated using the dissolution test results presented in Figure 4.10 (M: molarity).

As illustrated in Figure 4.11, the Si/Al molar ratio in the filtrate of MBA fluctuates around 0.9, lower than the ratio in the filtrate of FA and BFS. The molar ratio of Si and Al released by MBA is far below the optimal value found by Duxson et al. [292]. This low Si/Al molar ratio is not favorable for the strength development of alkali-activated MBA at an early age. In our preliminary research, alkali-activated MBA paste did not harden within 24 hours at room temperature when NaOH solution (4M) was used as activator. The hardened paste samples can be obtained after increasing the Si content in the AAM system by adding water glass to the activating solution. Therefore, when MBA is used to prepare AAM, it is recommended to increase the Si/Al ratio in the mixture of precursor and activator by adding Si-enriched precursors or  $\text{Na}_2\text{SiO}_3$  solution.

#### 4.3.4 Thermodynamic modeling of the reactions in alkali-activated MBA paste

Thermodynamic modeling was used to predict the solid phase assemblages and the pore solution in alkali-activated MBA paste. The modeling results provide insight into the evolution of the reaction products and the pore solution in alkali-activated MBA paste when the  $\text{Na}_2\text{O}$  content in the activating solution changes from a low level (2 wt.%) to a high level (10 wt.%). This information can also be used as a rough guide to the mix design, making it possible to control the reaction product formation and tailor the properties of MBA-based AAM.

##### *Total amount of reaction products*

The amount of reaction products that can form upon alkali activation is strongly influenced by the proportions of reactive phases (mainly the amorphous phase) in AAM precursors. MBA contains less amorphous phase than FA and BFS (see Table 4.8), suggesting that the reaction products formed in alkali-activated MBA paste would be less than that in alkali-activated FA paste and alkali-activated BFS paste. Figure 4.12 presents the solid phase assemblages predicted by thermodynamic modeling in alkali-activated MBA paste, alkali-activated FA paste, and alkali-activated BFS paste. According to the prediction, the reaction products obtained after activating 100g BFS with NaOH solution would be much more than those obtained from the reaction of 100 g MBA or 100g FA. Compared with alkali-activated FA paste, the mass of reaction products formed in alkali-activated MBA paste would be slightly lower.

Apart from the reaction products, Figure 4.12 also shows that the un-reactive fraction in MBA is larger than in FA and BFS. The un-reactive fraction illustrated in Figure 4.12 refers to the crystalline phases and part of the amorphous phase. In the modeling, only the components including  $\text{SiO}_2$ ,  $\text{CaO}$ ,  $\text{Al}_2\text{O}_3$ ,  $\text{Fe}_2\text{O}_3$ ,  $\text{Na}_2\text{O}$ ,  $\text{K}_2\text{O}$ , and  $\text{MgO}$  of the amorphous phase were assumed to participate in reaction product formation. The remaining components of the amorphous phase were considered to be unreactive. Regarding the pore solution, its mass in alkali-activated MBA paste was forecast to be roughly equivalent to that of alkali-activated FA paste but much larger than that of alkali-activated BFS paste (Figure 4.12).

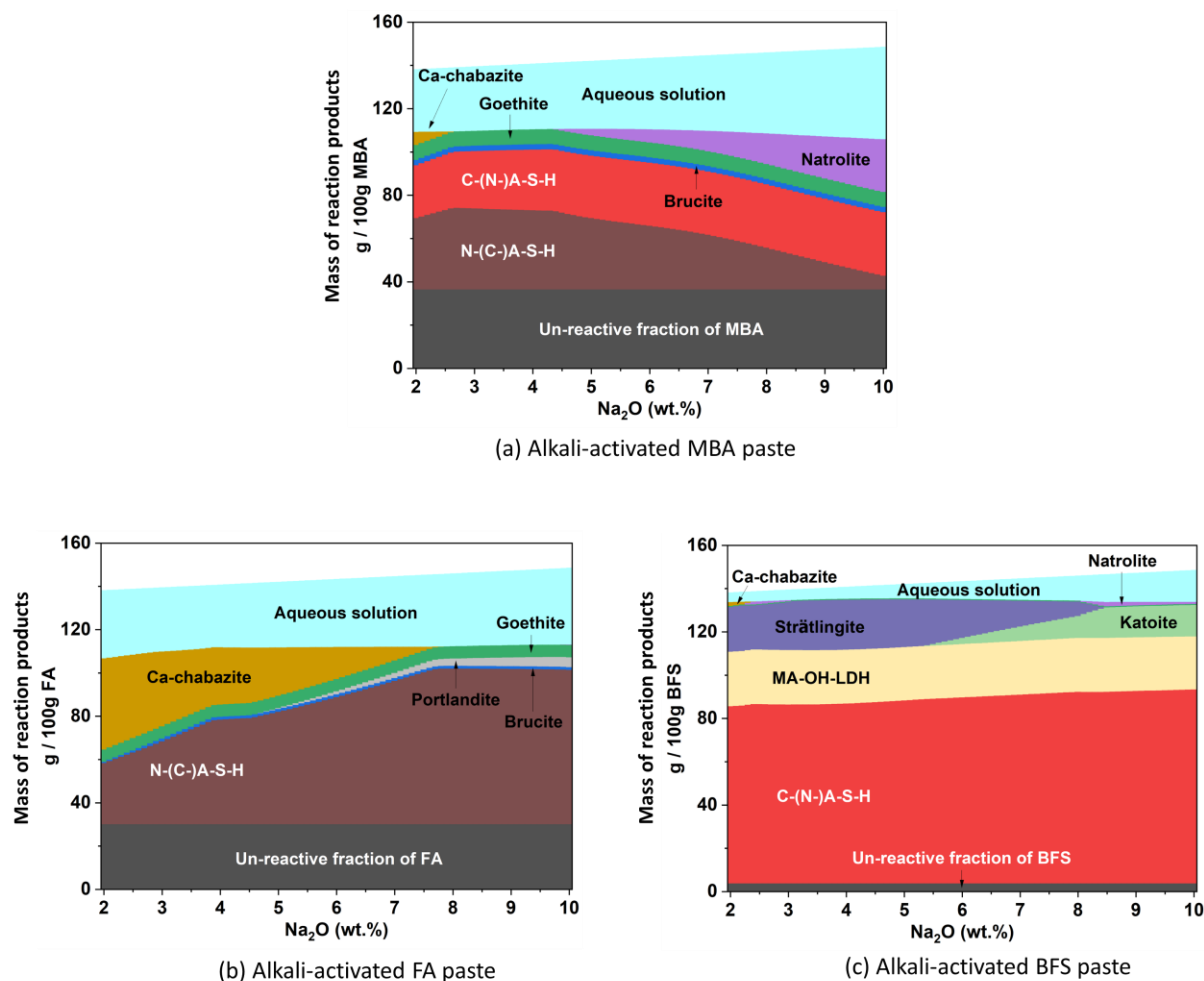


Figure 4.12 Thermodynamically simulated phase assemblage, solid reaction product mass, and pore solution mass after activating 100 g MBA, 100 g FA, or 100g BFS with NaOH solution. The simulation was performed with GEMS-Selektor v.3 [205,206]. The data is presented as a function of the Na<sub>2</sub>O content in the activator. The percentage of Na<sub>2</sub>O is with respect to the mass of the precursor.

### Predicted solid phase assemblages

It is meaningful to predict the gel phases that can form in alkali-activated MBA. This information can be used as a reference when designing MBA-based AAM mixtures. The nanostructure of the gel phases formed in alkali-activated materials has a significant effect on the mechanical properties of synthesized alkali-activated materials [44]. According to thermodynamic modeling (Figure 4.12 (a)), the major reaction products formed after MBA reacting with NaOH solution are C-(N-)A-S-H gel, N-(C-)A-S-H gel, and zeolite. The details about the chemical compositions of predicted C-(N-)A-S-H gel and N-(C-)A-S-H gel can be found in Appendix C. The zeolite minerals predicted in alkali-activated MBA paste include natrolite ( $\text{Na}_2\text{Al}_2\text{Si}_3\text{O}_{10} \cdot 2\text{H}_2\text{O}$ ) and Ca-chabazite ( $\text{Ca}_{0.111}\text{Al}_{0.111}\text{Si}_{0.778} \cdot 0.667\text{H}_2\text{O}$ ). The mass of C-(N-)A-S-H gel shows little changes with the increase of the Na<sub>2</sub>O in the NaOH solution. When the Na<sub>2</sub>O content was higher than 4.5 wt.%, the amount of N-(C-)A-S-H gel in alkali-activated MBA paste started to decrease with the increase of Na<sub>2</sub>O content. Meanwhile, more natrolite was



expected to be found in alkali-activated MBA paste [165]. The Ca-chabazite was forecast to form only when the  $\text{Na}_2\text{O}$  content was lower than 2.5 wt.%.

The prediction about the solid phase assemblages in alkali-activated MBA paste at the  $\text{Na}_2\text{O}$  content of 10 wt.% agrees with the experimental results reported by Maldonado-Alameda et al. [29]. The MSWI bottom ash used by Maldonado-Alameda et al. [29,47] has a chemical composition (determined by XRF) and amorphous phase content (determined by QXRD analysis) falling within the same range as that of MBA. In their work, the 28-day alkali-activated MSWI bottom ash paste was prepared using an activator containing 9.7 wt.%  $\text{Na}_2\text{O}$  with  $\text{SiO}_2/\text{Na}_2\text{O}$  molar ratio of 2.9. In the synthesized paste specimen, the C-(A)-S-H gel, N-A-S-H gel, and zeolite were all identified. The total amount of N-A-S-H gel, zeolite, and C-(A)-S-H dissolved in HCl extraction was 59.9 wt.%. The amount of C-(A)-S-H gel was around 33.5 wt.%, as determined by the salicylic acid/methanol (SAM) extraction. By subtracting the amount of C-(A)-S-H gel dissolved by HCl extraction, the total amount of N-A-S-H gel and zeolite is around 26.4 wt.%. The mass ratio between C-A-S-H gel and the sum of N-A-S-H gel and zeolite is 1.26. This value is slightly higher than 0.95, the mass ratio predicted by thermodynamic modeling at the  $\text{Na}_2\text{O}$  content of 10 wt.%. This discrepancy in the mass ratio may be due to the difference in the  $\text{SiO}_2$  content in the activator.

The types of zeolite phases predicted in alkali-activated MBA paste are the same as those in alkali-activated BFS paste. The Ca-chabazite and natrolite formed in alkali-activated BFS paste are expected to be much less, only in trace amounts. According to the modeling results, the alkali activation of FA only leads to the formation of Ca-chabazite, and its content decreases with the increase in the  $\text{Na}_2\text{O}$  content. Previous researchers also detected zeolite minerals in alkali-activated MSWI bottom ash. However, instead of Ca-chabazite and natrolite, the zeolite mineral found in literature was gismondine ( $\text{CaAl}_2\text{Si}_2\text{O}_8 \cdot 4\text{H}_2\text{O}$ ) [29]. This zeolite mineral was formed after the MSWI bottom ash reacted with a mixture of NaOH and  $\text{Na}_2\text{SiO}_3$  solution for 28 days. In the activator, the  $\text{Na}_2\text{O}$  content was 10.7 wt.% with respect to the content of MSWI bottom ash, and the  $\text{SiO}_2/\text{Na}_2\text{O}$  molar ratio was 2.6 [29].

The minor reaction products in alkali-activated MBA paste were predicted to be goethite ( $\text{FeO}(\text{OH})$ ) and brucite ( $\text{Mg}(\text{OH})_2$ ). These two phases with small quantities were also likely to form in alkali-activated FA paste. The formation of goethite and brucite could be attributed to the existence of  $\text{Fe}_2\text{O}_3$  and  $\text{MgO}$  in the amorphous phase of MBA (Table 4.8). However, the detection of these two phases in alkali-activated MSWI bottom ash is rarely reported in the literature. It is worth mentioning that the primary crystalline reaction products of alkali-activated BFS paste, including katoite ( $3\text{CaO} \cdot \text{Al}_2\text{O}_3 \cdot 6\text{H}_2\text{O}$ ), strätlingite ( $2\text{CaO} \cdot \text{Al}_2\text{O}_3 \cdot \text{SiO}_2 \cdot 8\text{H}_2\text{O}$ ), and hydrotalcite-like phases (MA-OH-LDH), were not expected to form in alkali-activated MBA paste. Portlandite, the reaction product of alkali-activated FA paste, was not likely to form after MBA reacted with NaOH solution.

#### *Predicted pore solution*

The prediction of the pore solution in alkali-activated MBA paste can help people understand the role of MBA in the formation of reaction products. Figure 4.13 provides information about simulated pore solution of alkali-activated MBA paste, alkali-activated FA paste, and alkali-activated BFS paste. The concentrations of Al, Ca, Fe, and Mg in the pore solution were



forecast to be very small (close to zero) for alkali-activated MBA paste, alkali-activated FA paste, and alkali-activated BFS paste. This prediction indicates that most of these elements released by MBA, FA, and BFS were incorporated into the reaction products. The main differences in the pore solution of these three AAM systems were predicted to lie in the pH and the concentrations of Na and Si.

The alkalinity of the pore solution affects the leaching of heavy metals [293] and the long-term stability of calcium-aluminosilicate hydrates [294] and alkali-aluminosilicate gels [295] in AAM. Therefore, it is useful to predict the pH of the pore solution in alkali-activated MBA paste. As shown in Figure 4.13, the pH of the pore solution of alkali-activated BFS paste was expected to be the highest (14.43 to 14.92). The predicted alkalinity in the pore solution of alkali-activated MBA paste, ranging from 13.8 to 14.74, was higher than that of alkali-activated FA paste, between 9.17 and 14.48. This difference in predicted pH of pore solution could be explained by the CaO content difference in the amorphous phase of precursors. The CaO content in the amorphous phase, from the largest to the smallest, was in the following order: BFS, MBA, and FA. This order was the same as that of the predicted pH of the pore solution in synthesized alkali-activated materials. This finding was consistent with the thermodynamic modeling results reported by Xiao et al. [197]. When the Na<sub>2</sub>O content in the activator was fixed, increasing the CaO content of the amorphous phase would also increase the pH of the pore solution [197].

Figure 4.13 shows the predicted concentrations of Na in the pore solution of alkali-activated MBA paste, alkali-activated FA paste, and alkali-activated BFS paste. The Na concentration in the pore solution of alkali-activated MBA paste was forecast to be slightly higher than that of alkali-activated BFS paste. The pore solution of alkali-activated FA paste was predicted to have the lowest Na concentration. The concentration of Na in the pore solution AAM would increase due to the release of Na after the dissolution of precursors. The Na<sub>2</sub>O content in the amorphous phase of MBA (3.8 wt.%) is much higher than that in FA and BFS. The Na dissolved from MBA could be much more than FA and BFS, dramatically increasing the Na concentration in the pore solution.

It is worth noting that the Na<sub>2</sub>O content in the amorphous phase of FA (0.9 wt.%) is much higher than that in BFS (0.2 wt.%). However, the Na concentration in the pore solution of alkali-activated FA paste is lower than that of alkali-activated BFS paste. One possible explanation for the lower Na concentration in the pore solution of alkali-activated FA paste can be that more Na was incorporated in the Na-bearing reaction products. The Na concentration would decrease when the Na in the pore solution was consumed in the reaction product formation. As predicted by the thermodynamic modeling, the N-(C)-A-S-H gel formed after the alkali activation of FA was more than that obtained from the reaction of MBA and BFS (Figure 4.12).

In the pore solution of alkali-activated MBA paste, the concentration of Si was forecast to become higher with the increase of Na<sub>2</sub>O content in the activator. When the Na<sub>2</sub>O content exceeds 4 wt.%, the concentration of Si in the pore solution of alkali-activated MBA paste is the highest among these three AAM systems. The increase in the concentration of Si in the pore solution of alkali-activated MBA paste could be attributed to the reduction in N-(C)-A-S-

H gel formation. The Si/Al ratio of the N-(C)-A-S-H gel could reach as high as four. However, at the  $\text{Na}_2\text{O}$  content above 5 wt.%, the N-(C)-A-S-H gel mass was predicted to decrease while more natrolite was formed (Figure 4.12). The Si/Al molar ratio of natrolite is around 1.5, less than half of that in the amorphous phase of MBA (3.67). In this case, only part of the Si released by the amorphous phase of MBA could be incorporated into the reaction products. The remaining Si could not form stable reaction products with Na. Introducing Ca- or Al-enriched resources into MBA-based AAM is recommended. In this case, the excessive Si and Na in the pore solution can be consumed, forming stable N-(C)-A-S-H gel or C-(N)-A-S-H gel.

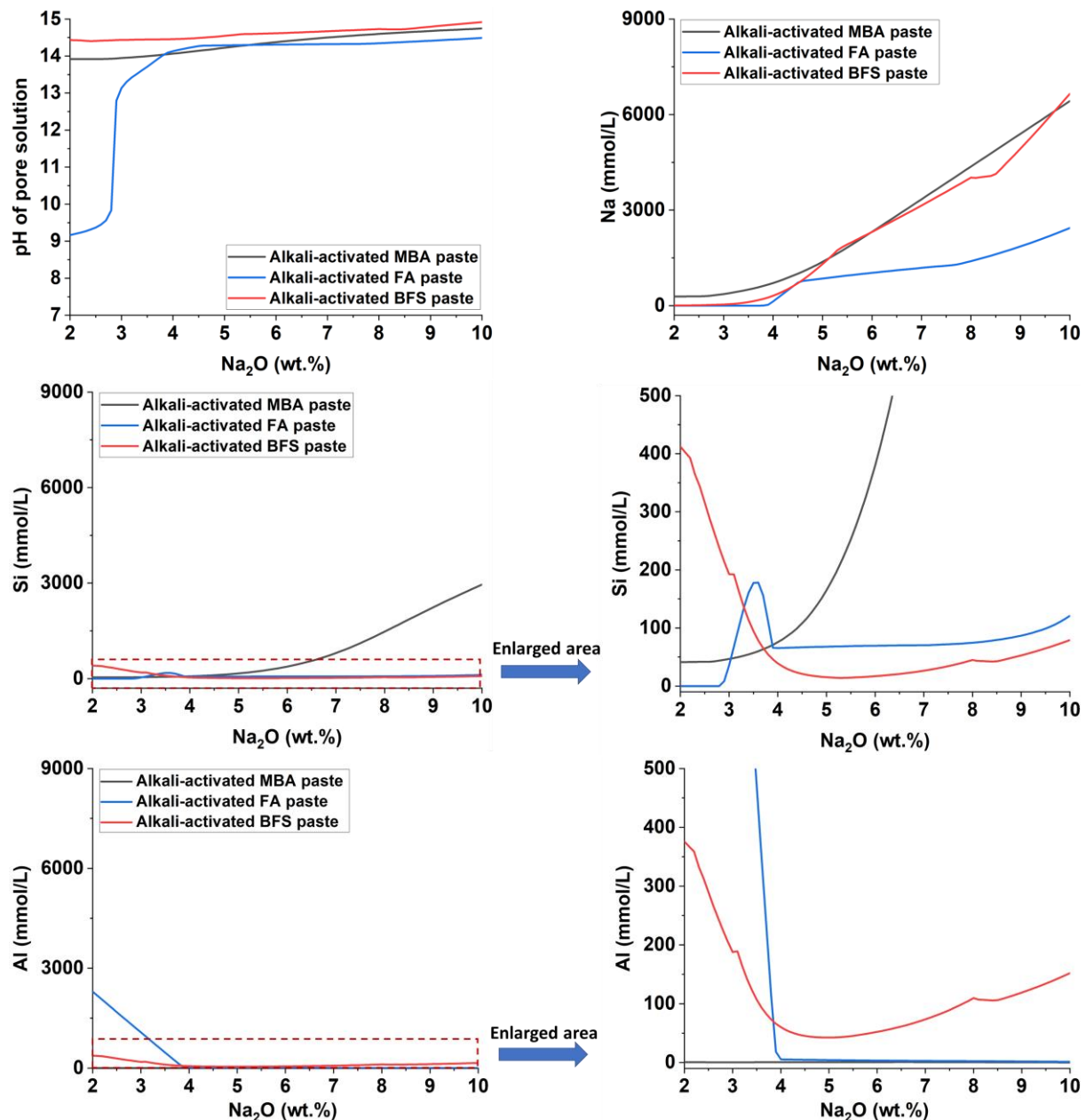


Figure 4.13 Simulated pH of the pore solution and simulated concentration of Na, Si, Al, Mg, Ca, and Fe in the pore solution. The data is presented as a function of the  $\text{Na}_2\text{O}$  content in the activator. The percentage of  $\text{Na}_2\text{O}$  is with respect to the mass of the precursor.

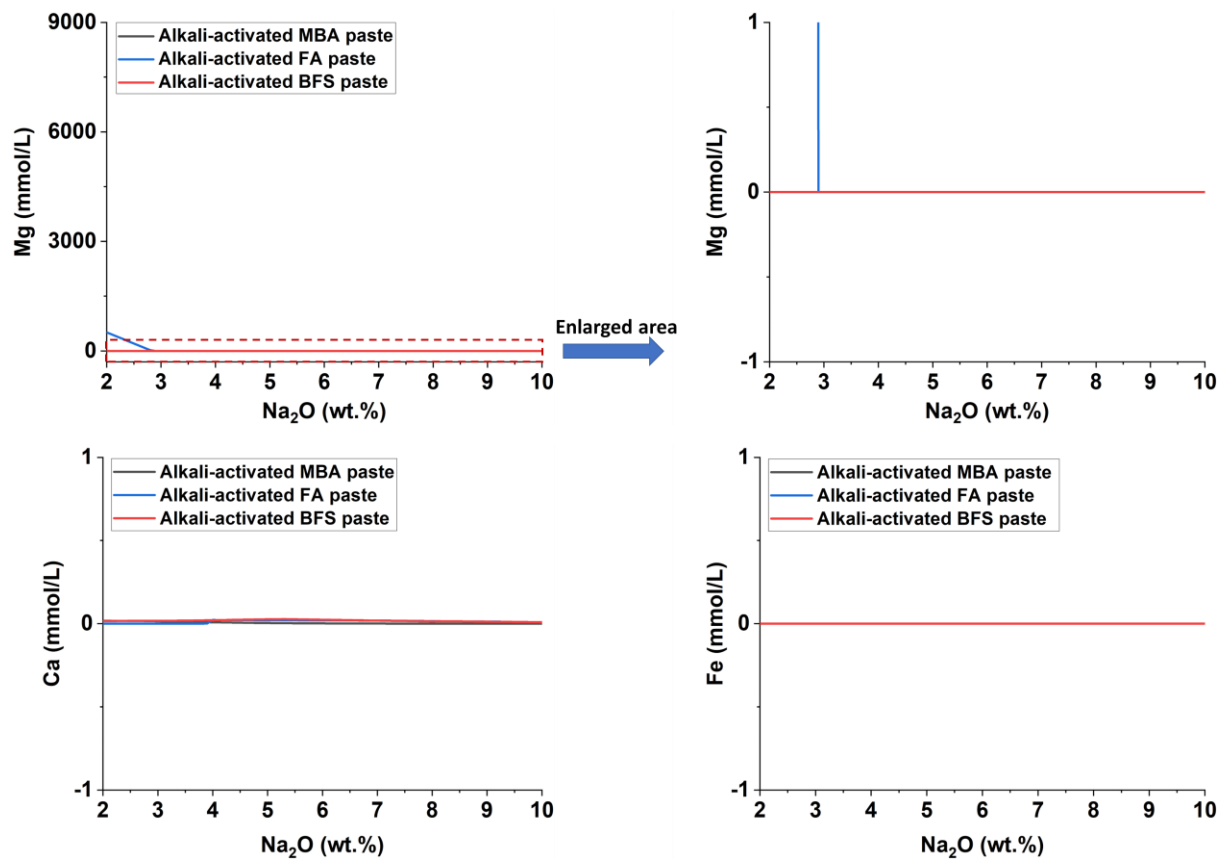


Figure 4.13 (Continued) simulated pH of the pore solution and simulated concentration of Na, Si, Al, Mg, Ca, and Fe in the pore solution. The data is presented as a function of the  $\text{Na}_2\text{O}$  content in the activator. The percentage of  $\text{Na}_2\text{O}$  is with respect to the mass of the precursor.

#### 4.3.5 Leaching potential of MBA

Possible leaching of contaminants from MBA should be checked prior to its application as SCM and AAM. This information is required to guide the mix design and prevent environmental contamination caused by using MBA in construction materials. Figure 4.14 provides information about the mass of heavy metals, chloride, bromide, and sulfate leached from 1 kg MBA. Among all the tested constituents, only the leaching of sulfate and antimony (Sb) is above the threshold values specified in the Dutch Soil Quality Decree 2015 [212]. The amount of sulfate and Sb leached from MBA is almost twice the threshold value. The leaching of bromide, fluoride, and most heavy metals is below the allowable level. The amount of Cl released by 1 kg MBA is 610 mg, just below the upper limit set by the Dutch government (616 mg/kg). The Cl detected in the leachate can be traced back to the soluble salt in MBA, as halite ( $\text{NaCl}$ ) was detected in the XRD analysis of MBA.

##### *Leaching of sulfate*

Sulfate is usually leached from the mineral phases in MSWI bottom ash, such as ettringite and gypsum [68]. However, ettringite and gypsum were not found in the XRD analysis of MBA. The  $\text{SO}_3$  content in MBA was lower than FA, BFS, and Portland cement clinker. Given that the  $\text{SO}_3$  content determined by XRF analysis is very low (0.7 wt.%), the contents of sulfate-containing mineral phases may be too small to be detected. It is worth mentioning that the leaching of

sulfate may not be an issue when MBA is used as SCM. The sulfate released by MSWI bottom ash can be immobilized by forming ettringite (AFt) and monosulfate (AFm) [53].

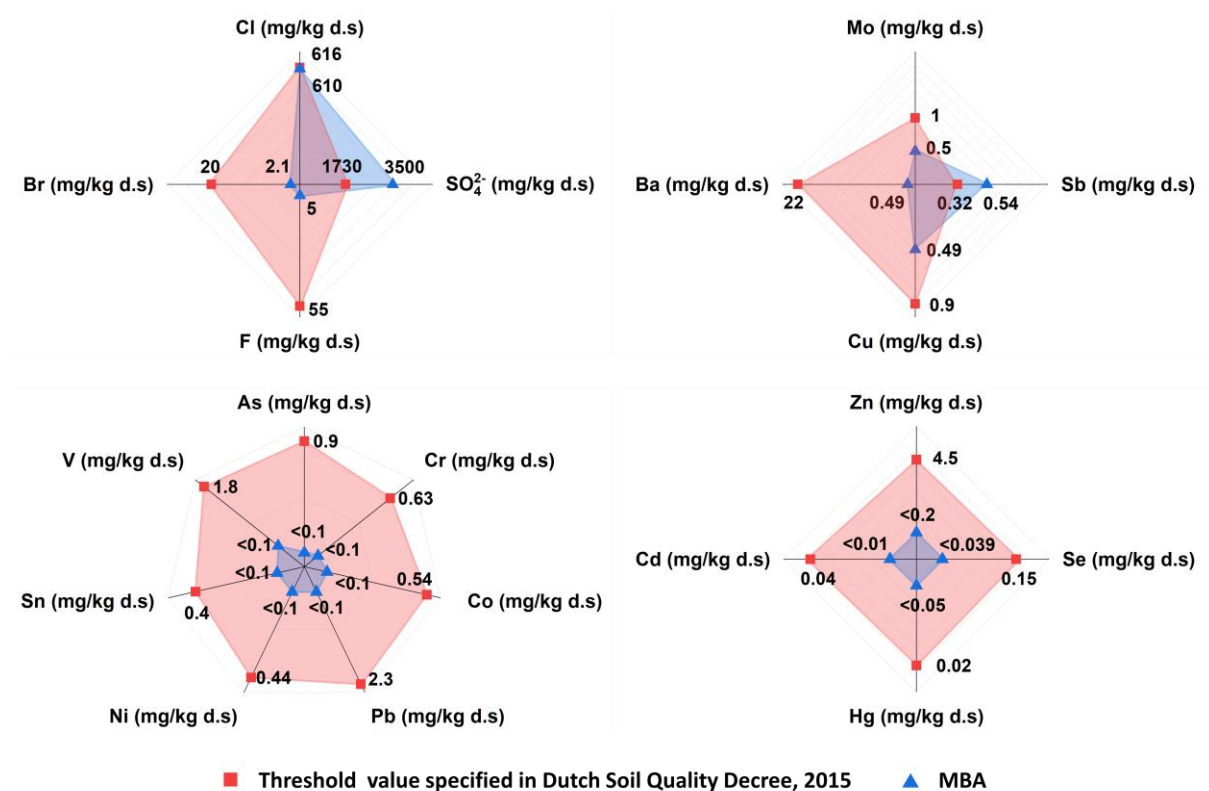


Figure 4.14 The quantities of soluble constituents leached from MBA and the threshold values specified in Dutch Soil Quality Decree, 2015 [212]. The unit is in mg/kg of dry matter (d.s).

### Leaching of antimony

The excessive leaching of Sb can be attributed to the organic acids (such as humic and fulvic acids) in MBA and the alkalinity of MBA. The organic acids would form mobile organo-metallic complexes with Sb, promoting the leaching of Sb from MBA [296–300]. Tang et al. [53] found that the leaching of Sb is associated with the organics in MSWI bottom ash. The leaching of Sb reduced after removing the decarboxylation of organic acids from MSWI bottom ash via heat treatment at 400 °C [301]. The end pH of the leachate obtained after the leaching test of MBA is 9.7. Verbinen et al. [301] performed the leaching test at a liquid-to-solid ratio of 10 L/kg, the same as that used in this research. The leaching of Sb from MSWI bottom ash was highest at the pH between 8 and 10.

Using MBA as SCM would dramatically reduce the leaching of Sb. In cement system, the pore solution is supersaturated with Ca(OH)<sub>2</sub>. The pH value of the pore solution lies in the range of 12.4–13.5 [302]. Verbinen et al. [301] found that the leaching of Sb from MSWI bottom ash reached the lowest value at the pH between 12–14, which was around one-quarter of the amount of Sb leached at pH of 9. Accordingly, the leaching of Sb under the alkalinity of cement pore solution would be much lower than that at the pH of 9.7. Besides, the Ca<sup>2+</sup> dissolved by Portland cement clinker could react with Sb released from MBA to form calcium antimonate precipitates [303], which could inhibit the leaching of Sb. The hydration products, such as C-

S-H gel and ettringite, could also incorporate the heavy metals released by MSWI bottom ash via physical and chemical adsorption [27,304].

The excessive leaching of Sb would not be an issue when using 100% MBA to prepare AAM. According to the thermodynamic simulation results illustrated in Figure 4.13 (a), the pore solution of alkali-activated MBA paste would have a pH of around 13.8 to 14.74. At this alkalinity, the leaching of Sb from MSWI bottom ash would be very small [301]. The zeolite minerals (including natrolite and Ca-chabazite) predicted to form in alkali-activated MBA paste could function as adsorbents to immobilize heavy metals [305]. The N-(C-)A-S-H gel and C-(N-)A-S-H gel, the predicted reaction products in alkali-activated MBA paste, also have the potential to encapsulate the heavy metals [306,307].

It is recommended to add BFS to MBA-based AAM systems in order to reduce the leaching of contaminants. Blending MBA with BFS can reduce the proportion of MBA in the AAM, decreasing the total amount of heavy metals in the system. Adding BFS also increases the amount of reactive Ca in the MBA-based AAM system, which in turn raises the pH of the pore solution [197] and promotes the formation of calcium antimonate precipitates [303]. In this way, the Sb released from MBA would be immobilized. Since BFS is much more reactive than MBA, the reaction products formed in AAM prepared with blends of BFS and MBA would be more than that in AAM prepared with MBA. The gel phases formed in AAM would contribute to the encapsulation of heavy metals.

#### 4.3.6 Remarks on using MBA as SCM and AAM precursor

Based on the above analysis of the composition, reactivity, and leaching potential of MBA, the following remarks are made about how to use MBA for the preparation of blended cement pastes and alkali-activated pastes. These comments will serve as guidance for the utilization of MBA as SCM in Chapter 5 and the utilization of MBA as AAM precursor in Chapter 6.

##### *Quality upgrade treatments of MBA*

It is not recommended to increase the reactivity of MBA by increasing its amorphous phase because the amorphous phase already accounts for 70 wt.% in MBA, which is close to the amorphous content in FA. The amorphous phase of MBA is rich in  $\text{SiO}_2$  but deficient in  $\text{CaO}$  and  $\text{Al}_2\text{O}_3$ . Increasing the contents of reactive  $\text{CaO}$  and  $\text{Al}_2\text{O}_3$  in MBA is more beneficial to the reactivity enhancement of MBA.

It is possible to use MBA as SCM and AAM precursor even without removing heavy metals and soluble salts. The leaching of contaminants from the construction materials prepared with MBA can be minimized by limiting the addition of MBA to a low level. The reaction products formed in MBA blended cement pastes or MBA-based AAM can immobilize sulfate and Sb released by MBA.

It is important to reduce the metallic Al content in MBA and determine a threshold value before using MBA as SCM and AAM precursor. The metallic Al in MBA will pose risks of volume expansion and strength reduction to pastes prepared with MBA.

### *Mix design of using MBA in blended cement pastes and AAM*

When preparing blended cement pastes and alkali-activated pastes with MBA, previous experience with Class F coal fly ash-based pastes can be used as a reference because the reactivity of MBA is similar to that of FA. However, it is challenging to obtain equivalent compressive strength when the same mix design is used for MBA and FA. The presence of metallic Al in MBA can lead to a strength decrease of MBA-based pastes.

The content of alkalis and Cl in MBA exceeds the acceptable upper limits in Portland cement clinker. A threshold value for the dosage of MBA in the binder of steel-reinforced concretes should be specified to prevent the risk of steel corrosion. When using MBA in the binder of concretes, the total amount of alkalis in the system should be controlled to avoid the alkali-silica reaction caused by excessive addition of MBA.

According to the dissolution test results of MBA, the molar ratio of dissolved Si/Al is much lower than the optimal value (1.9), indicating that alkali-activated MBA may have low early-age strength. For the mix design of MBA-based AAM, it is recommended to add an appropriate amount of water glass or more reactive Si-enriched precursors to the MBA-based AAM system to increase the early-age strength.

The results of thermodynamic modeling indicate that when the  $\text{Na}_2\text{O}$  content in the activator is higher than 5 wt.%, some of the Si released by MBA cannot form stable reaction products with the Na provided by the activator. This information needs to be considered when designing the mix of MBA-based AAM. The  $\text{Na}_2\text{O}$  content in the activator may not exceed 5 wt.% to ensure that all the Si released by MBA is incorporated into the reaction products. If the  $\text{Na}_2\text{O}$  content in the activator is set to be higher than 5 wt.%, it is recommended to add Ca- or Al-enriched precursors, such as blast furnace slag, to MBA-based AAM. Adding Ca- or Al-enriched precursors can promote gel formation by consuming Si dissolved from MBA, resulting in a strength increase of MBA-based AAM. The  $\text{Ca}^{2+}$  dissolved from Ca-enriched precursors could also facilitate the immobilization of Sb by forming calcium antimonate precipitates.



## 4.4 Conclusions

In this chapter, the reactivity and leaching potential of *mechanically treated MSWI bottom ash (MBA)* as supplementary cementitious material (SCM) and precursor for alkali-activated materials (AAM) were studied. Based on the experimental results and analysis, recommendations about how to use MBA in blended cement pastes and AAM were provided. The findings of this study are summarized as follows:

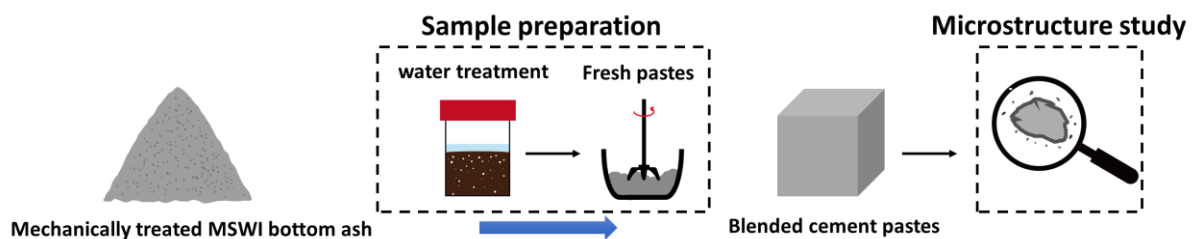
- The amorphous content in MBA is slightly lower than Class F coal fly ash (FA), but much lower than blast furnace slag (BFS). The amorphous phase of MBA has a chemical composition falling within the same range as that of Class F coal fly ash. Calculating the relative contents of  $\text{SiO}_2$ ,  $\text{CaO}$ , and  $\text{Al}_2\text{O}_3$  in the amorphous phase can be used as a simplified method to select the AAM precursors that may have high reactivity.
- When using the rapid, relevant, and reliable ( $R^3$ ) methods to measure the pozzolanic reactivity of MBA, the effect of metallic Al on the test results needs to be considered. The reactivity of MBA as AAM precursor can be measured by dissolution tests. The dissolution test results provide information about the early-age reaction of MBA. According to the dissolution test of MBA, the molar ratio of dissolved Si/Al is much lower than the optimal value (1.9), indicating that alkali-activated MBA may have low early-age strength. It is recommended to add soluble Si or more reactive Si-enriched precursors into MBA-based AAM to increase the early-age strength.
- Thermodynamic modeling is a promising method to guide the mix design of MBA-based AAM. The chemical and mineralogical compositions of MBA are within the same ranges as the compositions of MSWI bottom ash used by previous researchers. The phase assemblages of alkali-activated MBA paste predicted by thermodynamic modeling are in good agreement with the experimental results reported in the literature. The modeling results for the composition and the pH of the pore solution in alkali-activated MBA provide indications about the reaction of MBA. The predicted pH value can be used to analyze the risk of contaminants leaching from the MBA-based AAM.
- As SCM and AAM precursor, the reactivity of MBA is close to FA but much lower than BFS. When MBA is used to prepare blended cement pastes and alkali-activated pastes, the mix design can refer to previous experience with the pastes prepared with Class F coal fly ash. However, it is necessary to determine the threshold value for the metallic Al content in MBA. The dosage of MBA in blended cement pastes and alkali-activated pastes should not exceed 50 wt.% to avoid the excessive leaching of contaminants (especially antimony and sulfates) into the environment.



# Chapter 5

## Blended cement pastes prepared with mechanically treated MSWI bottom ash as supplementary cementitious material

*water treatment, microstructure formation, and strength development*



### Highlights

- For the application of supplementary cementitious material, the metallic Al content in *mechanically treated MSWI bottom ash (MBA)* needs to be further reduced to prevent the cracking of blended cement pastes caused by hydrogen gas generation.
- Most of the metallic Al in MBA can be oxidized at room temperature by allowing MBA to react with water in advance during the sample preparation process.
- After water treatment of MBA, the compressive strength of MBA blended Portland cement pastes increased dramatically and was close to that of Portland cement pastes blended with Class F coal fly ash.
- Blending Portland cement with *water-treated MBA (WMBA)* enhanced the hydration of clinker at later ages. The reaction products of WMBA contributed to the strength development of blended cement pastes.

## 5.1 Introduction

This chapter focuses on the utilization of *mechanically treated MSWI bottom ash (MBA)* as supplementary cementitious material (SCM) to prepare blended cement pastes. Given that the pozzolanic reactivity of MBA is similar to that of Class F coal fly ash (FA) (see Chapter 4), one of the research goals is to use MBA as a substitute for FA in blended cement and achieve similar compressive strength by optimizing the sample preparation process. The other goal is to understand the contribution of MBA to compressive strength by studying the effects of MBA on the reaction products and microstructure of blended cement pastes.

Unlike Class F coal fly ash, MBA contains metallic Al. As reported in Chapter 3, mechanical treatments cannot completely remove the metallic Al in as-received MSWI bottom ash. The remaining metallic Al in MBA will oxidize upon its contact with the alkaline pore solution of blended cement pastes. The hydrogen gas released after the oxidation of metallic Al can significantly reduce the compressive strength of Portland cement pastes blended with MBA. Before substituting Portland cement (PC) with MBA, it is necessary to reduce the metallic Al content in MBA.

Apart from mechanical treatments, water treatment was also employed to oxidize the metallic Al embedded in MSWI bottom ash, especially when it was used as SCM (see Chapter 2). The oxidation rate of metallic Al in water depends on the particle size of MSWI bottom ash, the pH in the mixture of MSWI bottom ash and water, the temperature of the environment, and the duration of treatment [30,56]. There is a significant difference in the time required to complete the oxidation of metallic Al in water. With water treatment, the decrease in the metallic Al content of MSWI bottom ash is slow at room temperature [30]. The reaction of metallic Al can be accelerated by increasing the temperature from room temperature to 105 °C [56] or by reducing the particle size of MSWI bottom ash to 3 µm [30]. However, these two approaches are both energy-consuming. Previous studies mainly focused on the effectiveness and efficiency of water treatment on metallic Al content reduction. Little attention has been devoted to investigating the composition changes induced by the water treatment of MSWI bottom ash.

When using MSWI bottom ash as SCM, compressive strength is the primary index used in the selection of mix design. However, other properties, such as volume stability and durability, are strongly influenced by the microstructure of hardened pastes [308]. Previous researchers mainly studied the effects of MSWI bottom ash addition on cement hydration via calorimetry (see Chapter 2). The contribution of MSWI bottom ash to the microstructure development of hardened pastes was rarely reported. Investigating the reaction process and the reaction products of MSWI bottom ash in blended cement pastes can provide a theoretical basis for the wide application of MSWI bottom ash as SCM.

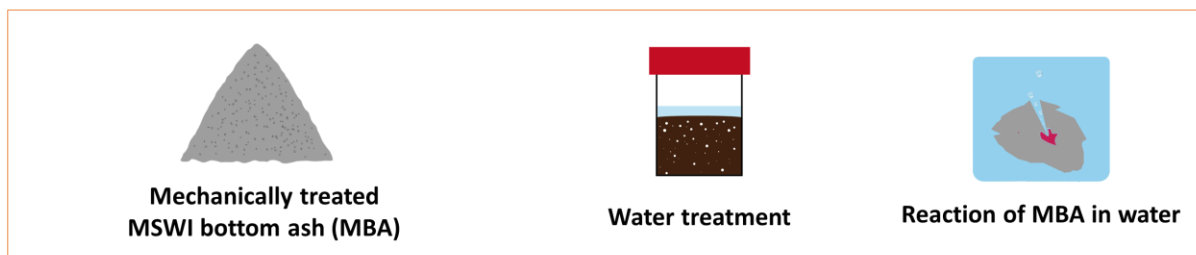
This chapter consists of three parts (Figure 5.1):

- In part 1, MBA is treated with water at room temperature to reduce its metallic Al content. The limitations of water treatment on the reduction of metallic Al content in MBA are explored. The reaction of MBA during water treatment is also studied.
- In part 2, Portland cement pastes blended with *water-treated MBA (WMBA)* are prepared, and their compressive strength is compared with that of Portland cement pastes blended

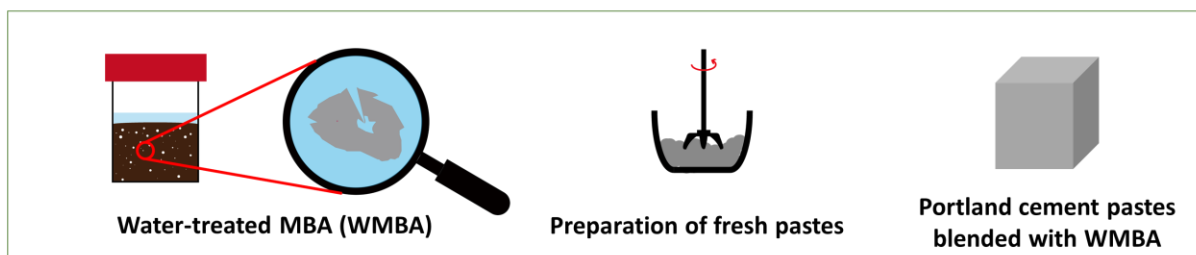
with FA. The effectiveness of water treatment in eliminating expansive cracks in blended cement paste prepared with MBA is examined.

- In part 3, Portland cement pastes blended the highest amount WMBA are characterized to study the reaction of WMBA in blended cement pastes. The Portland cement pastes blended with WMBA are compared with plain cement paste and Portland cement pastes blended with micronized sand to clarify the effects of WMBA on cement hydration, reaction product formation, and strength development.

### Part 1 Water treatment of mechanically treated MSWI bottom ash



### Part 2 Preparation of Portland cement pastes blended with WMBA



### Part 3 Microstructure study of Portland cement pastes blended with WMBA



Figure 5.1 The content of this chapter.

## 5.2 Materials and methods

### 5.2.1 Materials

The materials used in this chapter include PC (CEM I 52.2R), MBA, FA, and micronized sand (M300). Table 5.1 and Table 5.2 provide information about the chemical and mineralogical compositions of PC. This information was acquired via the X-ray fluorescence (XRF) and quantitative X-ray diffraction (QXRD) analysis described in Chapter 3. The density of PC and

M300 is 3.2 g/cm<sup>3</sup> and 2.7 g/cm<sup>3</sup>, respectively. The detailed composition information of MBA and FA can be found in Chapter 4. The micronized sand, a chemically inert quartz powder provided by SIKRON®, was used as a reference for MBA. As shown in Figure 5.2, the D<sub>50</sub> of M300 is 17 µm, almost the same as that of PC. Compared with MBA and FA, the particle size of M300 is smaller. However, it is difficult to find commercially available micronized sand with the same particle size as MBA. M300 is the one that has particle size distribution most similar to MBA.

Table 5.1 Chemical composition of PC (CEM I 52.5 R) determined by XRF analysis.

Compound	SiO <sub>2</sub>	CaO	Al <sub>2</sub> O <sub>3</sub>	Fe <sub>2</sub> O <sub>3</sub>	Na <sub>2</sub> O	K <sub>2</sub> O	SO <sub>3</sub>	Cl	MgO	Others	LOI <sub>550</sub>	Sum
wt. %	20.58	63.74	4.74	2.47	0.36	0.71	3.07	0.10	2.76	1.32	0.16	100

Table 5.2 Mineralogical composition of PC (CEM I 52.5 R) determined by QXRD analysis.

Phases	wt. %	Formulae	ICSD codes
Alite (C <sub>3</sub> S)	66.1	Ca <sub>3</sub> SiO <sub>5</sub>	94742
Belite (C <sub>2</sub> S)	15.5	Ca <sub>2</sub> SiO <sub>4</sub>	963
C <sub>3</sub> A <sub>cubic</sub>	2.1	Ca <sub>9</sub> (Al <sub>2</sub> O <sub>6</sub> ) <sub>3</sub>	1841
C <sub>3</sub> A <sub>orthorombic</sub>	2.9	Al <sub>5.176</sub> Ca <sub>8.393</sub> Fe <sub>0.46</sub> Na <sub>0.875</sub> O <sub>18</sub> Si <sub>0.375</sub>	100220
C <sub>4</sub> AF	6.9	Ca <sub>2</sub> FeAlO <sub>5</sub>	51265
Calcite	0.8	CaCO <sub>3</sub>	80869
Mayenite	1.3	Ca <sub>12</sub> Al <sub>14</sub> O <sub>33</sub>	6287
Bassanite	0.6	Ca(SO <sub>4</sub> )(H <sub>2</sub> O) <sub>0.5</sub>	380286
Anhydrite	1.2	CaSO <sub>4</sub>	16382
Quartz	0.4	SiO <sub>2</sub>	174
Arcanite	1.4	K <sub>2</sub> SO <sub>4</sub>	79777
Amorphous phase	1.0	-	-
Sum	100	-	-

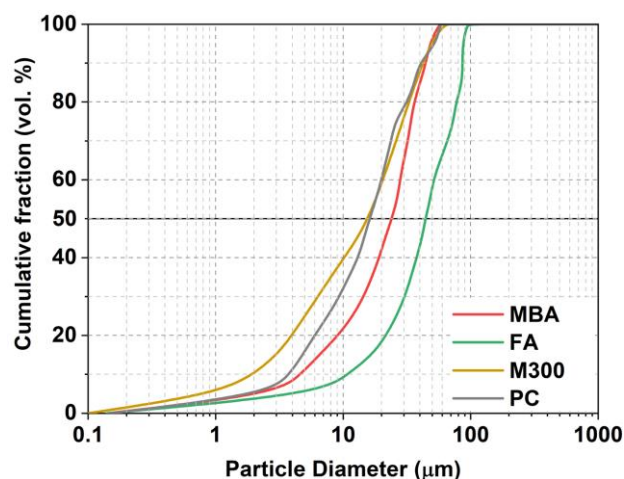


Figure 5.2 Particle size distribution of MBA, FA, M300, and PC, determined by laser diffraction method.

### 5.2.2 Mix design

According to the remarks of Chapter 4, the mix design of Portland cement blended with MBA can refer to the experience with Portland cement blended with Class F coal fly ash. Since the percentage of coal fly ash added as SCM in concretes usually ranges from 15 wt.% to 35 wt.% [309], the percentages of PC replaced by MBA in blended cement were chosen to be the same. The heavy metal contents in blended cement system will increase with the addition of MBA. The low percentage of MBA in blended cement also prevents the leaching of contaminants into the environment. Table 5.3 provides detailed information about the mix design used in this work. The water-to-binder ratio is the same for all mixtures (0.4). The binder includes PC and supplementary cementitious materials (SCMs).

In total, five series of paste samples were prepared. Table 5.3 provides details about the mix design of these paste samples. 100 CEM, FA CEM, and M300 CEM are reference paste samples. 100 CEM was made by mixing PC with water. FA CEM and M300 CEM are pastes of Portland cement blended with FA and M300, respectively. MBA CEM and WMBA CEM are blended cement pastes made from the same raw materials (Portland cement and MBA) but following different sample preparation procedures. The percentages of FA, M300, and MBA added in blended cement are 15 %, 25 %, and 35 % by weight.

Table 5.3 Mix design of the paste samples.

Paste samples	Raw materials (wt.%)				Water-to- PC ratio	Water-to- binder ratio
	FA	MBA	M300	PC		
100 CEM	-	-	-	100	0.4	
15 FA CEM	15	-	-			
15 MBA CEM	-	15	-	85	0.47	
15 WMBA CEM*	-	15	-			
25 FA CEM	25	-	-			
25 MBA CEM	-	25	-	75	0.53	0.4
25 WMBA CEM*	-	25	-			
25 M300 CEM	-	-	25			
35 FA CEM	35	-	-			
35 MBA CEM	-	35	-	65	0.62	
35 WMBA CEM*	-	35	-			

\*The water treatment of MBA was included in the sample preparation process.

### 5.2.3 Samples preparation

Figure 5.3 (a) demonstrates the sample preparation procedure of WMBA CEM. The water used to prepare WMBA CEM was divided into two portions. One portion was used to treat MBA prior to the addition of PC. The remaining water was added when mixing the fresh pastes. The aim of water treatment is to oxidize the metallic Al embedded in MBA. The deionized water was mixed with MBA at a mass ratio of 0.4. The mixture obtained was named “slurry” in this context. As shown in Figure 5.4, the slurry was sealed in a polyethylene container at

room temperature (between 22 to 25 °C). The solids in the slurry are called *water-treated MBA (WMBA)*.

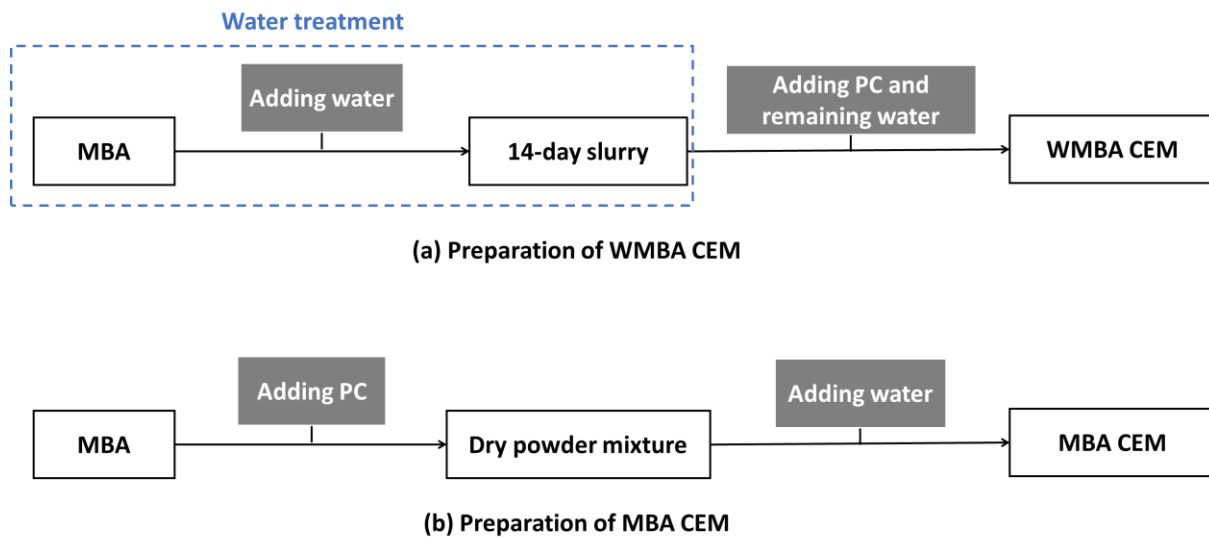


Figure 5.3 Illustration of the sample preparation process of (a) WMBA CEM and (b) MBA CEM.

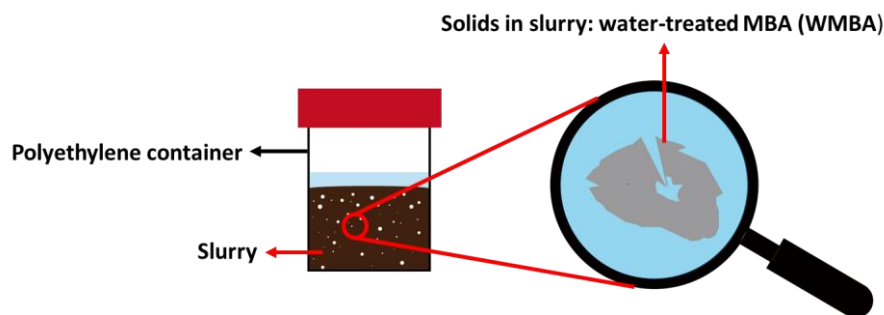


Figure 5.4 illustration of water treatment of MBA.

The water treatment lasted until the metallic Al content in WMBA reached the lowest achievable value. The metallic Al content in WMBA at different time intervals of water treatment was monitored by measuring the metallic Al content in the slurry with the water displacement method described in Chapter 3. Considering the low metallic Al content in the slurry, around 140 g of the slurry was used for each measurement. The hydrogen gas collected during the measurement of 140 g slurry equals the hydrogen gas released by the metallic Al present in 100 g WMBA. With the volume of released hydrogen gas, the metallic Al content in WMBA can be calculated by following Eq. 3.2. In the end, the water treatment lasted for 14 days. The obtained slurry, also named 14-day slurry, was mixed with PC and the remaining water to make WMBA CEM.

The raw materials used to prepare MBA CEM are the same as that of WMBA CEM. However, the sample preparation procedure of MBA CEM differs from that of WMBA CEM. As illustrated in Figure 5.3 (b), for the preparation of MBA CEM, the MBA was first blended with PC. Afterward, the dry powder blends were directly mixed with water to prepare MBA CEM. FA

CEM and M300 CEM were prepared following the same procedure as MBA CEM. 100 CEM was prepared by directly mixing PC with water.

All the fresh pastes were mixed for 4 minutes with a high-shear mixer (model IKA® T 50 ULTRA-TURRAX®) and then cast in the mold with the dimension of  $20 \times 20 \times 20 \text{ mm}^3$ . The paste specimens were first cured at room temperature for 24 hours. After demolding, the specimens were sealed with cling film and cured in a fog room ( $20^\circ\text{C}$ , 99 % RH) until the test ages.

#### 5.2.4 Studies of reaction between MBA and water

The dissolution of MBA during water treatment was studied by measuring the pH and elemental concentration of the liquid in the slurry at time intervals of 1 day, 7 days, and 14 days. The slurry tested at each time interval was prepared by mixing 500 g of MBA with 200 g of water. The liquid in the slurry was filtered through Whatman™ 42 filter paper with a pore size of  $1.1 \mu\text{m}$ . The pH of filtered liquid was measured with a pH meter from Metrohm (model 827). The pH meter was calibrated with buffer solution with pH of 7 and 10.01 produced by HACH®. The filtered solutions were diluted with nitric acid (0.2 vol.%) or sodium hydroxide solution (0.1 mol/L). It is worth mentioning that the sodium hydroxide solution was only used for dilution when measuring the concentration of sulfur in the filtered solution. The diluted solutions were analyzed through inductively coupled plasma-optical emission spectroscopy (ICP-OES), model PerkinElmer Optima 5300DV.

The reaction of MBA in the process of water treatment was also investigated by measuring the reaction heat with a TAM-AIR-314 isothermal conduction calorimeter. Around 10 g of slurry, after being poured and sealed in a glass ampoule, was loaded in the calorimeter. The temperature of the calorimeter was controlled at  $20^\circ\text{C}$ .

After water treatment, the 14-day slurry was dried in a vacuum freeze-dryer ( $-24^\circ\text{C}$  and 0.1 Pa) for more than three months to remove the water in WMBA. After drying, the mineralogical composition of WMBA was measured with X-ray diffraction (XRD). The QXRD analysis was performed to quantify the contents of the phases present in WMBA. The molecular structure of WMBA was studied by identifying its chemical bonds with Attenuated Total Reflectance-Fourier Transform Infrared (ATR-FTIR) spectroscopy (model Perkin Elmer Spectrum 100). The measurement covers the wavenumber from  $600$  to  $4000 \text{ cm}^{-1}$ , and the resolution is  $1 \text{ cm}^{-1}$ .

#### 5.2.5 Paste sample characterization

##### *Compressive strength measurements*

The compressive strength of cubic paste samples ( $20 \times 20 \times 20 \text{ mm}^3$ ) was measured for 100 CEM, FA CEM, MBA CEM, WMBA CEM, and M300 CEM, at the curing ages of 1 day, 7 days, 28 days, and 90 days. The test procedure was the same as that described in NEN-EN 196-1:2016 [100]. The compressive strength was determined by calculating the arithmetic mean of 12 repeated test results.



### *X-ray computed tomography (CT) scan*

The X-ray computed tomography scan is a non-destructive testing technique that can be used to examine whether the metallic Al in MBA and WMBA causes cracking inside MBA CEM and WMBA CEM. The corrosion of metallic Al is very fast at the pH of cement pore solution [30]. The hydrogen gas released by the reaction of metallic Al in Portland cement pastes blended with MSWI bottom ash could cause volume expansion before setting [30] or even cracking upon hardening [53]. Given that the damage induced by the corrosion of metallic Al usually occurred within the first day, the 1-day cubic samples prepared for the strength measurement were scanned using a Phoenix Nanotom Micro-CT scanner. During scanning, the samples were sealed with plastic film to prevent drying. The X-ray source tube worked at 120 kV and 130  $\mu\text{A}$ , and the voxel resolution was 15  $\mu\text{m}^3$ .

The image analysis process of the projections obtained after CT scan is shown in Figure 5.5. The 3D reconstruction of acquired projections was carried out with the software Phoenix Datos|x Reconstruction 2.0 to obtain greyscale value images. ImageJ, an image processing program, was used to process the greyscale value images. The pores and cracks were segmented using the triangle thresholding algorithm proposed by Zack et al.[310]. After the thresholding operation, the 2D binary images were created from the greyscale value images. The 2D binary image stacks were visualized with the ImageJ 3D viewer [311]. The region of interest was the cube of edge 12 mm located in the center of the specimen. A 3D image of the binary image stacks for this cube was used to illustrate the spatial distribution of the pores and cracks in MBA CEM and WMBA CEM.

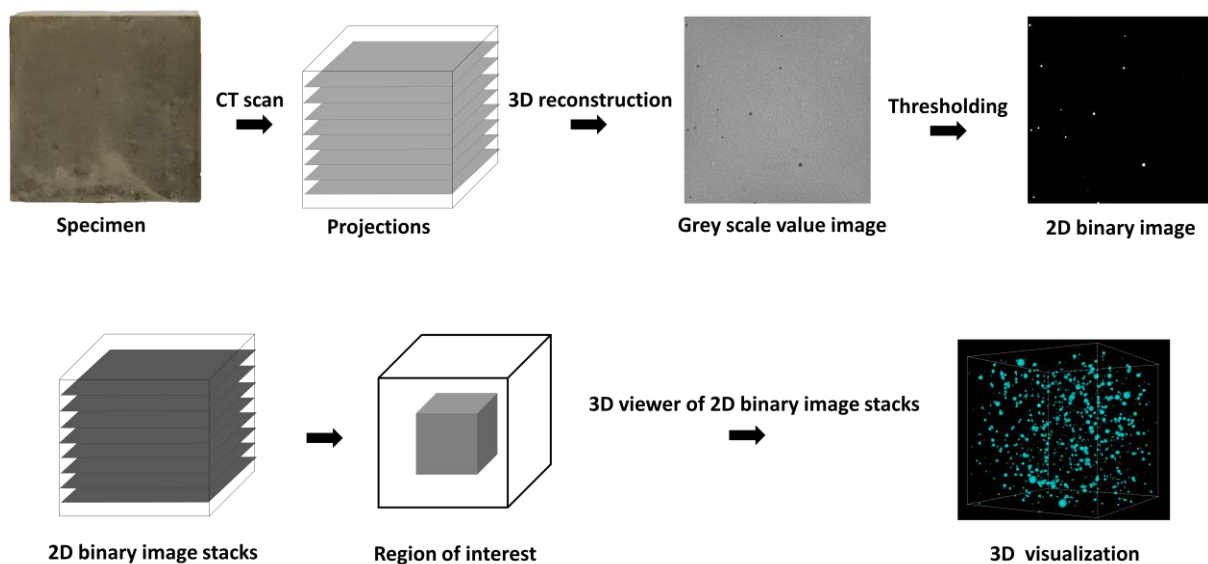


Figure 5.5 The image analysis process of the projections obtained after the CT scan of 1-day paste sample with water-to-binder ratio of 0.4.

### *Pore solution analysis*

Comparing the ion concentrations in the pore solution derived from 1-day paste samples of WMBA CEM and M300 CEM can provide insight into the reaction of WMBA in blended cement within the first day of reaction. The samples used for pore solution extraction were prepared in the same way as those used for strength measurement. The only difference is the size of the mold. The pastes were cast and sealed in polyethylene bottles with a diameter of 35 mm and a height of 70 mm. The pore solution of 1-day hardened pastes was extracted by the steel die method [312] using pressure up to 300 MPa. The extracted solution was immediately filtered through Whatman™ 42 filter paper. The pH and the elemental concentration of filtrated solution were determined by pH meter and ICP-OES spectrometer, respectively, in the same way as for the analysis of the liquid part of the slurry (section 5.2.4). The elements under consideration are Ca, Na, K, Mg, Si, Al, Zn, Fe, and S.

### *Isothermal calorimetry*

Isothermal calorimetry was used to study the hydration kinetics. The heat flow of the hydration during the first eight days was measured by TAM-AIR-314 isothermal conduction calorimeter. The fresh pastes were prepared the same way as that used for the strength measurements. The tests were performed at 20 °C following the ASTM C1697 [313].

### *Hydration stoppage*

The hydration process was stopped using the solvent exchange method. The fresh pastes were cast and sealed in polyethylene bottles (d=35 mm, h=70 mm). The curing condition was the same for the samples prepared for strength measurement. After curing for 1 day, 7 days, 28 days, and 90 days, the hardened pastes were demolded and cut into slices with a diameter of 35 mm and a thickness of 2 mm. These slices were immersed in isopropanol for 7 days, during which the isopropanol was refreshed after 24 hours. After 7 days of immersion, the slices were dried and stored in a low-humidity, low-vacuum desiccator.

The dried slices were directly used to prepare test samples for scanning electron microscopy (SEM) and nitrogen adsorption tests. The dried slices were manually ground into powder using mortar and pestle to prepare the samples for XRD analysis and thermogravimetric analysis (TGA). Before grinding, the layer on the surface of dried slices was removed by dry polishing with sandpaper. The polishing and grinding were performed in a glove box under N<sub>2</sub> atmosphere to prevent carbonation.

### *X-ray diffraction analysis*

The XRD analysis was used to identify the newly formed crystalline products. The changes in the contents of the crystalline and amorphous phases in hardened pastes with curing ages were determined by the QXRD analysis. Silicon powder was used as internal standard to mix with test powder samples. The experiments and the analysis of obtained XRD spectra were performed in the same way as that described in Chapter 3.

### *Thermogravimetric analysis*

The reaction of SCMs in blended cement is usually accompanied by the consumption of portlandite [314]. The portlandite content in hardened cement pastes at different curing ages

was determined by TGA. The thermal analyzer NETZSCH STA 449 F3 Jupiter® was used for the analysis. The experiment was performed under argon atmosphere. The temperature increased from 40 to 1000 °C at a rate of 10 °C/min. The weight loss of  $\text{Ca(OH)}_2$  ( $\text{WL}_{\text{Ca(OH)}_2}$ ) was determined using the tangential method described in [142]. The amount of portlandite in 100 g of anhydrous paste sample was determined following the equation:

$$\text{Ca(OH)}_{2,\text{anhydrous}} = \frac{\text{WL}_{\text{Ca(OH)}_2} \times \frac{74}{18}}{\text{weight at } 600^\circ\text{C}}.$$

#### *Scanning electron microscopy*

The hydration products in hardened pastes samples were analyzed using FEI QUANTA FEG 650 ESEM. After being mounted in epoxy resin, the samples were ground and polished with pure ethanol ( $\geq 96\%$  v/v, TechniSolv®) as lubricant. The polished samples were coated with a thin layer of carbon (around 10 nm) to improve their conductivity under a high vacuum. The electron beam voltage and working distance were set at 15 kV and 10 mm, respectively. The morphology of hydration products was observed by backscattered electron (BSE) imaging in scanning electron microscopy (SEM). The chemical composition of the hydration products was measured with integrated Energy Dispersive X-rays spectroscopy (EDS) detector. The spot analysis was performed at around 200 manually selected locations in the region of hydration products. It is worth mentioning that the inner products that form rims around the unhydrated cement grains were not measured. The settings of the measurements and the selection of measured locations follow recommendations proposed by Rossen et al. [315].

#### *Porosity measurements*

The porosity in 90-day hardened pastes was analyzed using nitrogen adsorption tests. The test was conducted by using Gemini VII 2390. The pore volume and size were determined according to the Barret-Joyner-Halenda model [316].

## 5.3 Results and discussion

### 5.3.1 Water treatment of MBA

#### *Effectiveness of water treatment on metallic Al content reduction*

Water treatment was applied to MBA to reduce its metallic Al content. As illustrated in Figure 5.6, the MBA obtained after the mechanical treatments of as-received MSWI bottom ash contains an average of 0.13 wt.% metallic Al. The metallic Al content decreased by 46 % within the first day of water treatment. The decrease of metallic Al content became slower with the prolonging of water treatment. From the 7<sup>th</sup> to the 14<sup>th</sup> day, the metallic Al content only decreased by around 0.01 wt.%. After 14 days, the metallic Al content was reduced by 85 %, reaching 0.02 wt.% in WMBA.

The duration of water treatment was set at 14 days because the corrosion of the residual metallic Al in water was slower in later stages. The reaction products of metallic Al and water can function as protective layers to inhibit further corrosion of metallic Al. After 14 days of water treatment, the metallic Al content in WMBA was minimal. When water treatment was prolonged to more than 14 days, it became more difficult to detect the change of metallic Al content by water displacement method.

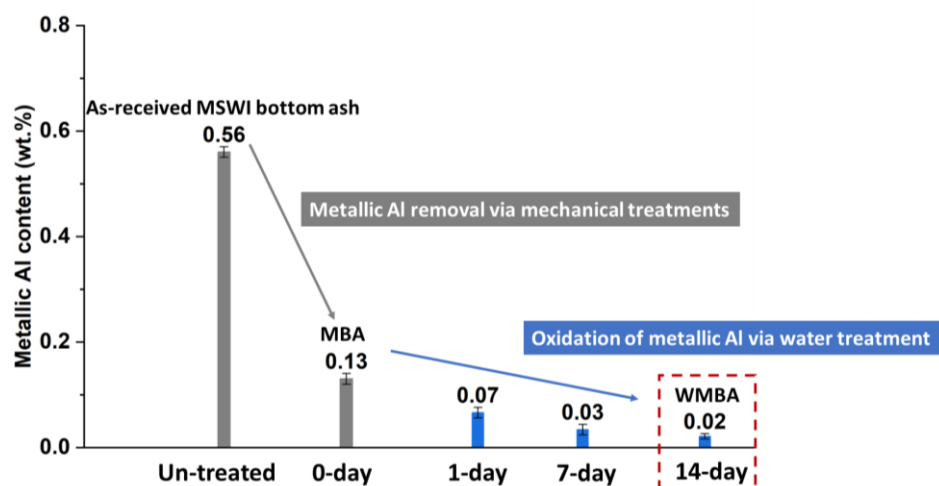
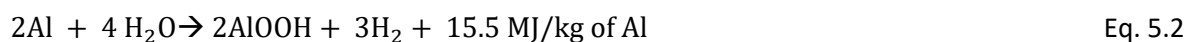
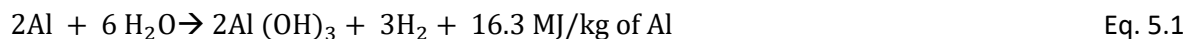


Figure 5.6 The changes of metallic Al content after mechanical treatments and water treatment. The metallic Al was separated from as-received MSWI bottom ash by sieving during the mechanical treatments. Due to water treatment, the metallic Al in MBA transformed into the oxidized form.

#### *Mechanism of water treatment on metallic Al oxidation*

The mechanism of water treatment on metallic Al oxidation was studied by analyzing reaction products and the influencing factors of metallic Al corrosion. The types of reaction products formed after the reaction of metallic Al and water largely depend on temperature [289]. Possible reaction products of metallic Al and water are  $\text{Al}(\text{OH})_3$  (Eq. 5.1),  $\text{AlOOH}$  (Eq. 5.2), and  $\text{Al}_2\text{O}_3$  (Eq. 5.3) [289]. At the temperature between room temperature and 280 °C, the formation of  $\text{Al}(\text{OH})_3$  is thermodynamically favored over  $\text{AlOOH}$  and  $\text{Al}_2\text{O}_3$  [289]. Since the

water treatment of MBA was performed at room temperature, the reaction between metallic Al and water will produce  $\text{Al}(\text{OH})_3$  and hydrogen gas.



The liquid filtered from the slurry was tested to be alkaline (see Table 5.4). This alkaline condition, which is beneficial to the corrosion of metallic Al, was created through the dissolution of MBA during water treatment. The pH of filtered liquid increased slightly when water treatment lasted from 1 day to 14 days. It is worth mentioning that the measuring accuracy of pH is  $\pm 0.003$  [317]. The increased pH of filtered liquid suggests a continuous formation of  $\text{Al}(\text{OH})_3$  during water treatment because the dissociation of the  $\text{Al}(\text{OH})_3$  in water releases  $\text{OH}^-$ . This test result is consistent with that reported by Teng et al. [318], who found the pH of the solution increased after the reaction of metallic Al with water.

As reported in Chapter 4, halite ( $\text{NaCl}$ ) was detected in the XRD measurement of MBA. The halite in MBA may facilitate the corrosion of metallic Al during water treatment. The concentration of  $\text{Na}^+$  increased with time during water treatment (see Table 5.4), indicating a continuous dissolution of MBA. With the dissolution of MBA, halite releases  $\text{Na}^+$  and  $\text{Cl}^-$  ions into the slurry. The  $\text{Cl}^-$  ions provided by halite could easily penetrate the aluminum oxide film to reach the surface of metallic Al, causing the corrosion pitting of metallic Al and thus accelerating the corrosion of metallic Al [319].

Table 5.4 The pH and elemental concentrations of the liquid filtered from the slurry during the water treatment.

Water treatment intervals	pH	Concentration (mg/L)								
		Ca	Na	K	Mg	Si	Al	Zn	Fe	S
1 day	8.14	833	749	142	45.3	2	1.1	< 0.1	0.3	836
7 days	8.12	840	860	155	45.7	2.1	0.8	< 0.1	< 0.1	882
14 days	8.33	845	966	165	43.4	2.3	0.4	< 0.1	< 0.1	860

### *Reaction of MBA during water treatment*

The reaction of MBA during water treatment was investigated by recording heat flow. There are two peaks in the heat evolution rate curve (Figure 5.7 (a)). Figure 5.7 (a) shows that the first peak appeared at 0.0016 day (2.3 min). This peak can be attributed to the wetting and dissolution of MBA in water. After the first peak, the second peak was observed at 0.14 day (see Figure 5.7 (c)). The appearance of the second calorimetric peak is mainly due to the reaction between metallic Al and water.

For the water treatment of MBA, the water to MBA mass ratio is 0.4. Thus, the amount of MBA used to prepare 1 g of slurry for water treatment is 0.71 g. After 1 day of water treatment, the metallic Al content decreased by 0.06 wt.% relative to the mass of MBA (Figure 5.6), which means 0.00043 g metallic Al in the slurry was reacted. Considering the reaction of 1 g of

metallic Al with water will generate 16.3 kJ (Eq. 5.1), the heat released after 0.00043 g of metallic Al reacting with water will be 7 J. This calculated value is only slightly lower than the total heat (8.1 J) recorded from the beginning (0.09 day) to the end (0.6 day) of the second calorimetric peak (see Figure 5.7 (d)).

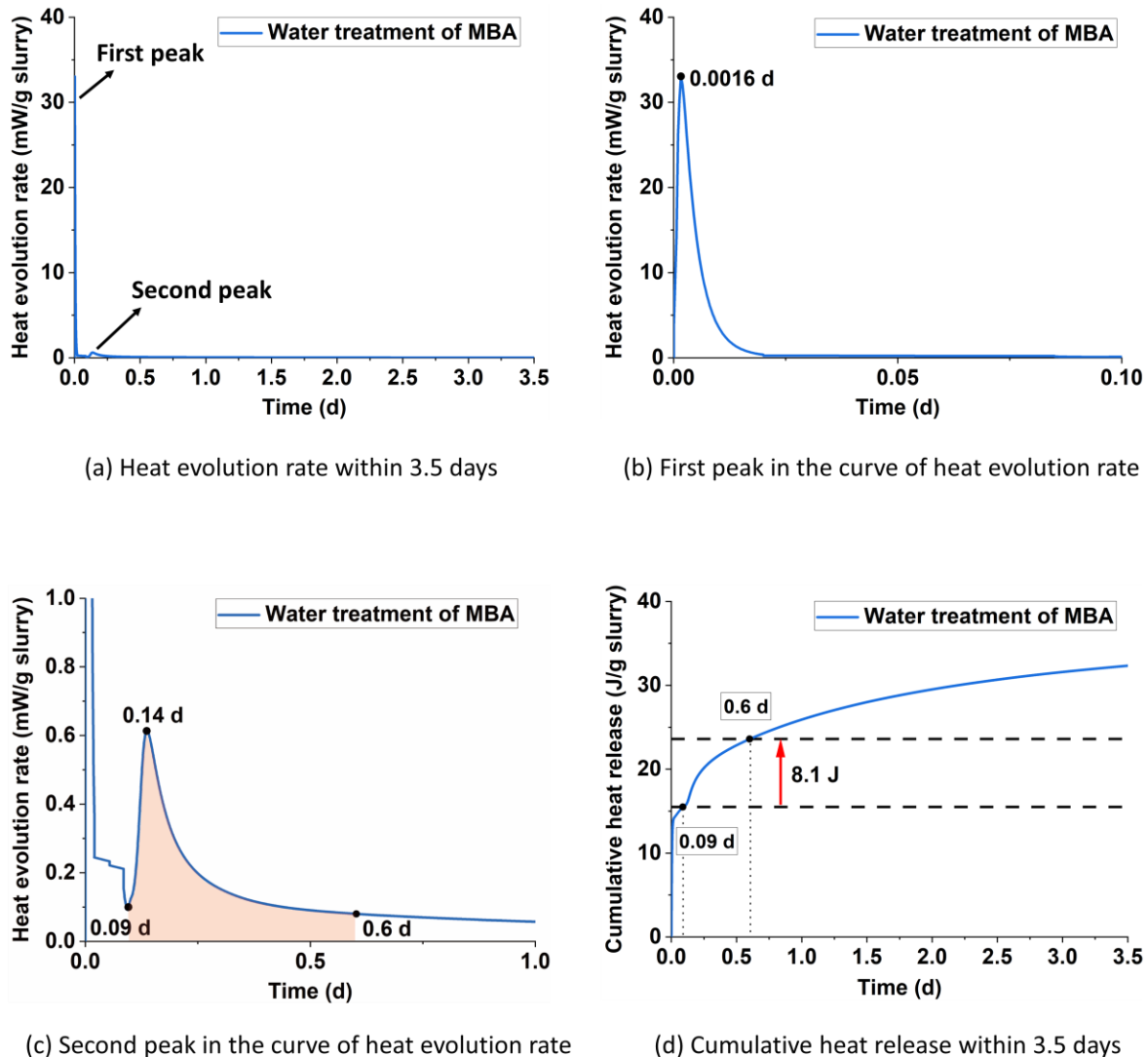


Figure 5.7 (a)-(c) Heat evolution rate and (d) cumulative heat release during water treatment of MBA

### Composition change induced by water treatment

The changes in the mineralogical composition and the molecular structure of MBA were examined after water treatment. The XRD and the FTIR patterns of WMBA and MBA are presented in Figure 5.8. The XRD and FTIR spectra of WMBA are almost the same as that of MBA. The peaks in the XRD spectrum of WMBA are also identified in the XRD measurement of MBA (Figure 5.8 (a)). Although  $\text{Al}(\text{OH})_3$  is expected to form after the metallic Al in MBA reacted with water, the gibbsite content remained unchanged (0.2 wt.%) after water treatment (Table 5.5). There are two possible explanations for this QXRD result. First, the increase in the gibbsite content is too small to be detected by XRD. Second, the  $\text{Al}(\text{OH})_3$  formed after water treatment is semi-crystalline or has an amorphous structure. Compared

with the FTIR spectrum of WMBA, the bands detected in MBA did not change their shape or location after the water treatment (Figure 5.8 (b)). These observations indicate that the water treatment of MBA did not lead to a noticeable change in its mineralogical composition and molecular structure.

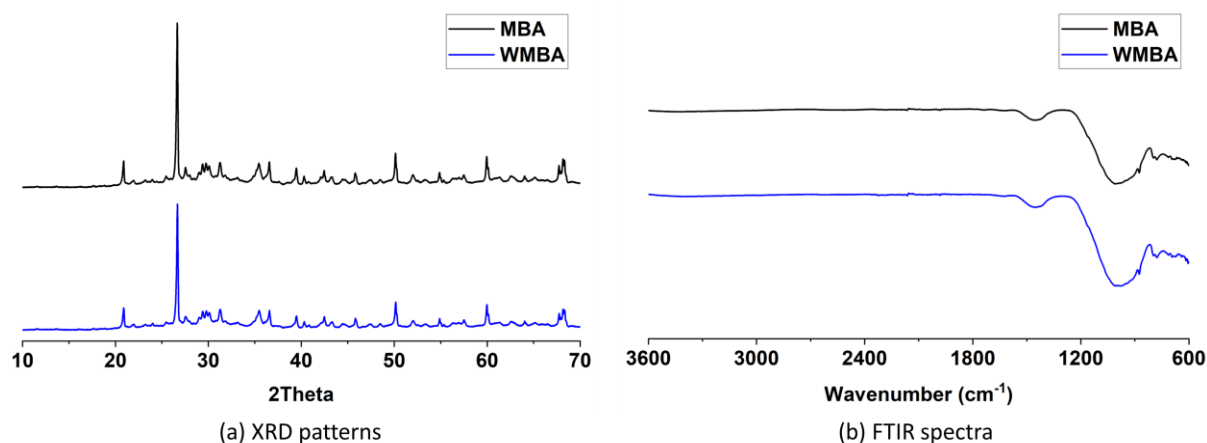


Figure 5.8 (a) XRD spectra and (b) FTIR spectra of WMBA and MBA.

Table 5.5 Mineral phases present in MBA and WMBA and QXRD analysis results.

Phases	MBA (wt.%)	WMBA (wt.%)	Formulae	ICSD codes
Quartz	12.1	12.1	SiO <sub>2</sub>	541929
Cristobalite	0.4	0.4	SiO <sub>2</sub>	1251919
Magnetite	0.9	0.9	Fe <sub>3</sub> O <sub>4</sub>	92356
Hematite	0.4	0.4	Fe <sub>2</sub> O <sub>3</sub>	453828
Wustite	0.2	0.2	FeO	309924
Gehlenite	2.8	2.8	Ca <sub>2</sub> Al <sub>2</sub> SiO <sub>7</sub>	1411155
Albite	1.9	1.1	NaAlSi <sub>3</sub> O <sub>8</sub>	1402109
Orthopyroxene	1.4	0.9	Ca <sub>0.02</sub> Mg <sub>0.30</sub> Fe <sub>0.68</sub> SiO <sub>3</sub>	1615622
Diopside	4.4	4.0	CaMg <sub>0.69</sub> Fe <sub>0.31</sub> Si <sub>2</sub> O <sub>6</sub>	77809
Wollastonite	2.6	2.6	CaSiO <sub>3</sub>	1253098
Calcite	2.1	2.2	CaCO <sub>3</sub>	1611066
Halite	0.4	0.3	NaCl	311644
Phosphammite	1.1	1.1	H(NH <sub>4</sub> ) <sub>2</sub> (PO <sub>4</sub> )	1401715
Corundum	0.7	0.7	Al <sub>2</sub> O <sub>3</sub>	527601
Goethite	0.4	0.4	FeO(OH)	71810
Gibbsite	0.2	0.2	Al(OH) <sub>3</sub>	1005040
Iron	0.1	0.1	Fe	1503158
Amorphous phase	68.1	69.7	-	-
Sum	100	100	-	-

According to the QXRD results illustrated in Table 5.5, water treatment changed the contents of the amorphous phase, calcite, albite, diopside, orthopyroxene, and halite. The contents of



the amorphous phase and calcite in WMBA are slightly higher than in MBA. The higher amount of amorphous phase in WMBA indicates that amorphous phase can be the reaction product formed after water treatment, such as  $\text{Al}(\text{OH})_3$  with a semi-crystalline or amorphous structure. The increase in the calcite content may result from the precipitation of the  $\text{Ca}^{2+}$  ions released by MBA during water treatment (Table 5.4). Compared with MBA, WMBA contains a smaller amount of albite, diopside, orthopyroxene, and halite. The decrease in the contents of these phases can be attributed to their dissolution during water treatment [320–322].

### 5.3.2 Effectiveness of water treatment in improving compressive strength of blended cement pastes prepared with MBA

As shown in Figure 5.9 (a), the 28-day compressive strength of WMBA CEM is much higher than that of MBA CEM. This result indicates that the water treatment of MBA facilitates the strength improvement of blended cement pastes prepared with MBA. The main difference between MBA and WMBA is the metallic Al content. The water treatment caused little changes to the mineralogical compositions and molecular structure of MBA (see section 5.3.1). Therefore, the higher compressive strength of WMBA blended Portland cement pastes is mainly due to the lower metallic Al content in WMBA.

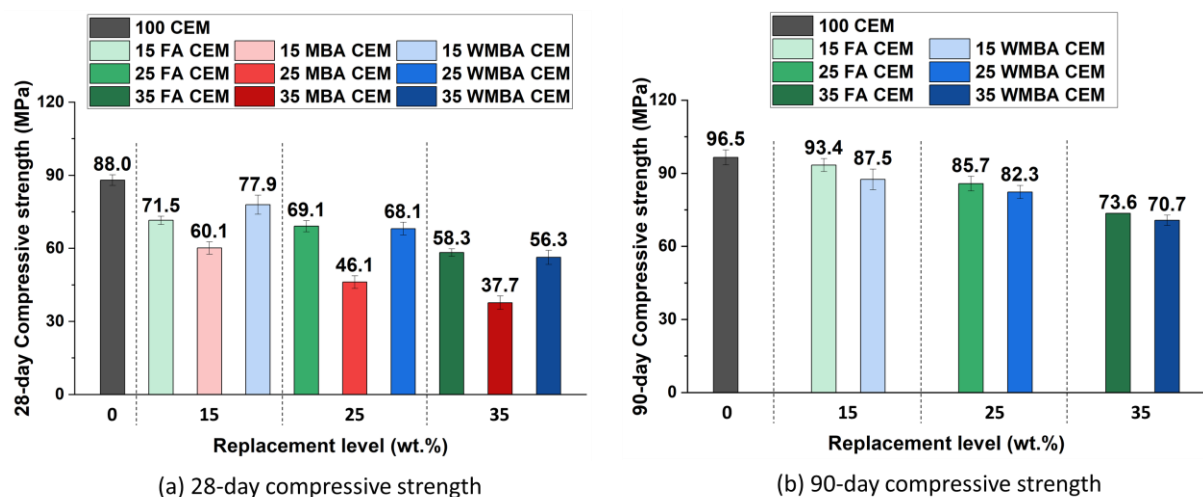


Figure 5.9 Compressive strength of (a) 28-day cement pastes and (b) 90-day cement pastes. The water-to-binder ratio of cement pastes is 0.4.

The 28-day and 90-day compressive strength of WMBA CEM are close to that of FA CEM when the replacement level is between 15 wt.% and 35 wt.% (Figure 5.9). This finding suggests that MBA, after water treatment, can be used as an alternative to FA in blended cement. It is worth noting that the 28-day 15 WMBA CEM is stronger than the 28-day 15 FA CEM. Although the reactivity of FA is similar to MBA, the particle size of FA is larger than MBA. The lower 28-day strength of 15 FA CEM can be attributed to the slower reaction rate of FA at room temperature. The contribution of FA to strength development is more significant at later ages. The compressive strength of 15 FA CEM is slightly higher than that of 15 WMBA CEM (Figure 5.9 (b)). Apart from the influence of reactivity, the lower strength of 15 WMBA CEM is also related to its higher porosity caused by residual metallic Al in WMBA.

Compared with 100 CEM, the compressive strength of WMBA CEM is lower. After being cured for 28 days, the plain cement paste sample had a compressive strength of 88 MPa. The 28-day compressive strength of 15 WMBA CEM was 77.9 MPa, decreasing by 11 % relative to 100 CEM. The 28-day compressive strength of 25 WMBA CEM was 23 % lower than 100 CEM. The differences in the compressive strength between 100 CEM and WMBA CEM became smaller with the prolonging of curing time. Compared with 100 CEM, the 90-day compressive strength of 15 WMBA CEM and 25 WMBA CEM was 9 % and 15 % lower, respectively.

### **5.3.3 Effectiveness of water treatment in eliminating expansive cracks in blended cement pastes prepared with MBA**

As demonstrated in Figure 5.10 and Figure 5.11, the cracks and pores in MBA CEM are generally more than those in WMBA CEM due to the higher metallic Al content in MBA. The volume of cracks and pores in blended cement pastes increased with the addition of MBA (see Figure 5.10). Although cracks were not found on the surface of 15 MBA CEM, cracks inside cement paste samples can be observed clearly in the 2D binary image obtained after CT scan and image analysis. Cracks can be observed on the surface of 25 MBA CEM and 35 MBA CEM. Therefore, MBA with 0.13 wt.% metallic Al is not suitable to be directly used as SCM in blended cement pastes. In comparison, at the same replacement level (15 wt.%, 25 wt.%, and 35 wt.%), cracks were not observed on the surface of WMBA CEM (Figure 5.11).

As illustrated in the 2D binary images and the 3D images, the volume occupied by air voids inside WMBA CEM increased with the incorporation of WMBA, from 15 to 35 wt.% WMBA. There are no cracks within 15 WMBA CEM and 25 WMBA CEM. Cracks were observed in the 2D binary image of 35 WMBA CEM, and cracking surfaces were found inside 35 WMBA CEM on its 3D image. Considering the adverse effects of metallic Al on strength development, for WMBA with metallic Al content of 0.02 wt.%, its replacement for PC may not exceed 25 wt.% to avoid cracking of blended cement pastes. The paste sample of 25 WMBA CEM was used in the microstructure analysis to study the reaction of WMBA in blended cement pastes, as will be discussed in the following sections.

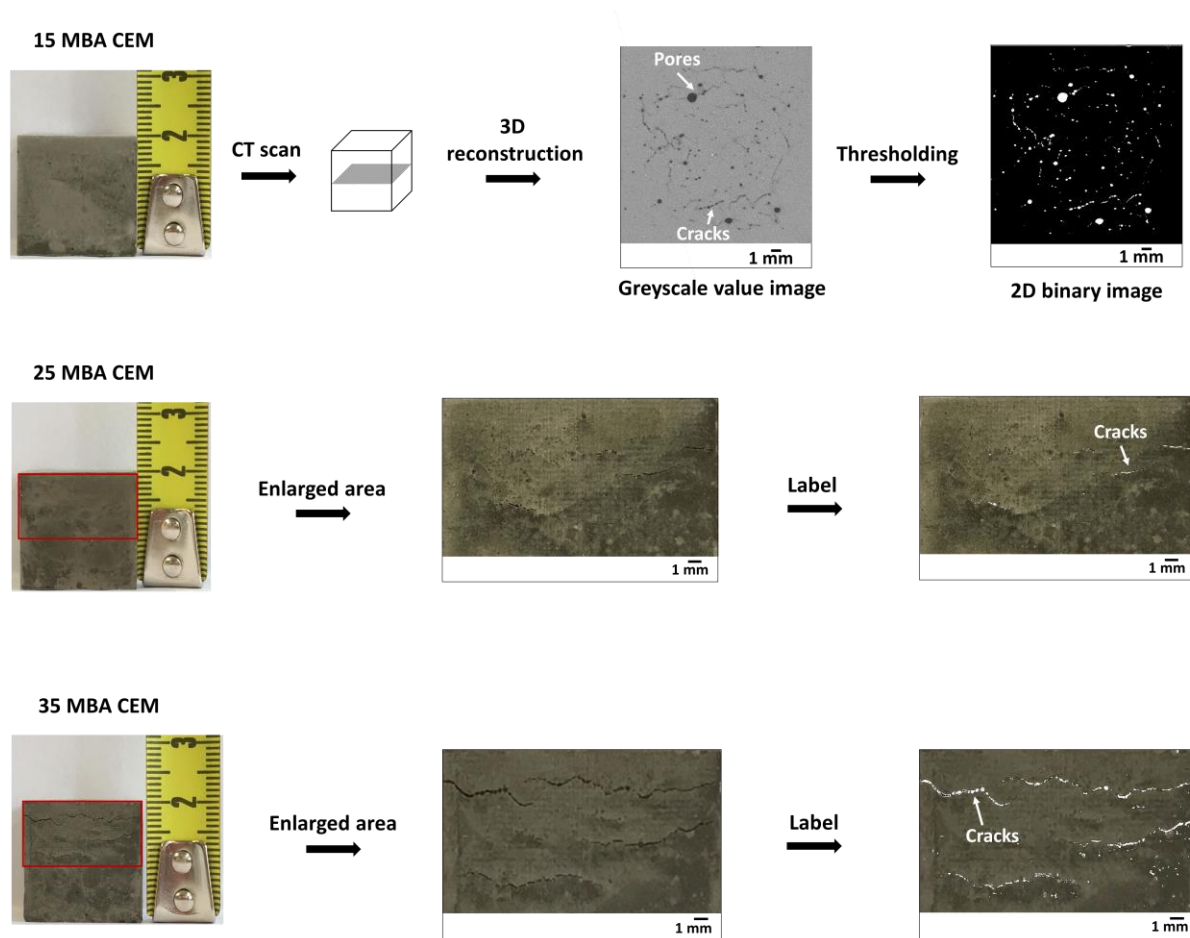


Figure 5.10 The cracks and pores of 1-day MBA CEM with water-to-binder ratio of 0.4: Photos of 1-day MBA-CEM samples indicate the cracks and pores on the surface. The greyscale value images and 2D binary images obtained after CT scan and image analysis illustrate the cracks and pores inside 1-day MBA CEM samples. The white areas in the 2D binary images represent the pores and cracks.

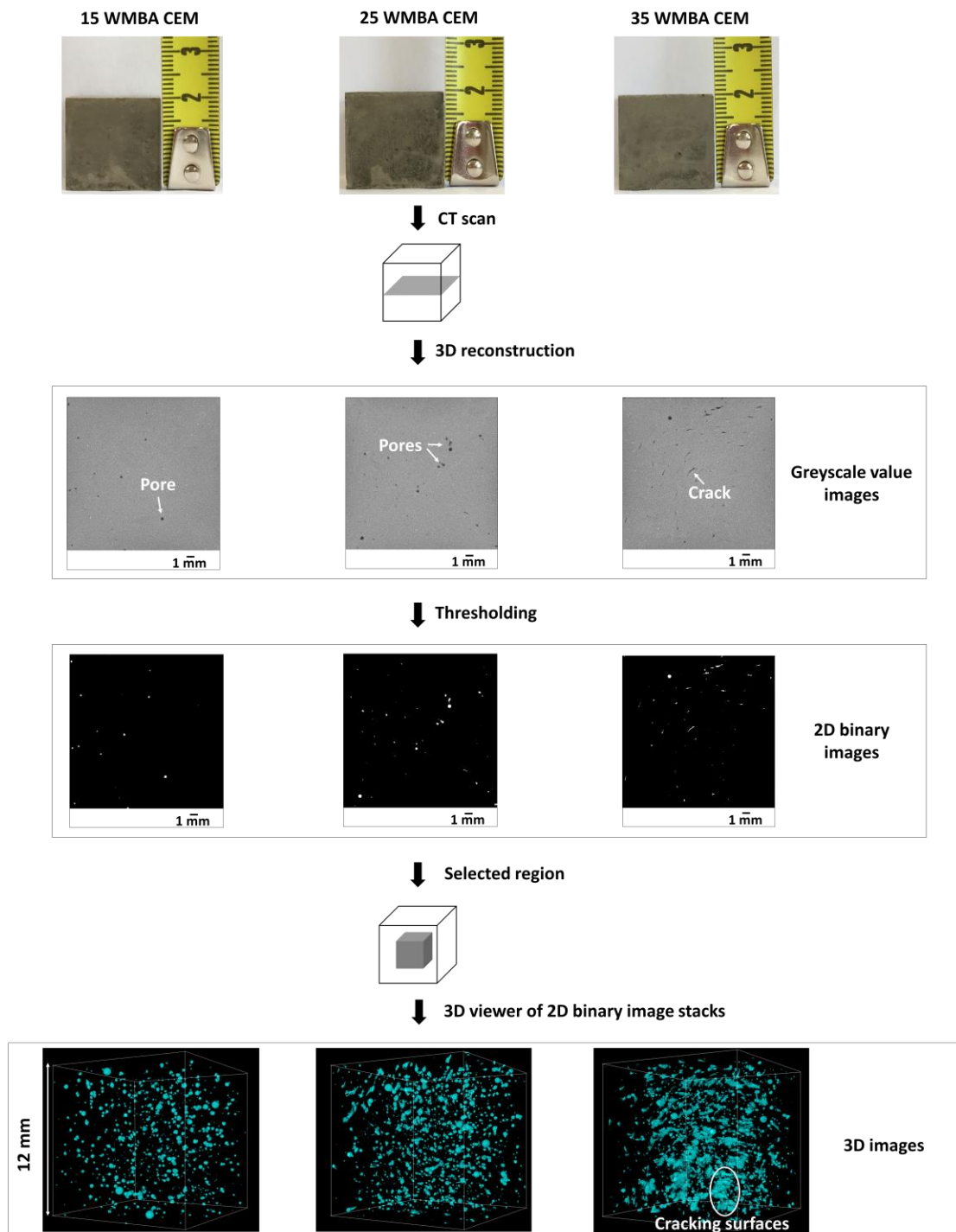


Figure 5.11 The cracks and pores of 1-day WMBA CEM with water-to-binder ratio of 0.4: Photos of 1-day WMBA CEM samples indicate that there are no cracks or pores on the surface. The greyscale value images, 2D binary images, and 3D images obtained after CT scan and image analysis show the cracks and pores inside 1-day WMBA CEM samples. The white areas in the 2D binary image represent the pores and cracks. The regions colored cyan in 3D images refer to the space occupied by cracks and pores.

### 5.3.4 Formation and analysis of the microstructure of cement pastes

As discussed above, after water treatment of MBA, its dosage in blended cement pastes can reach up to 25 wt.%. The compressive strength of 25 WMBA CEM is similar to that of 25 FA CEM. In this section, the paste sample of 25 WMBA CEM is analyzed to investigate the role of *water-treated MBA* in the formation of cement paste microstructure. For comparison purposes, the microstructure formation of plain cement paste (100 CEM) and Portland cement paste blended with 25 wt.% inert micronized sand (25 M300 CEM) is also studied.

#### 5.3.4.1 Effect of WMBA on cement hydration

##### *Kinetics of hydration*

The heat release of 25 WMBA CEM during the first eight days of reaction was studied by isothermal calorimetry (Figure 5.12 (a)). As a reference, the reaction heat of 100 CEM and 25 M300 CEM was also recorded. Figure 5.12 (b) shows the heat evolution curves during the first two days of hydration. The results demonstrate that the substitution of PC with 25 wt.% M300 did not retard cement hydration, while cement hydration was delayed by around 2.5 hours in 25 WMBA CEM. The retardation effect of MSWI bottom addition on cement hydration was also reported in previous research, especially when the replacement level of MSWI bottom ash was between 20 and 30 wt.% [28,53,56,103,125,143].

The retardation of cement hydration in 25 WMBA CEM is mainly caused by the  $\text{Ca}^{2+}$  ions released by MBA during water treatment. After 14 days of water treatment, the  $\text{Ca}^{2+}$  concentration in the liquid filtered from the 14-day slurry reached 845 mg/L (see Table 5.4). These  $\text{Ca}^{2+}$  ions increased the initial  $\text{Ca}^{2+}$  concentration in Portland cement pastes blended with WMBA, thus hindering the release of  $\text{Ca}^{2+}$  from the hydration of  $\text{C}_3\text{S}$ . Chen et al. [143] also reported that the retardation effect became more severe when MSWI bottom ash with a higher amount of soluble Ca-bearing substances (such as anhydrite and lime) was used as SCM.

The  $\text{Zn}^{2+}$  ions and organics released due to the water treatment of MBA may also influence cement hydration in 25 WMBA CEM. The  $\text{CaZn}_2(\text{OH})_6 \cdot 2\text{H}_2\text{O}$  formed in the presence of zinc ions could inhibit cement hydration at an early age by depositing on the surface of  $\text{C}_3\text{S}$  grains [146,148,323]. Additionally, the formation of metal hydroxides would reduce the pH in the blended cement system, leading to a retardation in the precipitation of portlandite [323]. A delay in the formation of portlandite would decrease the rate of  $\text{C}_3\text{S}$  hydration. Since MBA contains organics, the adsorption of organics onto the calcium hydroxide nuclei or the initial hydration products of tricalcium aluminate ( $\text{C}_3\text{A}$ ) could both impede cement hydration [324].

In the heat evolution curve (in Figure 5.12 (b)), the main peak, which came after the induction period, is assigned to cement hydration [325]. The replacement of PC with WMBA reduced the intensity of this peak. The intensity of the main peak of 25 WMBA CEM is lower than the main peak of 25 M300 CEM. The reason for the lower peak intensity in 25 WMBA CEM is that the incorporation of WMBA in blended cement impeded cement hydration in the initial stage. The shoulder peak observed at around 0.9 day in the deceleration period can be attributed to the heat released during ettringite formation [325]. The shoulder peak of 25 WMBA CEM exhibits a slightly higher intensity than that of 25 M300 CEM (Figure 5.12 (b)), suggesting that

more ettringite was formed in 1-day 25 WMBA CEM. This deduction was confirmed by the QXRD analysis results (see Figure 5.15).

The cumulative heat released by 100 CEM, 25 WMBA CEM, and 25 M300 CEM during the first eight days of reaction is shown in Figure 5.12 (c). The hydration of 100 CEM released more heat than that of 25 WMBA CEM and 25 M300 CEM. After eight days of reaction, the reduction in the cumulative heat release caused by substituting PC with 25 wt.% M300 or WMBA was around 19 % (Figure 5.12 (c)). The heat generated by 25 WMBA CEM started to exceed 25 M300 CEM after 4.5 days of reaction. As illustrated in Figure 5.12 (d), the difference in the cumulative heat between 25 WMBA CEM and 100 CEM was smaller than that between 25 M300 CEM and 100 CEM after 4.5 days of curing. This higher amount of heat release in 25 WMBA CEM is caused by the higher degree of clinker hydration and the reaction of WMBA. More explanations will be provided in the following sections.

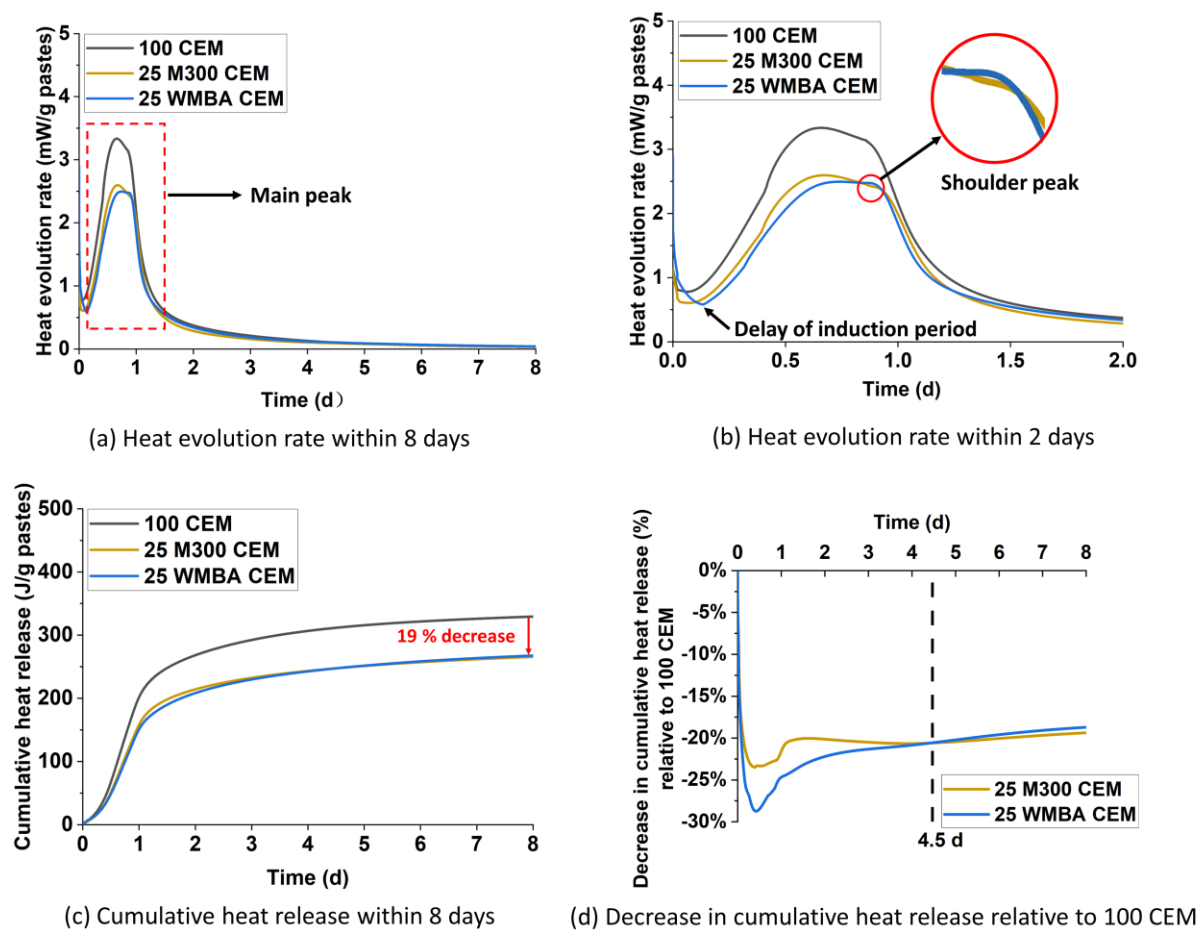


Figure 5.12 (a) and (b) Heat release per gram of paste for 100 CEM, 25 M300 CEM, and 25 WMBA CEM. (c) Cumulative heat release per gram of pastes for 100 CEM, 25 M300 CEM, and 25 WMBA CEM. (d) Decrease in cumulative heat release of 25 M300 CEM and 25 WMBA CEM relative to 100 CEM. The water-to-binder ratio of the paste samples is 0.4.



### Hydration degree of clinker

The hydration degree of clinker in 100 CEM, 25 WMBA CEM, and 25 M300 CEM is illustrated in Figure 5.13. The degree of clinker hydration at specific curing age ( $DoH_{clinker, t}$ ) equals the percentage of clinker that has been reacted relative to the clinker initially added to the system. In the calculation, only the main phases in the clinker, including  $C_3S$ ,  $C_2S$ ,  $C_3A$ , and  $C_4AF$ , are considered. The content of these phases in cement pastes was obtained by QXRD analysis, as presented in Table D 1, Table D 2, and Table D 3. The  $DoH_{clinker, t}$  was calculated using the following equation:

$$DoH_{clinker, t} = \frac{\sum(C_3S + C_2S + C_3A + C_4AF)_{initial} - \sum(C_3S + C_2S + C_3A + C_4AF)_t}{\sum(C_3S + C_2S + C_3A + C_4AF)_{initial}}$$

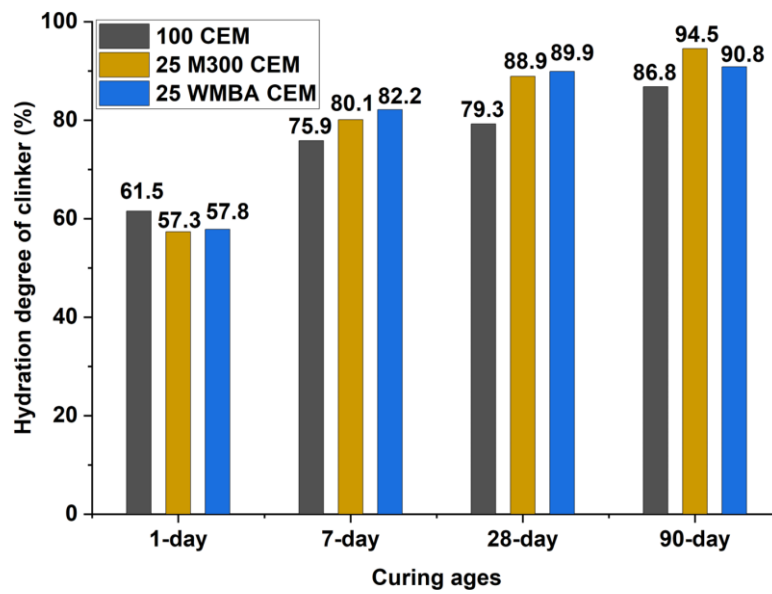


Figure 5.13 Hydration degree of clinker in cement pastes with water-to-binder ratio of 0.4, determined according to the QXRD results.

According to Figure 5.13, after 1 day of curing, the fraction of reacted clinker in 100 CEM is 61.5 %, more than that in 25 WMBA CEM and 25 M300 CEM. However, from 7 days to 90 days, the hydration degree of clinker in 25 WMBA CEM and 25 M300 CEM was higher than that in 100 CEM. The heterogeneous nucleation and dilution effect could be the main physical effects responsible for the enhancement of cement hydration in 25WMBA CEM and 25 M300 CEM [326,327]. The M300 and WMBA particles could provide nucleation sites for the heterogeneous precipitation of hydrates [314,326]. Due to the replacement of PC with M300 and WMBA, the water-to-cement ratio in 25 M300 CEM and 25 WMBA CEM is higher than that in 100 CEM (Table 5.3), resulting in larger water-to-cement distance in 25 M300 CEM and 25 WMBA CEM [328]. The hydrates in 25 M300 CEM and 25 WMBA CEM could have more space to grow, enhancing the clinker hydration [99].

There is no significant difference between 25 WMBA CEM and 25 M300 CEM in the hydration degree of clinker from 1 day to 28 days. The difference in clinker hydration degree between these two samples is more noticeable at 90-days. In the 90-day samples, the hydration degree

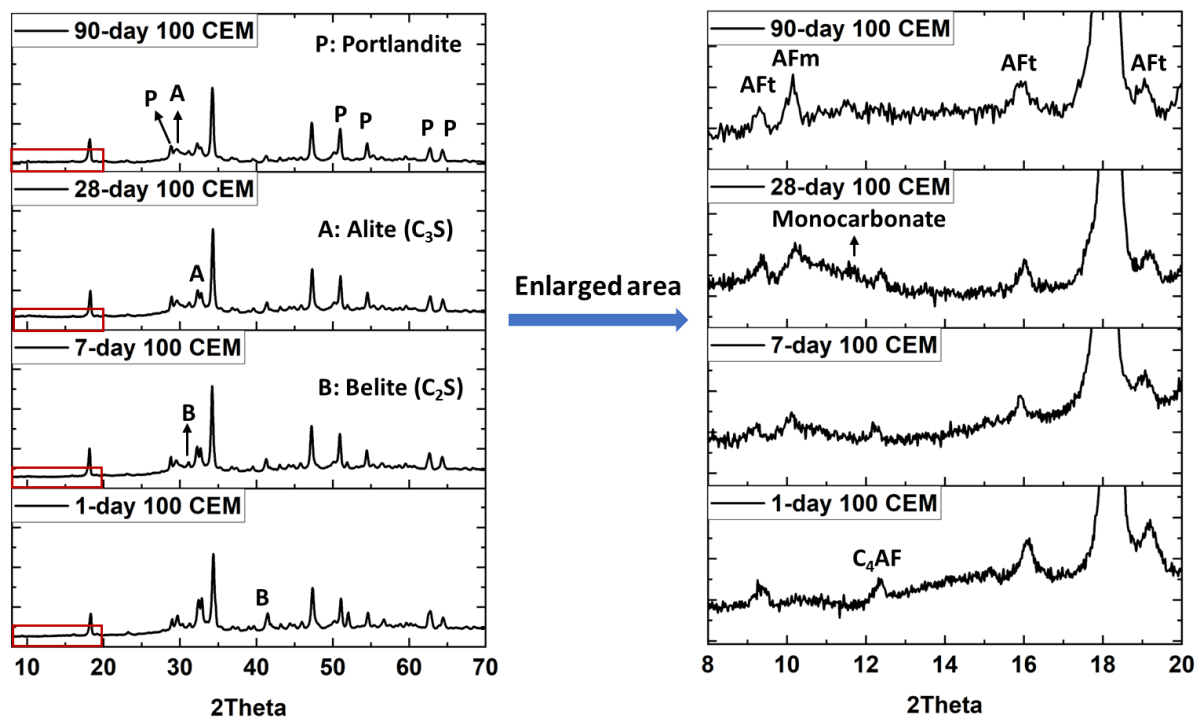


of clinker reaches 94.5% in 25 M300 CEM and 90.8% in 25 WMBA CEM. The higher hydration degree of clinker in 25 M300 CEM can be attributed to the smaller particle size of M300 (see Figure 5.2).

### 5.3.4.2 Reaction products in hardened cement pastes

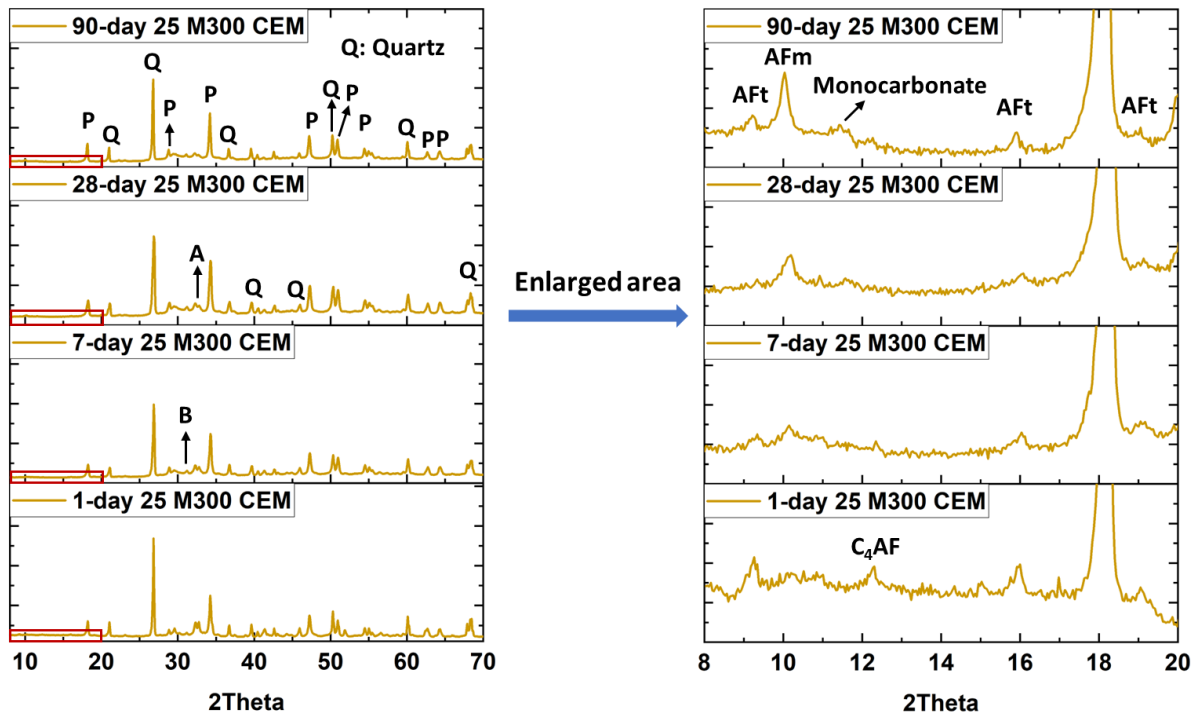
The mineralogical composition of 25 WMBA CEM was analyzed with XRD to study the effect of WMBA on reaction product formation in blended cement. 100 CEM and 25 M300 CEM were also characterized and compared with 25 WMBA CEM. As shown in Figure 5.14, the XRD patterns of 100 CEM, 25 M300 CEM, and 25 WMBA CEM change slightly from 1 day to 90 days. The differences among 100 CEM, 25 M300 CEM, and 25 WMBA CEM are most evident at  $2\theta$  below  $20^\circ$  in the XRD patterns.

According to the XRD analysis, the reaction products detected in 100 CEM include portlandite ( $\text{Ca}(\text{OH})_2$ , ICSD code 202220), monocarbonate ( $\text{Ca}_4\text{Al}_2(\text{OH})_{12}(\text{CO}_3)(\text{H}_2\text{O})_5$ , ICSD code 59327), monosulfate (AFm) ( $\text{Ca}_2\text{Al}(\text{OH})_6(\text{SO}_4)_{0.5}(\text{H}_2\text{O})_3$ , ICSD code 100138), and ettringite (AFt) ( $\text{Ca}_6\text{Al}_2(\text{SO}_4)_3(\text{OH})_{12}(\text{H}_2\text{O})_{26}$ , ICSD code 155395). The reaction products found in 100 CEM were also detected in 25 M300 CEM. However, the types of reaction products in 25 WMBA CEM are slightly different from that of 100 CEM. Monocarbonate and monosulfate (AFm) were not identified in 25 WMBA CEM. Sodicgedirte ( $\text{Na}_{0.55}(\text{Ca}_{0.04}\text{Al}_{1.37}\text{Mg}_{3.01}\text{Fe}_{2.57})(\text{Si}_{5.95}\text{Al}_{2.05})\text{O}_{22}(\text{OH})_2$ , ICSD code 34833) is the crystalline reaction product only found in 25 WMBA CEM. The QXRD results of the reaction products formed in these three cement systems are compared in Figure 5.15.

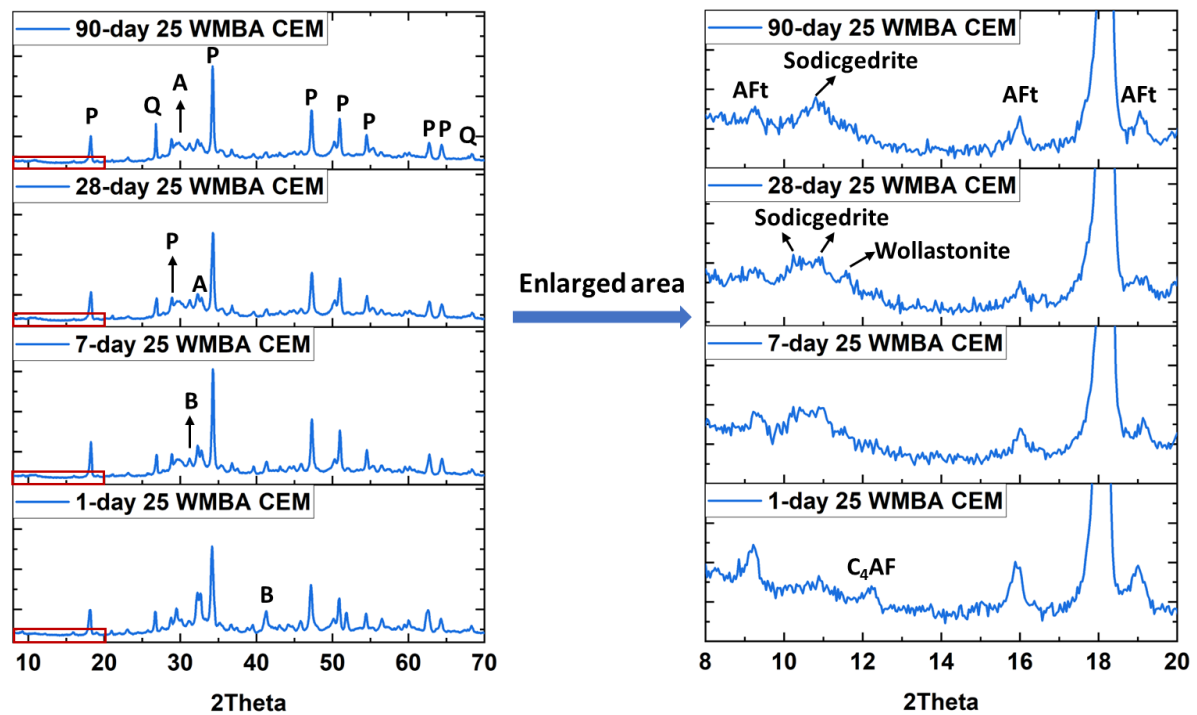


(a) 100 CEM

Figure 5.14 XRD patterns of 100 CEM, 25 M300 CEM, and 25 WMBA CEM with water-to-binder ratio of 0.4 at different curing ages.



(b) 25 M300 CEM



(c) 25 WMBA CEM

Figure 5.14 (continued) XRD patterns of 100 CEM, 25 M300 CEM, and 25 WMBA CEM with water-to-binder ratio of 0.4 at different curing ages.

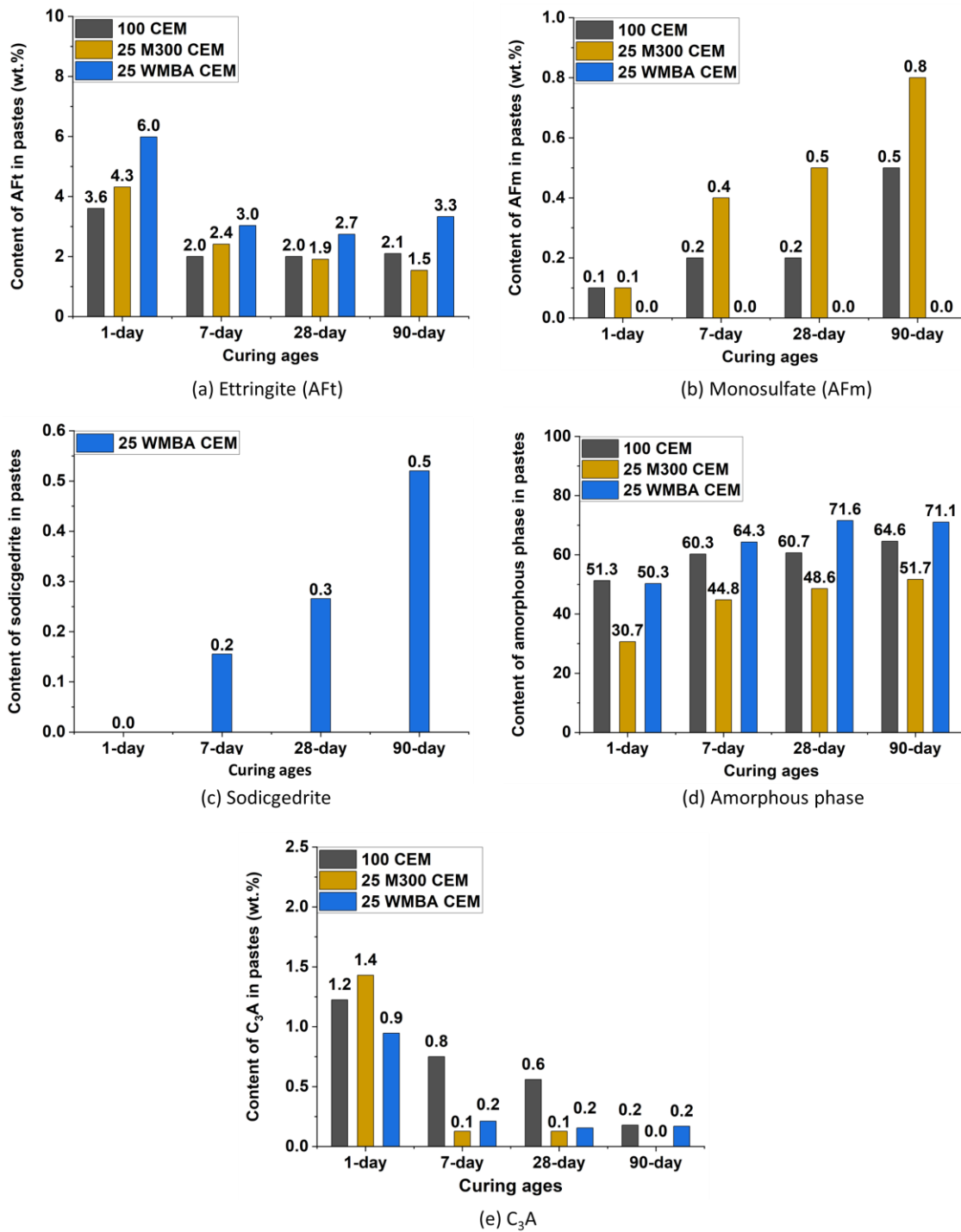


Figure 5.15 Content of ettringite, monosulfate, sodicgedrite, amorphous phase, and C<sub>3</sub>A in 100 CEM, 25 M300 CEM, and 25 WMBA CEM with water-to-binder ratio of 0.4 as a function of curing ages, determined by QXRD analysis. This figure was made based on the data presented in Table D 1, Table D 2, and Table D 3.

### *Ettringite and monosulfate*

At 1 day, the ettringite content in 25 WMBA CEM is higher than in 100 CEM and 25 M300 CEM (Figure 5.15 (a)). The higher ettringite content in 25 WMBA CEM is related to the sulfate dissolved from MBA during water treatment. In the solution filtered from the 14-day slurry, the concentration of sulfur (S) is 860 mg/L (Table 5.4). The  $\text{SO}_4^{2-}$  supplied by MBA increased the sulfate concentrations in the pore solution of 25 WMBA CEM in the initial stage. This increased sulfate concentration would promote the consumption of  $\text{C}_3\text{A}$ , resulting in the formation of a higher amount of ettringite. As illustrated in Figure 5.15 (e), the  $\text{C}_3\text{A}$  remained in 1-day 25 WMBA CEM is 0.9 wt.%, less than that in 1-day 25 M300 CEM (1.4 wt.%).

Figure 5.15 (a) shows that the ettringite content in 100 CEM, 25 M300 CEM, and 25 WMBA CEM decreases by around 50 % from 1 day to 7 days. Ettringite usually converts to monosulfate with the decrease of the sulfate content in the pore solution after the consumption of calcium sulfate [329]. The ettringite content decreased, while the monosulfate content increased with the prolonging of curing ages (Figure 5.15). However, the reduction in the ettringite content is much higher than the increase in the monosulfate content. One possible explanation is that most of the monosulfate converted from ettringite was poorly crystalline and did not exhibit sharp diffraction peaks in the XRD measurements [330].

It is worth noting that, unlike 25 M300 CEM, the peaks of monosulfate were not found in the XRD patterns of 25 WMBA CEM (Figure 5.14). The lower monosulfate content in 25 WMBA CEM can be attributed to the higher sulfate concentration in the pore solution of 1-day 25 WMBA CEM (see Table 5.6). Since WMBA contains sulfur, sulfate could be released by WMBA in later stages, leading to a higher sulfate concentration in 25 WMBA CEM than in 25 M300 CEM. Thus, the conversion of ettringite to monosulfate was more difficult in 25 WMBA CEM.

Table 5.6 Elemental concentration of the pore solution of 1-day cement pastes with water-to-binder ratio of 0.4.

1-day paste samples	Concentration in pore solution (mg/L)				Ca/Si molar ratio
	Ca	Si	Al	S	
100 CEM	118	13.1	3.1	336	6.3
25 M300 CEM	310	52	13.1	72	4.2
25 WMBA CEM	134	9.8	2.3	90	9.6

From 7 days to 90 days, the ettringite content in 100 CEM, 25 M300 CEM, and 25 WMBA CEM only changed slightly. The majority of the ettringite present in the 7-day samples did not convert to monosulfate. There are two possible reasons for this phenomenon. First, the  $\text{C}_3\text{A}$  content in PC is limited (around 5 wt.%). After 7 days of hydration, only traces of  $\text{C}_3\text{A}$  (< 1 wt.%) remained in plain cement paste and blended cement pastes, which is unfavorable to the conversion of ettringite to monosulfate. Second, the calcite present in PC and WMBA may prevent ettringite from reacting with  $\text{C}_3\text{A}$  to form monosulfate. In the presence of carbonate, the crystallization of monocarbonate was favored over monosulfate, as the monocarbonate

is more stable at room temperature [331]. Monocarbonate was found in 100 CEM and 25 M300 CEM after 28 days of curing, as illustrated in Table D 1 and Table D 2.

### *Sodicgedrite*

After 7 days of reaction, the peaks of sodicgedrite, the magnesium sodium iron aluminate silicate hydroxide, appeared in the XRD patterns of 25 WMBA CEM (Figure 5.14 (c)). The peak intensity of this crystalline phase increased with the progress of hydration. The QXRD results show that the content of sodicgedrite increased from 7 days to 90 days (Figure 5.15 (c)). Sodicgedrite is not the reaction product of Portland cement hydration. Therefore, sodicgedrite can be the reaction product of WMBA and portlandite, which will be discussed in detail in section 5.3.4.3.

### *Amorphous phase*

The amorphous phase content in 100 CEM, 25 M300 CEM, and 25 WMBA CEM increased from 1 day to 90 days, which is mainly due to the hydration of clinker. While M300 is unreactive in blended cement, WMBA can contribute to the formation of the amorphous phase from the first day of hydration. The degree of clinker hydration in 1-day 25 WMBA CEM is roughly equivalent to that in 1-day 25 M300 CEM (Figure 5.13). In this case, the portlandite content and the  $\text{Ca}^{2+}$  concentration in 1-day 25 WMBA CEM and 1-day 25 M300 CEM should be within the same range. However, the portlandite content in 25 WMBA CEM is lower than in 25 M300 CEM (Figure 5.16). The concentrations of Ca, Al, and Si in the pore solution of 1-day 25 WMBA CEM are much lower than that in 1-day 25 M300 CEM (Table 5.6). The possible reason could be that the reaction of WMBA consumed portlandite. The reaction product of WMBA may have amorphous structure, such as calcium silicate hydrate (C-S-H), because new crystalline phases were not identified in 1-day 25 WMBA CEM.

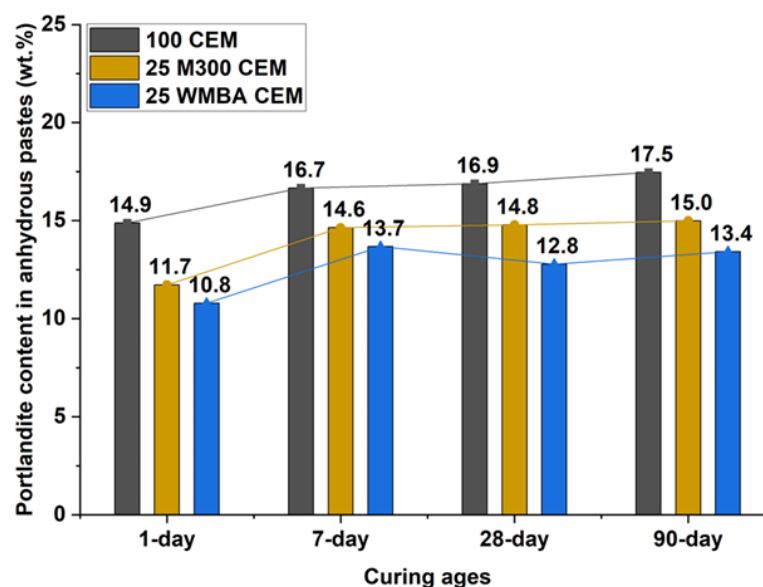


Figure 5.16 Portlandite content in anhydrous paste samples with water-to-binder ratio of 0.4, determined by TGA.

There is a drop in the content of portlandite determined by TGA in 25 WMBA CEM (Figure 5.16) from 7 days to 28 days. From 7 days to 28 days, the amount of clinker hydrated in 25 WMBA CEM was less than that in 25 M300 CEM (see Figure 5.13). In contrast, the content of the amorphous phase in 25 WMBA CEM increased by 7.3 wt.%, almost doubling that in 25 M300 CEM (3.8 wt.%) (Figure 5.15 (d)). For these reasons, some of the portlandite produced after clinker hydration in 25 WMBA CEM should be consumed by WMBA, and the reaction product was the amorphous phase.

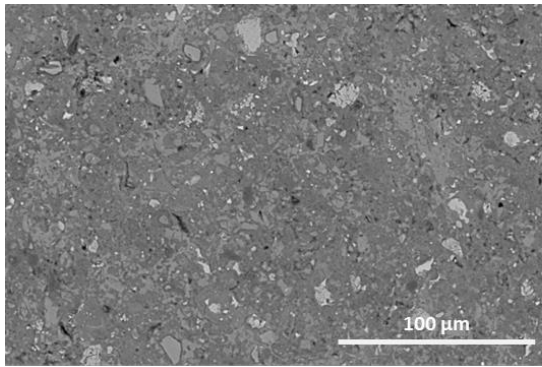
### 5.3.4.3 Morphology of hardened cement pastes

The morphology of 25 WMBA CEM was observed under SEM to investigate the influence of WMBA on the microstructural development of cement pastes. For comparison purposes, the morphology of 100 CEM and 25 M300 CEM was also studied. Figure 5.17 shows the SEM-BSE images of the 90-day hardened paste samples of 100 CEM, 25 M300 CEM, and 25 WMBA CEM. Since the pores were filled with epoxy during sample preparation, they were identified as the black areas of the SEM-BSE images. Compared with the Portland cement pastes blended with WMBA or M300, the plain cement pastes exhibited a denser microstructure. At the magnification of 1000, more pores were found in 25 WMBA CEM and 25 M300 CEM than in 100 CEM (see Figure 5.17 (a), (c), and (e)).

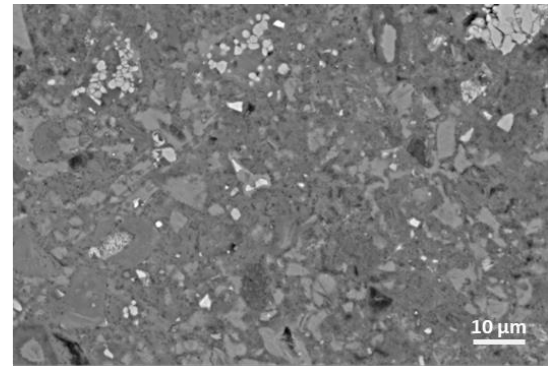
The area surrounding WMBA and M300 particles was examined under high magnification (4000). As shown in Figure 5.17 (d) and (f), the WMBA particles and M300 particles both have angular shapes. Unlike the intact M300 particles, cracks were found within the WMBA particles. The grey levels of different regions within a single WMBA particle can differ because of the heterogeneity in chemical compositions. The M300 and WMBA particles labeled in the BSE images were recognized by SEM-EDS spot analysis. The BSE images of 25 M300 CEM and 25 WMBA CEM indicate that a dense microstructure was formed around the M300 and WMBA particles.

Figure 5.18 (a) and (b) demonstrate two typical examples of partially reacted WMBA particles in 90-day 25 WMBA CEM. Layers of reaction products were deposited on the surface of these two particles (particle 1 and particle 2). In the SEM-BSE images, the reaction products formed in situ from WMBA have a thickness below 0.5  $\mu\text{m}$  and are brighter in color than the gel formed between unreacted particles. According to the SEM-EDS spot analysis (see Figure 5.18 (c)), the elements detected at location 1 of particle 1 and location 2 of particle 2 are mainly Na, Ca, Al, Mg, Fe, Si, and O. These elements are also the constituents of sodicgedrite ( $\text{Na}_{0.55}(\text{Ca}_{0.04}\text{Al}_{1.37}\text{Mg}_{3.01}\text{Fe}_{2.57})(\text{Si}_{5.95}\text{Al}_{2.05})\text{O}_{22}(\text{OH})_2$ ). It is possible that the in-situ reaction product of WMBA is sodicgedrite.

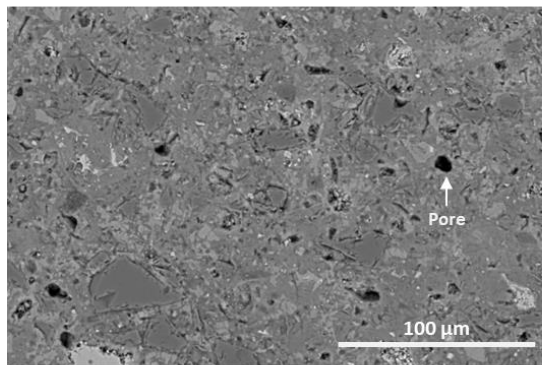




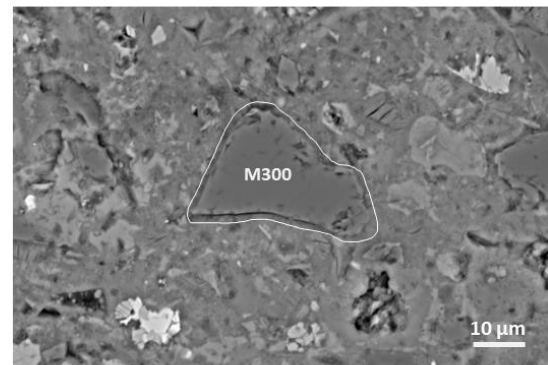
(a) 90-day 100 CEM (1000 ×)



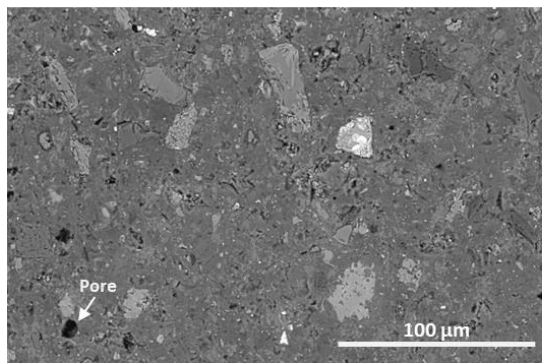
(b) 90-day 100 CEM (4000 ×)



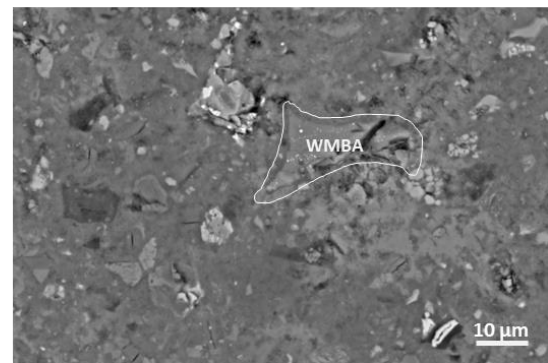
(c) 90-day 25 M300 CEM (1000 ×)



(d) 90-day 25 M300 CEM (4000 ×)



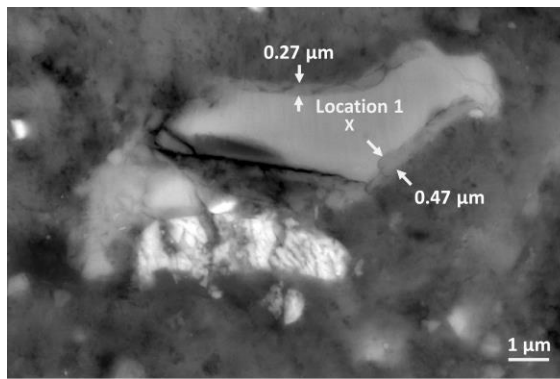
(e) 90-day 25 WMBA CEM (1000 ×)



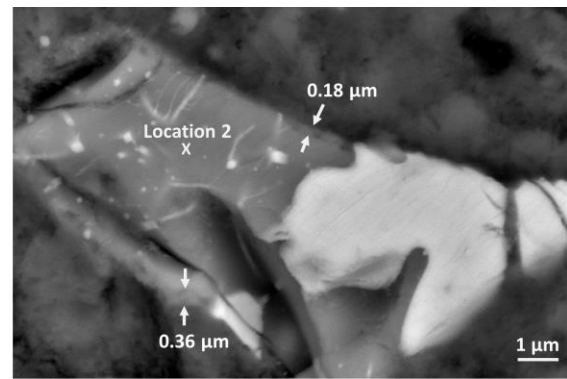
(f) 90-day 25 WMBA CEM (4000 ×)

Figure 5.17 SEM-BSE images of 100 CEM, 25 M300 CEM, and 25 WMBA CEM paste samples at 90 days. The magnifications are 1000 (left images) and 4000 (right images). The water-to-binder ratio of the paste samples is 0.4.

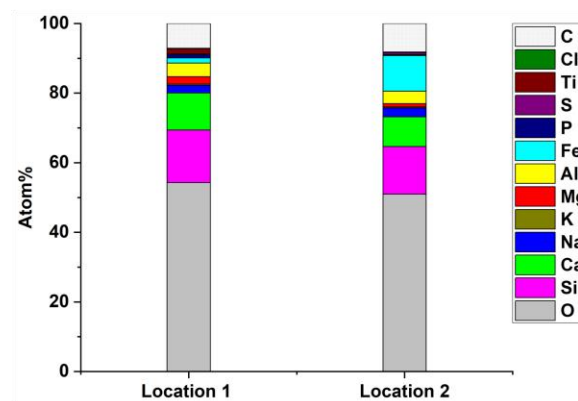




(a) Particle 1 of 90-day 25 WMBA CEM



(b) Particle 2 of 90-day 25 WMBA CEM



(c) Chemical compositions of the locations in particle 1 and particle 2 of 90-day 25 WMBA CEM

Figure 5.18 (a) and (b) SEM-BSE images of the partially reacted WMBA particles in 90-day 25 WMBA CEM with water-to-binder ratio of 0.4. (c) SEM-EDS spot analysis results of the locations labeled in particle 1 and particle 2.

The glass particles are the primary resources of the reactive phase in MBA (see Chapter 4). Given that the mineralogical composition of WMBA is almost the same as that of MBA (see section 5.3.1), the elemental compositions of particle 1 and particle 2 were compared with the chemical composition of the glass particles in MBA. The SEM-EDS spot analysis was performed on the glass particles separated from as-received MSWI bottom ash (see Figure 4.3 (b)) to determine the composition of the glass in MBA. The measured compositions were projected onto ternary diagrams (Figure 5.19). The ternary diagram depicts the ratios of three elements as positions in an equilateral triangle. As shown in Figure 5.19, the atomic ratios of the elements detected at location 1 and location 2 are within the same range as that of elements present in the glass particles. It can be deduced that particle 1 and particle 2, which are reactive in 25 WMBA CEM, are WMBA particles consisting of glass. The sodicgedrite detected in 25 WMBA CEM can be the reaction products of portlandite and the glass particles in WMBA.

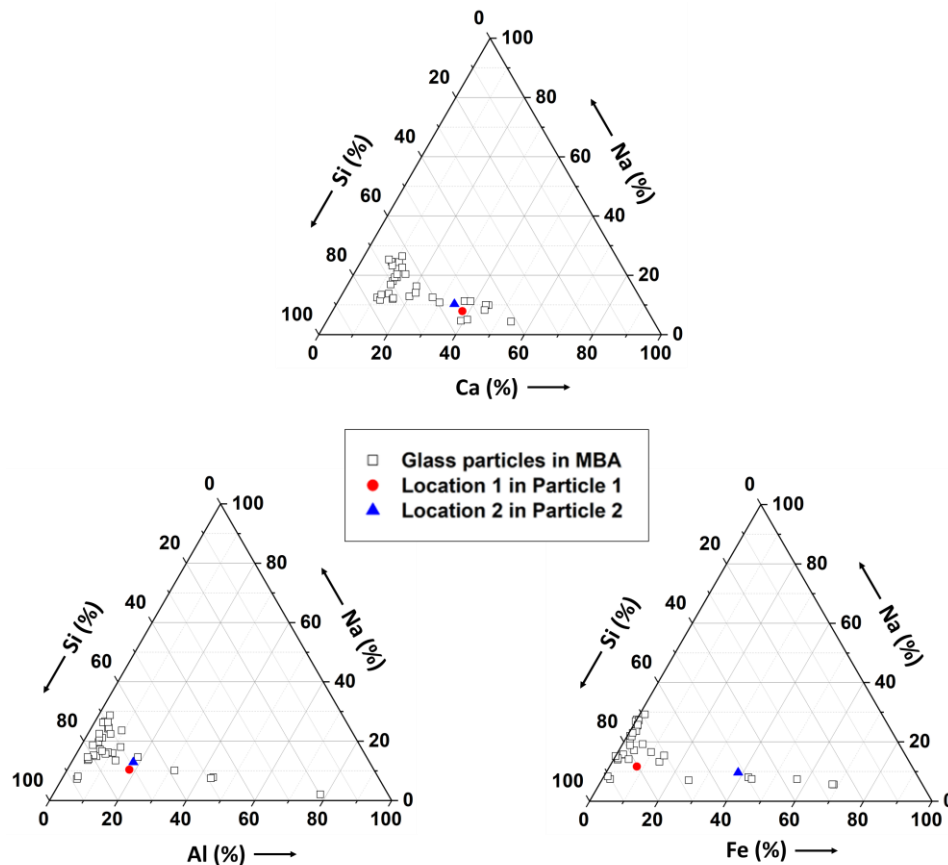


Figure 5.19 Comparison between the chemical compositions (atom %) of the glass particles in MBA and the chemical compositions measured at location 1 and location 2 (shown in Figure 5.18 (a) and (b)) in 90-day 25 WMBA CEM with water-to-binder ratio of 0.4. The ternary diagrams are plotted according to the atomic percentages of the elements.

#### 5.3.4.4 Chemical composition of C-S-H gel in hardened cement pastes

The chemical composition of the C-S-H gel formed in 25 WMBA CEM was compared with that of 100 CEM and 25 M300 CEM after 90 days of curing. The composition of C-S-H gel was measured at randomly selected locations in the region between unreacted particles, such as the “point 1” shown in Figure 5.20. It is worth mentioning that the chemical composition of the reaction products deposited on the surface of WMBA particles (see Figure 5.18) was not measured with SEM-EDS spot analysis. This is because the thickness of these in-situ reaction products is much smaller than the radius of interaction volume between the electron beams and gel phases at 15 kV [315].

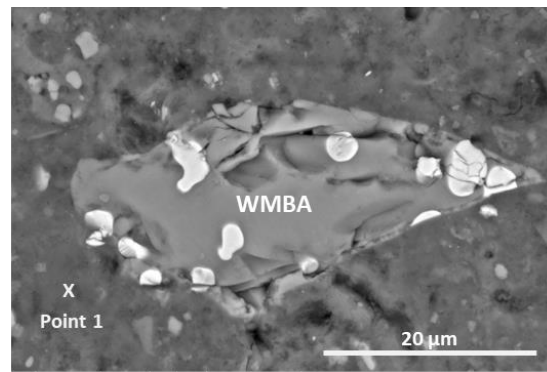


Figure 5.20 An example of the location selected for the measurement of C-S-H gel composition in SEM-EDS spot analysis. The sample is 90-day 25 WMBA CEM, and the magnification is 8000. The water-to-binder ratio of the paste samples is 0.4.

The Si/Ca and Al/Ca atomic ratios calculated from the analysis results were plotted in Figure 5.21 (a)-(c). The scatter plots indicate that the Si/Ca atomic ratio of the C-S-H gel in 100 CEM is between 0.3 and 0.6, while this ratio changes across a wider range (0.3 - 0.65) in the C-S-H gel of 25 M300 CEM and 25 WMBA CEM. It seems that replacing 25 wt.% PC with M300 or WMBA only had little effect on the Si/Ca atomic ratio of the C-S-H gel. However, in addition to C-S-H gel, the composition information collected at a single location in the SEM-EDS spot analysis may also include signals from other phases, such as ettringite and portlandite. When an electron beam strikes the specimen, the interaction volume may contain two or more phases [142]. It is necessary to separate the signals of C-S-H gel from those of the other phases so as to compare the composition of the gel phases formed in 100 CEM, 25 M300 CEM, and 25 WMBA CEM.

According to the method proposed by Scrivener et al. [142], the Si/Ca and Al/Ca atomic ratios in the C-S-H gel can be estimated by taking the value at the right edge of the cloud of measured C-S-H compositions in the scatter plots. The point at the right edge is the “least-intermixed point”, and its value is very close to the atomic ratio of C-S-H gel. The value represented by the point at the right edge is determined by fitting the dataset of measured composition with Gaussian distribution [315]. Figure 5.21 (d)-(f) illustrate the distribution plots of the dataset of the measured Si/Ca and Al/Ca atomic ratios plotted in Figure 5.21 (a)-(c). The mean value ( $\mu$ ) of the fitted distribution is taken as the Al/Ca atomic ratio for the C-S-H gel. The Si/Ca atomic ratio of the C-S-H gel is taken to be  $\mu+2\sigma$ , where  $\sigma$  represents the standard deviation of the fitted distribution. The locations of fitted compositions are also labeled in the scattering plots (Figure 5.21 (a)-(c)).

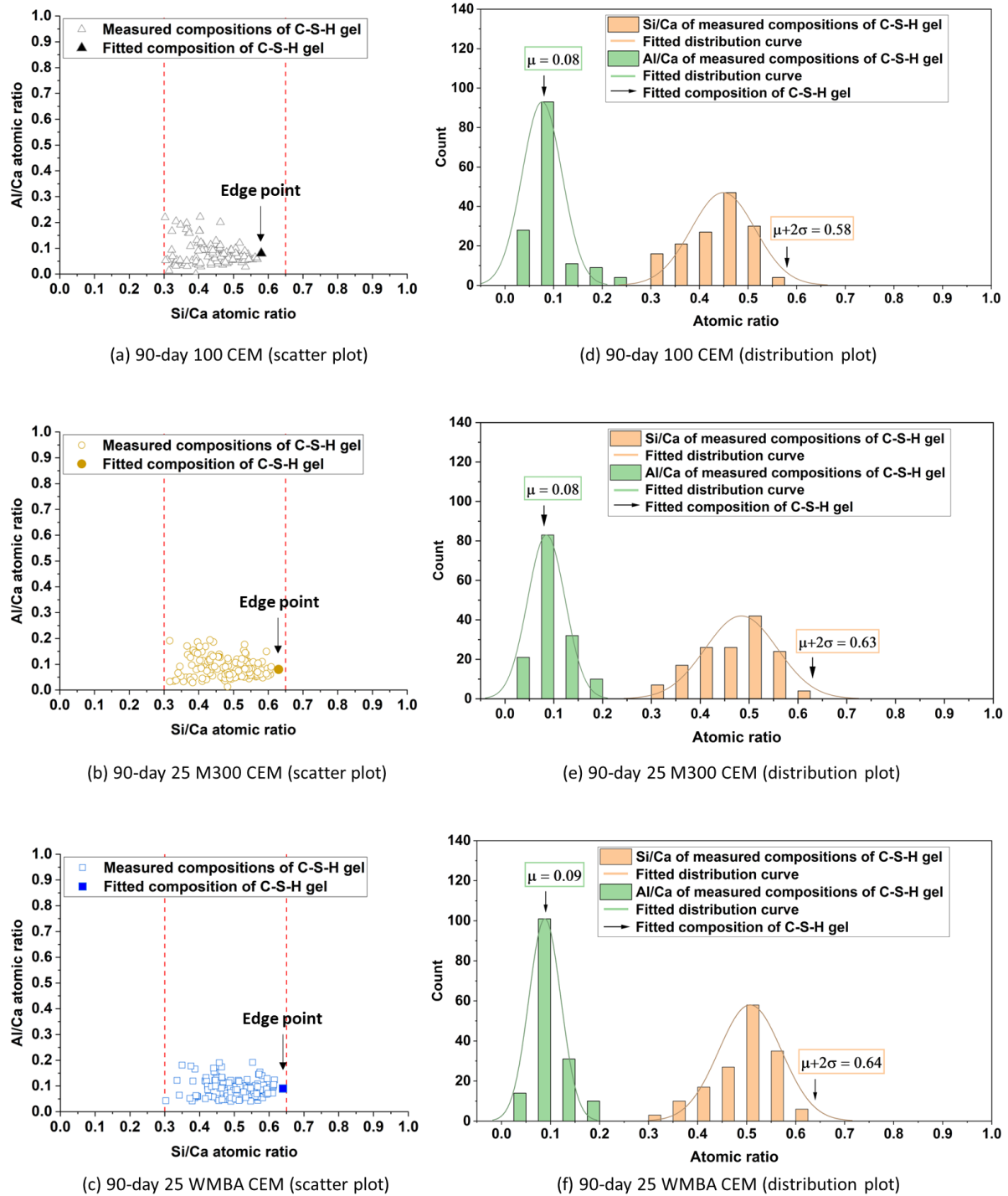


Figure 5.21 (a)-(c) The 2D scatter plot of the SEM-EDS analysis results of the C-S-H gel in 100 CEM, 25 M300 CEM, and 25 WMBA CEM at 90 days. (d)-(f) The distribution plot of the SEM-EDS analysis results shown in (a)-(c). The distribution of the data is fitted with a Gaussian curve. The mean ( $\mu$ ) and the standard deviation of the fitted distribution ( $\sigma$ ) are used to find the atomic ratio of the elements in C-S-H: Al/Ca (at  $\mu$ ), Si/Ca (at  $\mu+2\sigma$ ). The points representing fitted compositions are referred to as the “edge points”. The water-to-binder ratio of the paste samples is 0.4.

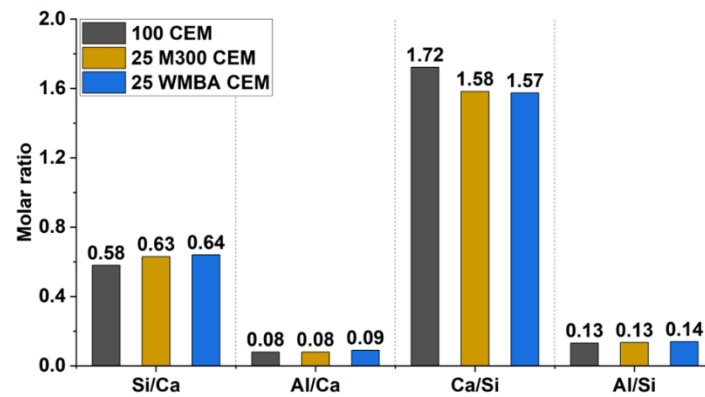


Figure 5.22 Comparison of atomic ratios of fitted compositions (at edge points) of the C-S-H in 100 CEM, 25 M300 CEM, and 25 WMBA CEM at 90 days. The water-to-binder ratio of the paste samples is 0.4.

The Si/Ca and Al/Ca atomic ratios represented by the edge points of 100 CEM, 25 M300 CEM, and 25 WMBA CEM were summarized in Figure 5.22. The Al/Si and Ca/Si atomic ratios were also calculated from the atomic ratios of Si/Ca and Al/Ca. Figure 5.22 shows that the Al/Si atomic ratio is almost the same in the C-S-H gel of 100 CEM, 25 M300 CEM, and 25 WMBA CEM. The Ca/Si atomic ratio of the C-S-H gel in 25 WMBA CEM and 25 M300 CEM are nearly equal. Both are lower than the Ca/Si atomic ratio of the C-S-H gel in 100 CEM.

The low Ca/Si atomic ratio of the C-S-H gel in 25 M300 CEM can be attributed to the low Ca/Si molar ratio in the pore solution. Blending PC with M300 reduced the Ca/Si molar ratio in the pore solution. As shown in Table 5.6, the Ca/Si molar ratio in the pore solution of 1-day 25 M300 CEM is 4.2, lower than that in the pore solution of 1-day 100 CEM (6.3). The Ca/Si molar ratio in the pore solution of Portland cement paste decreased with the prolonging of curing time [332]. Given that the addition of M300 enhanced cement hydration, the decrease of the Ca/Si molar ratio in the pore solution of 25 M300 CEM would be faster than that in the pore solution of 100 CEM. From 1 day to 90 days, the Ca/Si molar ratio in the pore solution of 25 M300 CEM remained lower than that in the pore solution of 100 CEM, resulting in a lower Ca/Si atomic ratio of the C-S-H gel.

In the case of 25 WMBA CEM, the low Ca/Si atomic ratio of the C-S-H gel is mainly caused by the reaction of WMBA. There are three possible explanations:

- First, like the situation in 25 M300 CEM, cement hydration was also accelerated in 25 WMBA CEM due to the heterogeneous nucleation and dilution effect. The Ca/Si molar ratio would decrease faster than that in the pore solution of Portland cement. Besides, as discussed in section 5.3.4.2, the reaction of WMBA in 25 WMBA CEM consumed portlandite. The Ca/Si molar ratio in the pore solution may also decrease after some  $\text{Ca}^{2+}$  ions were consumed by the reaction of WMBA, resulting in a low Ca/Si atomic ratio of the C-S-H gel.
- Second, the Ca/Si atomic ratio of the C-S-H gel could be lower after incorporating the Si dissolved from WMBA. The mineralogical composition of MBA only slightly changed after water treatment (see section 5.3.1). Like MBA, the amorphous phase of WMBA also has

much more Si than Ca (see Chapter 4). The dissolution of WMBA mainly provided Si to the formation of C-S-H gel, which would increase the Si content in the gel.

- Third, the pozzolanic reaction of WMBA may produce C-S-H gel with a low Ca/Si atomic ratio. Since the chemical compositions of the amorphous phase in WMBA and Class F coal fly ash are within the same range (see Chapter 4), the pozzolanic reaction products of WMBA and Class F coal fly ash could be similar. According to Bentz et al. [333], the pozzolanic reaction products of coal fly ash can be calcium silicate hydrate ( $C_{1.1}SH_{3.9}$ ) and strätlingite ( $C_2ASH_8$ ). It is possible that in 25 WMBA CEM, the  $C_{1.1}SH_{3.9}$  also formed after the pozzolanic reaction of WMBA. When C-S-H gel with a low Ca/Si atomic ratio was mixed with the C-S-H gel formed after cement hydration, the overall Ca/Si atomic ratio of the C-S-H gel in 25 WMBA CEM was decreased.

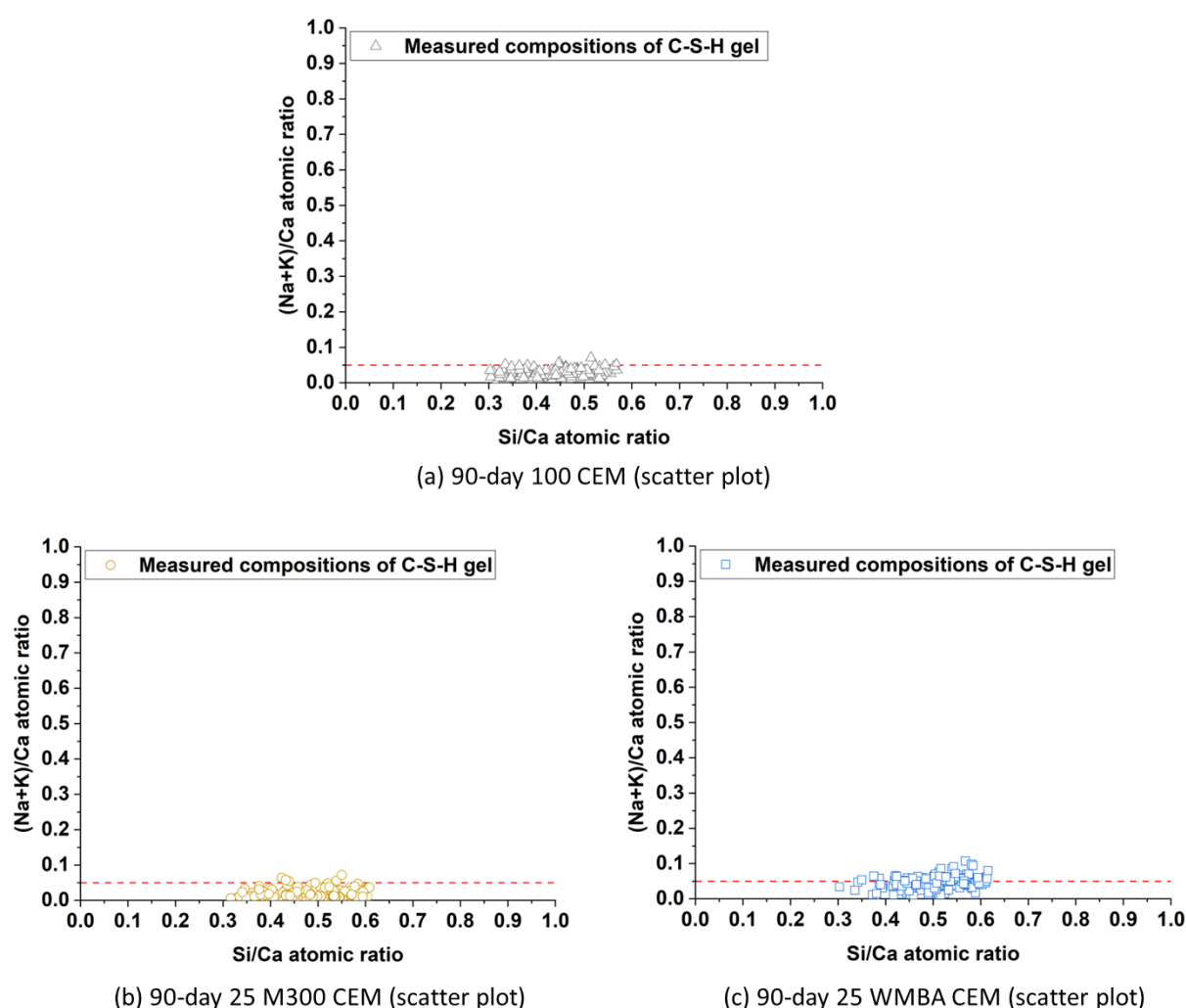


Figure 5.23 (a)-(c) The 2D scatter plot of the SEM-EDS analysis results of the C-S-H gel in 100 CEM, 25 M300 CEM, and 25 WMBA CEM at 90 days. The water-to-binder ratio of the paste samples is 0.4. For comparison purposes, the axis scale settings are the same as those of the scatter plots shown in Figure 5.21.

Based on what has been discussed above, it is difficult to distinguish the C-S-H gel formed in 25 WMBA CEM and 25 M300 CEM by comparing the Ca/Si or the Al/Si atomic ratio. However,

the alkali contents are different in the C-S-H gel of 25 WMBA CEM and 25 M300 CEM. As shown in Figure 5.23, blending PC with M300 did not change the (Na+K)/Si atomic ratio of the C-S-H gel. Comparatively, more alkali ions were incorporated in the C-S-H gel formed in 25 WMBA CEM. These extra alkali ions were released by WMBA (Figure 5.18 (c)).

#### 5.3.4.5 Porosity of hardened cement pastes

The porosity of the 90-day 25 WMBA CEM was measured by the nitrogen adsorption test. The test result was compared with that of 90-day 100 CEM and 25 M300 CEM (see Figure 5.24). The nitrogen adsorption test mainly measured the volumes of the capillary pores ranging from 2 to 500 nm [334]. The gel pores with their characteristic size of 1.5 to 2 nm [335] cannot be measured with this technique.

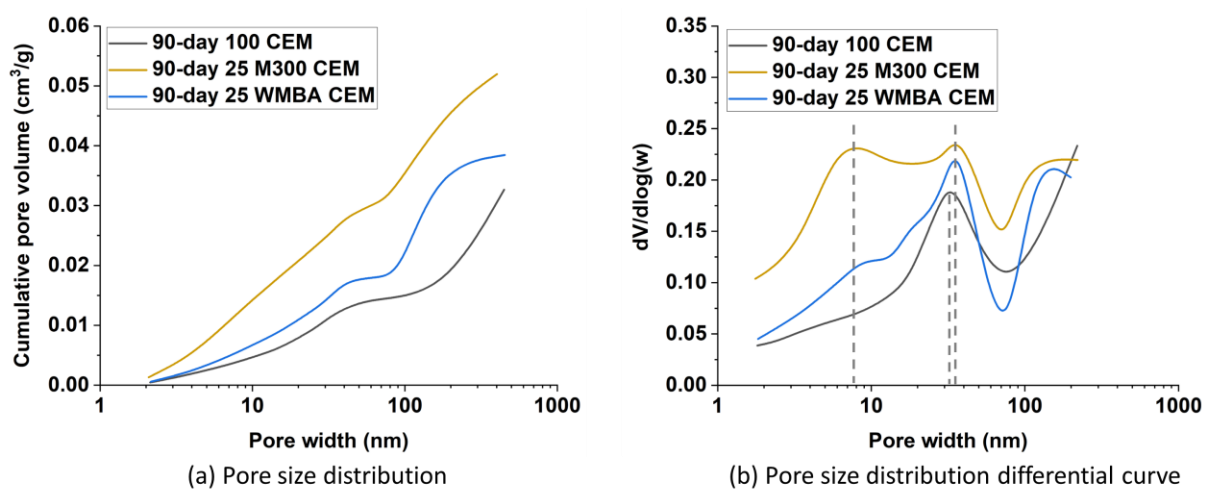


Figure 5.24 Pore size distribution of 100 CEM, 25 M300 CEM, and 25 WMBA CEM at 90 days, determined using the nitrogen adsorption method. The water-to-binder ratio of the paste samples is 0.4.

As illustrated in Figure 5.24 (a), the total pore volume in 90-day hardened pastes increased in the following order: 100 CEM < 25 WMBA CEM < 25 M300 CEM. The differential curve of 90-day 100 CEM displays a unimodal distribution (Figure 5.24 (b)). The corresponding critical pore width is 20 nm. In the differential curve of 90-day 25 WMBA, the main peak was observed at 22.5 nm, which shifted slightly to the larger pore width relative to the peak of 90-day 100 CEM. Unlike 90-day 100 CEM and 25 WMBA CEM, the differential curve of 90-day 25 M300 CEM shows a bimodal distribution. The first peak was found at the same pore width as the main peak of 90-day 25 WMBA CEM. The second peak of 90-day 25 M300 CEM appeared at the pore width of 8 nm.

Compared with 100 CEM, less PC was used for the preparation of 25 WMBA CEM and 25 M300 CEM, reducing the quantities of reaction products. As a result, the porosity of 25 WMBA CEM and 25 M300 CEM is higher. When comparing 90-day 25 WMBA CEM and 25 M300 CEM, the reaction products formed after clinker hydration are less in 25 WMBA CEM (Figure 5.13). The formation of a denser microstructure in 90-day 25 WMBA CEM can be attributed to the



reaction products of WMBA particles filling the capillary pores, especially those smaller than 10 nm.

### 5.3.5 Strength development of hardened cement pastes

Figure 5.25 shows the compressive strength of 25 WMBA CEM at different curing ages. The compressive strength of 100 CEM and 25 M300 CEM was also provided for comparison. Regardless of the curing age, the compressive strength of 100 CEM is the highest among all these three mixtures. Compared with 100 CEM, the replacement of 25 wt.% PC with WMBA reduced the compressive strength by around 15 % at the age of 90 days. The compressive strength of 25 WMBA CEM is higher than that of 25 M300 CEM, which is more evident at 1 day and 90 days.

The 1-day compressive strength of 25 WMBA CEM is 29.8 MPa, which is 5 MPa higher than the strength of 1-day 25 M300 CEM. The higher 1-day compressive strength of 25 WMBA CEM is mainly due to the formation of a larger amount of ettringite. As discussed in section 5.3.4.1 and section 5.3.4.2, clinker hydration degree in 25 WMBA CEM is almost equal to that in 25 M300 CEM. The  $\text{SO}_4^{2-}$  dissolved from WMBA particles facilitates ettringite formation. After 1-day curing, the total amount of reaction products in 25 WMBA CEM is more than that in 25 M300 CEM.

At 90 days, the compressive strength of 25 WMBA CEM reaches 82.3 MPa, which is 10.8 MPa larger than that of 25 M300 CEM. A denser microstructure in 90-day 25 WMBA CEM explains its higher compressive strength. The porosity of 90-day 25 WMBA CEM is smaller than that of 25 M300 CEM. Unlike M300, WMBA is reactive, and its reaction products can fill the capillary pores, thereby reducing the volume of capillary pores in 25 WMBA CEM (see section 5.3.4.5).

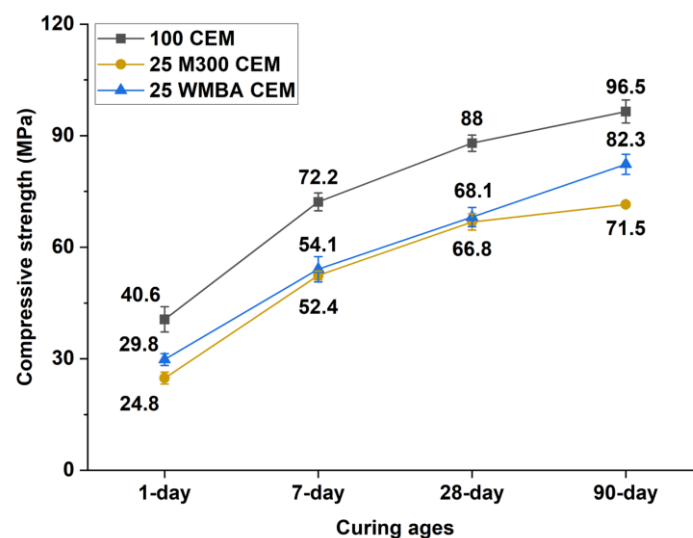


Figure 5.25 Compressive strength of cement pastes as a function of curing ages. The water-to-binder ratio of the paste samples is 0.4.

## 5.4 Conclusions

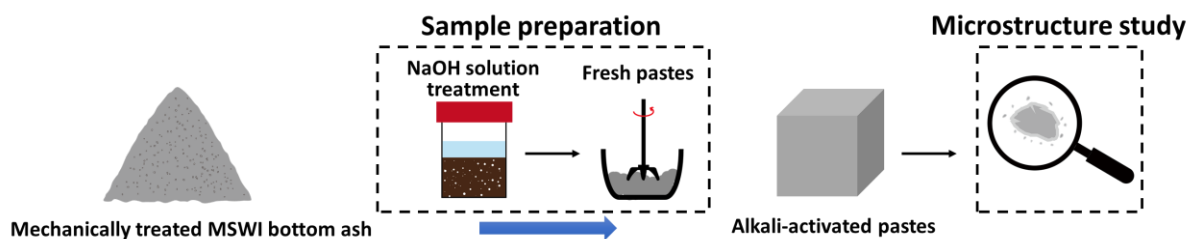
In this chapter, the use of *mechanically treated MSWI bottom ash (MBA)* as an alternative to Class F coal fly ash (FA) in blended cement pastes was discussed. Compared with plain cement paste (100 CEM), adding MBA to Portland cement paste affected clinker hydration and changed the reaction products and microstructure of cement pastes. MBA also participated in the reaction product formation in blended cement pastes and contributed to the strength development. The following are the findings of this work:

- The water treatment of MBA, performed at room temperature during the preparation of blended cement pastes, could reduce the metallic Al content by 85 %, reaching 0.02 wt.% in *water-treated MBA (WMBA)*. Due to water treatment, the replacement level of MBA in blended cement pastes can reach up to 25 wt.% without the formation of cracks caused by hydrogen gas release. The 28-day and 90-day compressive strength of Portland cement pastes blended with WMBA (WMBA CEM) was close to that of Portland cement pastes blended with FA.
- In the process of water treatment, the dissolution of MBA in water created an alkaline environment to facilitate the corrosion of metallic Al embedded in MBA. The water treatment only slightly changed the mineralogical compositions of MBA by increasing the contents of amorphous phase and calcite.
- Compared with 100 CEM, the incorporation of WMBA delayed cement hydration on the first day, but the hydration of clinker was enhanced at later ages in blended cement pastes prepared with 25 wt.% MBA and 75 wt.% Portland cement (25 WMBA CEM). After 90 days, the hydration degree of clinker in 25 WMBA CEM was higher than that in 100 CEM. The sulfate dissolved from MBA during water treatment increased the initial sulfate concentration in blended cement and thus promoted the ettringite formation in 1-day 25 WMBA CEM.
- In 25 WMBA CEM, the reaction of WMBA consumed portlandite, and the reaction products of WMBA were sodicgedrite and amorphous phase. The pozzolanic reaction of WMBA may produce C-S-H gel with a lower Ca/Si ratio. The Ca/Si ratio of the C-S-H gel was smaller than that of the C-S-H gel generated in 100 CEM.
- Although the Al/Si and Ca/Si atomic ratios were almost the same in the C-S-H gel formed in 25 WMBA CEM and Portland cement pastes blended with 25 wt.% M300 (25 M300 CEM), the C-S-H gel in 25 WMBA CEM incorporated more alkali ions. More reaction products were formed in 25 WMBA CEM than in 25 M300 CEM to fill the capillary pores. The compressive strength of 25 WMBA CEM was higher than 25 M300 CEM.

# Chapter 6

## Alkali-activated pastes<sup>(1)</sup> prepared with mechanically treated MSWI bottom ash as precursor

*NaOH solution treatment, microstructure formation, and strength development*



### Highlights

- When used as precursor for alkali-activated materials (AAM), the metallic Al content of *mechanically treated MSWI bottom ash (MBA)* needs to be reduced to zero to prevent the volume expansion of alkali-activated pastes.
- The metallic Al in MBA can be completely oxidized at room temperature by allowing MBA to react with NaOH solution in advance during the sample preparation process.
- After NaOH solution treatment of MBA, the compressive strength of alkali-activated pastes prepared with MBA and blast furnace slag (BFS) was similar to that of the alkali-activated pastes made from BFS and Class F coal fly ash.
- Blending BFS with *NaOH solution-treated MBA (CMBA)* enhanced the reaction of BFS at later ages. The reaction products of CMBA contributed to the strength development of alkali-activated CMBA-BFS pastes.

<sup>(1)</sup> Alkali-activated paste, alkali-activated mortar, and alkali-activated concrete all belong to alkali-activated materials.

## 6.1 Introduction

This chapter is about using *mechanically treated MSWI bottom ash (MBA)* to prepare alkali-activated materials (AAM). Given that the reactivity of MBA as precursor for AAM is similar to that of Class F coal fly ash (FA) (see Chapter 4), one of the research goals is to use MBA as an alternative to FA for the preparation of AAM and obtain similar compressive strength by optimizing the sample preparation process. The other goal is to understand the contribution of MBA to compressive strength by studying the effects of MBA addition on the reaction products and microstructure of alkali-activated pastes.

The prerequisite for preparing MBA-based AAM with compressive strength close to FA-based AAM is to reduce the metallic Al content of MBA to zero. The residual metallic Al in MBA is detrimental to the strength development, as it can easily oxidize and release hydrogen under high alkaline conditions in AAM [29,131,155,156,169]. The NaOH solution treatment of MSWI bottom ash has been performed by previous researchers to eliminate the adverse effects of metallic Al on strength development [131,157,172–174,178]. The NaOH solution treatment of MSWI bottom ash accelerated the oxidation of metallic Al, as well as the release of hydrogen gas.

At present, there is no protocol for the NaOH solution treatment of MSWI bottom ash (see Chapter 2). The concentration of the NaOH solution and the duration of the treatment was usually tailored according to the properties of as-received MSWI bottom ash. Current studies mainly focused on the effectiveness of NaOH solution treatment in reducing metallic Al content [131,157,172–174,178]. The reaction of MSWI bottom ash during NaOH solution treatment has not been extensively investigated yet. The compositional change caused by NaOH solution treatment can affect the reaction of MSWI bottom ash upon alkali activation, which in turn influences the mechanical properties of synthesized AAM.

As described in Chapter 2, AAM prepared with 100 wt.% MSWI bottom ash usually exhibits low strength at an early age. Compared with un-reacted MSWI bottom ash, AAM prepared with 100 wt.% MSWI bottom ash leaches more heavy metals into the environment [29,102,168]. MSWI bottom ash was used together with more reactive precursors to improve the compressive strength of MSWI bottom ash-based AAM. Blast furnace slag (BFS) is a more commonly selected precursor for blending with MSWI bottom ash than coal fly ash and metakaolin.

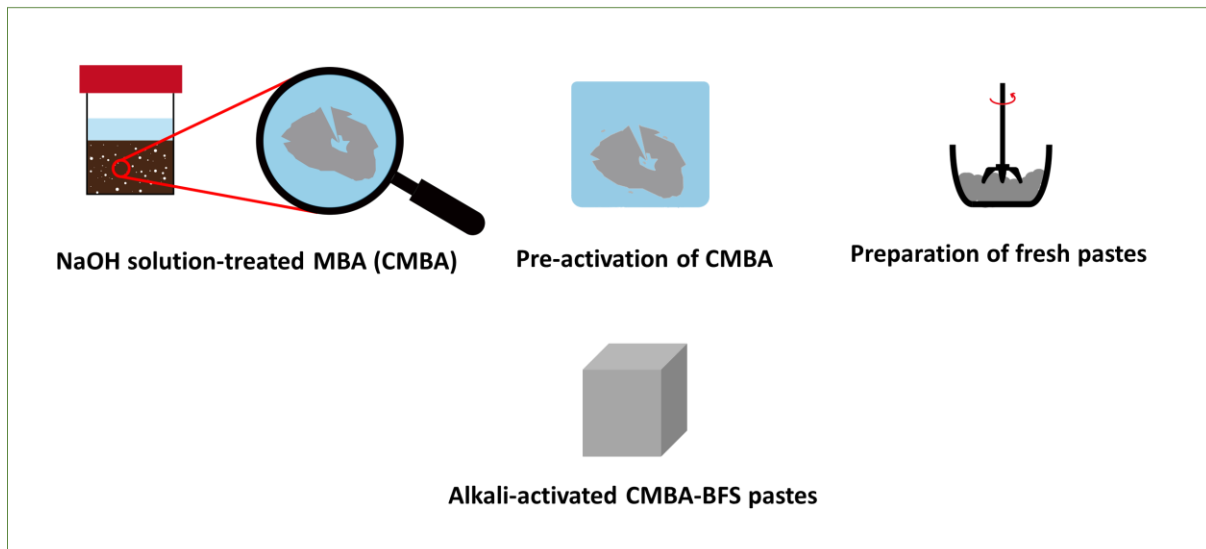
Previous researchers mainly studied the factors influencing the compressive strength of AAM prepared with blends of MSWI bottom ash and BFS (see Chapter 2). The influencing factors include the metallic Al content and the reactivity of MSWI bottom ash, the mass ratio between MSWI bottom ash and BFS in the precursor, the alkali modulus of the activator, and the curing condition [131,157,173]. There is little information about the reaction kinetics and the microstructure formation of AAM prepared with a blend of MSWI bottom ash and BFS. The engineering properties of AAM are determined by its microstructure. For a detailed understanding of the microstructural development, the reaction of MSWI bottom ash in AAM prepared with blends of MSWI bottom ash and BFS needs to be better understood.

This chapter consists of three parts (Figure 6.1):

### Part 1 NaOH solution treatment of mechanically treated MSWI bottom ash



### Part 2 Preparation of alkali-activated CMBA-BFS pastes



### Part 3 Microstructure study of alkali-activated CMBA-BFS pastes



Figure 6.1 The content of this chapter.

- In part 1, MBA is treated with NaOH solution to reduce its metallic Al content to zero. The effects of NaOH solution treatment on the mineralogical composition and the molecular structure of MBA are studied.
- In part 2, the *NaOH solution-treated MBA (CMBA)* in the slurry obtained after NaOH solution treatment is pre-activated before the alkali activation of BFS. The reaction products formed during the pre-activation of CMBA are investigated. The compressive strength of alkali-activated CMBA-BFS pastes is compared with that of the alkali-activated FA-BFS pastes.
- In part 3, the alkali-activated CMBA-BFS paste prepared with the highest amount of MBA is used for microstructure analysis to study the contribution of CMBA to compressive

strength. The samples of alkali-activated BFS paste and alkali-activated micronized sand-BFS pastes are used as references. The effects of CMBA on the reaction of BFS are studied from the perspectives of reaction kinetics, reaction degree, reaction product formation, porosity, and strength development.

## 6.2 Materials and methods

### 6.2.1 Materials

The materials used in this chapter include MBA, BFS, FA, and micronized sand (M300). For MBA, BFS, and FA, detailed information about their chemical and mineralogical compositions and particle size distribution can be found in Chapter 4. The micronized sand used in this chapter is the same as that used in Chapter 5.

### 6.2.2 Mix design

The mix was designed according to the reactivity of MBA, the leaching potential of MBA, and the thermodynamic modeling results of alkali-activated MBA paste (see Chapter 4). MBA was used together with BFS to prepare AAM and avoid the risks associated with the excessive leaching of heavy metals into the environment. As discussed in Chapter 4, the dosage of MBA in alkali-activated pastes should be lower than 50 wt.%. In addition to solving the problem of excessive leaching, the addition of more BFS than MBA is beneficial to the strength development of AAM, as BFS is much more reactive than MBA. The percentage of MBA in the precursor is 10 wt.%, 20 wt.%, or 30 wt.%.

The weight percentage of  $\text{Na}_2\text{O}$  in the activator was set to be 5 wt.%, relative to the mass of the precursor. This is because when the  $\text{Na}_2\text{O}$  content in the activator (NaOH solution) exceeds 5 wt.%, some of the Si released from MBA was predicted to present in the pore solution rather than forming stable reaction products with the Na provided by the activator (see Chapter 4). Besides, the reactivity of MBA is similar to that of FA. For BFS and FA used in this work, the experimental results of Nedeljković et al. [336] indicated that the optimal  $\text{Na}_2\text{O}$  wt.% in the activator was 4.8 wt.% for obtaining high compressive strength when blends of BFS and FA were used as precursor to prepare AAM.

The activator is composed of NaOH solution and water glass solution. The water glass solution contains 8 wt.%  $\text{Na}_2\text{O}$  and 26.9 wt.%  $\text{SiO}_2$ . The molar ratio between  $\text{SiO}_2$  and  $\text{Na}_2\text{O}$  in the activator, also referred to as the alkali modulus ( $M_s$ ) of the activator, is chosen to be one. Considering that the reactivity of MSWI bottom ash is similar to that of FA, the value of  $M_s$  is determined with reference to the optimal range of the alkali modulus (between 1 and 1.5 [337]) for the preparation of AAM with a mixture of BFS and FA. The experience of Huang et al. [157,174] is also used as a reference. They reported that the mixture of water NaOH solution and water glass with the alkali modulus of 1.04 was the optimal activator for AAM prepared with MSWI bottom ash and BFS [157,174].

For all mixtures, the water-to-precursor mass ratio was kept constant at 0.35. In total, five series of alkali-activated paste samples were prepared. The mix design of these paste samples can be found in Table 6.1. 100 BFS AAM, FA-BFS AAM, and M300-BFS AAM were prepared as

references to MBA-BFS AAM and CMBA-BFS AAM. 100 BFS AAM is alkali-activated paste prepared with 100 % BFS. FA-BFS AAM, MBA-BFS AAM, CMBA-BFS AAM, and M300-BFS AAM are alkali-activated pastes made from BFS and another type of precursor. The raw materials used to prepare MBA-BFS AAM and CMBA-BFS AAM are the same, but the sample preparation procedures are different. In binary AAM systems, the percentages of BFS replaced by FA, M300, or MBA are 10 wt.%, 20 wt.%, and 30 wt.%. It is worth mentioning that if the dosage of MBA exceeds 30 wt.%, the amount of solution required for the NaOH solution treatment of MBA is more than can be taken from the activator used for the preparation of CMBA-BFS AAM.

Table 6.1 Mix design of alkali-activated paste samples.

Paste samples	Precursors (wt.%)				Activator
	FA	MBA	M300	BFS	
100 BFS AAM	-	-	-	100	
10 FA-BFS AAM	10	-	-		
10 MBA-BFS AAM	-	10	-	90	
10 CMBA-BFS AAM*	-	10	-		
20 FA-BFS AAM	20	-	-		
20 CMBA-BFS AAM*	-	20	-	80	
30 FA-BFS AAM	30	-	-		
30 CMBA-BFS AAM*	-	30	-	70	
30 M300-BFS AAM	-	-	30		

- Water-to-precursor mass ratio: 0.35
- Na<sub>2</sub>O content: 5 wt.%
- Alkali modulus: 1

\*The NaOH solution treatment of MBA was included in the sample preparation process.

### 6.2.3 Sample preparation

Figure 6.2 (a) depicts the sample preparation procedure of CMBA-BFS AAM. MBA and BFS are the precursors used to prepare CMBA-BFS AAM. The activator used for the preparation of CMBA-BFS AAM is divided into two parts. One part is the NaOH solution (3 mol/L) prepared by dissolving the NaOH pellets (analytical grade, purity  $\geq 98\%$ ) in distilled water. The other part, also referred to as the remaining activator, is made by mixing NaOH pellets, distilled water, and Na<sub>2</sub>SiO<sub>3</sub> solution.

When preparing CMBA-BFS AAM, MBA was first treated with NaOH solution, and the goal was to oxidize the metallic Al in MBA. The mass ratio between NaOH solution and MBA is 0.7. As shown in Figure 6.3, the mixture of MBA and NaOH solution was sealed in a polyethylene container at room temperature (between 22 to 25 °C). This mixture is named “slurry” in this context. The NaOH solution treatment lasted until the metallic Al content in the slurry was reduced to zero. During NaOH solution treatment, the water displacement method described in Chapter 3 was used to measure the metallic Al content in the slurry and to monitor its changes with time. In the end, the NaOH solution treatment lasted for 5 days. The solids in the 5-day slurry are the *NaOH solution-treated MBA (CMBA)*.

After NaOH solution treatment, the remaining activator was added to the 5-day slurry. The mixture of slurry and activator was kept for 1 day at room temperature. During this process,



the CMBA in the slurry was pre-activated. After the pre-activation of CMBA, the 1-day mixture was blended with BFS using a high-shear mixer (model IKA® T 50 ULTRA-TURRAX®) to prepare CMBA-BFS AAM.

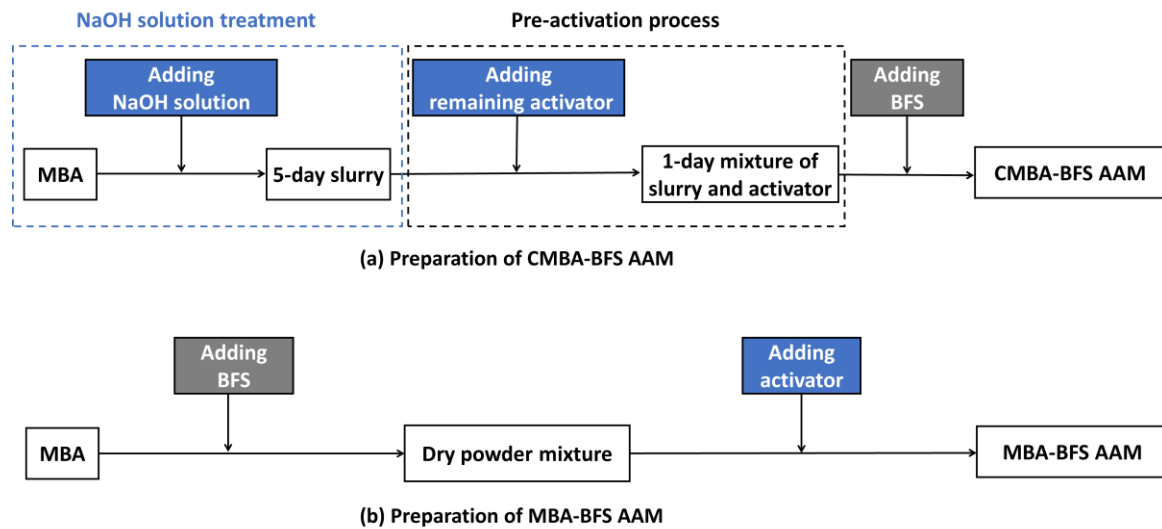


Figure 6.2 Illustration of the sample preparation process of (a) CMBA-BFS AAM and (b) MBA-BFS AAM.

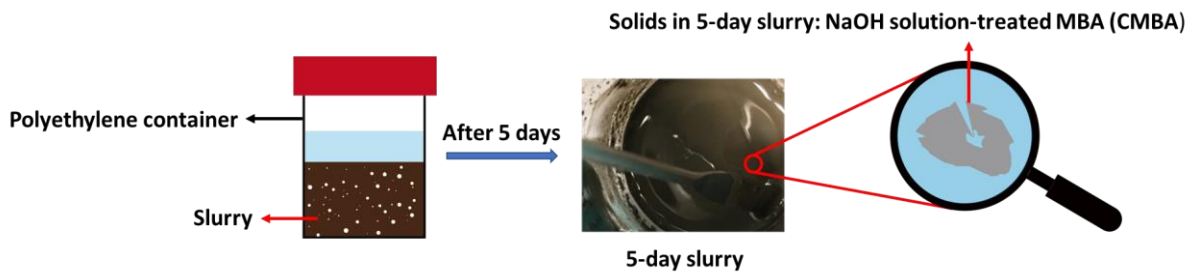


Figure 6.3 Illustration of the NaOH solution treatment of MBA.

Although the raw materials were the same, MBA-BFS AAM was prepared in a way different from CMBA-BFS AAM. As illustrated in Figure 6.2 (b), the precursors of MBA-BFS AAM were dry mixed before the addition of the activator. The activator, which was prepared with NaOH pellets, distilled water, and  $\text{Na}_2\text{SiO}_3$  solution, was directly added to the dry powder mixture. The activator and precursors were mixed for 4 minutes using a high-shear mixer to prepare MBA-BFS AAM.

FA-BFS AAM and M300-BFS AAM were prepared following the same procedure as that of MBA-BFS AAM. 100 BFS AAM was prepared by mixing BFS with activator for 4 minutes with a high-shear mixer. The mold used for the casting of AAM fresh pastes has a dimension of  $20 \times 20 \times 20 \text{ mm}^3$ . The alkali-activated paste specimens were first cured at room temperature for 24 hours. After demolding, the specimens were sealed and cured in a fog room ( $20^\circ\text{C}$ , 99 % RH) until the test ages.

### 6.2.4 Studies of reactions during NaOH solution treatment and pre-activation process

#### Reaction between MBA and NaOH solution

The reaction of MBA during NaOH solution treatment was studied using a TAM-AIR-314 isothermal conduction calorimeter. The calorimeter was loaded with around 10 g of slurry that had been poured and sealed in a glass ampoule. The slurry was prepared by mixing MBA with NaOH solution. The temperature of the calorimeter was kept at 20 °C.

#### Characterization of CMBA

The effect of NaOH solution treatment on the composition change of MBA was investigated by characterizing CMBA. The CMBA used for characterization was obtained after drying the 5-day slurry in a vacuum freeze-dryer (-24 °C and 0.1 Pa) for more than three months (Figure 6.4). The mineralogical composition of CMBA was characterized using X-ray diffraction (XRD) measurements combined with quantitative X-ray diffraction (QXRD) analysis. The XRD measurements and data analysis follow the same procedure described in Chapter 3. The molecular structure of the amorphous phase was studied by identifying the chemical bonds of CMBA with Attenuated Total Reflectance-Fourier Transform Infrared spectroscopy (ATR-FTIR) (model Perkin Elmer Spectrum 100). The measurement covers the wavenumber from 600 to 4000  $\text{cm}^{-1}$ , and the resolution is 1  $\text{cm}^{-1}$ . The FTIR spectra of MBA and the glass particles present in MBA were measured as a reference. The glass particles used here are the same as those used in Chapter 4 (Figure 4.3(b)).

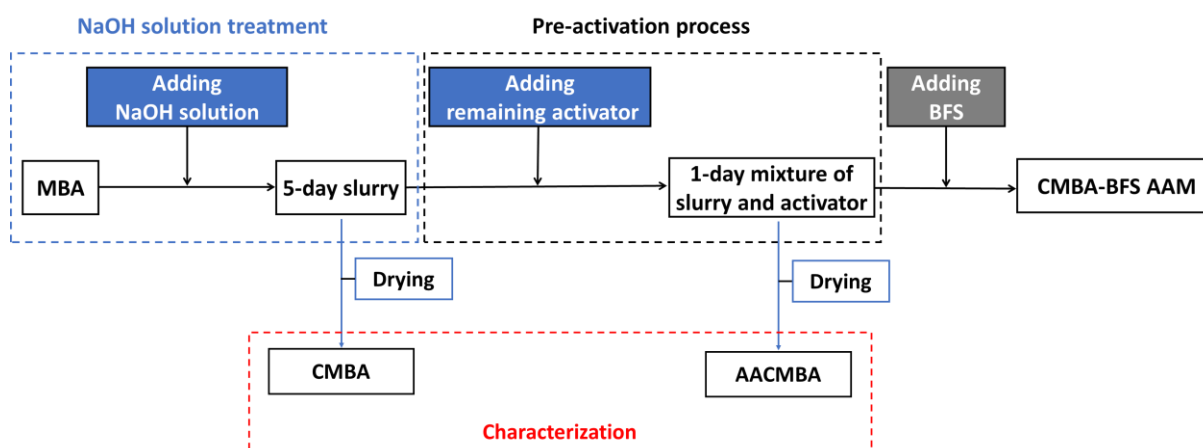


Figure 6.4 The preparation of NaOH solution-treated MBA (CMBA) and alkali-activated CMBA (AACMBA) used for characterization.

#### Reaction of CMBA during pre-activation process

After NaOH solution treatment, the 5-day slurry, which contains CMBA, was mixed with the remaining part of the activator for one day (see Figure 6.2). The reaction of CMBA during this pre-activation process was studied by measuring the reaction heat with a TAM-AIR-314 isothermal conduction calorimeter. For the test, around 10 g of the mixture of slurry and activator was loaded in the glass ampoule. The temperature of the calorimeter was kept at 20 °C.

### *Characterization of AACMBA*

The reaction products formed after the 1-day pre-activation of CMBA were studied by XRD and ATR-FTIR. The water in the 1-day mixture of the slurry and the activator was removed in a vacuum freeze-dryer (-24 °C and 0.1 Pa) (Figure 6.4). After drying, the solid obtained was named alkali-activated CMBA (AACMBA). The mineralogical composition of AACMBA was determined with XRD. The molecular structure of the amorphous phase in AACMBA was studied with ATR-FTIR. The measurement and data analysis were the same as that used in the analysis of CMBA.

### **6.2.5 Paste sample characterization**

The alkali-activated paste samples were characterized from the following perspectives: compressive strength, reaction kinetics, porosity, reaction products, and reaction degree. Except for the determination of reaction degree, the tests and analysis of the alkali-activated paste samples followed the same method used for the characterization of cement pastes (see Chapter 5). The compressive strength of the cubic samples was measured at the curing ages of 1 day, 7 days, 28 days, and 90 days. The X-ray computed tomography scan was performed on the paste samples to check whether cracks were formed in CMBA-BFS AAM. The reaction kinetics of AAM were measured using isothermal calorimetry tests.

The reaction in alkali-activated pastes was stopped using the solvent exchange method before the characterization of porosity, reaction products, and reaction degree. The porosity in hardened pastes was measured using nitrogen adsorption tests. The crystalline reaction products formed in AAM were identified with XRD. The contents of the crystalline and amorphous phases in AAM were determined with QXRD analysis. The molecular structure of the gel formed in AAM was characterized by ATR-FTIR. The morphology of the paste samples was observed under scanning electron microscopy (SEM). The backscattered electron (BSE) images of the hardened paste samples were taken with SEM. The chemical composition of the gel phases in AAM was measured with the Energy Dispersive X-rays spectroscopy (EDS) detector of the SEM.

### *Reaction degree of BFS in AAM*

The reaction degree of the BFS in AAM was determined to study the effects of CMBA or M300 on the reaction of BFS. The reaction degree of BFS in hardened alkali-activated pastes can be calculated with the equation:  $\alpha(t) = (1 - \frac{V_t}{V_0}) \times 100\%$ , where  $\alpha(t)$  is the degree of reaction at age  $t$ ,  $V_t$  is the volume fraction of BFS at age  $t$ , and  $V_0$  is the initial volume fraction of BFS in the pastes [159,338,339]. The volume fraction of unreacted BFS in hardened pastes was determined by image analysis. According to Chayes et al. [340], the volume fractions can be assumed to be equal to the area fraction calculated from two-dimensional images. The number of frames required for the image analysis was determined according to the method proposed by Ye [339]. This BSE image used for the image analysis was taken at the magnification of 1500. The frame area of this BSE image was 50770  $\mu\text{m}^2$ . The area fraction of BFS was plotted as a function of the total investigated area. Figure 6.5 indicates that the area fraction of BFS reached a stable value after the total investigated area exceeded  $7.6 \times 10^5 \mu\text{m}^2$ .

This means at least fifteen BSE images were required to get a representative area fraction of BFS in the pastes.

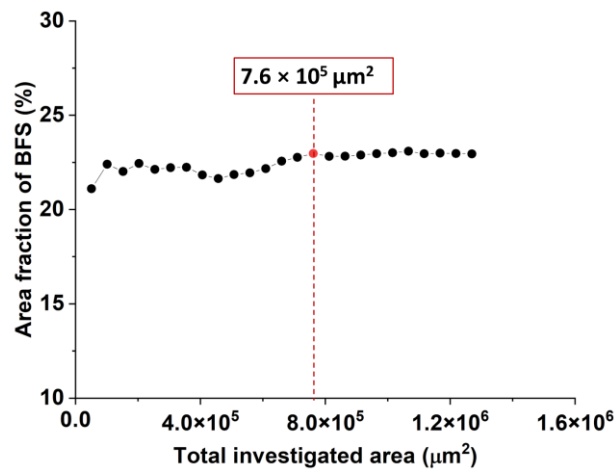


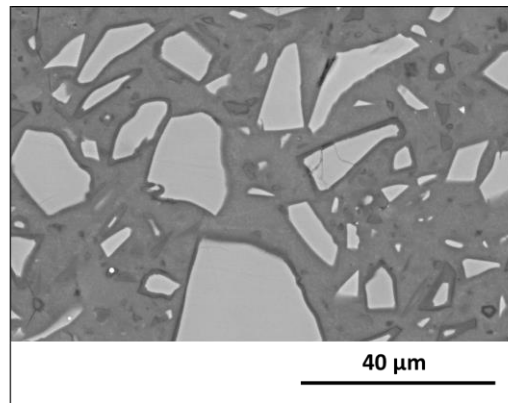
Figure 6.5 The area fraction of blast furnace slag as a function of total investigated area for 90-day 100 BFS AAM paste sample.

The area fraction of BFS in hardened pastes was calculated for the BSE images of 100 BFS AAM, 30 M300-BFS AAM, and 30 CMBA-BFS AAM paste samples. Examples of the phase segmentation process are shown in Figure 6.6 and Figure 6.7. The BSE image has 255 different shades of gray. The gray level ranges from 0 (black) to 255 (white). The grey level histogram indicates the number of pixels for each brightness level. The phase segmentation was performed with the image processing program ImageJ.

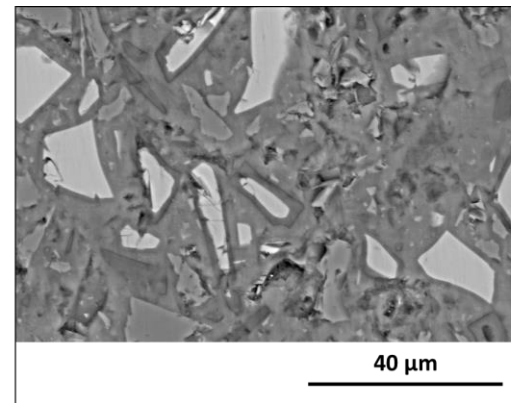
The unreacted BFS particles can be easily identified in the BSE images of 100 BFS AAM and 30 M300-BFS AAM (Figure 6.6). The unreacted BFS particles in 100 BFS AAM and 30 M300-BFS AAM were segmented using the thresholding method proposed by Prewitt et al. [341]. After the thresholding operation, pixels representing the unreacted BFS particles were separated. In obtained 2D binary images (Figure 6.6 (c) and (f)), the white area corresponds to the unreacted BFS particles. The chemical composition in the white area is consistent with the chemical composition of unreacted BFS particles measured by the SEM-EDS spot analysis.

It is difficult to distinguish the unreacted BFS particles from the unreacted CMBA particles based on the grey level histogram of 30 CMBA-BFS AAM (Figure 6.7 (b)). The BSE images were analyzed with Trainable Weka Segmentation plugin in ImageJ, the machine-learning tool. With this method, the pixels of the BSE image of 30 CMBA-BFS AAM were separated into two classes: gel phases and particles. The particles mentioned here include unreacted CMBA particles, unreacted BFS particles, and reaction products that are brighter than the surrounding gel phases. The reference pixels corresponding to the gel phases and particles were manually selected to train the classifier, then the remaining pixels of the BSE images can be segmented automatically. The output image of Trainable Weka Segmentation is illustrated in (Figure 6.7 (c)). The unreacted BFS particles (colored yellow in Figure 6.7 (d)) were manually selected from the particles shown in Figure 6.7 (c) by combining the composition information obtained by the SEM-EDS spot analysis and the characteristic morphology of unreacted BFS

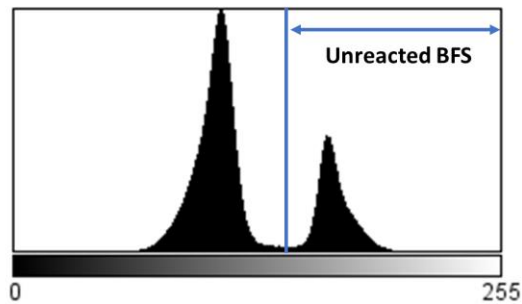
particles. The unreacted BFS particles are characterized by a layer of inner products located in their surroundings.



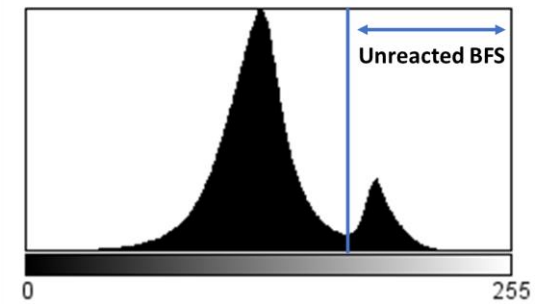
(a) BSE image of 90-day 100 BFS AAM



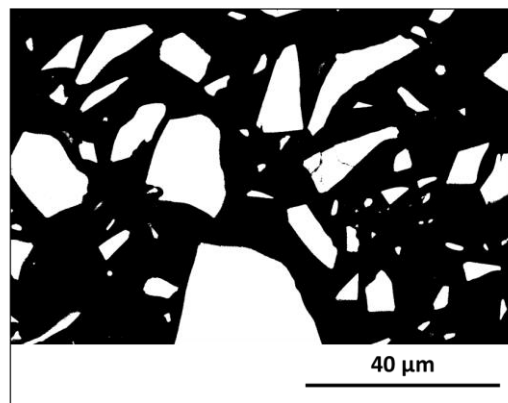
(d) BSE image of 90-day 30 M300-BFS AAM



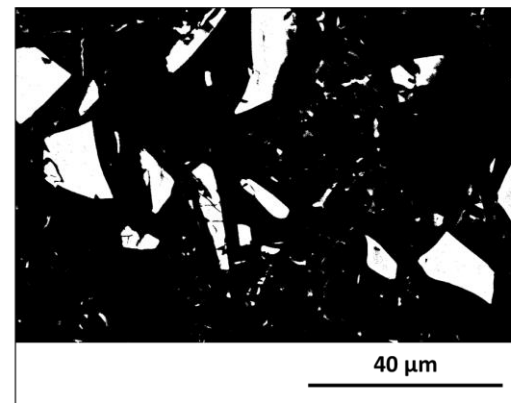
(b) Grey scale histogram



(e) Grey scale histogram

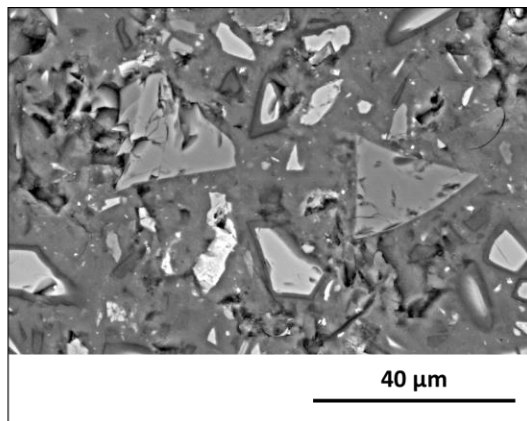


(c) 2D binary image of 90-day 100 BFS AAM

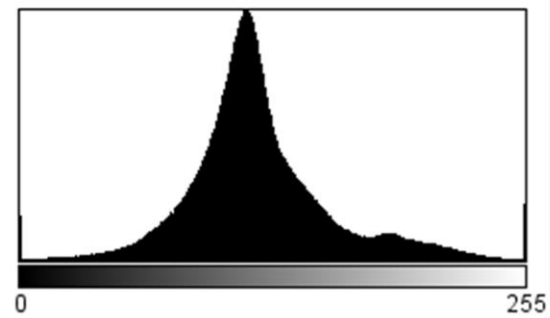


(f) 2D binary image of 90-day 30 M300-BFS AAM

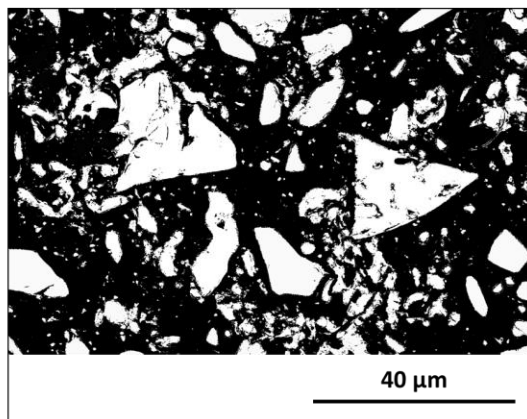
Figure 6.6 Phase segmentation of 90-day 100 BFS AAM and 90-day 30 M300-BFS AAM. The white particles in the 2D binary images are segmented unreacted BFS particles.



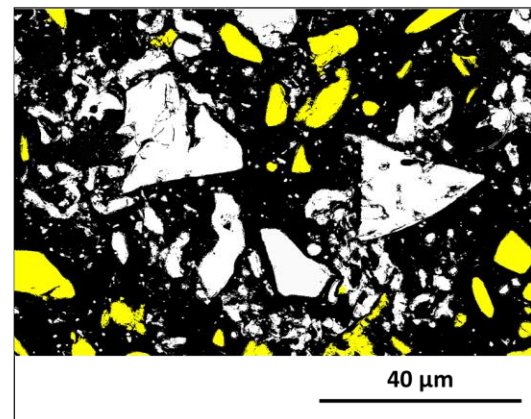
(a) BSE image of 90-day 30 CMBA-BFS AAM



(b) Grey scale histogram



(c) Output image of Trainable Weka Segmentation



(d) Manually separated unreacted BFS particles (yellow)

Figure 6.7 Phase segmentation of 90-day 30 CMBA-BFS AAM.

## 6.3 Results and discussion

### 6.3.1 Reactions during NaOH solution treatment and pre-activation process

When preparing CMBA-BFS AAM, MBA was treated with NaOH solution to reduce its metallic Al content to zero. Apart from metallic Al, the mineral phases of MBA also reacted during NaOH solution treatment, resulting in composition changes. After NaOH solution treatment, the obtained 5-day slurry was mixed with the remaining part of the activator for one day to allow CMBA to react prior to the alkali activation of BFS (see Figure 6.2 (a)). This pre-activation of CMBA may lead to the formation of reaction products. In the following sections, the reactions that occurred during the NaOH solution treatment of MBA and the pre-activation of CMBA are discussed.

#### *Reaction of MBA during NaOH solution treatment*

The reaction between MBA and the NaOH solution was studied by isothermal calorimetry. In the heat evolution curve (Figure 6.8 (a)-(c)), the first peak with an intensity of 18 mW/g corresponds to the wetting and dissolution of MBA. The dissolution of MBA mainly concerns



the oxidation of metallic Al and the dissolution of the amorphous phases. The second peak appeared at 1.5 days. Although the intensity of this peak is minimal (about 0.04 mW/g), the appearance of this peak still indicates the possible formation of gel phases. After 2 days, no other peaks were observed in the heat evolution rate curve, but the heat release continued. The cumulative heat collected after 5-day NaOH solution treatment of MBA is about 30 J/g (Figure 6.8 (d)).

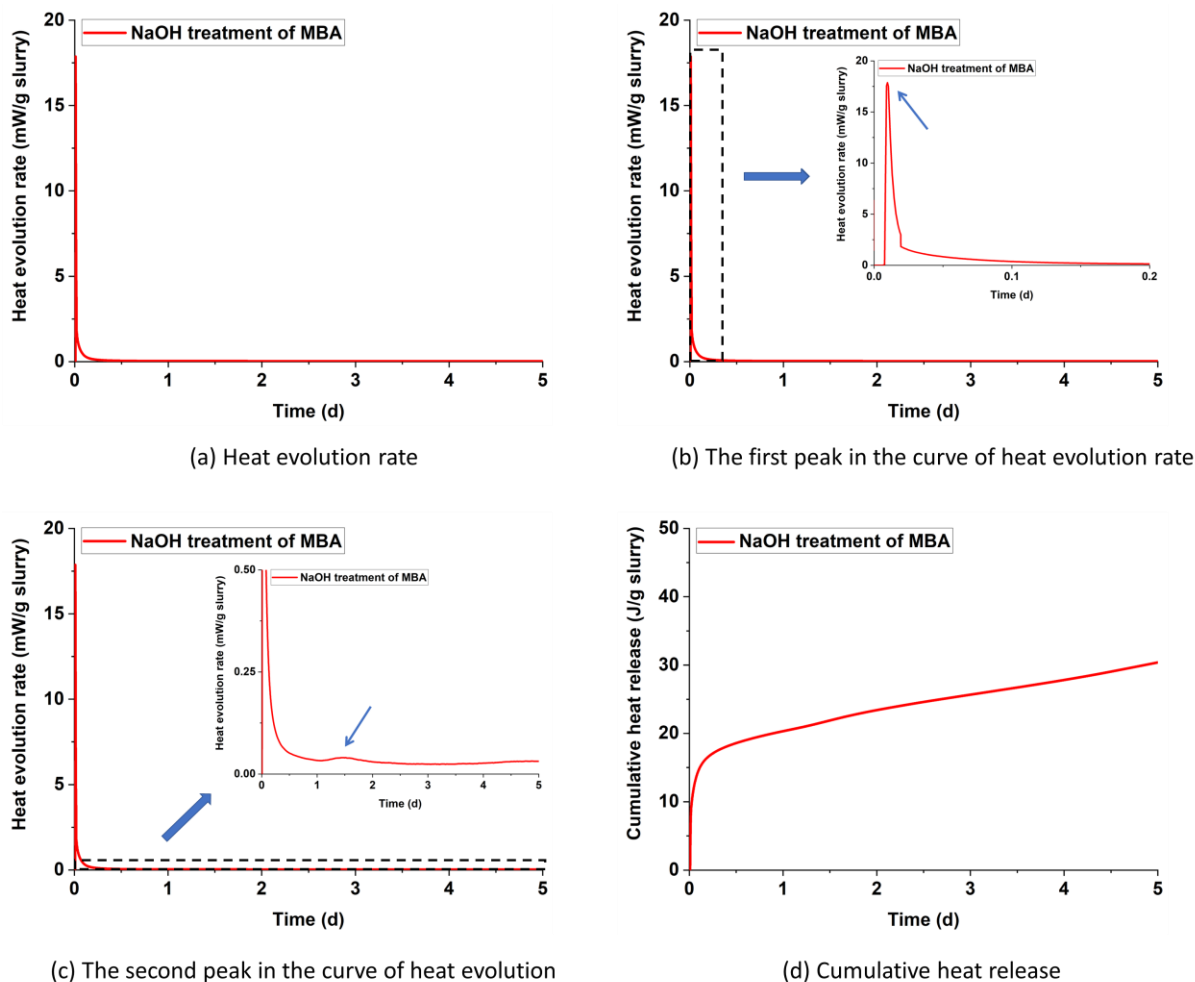


Figure 6.8 (a)-(c) Heat evolution rate and (b) cumulative heat release per gram of slurry. The slurry is prepared for the NaOH solution treatment of MBA.

#### *Composition change induced by NaOH solution treatment*

The mineralogical composition of MBA changed slightly after NaOH solution treatment. The XRD patterns of MBA and CMBA are nearly identical (Figure 6.9). The most notable differences are found at the  $2\theta$  of 29.4 and 37.7. The peak identified at 29.4° is assigned to calcite. Compared with MBA, the intensity of this calcite peak is lower in the XRD pattern of CMBA. According to the QXRD analysis, CMBA contains 1.3 wt.% calcite, lower than the calcite content in MBA (2.1 wt.%). The peak of natrite ( $\text{Na}_2\text{CO}_3$ ) was observed at 37.7° in the XRD pattern of CMBA, while sodium carbonate was not detected in MBA. The content of natrite in CMBA is 2.3 wt.% (Table 6.2). The CMBA used for characterization was prepared by drying the



5-day slurry obtained after NaOH solution treatment. During the drying process, the NaOH in the slurry can carbonate, leading to the formation of natrite.

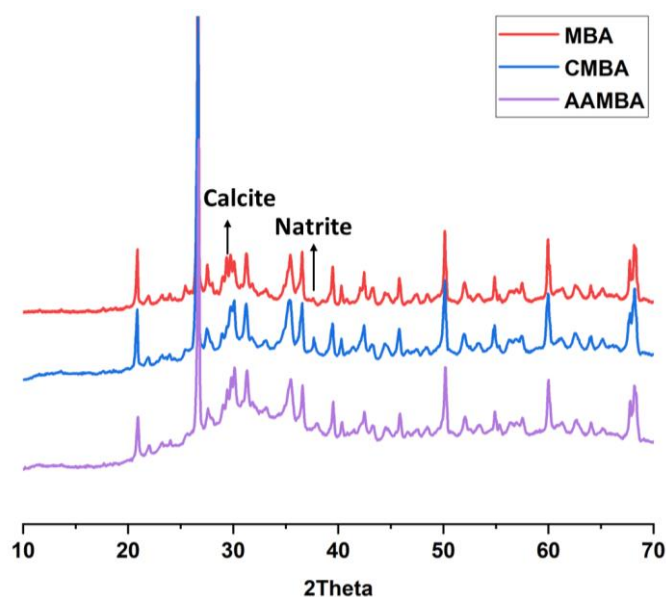


Figure 6.9 XRD patterns of MBA, CMBA, and AAMBA.

Table 6.2 Mineral phases present in MBA, CMBA, AACMBA, and QXRD analysis results.

Phases	MBA (wt.%)	CMBA (wt.%)	AACMBA (wt.%)	Formulae	ICSD codes
Quartz	12.1	11.7	10.7	SiO <sub>2</sub>	541929
Cristobalite	0.4	0.3	0.3	SiO <sub>2</sub>	1251919
Magnetite	0.9	0.9	0.6	Fe <sub>3</sub> O <sub>4</sub>	92356
Hematite	0.4	0.3	0.3	Fe <sub>2</sub> O <sub>3</sub>	453828
Wustite	0.2	0.2	0.0	FeO	309924
Gehlenite	2.8	2.0	0.9	Ca <sub>2</sub> Al <sub>2</sub> SiO <sub>7</sub>	1411155
Albite	1.9	2.0	3.1	NaAlSi <sub>3</sub> O <sub>8</sub>	1402109
Orthopyroxene	1.4	1.8	0.9	Ca <sub>0.02</sub> Mg <sub>0.30</sub> Fe <sub>0.68</sub> SiO <sub>3</sub>	1615622
Diopside	4.4	4.3	3.7	CaMg <sub>0.69</sub> Fe <sub>0.31</sub> Si <sub>2</sub> O <sub>6</sub>	77809
Wollastonite	2.6	3.0	3.5	CaSiO <sub>3</sub>	1253098
Calcite	2.1	1.3	1.6	CaCO <sub>3</sub>	1611066
Halite	0.4	0.4	0.3	NaCl	311644
Phosphammite	1.1	0.9	0.3	H(NH <sub>4</sub> ) <sub>2</sub> (PO <sub>4</sub> )	1401715
Corundum	0.7	0.6	0.4	Al <sub>2</sub> O <sub>3</sub>	527601
Goethite	0.4	0.5	0.3	FeO(OH)	71810
Gibbsite	0.2	0.2	0.2	Al(OH) <sub>3</sub>	1005040
Iron	0.1	0.1	0.1	Fe	1503158
Natrite	-	2.3	4.7	Na <sub>2</sub> CO <sub>3</sub>	168130
Amorphous phase	68.1	67.3	68.5	-	-
Sum	100	100	100	-	-

The FTIR spectrum of CMBA was compared with that of MBA to study the changes in molecular structure caused by NaOH solution treatment (Figure 6.10). In the spectra of MBA and CMBA, the bands at  $797\text{ cm}^{-1}$  and  $778\text{ cm}^{-1}$ , and  $693\text{ cm}^{-1}$  are characteristic vibrations of the Si-O in quartz [342]. The vibrations at  $1455\text{ cm}^{-1}$ ,  $1430\text{ cm}^{-1}$ ,  $876\text{ cm}^{-1}$ , and  $713\text{ cm}^{-1}$  are due to the presence of carbonates. The bands at  $1455\text{ cm}^{-1}$  and  $1430\text{ cm}^{-1}$  are attributed to the C-O stretching vibration mode [342,343]. The bands at  $876\text{ cm}^{-1}$  and  $713\text{ cm}^{-1}$  are assigned to the C-O bending vibration mode [342]. After the NaOH solution treatment of MBA, the intensity of the carbonate bands at  $1430\text{ cm}^{-1}$  and  $876\text{ cm}^{-1}$  was higher in the spectrum of CMBA. This band intensity increase is associated with the increased carbonate contents in CMBA (see Table 6.2).

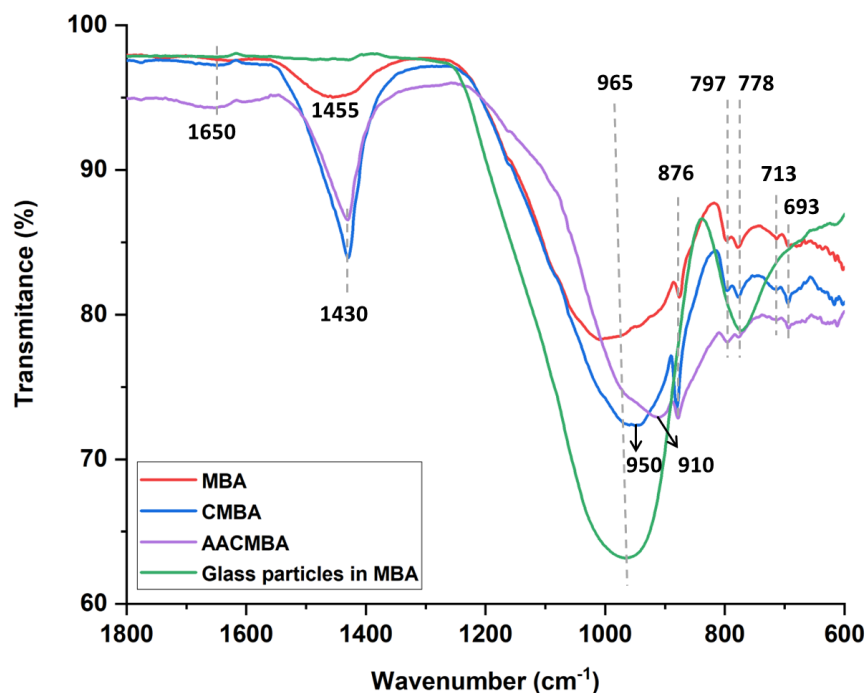


Figure 6.10 FTIR spectra of MBA, CMBA, AACMBA, and glass particles in MBA.

The main band observed in MBA is related to the stretching vibration of the Si-O-Si bond of the glass network [344]. This band is broad and centered at  $965\text{ cm}^{-1}$ , which corresponds to the location of the main band observed in the FTIR spectrum of the glass particles in MBA. Compared with MBA, the main band of CMBA is sharper, and its center is positioned at a lower wavenumber ( $950\text{ cm}^{-1}$ ). The differences in the main band between MBA and CMBA can be explained by the dissolution of the amorphous phase and the formation of calcium aluminosilicate hydrate (C-A-S-H) gel during NaOH solution treatment.

Since waste glass is one of the primary sources of the amorphous phase of MBA, the silicon released by MBA during NaOH solution treatment is likely to present as monomers. The silicate monomers were found after the dissolution of waste glass in NaOH solution [345]. The silicate monomers can react with each other to form dimers. The monomeric and dimeric silicate species exhibit vibrational bands between  $950$  and  $910\text{ cm}^{-1}$  [346], which overlap with the region of the main band of CMBA.

The silicate monomers can react with the  $\text{Al}(\text{OH})_4^-$  species dissolved by MBA, forming Si-O-Al complexes [347]. The asymmetric stretching vibration of Si-O-T bonds (T: tetrahedral Si or Al) in C-A-S-H gel [348–350] appeared at wavenumber the same as the main band of CMBA. A band at  $1650\text{ cm}^{-1}$ , albeit with low intensity, was detected in the FTIR measurements of CMBA. This band is usually assigned to the bending mode of the H-OH bond, which is the typical resonance of water within the gel phases [350]. These findings show that the C-A-S-H gel was formed during the NaOH solution treatment of MBA, but its content was very small.

#### *Reaction of CMBA during pre-activation process*

The reaction of CMBA during pre-activation process was studied by measuring the reaction heat. In the heat evolution curve (Figure 6.11 (a)), the peak associated with the wetting and dissolution was observed at the beginning of the measurement. However, the intensity of this peak was very small. A possible explanation is that no additional solid was added to the mixture, and CMBA was already wetted in the 5-day slurry. The main peak appeared at around 0.12 day. The appearance of this exothermic peak can be attributed to the gel phase formation. The cumulative reaction heat collected during the 1-day pre-activation of CMBA was about 10 J/g (Figure 6.11 (b)).

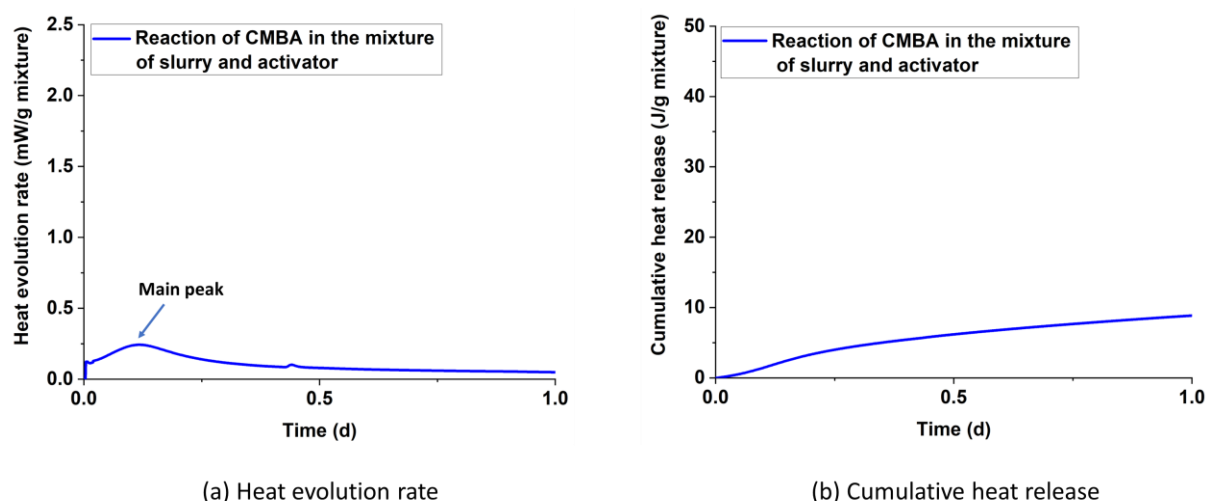


Figure 6.11 (a) Heat evolution rate and (b) cumulative heat release per gram of the mixture of 5-day slurry and activator. The 5-day slurry is obtained after the NaOH solution treatment of MBA and thus contains CMBA.

#### *Reaction products formed during pre-activation process*

The intensity of the main peak observed at around 0.12 day during the 1-day pre-activation of CMBA (Figure 6.11 (a)) is much higher than the second peak detected during the NaOH solution treatment of MBA (Figure 6.8 (c)). This observation suggests that more gel phases were formed after the pre-activation of CMBA. This statement is further supported by the results of XRD and FTIR measurements. Compared with MBA and CMBA, the hump representing the amorphous phase is more evident in the XRD pattern of AACMBA (Figure 6.9). According to the QXRD analysis, the amorphous phase in AACMBA is slightly higher than in MBA and CMBA (Table 6.2). In the FTIR spectra of AACMBA and CMBA (Figure 6.10), the

band at  $1650\text{ cm}^{-1}$  is assigned to the H-OH bond within the gel phases [350]. This band is more pronounced in the AACMBA spectrum than in the spectrum of CMBA. It is worth mentioning that a large amount of activator was not consumed by the pre-activation of CMBA, as the natrite content in AACMBA is higher than that in CMBA (Table 6.2).

The main band at  $910\text{ cm}^{-1}$  in the FTIR spectrum of AACMBA can be attributed to the silicate monomers present in the activator [346], the Al-O stretching vibration in octahedral Al species [351,352], and the Si-O-Na bond formed on the surface of CMBA due to the hydrolysis of silica [353]. The bands associated with the vibrations of silicate monomers and dimers are observed in the region of  $910\text{--}950\text{ cm}^{-1}$  [346]. As shown in Figure 6.10, the main band of AACMBA is narrower and positioned at a lower wavenumber than the main band of CMBA. The main band in CMBA is assigned to the stretching vibration of the Si-O-T bonds (T: tetrahedral Si or Al) in C-A-S-H gel [348–350]. The shift of the main band to a lower wavenumber in AACMBA indicates that some  $\text{Si}^{4+}$  ions have been substituted by  $\text{Al}^{3+}$ . The bonding force of Al-O is weaker than that of the Si-O bond [348,354]. Another factor that can cause a significant shift in the asymmetric stretch of the Si-O-T network to lower wavenumbers is the incorporation of  $\text{Na}^+$  [355]. The molecular vibrational constant of the Si-O-Na bond was lower compared to the Si-O-T bond.

The gel phases detected in AACMBA can be a mixture of C-A-S-H gel and sodium aluminosilicate hydrate (N-A-S-H) gel. The C-A-S-H gel already formed after the NaOH solution treatment of MBA, and this gel remains in AACMBA. The addition of NaOH solution and activator to MBA increased the total mass. As a result, the relative content of the minerals initially present in MBA should be lower in CMBA and AACMBA. However, the albite and wollastonite content increased continuously after the NaOH solution treatment of MBA and the pre-activation of CMBA (Table 6.2). This phenomenon indicates the possible formation of the C-A-S-H and N-A-S-H gel. The deduction about the co-existence of the C-A-S-H and N-A-S-H gel in AACMBA is consistent with the phase assemblage of alkali-activated MBA paste predicted by thermodynamic modeling (see Chapter 4) and the observations reported by previous researchers [29,47].

### 6.3.2 Effectiveness of NaOH solution treatment in eliminating volume expansion of alkali-activated pastes prepared with MBA and BFS

When MBA was used to substitute BFS in BFS-based AAM, volume expansion could already be observed at a replacement level of 10 wt.%. Figure 6.12 shows the side view of the alkali-activated paste sample prepared with blends of 10 wt.% MBA and 90 wt.% BFS (10 MBA-BFS AAM). This figure shows that the height of the 10 MBA-BFS AAM paste sample is higher than 2 cm, the height of the mold used for casting. The volume expansion of 10 MBA-BFS AAM was caused by the oxidation of metallic Al embedded in MBA. Metallic Al was oxidized upon its contact with activator. The hydrogen gas released after this reaction led to the volume expansion of unhardened alkali-activated pastes.

After the NaOH solution treatment of MBA, the metallic Al that remained in CMBA was zero. The risks of cracking and volume expansion associated with metallic Al were eliminated (Figure 6.13). Only pores were found within CMBA-BFS AAM, as illustrated in the 2D binary images and 3D images obtained after CT scan (Figure 6.13). These pores were mainly air bubbles entrained in the fresh pastes during the sample preparation. The total volume of the air bubbles can be minimized by optimizing the vibration process of the fresh pastes. As for metallic Al removal, the NaOH solution treatment of MBA is very effective.

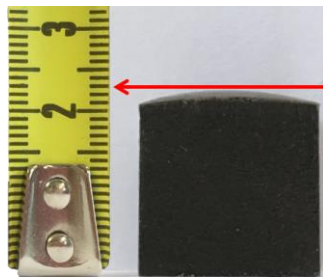


Figure 6.12 The side view of 1-day 10 MBA-BFS AAM paste sample.

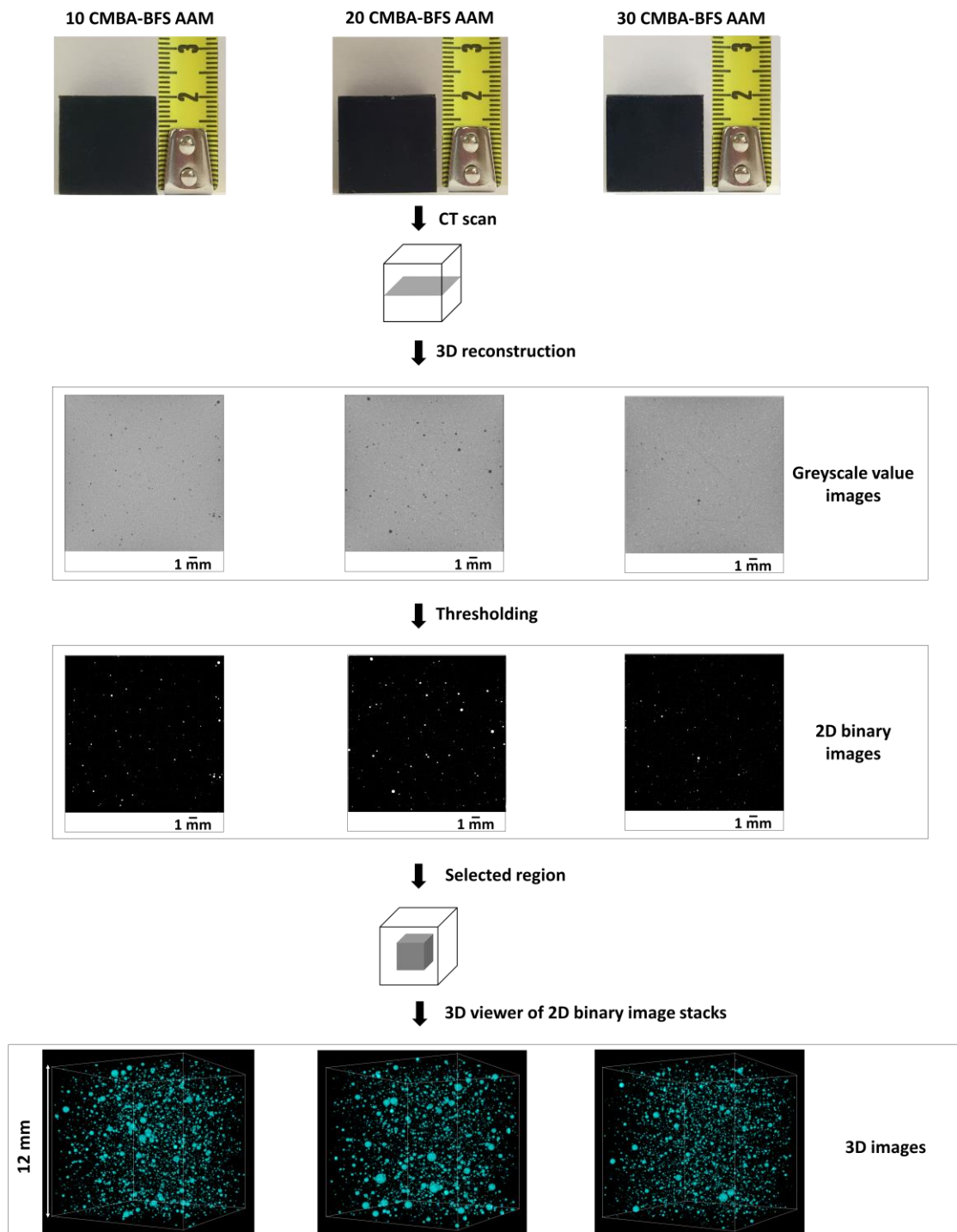


Figure 6.13 CMBA-BFS AAM paste samples: Photos of 1-day CMBA-BFS AAM paste samples indicate that there are no cracks or pores on the surface. The greyscale value images, 2D binary images, and 3D images obtained after CT scan and image analysis show the pores inside 1-day CMBA-BFS AAM paste samples. The white areas in the 2D binary image represent the pores. The regions colored cyan in 3D images refer to the space occupied by pores.

### 6.3.3 Comparison of compressive strength between CMBA-BFS AAM and FA-BFS AAM

The compressive strength of CMBA-BFS AAM was compared with FA-BFS AAM to examine the possibility of using MBA as an alternative to FA for the preparation of alkali-activated pastes. Figure 6.14 (a) shows that the 28-day compressive strength of 10 CMBA-BFS AAM is slightly lower than that of 10 FA-BFS AAM. At replacement levels of 20 wt.% and 30 wt.%, the 28-day CMBA-BFS AAM is stronger than the 28-day FA-BFS AAM. After 90 days of curing (Figure 6.14 (b)), the compressive strength of FA-BFS AAM is almost equal to that of CMBA-BFS AAM at the same replacement level (from 10 wt.% to 30 wt.%). Therefore, it is possible to replace FA with MBA in alkali-activated FA-BFS pastes without loss of compressive strength when NaOH solution treatment of MBA is included in the sample preparation process.

It is worth noting that the reactivity of MBA as AAM precursor is almost the same as that of FA (see Chapter 4). The NaOH solution treatment of MBA only slightly changed its compositions. The 28-day and 90-day compressive strength of CMBA-BFS AAM and FA-BFS AAM are expected to be within the same range. The higher 28-day compressive strength of 20 CMBA-BFS AAM and 30 CMBA-BFS AAM can be attributed to the fact that MBA had reacted with the activator prior to the addition of BFS. Due to the NaOH solution treatment and the pre-activation process, the reaction of MBA was accelerated and thus can contribute to the 28-day compressive strength. In the case of FA-BFS AAM, FA and BFS were mixed with the activator at the same time. The reaction rate of FA at room temperature is very slow and usually contributes to the strength development at later ages [159,225]. The contribution of FA to the 28-day compressive strength was much smaller than to the 90-day compressive strength.

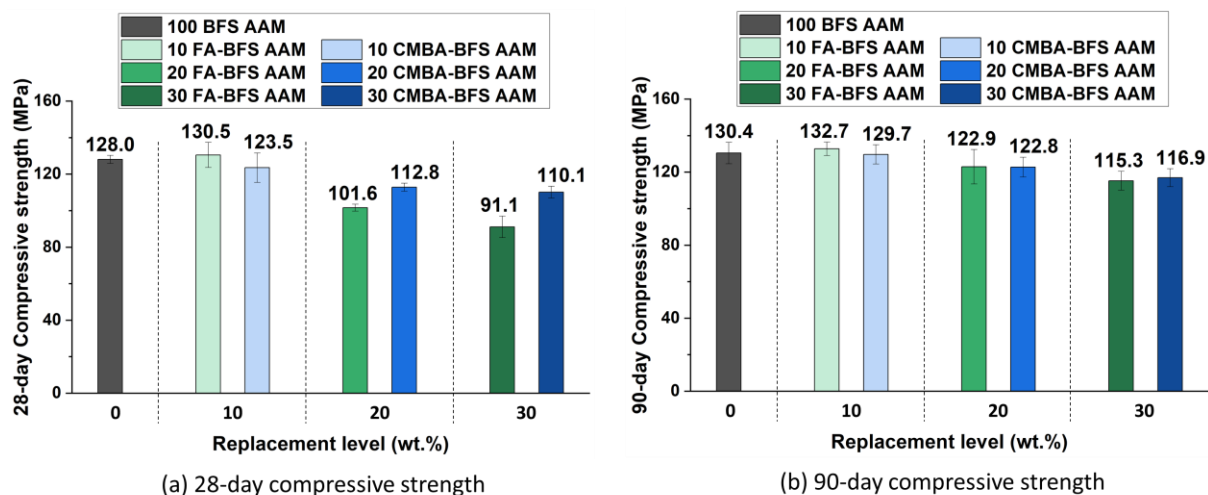


Figure 6.14 Compressive strength of (a) 28-day alkali-activated pastes and (b) 90-day alkali-activated pastes.



### 6.3.4 Formation and analysis of the microstructure of alkali-activated pastes

As discussed above, the compressive strength of CMBA-BFS AAM is close to that of FA-BFS AAM when the dosage of MBA and FA is the same. The highest achievable dosage of MBA in CMBA-BFS AAM is 30 wt.%. In this section, the paste sample of 30 CMBA-BFS AAM is analyzed to investigate the role of *NaOH solution-treated MBA* in the formation of alkali-activate paste microstructure. For comparison purposes, the microstructure formation of alkali-activated BFS paste (100 BFS AAM) and alkali-activated pastes prepared with blends of 30 wt.% inert micronized sand and 70 wt.% BFS (30 M300-BFS AAM) is also studied.

#### 6.3.4.1 Effects of CMBA on the reaction of BFS

##### Reaction kinetics

The heat evolution of 30 CMBA-BFS AAM was measured to determine its reaction kinetics. As a reference, the heat release of 100 BFS AAM and 30 M300-BFS AAM was also measured. The main peak in the heat evolution rate curve appeared between 0.5 and 1 day (Figure 6.15 (a)). The appearance of this peak is associated with the formation of reaction products. The intensity of the main peak is the highest in 100 BFS AAM, followed by 30 M300-BFS AAM and 30 CMBA-BFS AAM.

The heat released by 30 M300-BFS AAM and 30 CMBA-BFS AAM within the first two days is mainly due to the reaction of BFS, as the reactivity of BFS is much higher than M300 and MBA. The lower main peak intensity in 30 M300-BFS AAM and 30 CMBA-BFS AAM is because there is less BFS in the binary AAM system. Given that CMBA is more reactive than M300, the main peak of 30 CMBA-BFS AAM is expected to be stronger. However, 30 CMBA-BFS AAM exhibited smaller exotherm than 30 M300-BFS AAM, indicating that the reaction degree of BFS in 30 CMBA-BFS AAM was lower. As shown in Figure 6.15 (b), after 7 days, the cumulative heat collected for 30 CMBA-BFS AAM is around 133 J/g, less than the heat released by 30 M300-BFS AAM (149 J/g) and 100 BFS AAM (169 J/g).

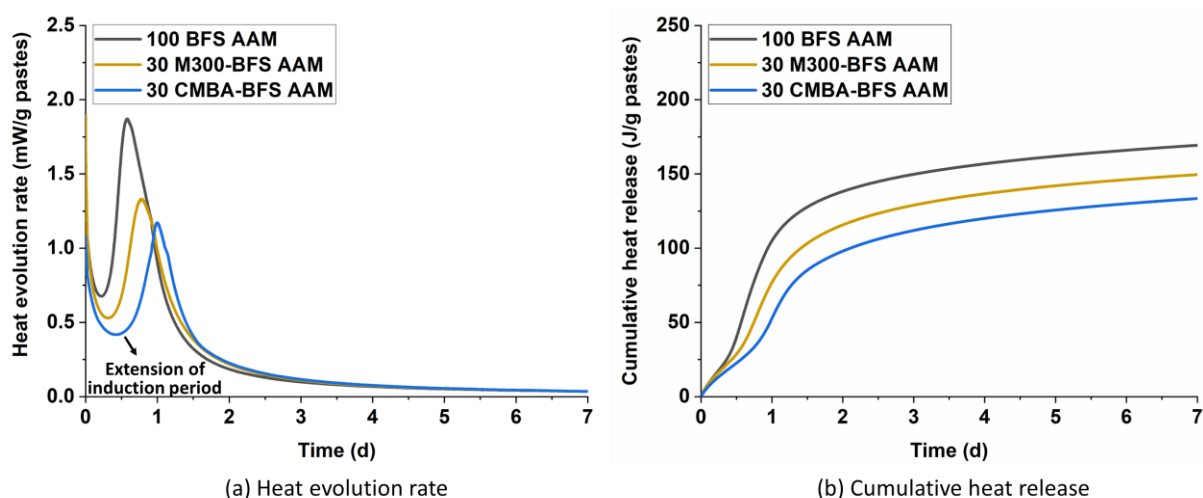


Figure 6.15 (a) Heat evolution rate and (b) cumulative heat release per gram of pastes for 100 BFS AAM, 30 M300-BFS AAM, and 30 CMBA-BFS AAM.

The main peak of 30 CMBA-BFS AAM was significantly delayed, appearing later than the peaks of 100 BFS AAM and 30 M300-BFS AAM. The substitution of 30 wt.% BFS with M300 only slightly prolonged the induction period. As M300 is unreactive, the amount of Si available for the reaction of BFS in 30 M300-BFS AAM is more than that in 100 BFS AAM. As a result of the higher Si concentration, the dissolution rate of BFS in 30 M300-BFS AAM is lower than in 100 BFS AAM in the initial stage. Regarding 30 CMBA-BFS AAM, the extension of the induction period is also caused by the delay of BFS reaction. However, the factors that lead to this reaction delay are different from the situation in 30 M300-BFS AAM. There are mainly three contributing factors for the delay of BFS reaction in 30 CMBA-BFS AAM. First, the Ca, Si, and Al released by MBA during the NaOH solution treatment increased the concentrations of these ions in the activator, which can inhibit the dissolution of BFS. Second, the pH of the activator was reduced after the NaOH solution treatment of MBA and the pre-activation of CMBA. Third, the monomers in the activator are the most reactive silicate species and are essential for gel formation [356]. Before adding BFS, the pre-activation of CMBA had already consumed a portion of the silicate monomers in the activator. Some silicate monomers may transform into dimers (see section 6.3.1), which are less reactive than the monomers.

#### *Reaction degree of BFS at 90 days*

At 90 days, the reaction degree of BFS in 30 CMBA-BFS AAM and 30 M300-BFS AAM was determined by image analysis. As shown in Figure 6.16, the reaction degree of BFS in 30 CMBA-BFS AAM is 66.7 %, higher than that in 30 M300-BFS AAM (59.4 %) and 100 BFS AAM (46.8 %). Compared with 100 BFS AAM, the reaction of BFS was enhanced in 30 M300-BFS AAM and 30 CMBA-BFS AAM. The enhancement of the reaction of BFS in the binary system can be attributed to the heterogeneous nucleation and dilution effect of M300 and CMBA. The particles of M300 and CMBA could provide nucleation sites for the heterogeneous precipitation of the gel phases [314,326]. Due to the partial substitution of BFS, the activator to BFS mass ratio in 30 M300-BFS AAM and 30 CMBA-BFS AAM is higher than that in 100 BFS AAM, which could promote the activation of BFS.

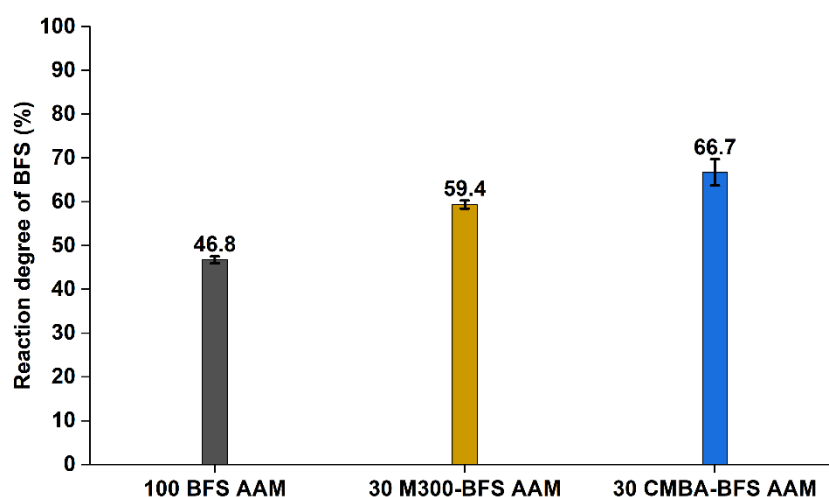


Figure 6.16 Reaction degree of BFS in 90-day 100 BFS AAM, 30 M300-BFS AAM, and 30 CMBA-BFS AAM.

The accelerating effect of CMBA on the reaction of BFS is more significant than that of M300. This finding can be explained from the following perspectives. First, the pH of the pore solution in 30 CMBA-BFS AAM should be higher than in 30 M300-BFS AAM. The alkali ions, such as  $\text{Na}^+$  and  $\text{K}^+$ , dissolved from MBA, increased the alkalinity of the pore solution of 30 CMBA-BFS AAM. The higher alkalinity of the pore solution facilitated the dissolution of BFS. Second, the C-A-S-H gel formed during the NaOH solution treatment of MBA and the pre-activation of CMBA may function as nuclei to promote the formation of this type of gel [357]. The accelerated gel phase formation was accompanied by a faster consumption of the released ions. As a result, the undersaturation degree of the pore solution was increased, which would, in turn, enhance the dissolution of BFS.

#### 6.3.4.2 Crystalline reaction products in hardened alkali-activated pastes

The mineralogical compositions of 30 CMBA-BFS AAM were compared with those of 100 BFS AAM and 30 M300-BFS AAM to investigate the effects of CMBA on the reaction product formation. According to the XRD analysis, the crystalline phases formed in 30 CMBA-BFS AAM include tobermorite ( $\text{Ca}_{4.9}(\text{Si}_{5.5}\text{Al}_{0.5}\text{O}_{16.3})(\text{OH})_{0.7}(\text{H}_2\text{O})_5$ , ICSD code 93590), hydrotalcite ( $(\text{Mg}_{0.667}\text{Al}_{0.333})(\text{OH})_2(\text{CO}_3)_{0.167}(\text{H}_2\text{O})_{0.5}$ , ICSD code 81963), and microcline ( $\text{K}(\text{AlSi}_3\text{O}_8)$ , ICSD code 83534). The peak of microcline was observed at  $2\theta$  of  $27.6^\circ$  (Figure 6.17). The formation of tobermorite and hydrotalcite was also detected in 100 BFS AAM and 30 M300-BFS AAM. Instead of microcline, another crystalline reaction product of 100 BFS AAM and 30 M300-BFS AAM is brucite ( $\text{Mg}(\text{OH})_2$ , ICSD code 28275). The peak of brucite was found at  $2\theta$  of  $38^\circ$  (see Figure 6.19 and Figure 6.21).

In the XRD patterns of 30 CMBA-BFS AAM, the peaks of tobermorite, albeit overlapping with the peaks of quartz, are evident at  $2\theta$  of  $49.5^\circ$  (Figure 6.18). Compared with 30 CMBA-BFS AAM, the peaks of tobermorite are more pronounced in the XRD pattern of 100 BFS AAM, at  $2\theta$  of  $31.9^\circ$ ,  $50^\circ$ , and  $55^\circ$  (Figure 6.19). The observation of the tobermorite peaks is more difficult in the XRD spectra of 30 M300-BFS AAM than in 30 CMBA-BFS AAM, as these peaks overlap with the amorphous hump and the peaks of quartz (Figure 6.21). The fitted curves of tobermorite obtained after the Rietveld refinement were also demonstrated together with the XRD patterns of 30 CMBA-BFS AAM and 30 M300-BFS AAM.

The hydrotalcite peaks were only observed at  $2\theta$  of  $11.5^\circ$  in the XRD patterns of 30 CMBA-BFS AAM (Figure 6.17). Comparatively, more hydrotalcite peaks were identified in the XRD spectra of 100 BFS AAM and 30 M300-BFS AAM, with higher peak intensities. The peaks of hydrotalcite were found at  $2\theta$  of  $11.5^\circ$ ,  $23.2^\circ$ , and  $61^\circ$  in the XRD spectra of 100 BFS AAM (Figure 6.19). In the XRD patterns of 30 M300-BFS AAM, the peaks of hydrotalcite appeared at the same locations as those in 100 BFS AAM (Figure 6.20 and Figure 6.21).

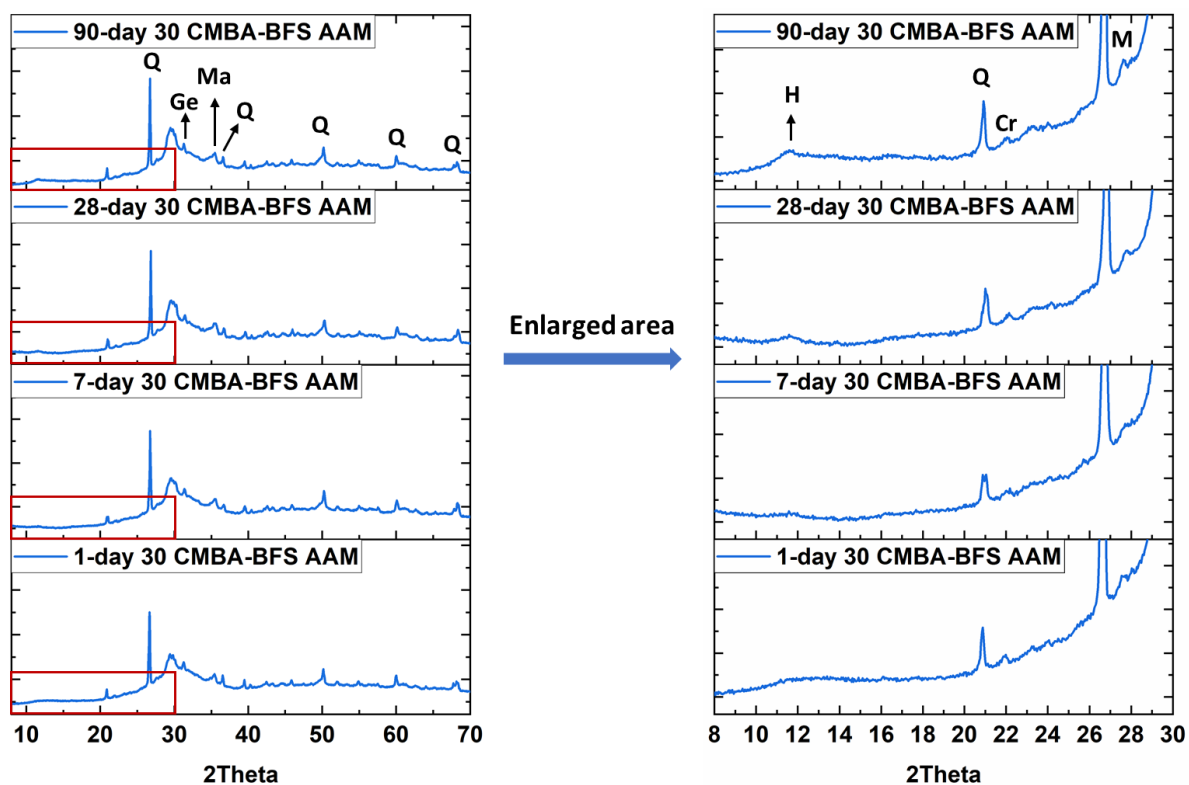


Figure 6.17 XRD patterns of 30 CMBA-BFS AAM at different curing ages (enlargement of low-angle area). Q: Quartz, H: Hydrotalcite, Cr: Cristobalite, Ge: Gehlenite, Ma: Magnetite, M: Microcline.

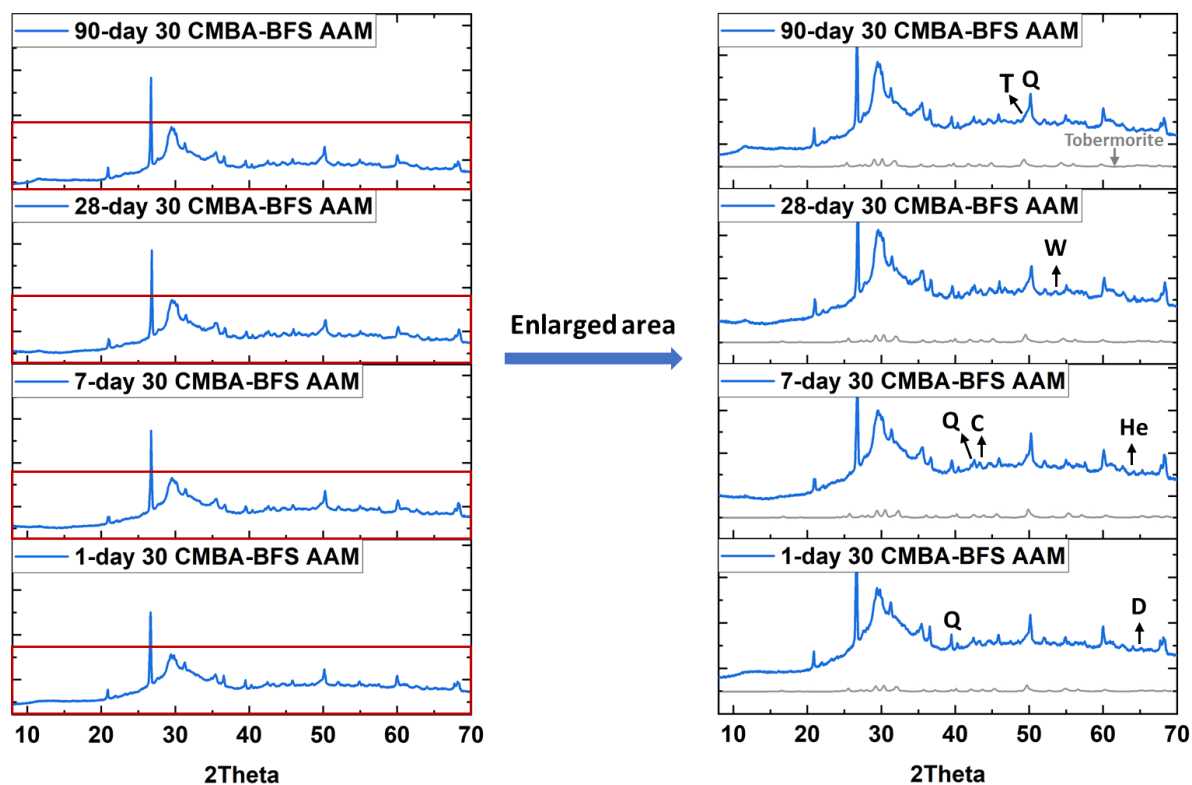


Figure 6.18 XRD patterns of 30 CMBA-BFS AAM at different curing ages (enlargement of low-intensity peaks). Q: Quartz, T: Tobermorite, W: Wollastonite, He: Hematite, D: Diopside, C: Calcite. The fitted pattern of tobermorite is obtained after Rietveld refinement.

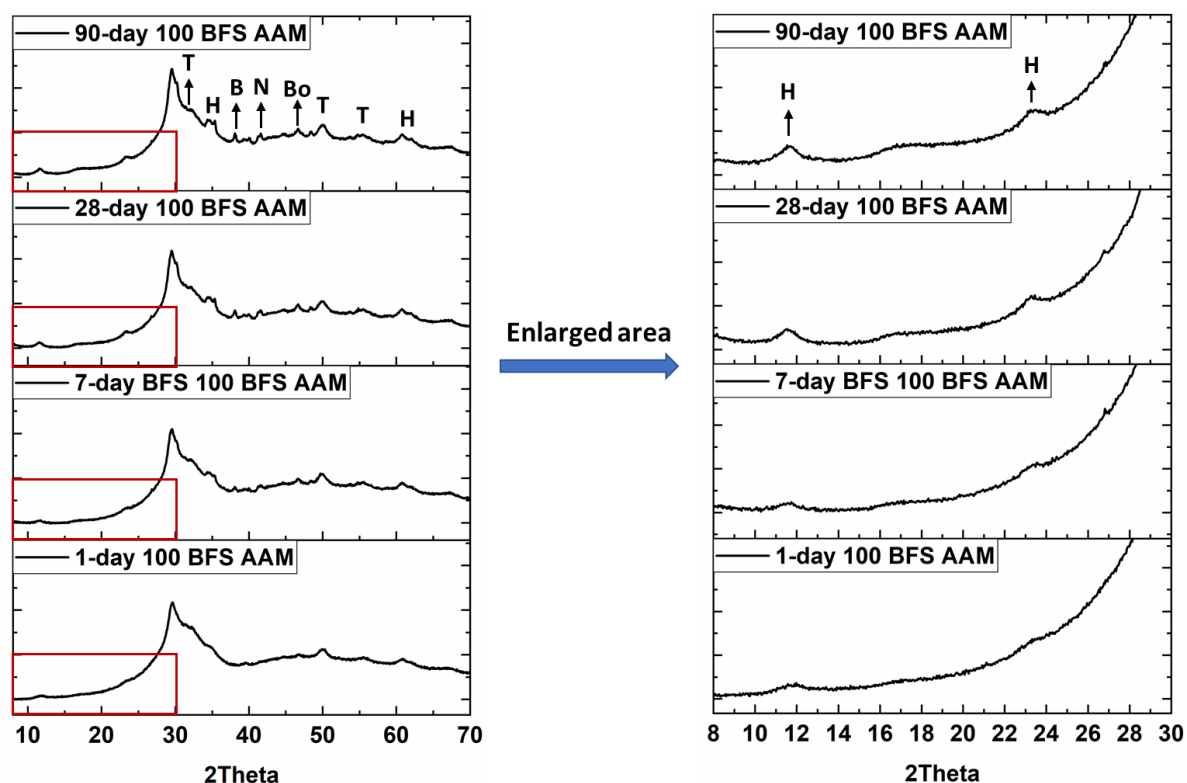


Figure 6.19 XRD patterns of 100 BFS AAM at different curing ages. H: Hydrotalcite, T: Tobermorite, B: Brucite, N: Nickel titanium, Bo: Bornite.

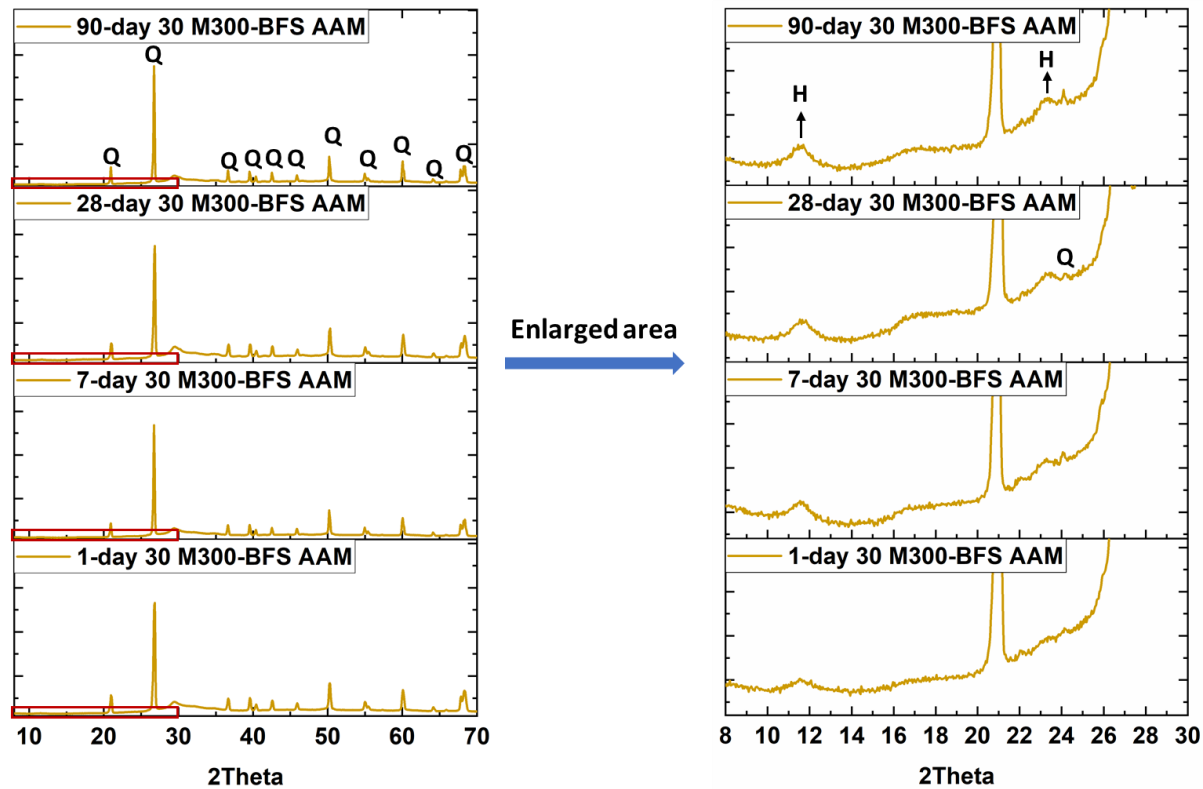


Figure 6.20 XRD patterns of 30 M300-BFS AAM at different curing ages (enlargement of low-angle area). Q: Quartz, H: Hydrotalcite.

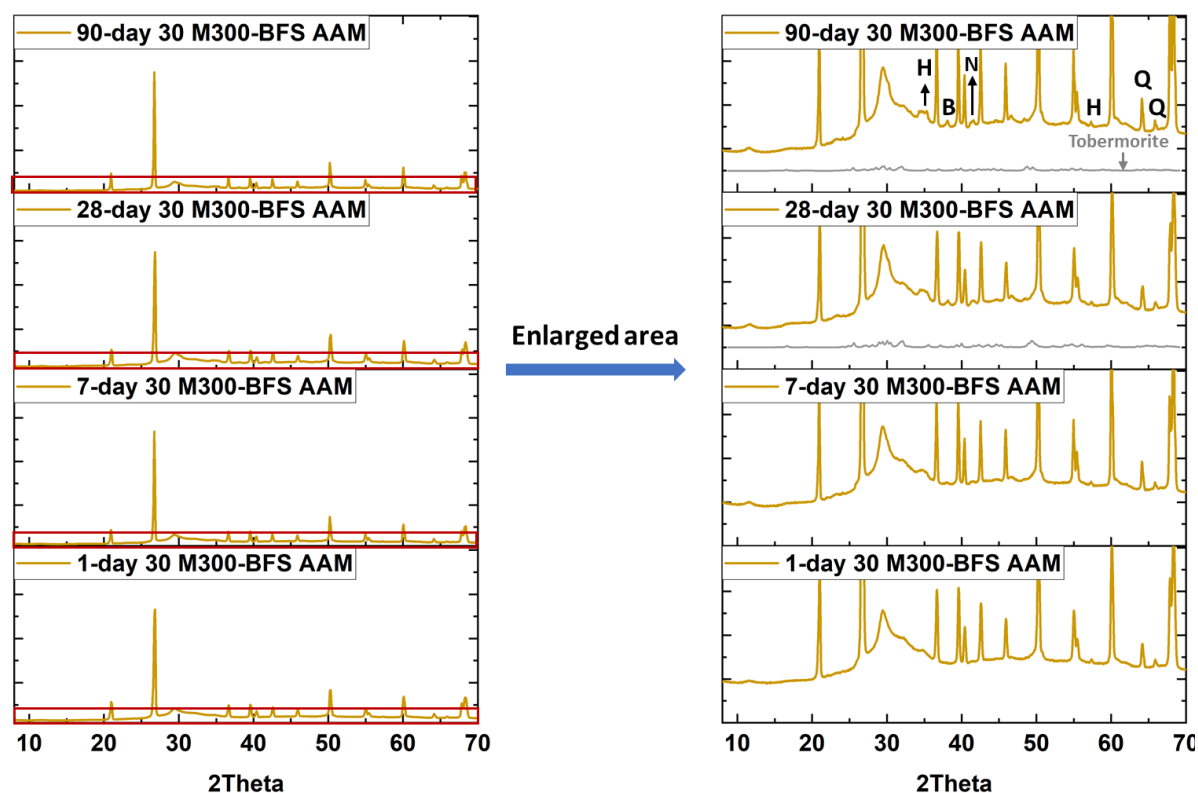


Figure 6.21 XRD patterns of 30 M300-BFS AAM at different curing ages (enlargement of low-intensity peaks). Q: Quartz, H: Hydrotalcite, B: Brucite, N: Nickel titanium. The fitted pattern of tobermorite is obtained after Rietveld refinement.

The QXRD results of the crystalline reaction products formed in 100 BFS AAM, 30 M300-BFS AAM, and 30 CMBA-BFS AAM were compared in Figure 6.22. Detailed information on the QXRD results can be found in Table E 1, Table E 2, and Table E 3. In 30 CMBA-BFS AAM, the content of microcline is slightly higher than that of hydrotalcite, but lower than that of tobermorite. In 100 BFS AAM and 30 M300-BFS AAM, the content of brucite is much lower (< 0.5 wt.%) than that of tobermorite or hydrotalcite.

As illustrated in Figure 6.22, the tobermorite content in 30 CMBA-BFS AAM is close to that in 100 BFS AAM but higher than that in 30 M300-BFS AAM. Blending BFS with CMBA stimulates the reaction of BFS, contributing to the formation of tobermorite in 30 CMBA-BFS AAM. The reaction degree of BFS in 30 CMBA-BFS AAM is higher than in 100 BFS AAM and 30 M300-BFS AAM (see section 6.3.4.1). However, the hydrotalcite content did not increase with the enhancement of the reaction of BFS. The hydrotalcite content in 30 CMBA-BFS AAM is much lower than in 30 M300-BFS AAM and 100 BFS AAM.

The formation of tobermorite and hydrotalcite in 30 CMBA-BFS AAM can be influenced by the C-A-S-H gel formed after the pre-activation of CMBA during the sample preparation process (see section 6.3.1). The C-A-S-H gel may function as nuclei to promote the growth of C-A-S-H gel and the formation of tobermorite [357]. Due to the existence of gel nuclei, the Al dissolved from BFS tends to form C-A-S-H gel, reducing the Al available in the system and consequently hindering the formation of hydrotalcite. Besides, the dissolution of CMBA also provides monomers to form C-A-S-H gel and tobermorite.

It is worth noting that the hydrotalcite content in 30 M300-BFS AAM is slightly higher than that in 100 BFS AAM. The enhancement in the formation of hydrotalcite is associated with the higher reaction degree of BFS in 30 M300-BFS AAM. As discussed in section 6.3.4.1, the reaction degree of BFS in 30 M300-BFS AAM is higher than 100 BFS AAM. Due to the higher reaction degree, a higher amount of Mg was released by BFS. The solubility product of the hydrotalcite-like phase is lower than that of C-A-S-H gel. Hence, the formation of hydrotalcite-like phases is thermodynamically favored over C-A-S-H gel [207,208]. Before being incorporated by C-S-H gel, the available Al would first combine with Mg to form hydrotalcite [358], resulting in an increased hydrotalcite content.

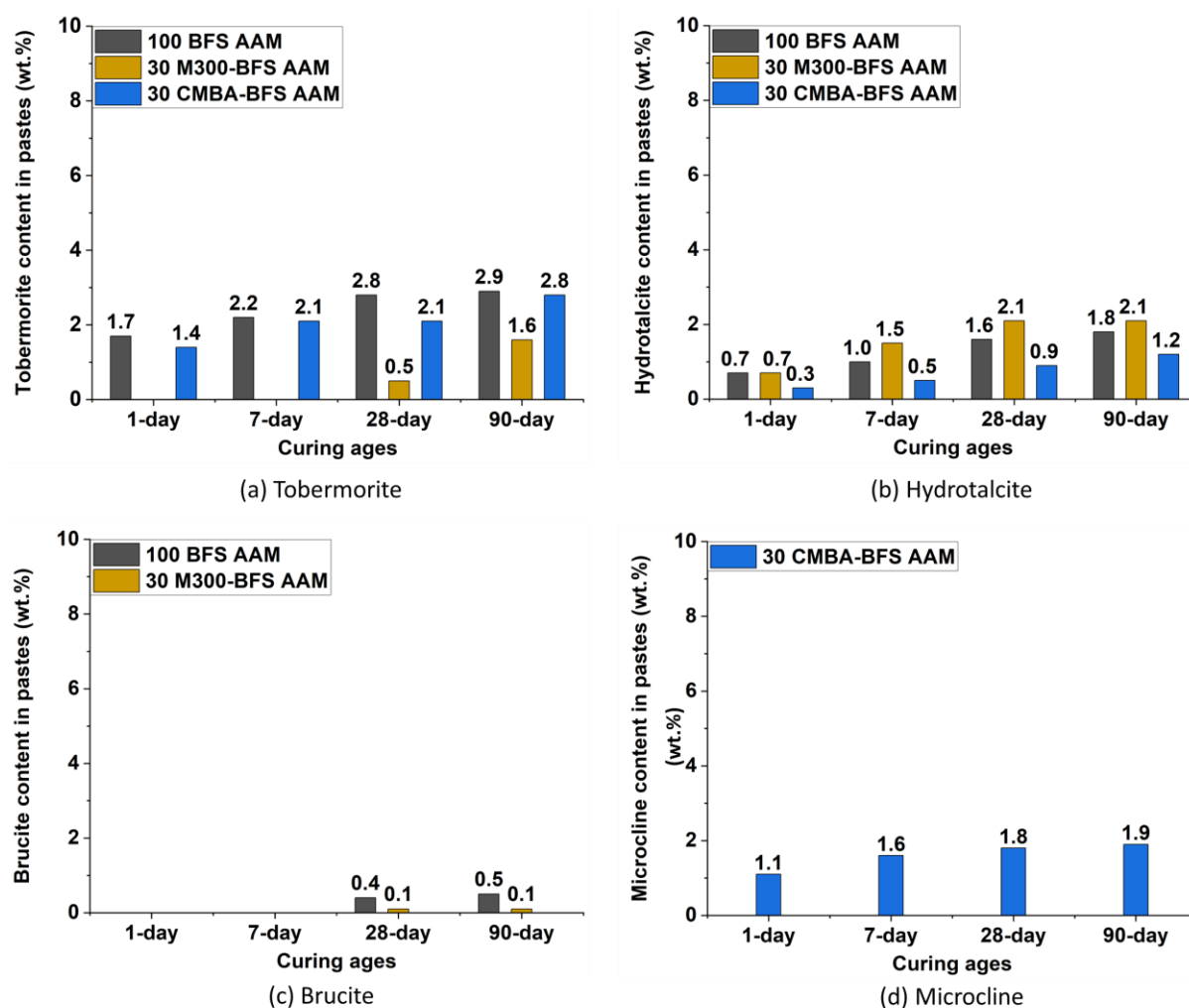


Figure 6.22 Contents of the reaction products formed in 100 BFS AAM, 30 M300-BFS AAM, and 30 CMBA-BFS AAM as a function of curing ages, determined by QXRD analysis. This figure was made based on the data presented in Table E 1, Table E 2, and Table E 3.



### 6.3.4.3 Chemical bonds in hardened alkali-activated pastes

The chemical bonds in 30 CMBA-BFS AAM were measured with FTIR to study the effect of CMBA on the structure of reaction products at the molecular level. The FTIR spectra of 100 BFS AAM and 30 M300-BFS AAM were also measured for comparison. Figure 6.23 shows the results of FTIR measurements for BFS, M300, and AAM pastes. The FTIR spectra of MBA and CMBA are illustrated in Figure 6.10, and detailed information is given in section 6.3.1.

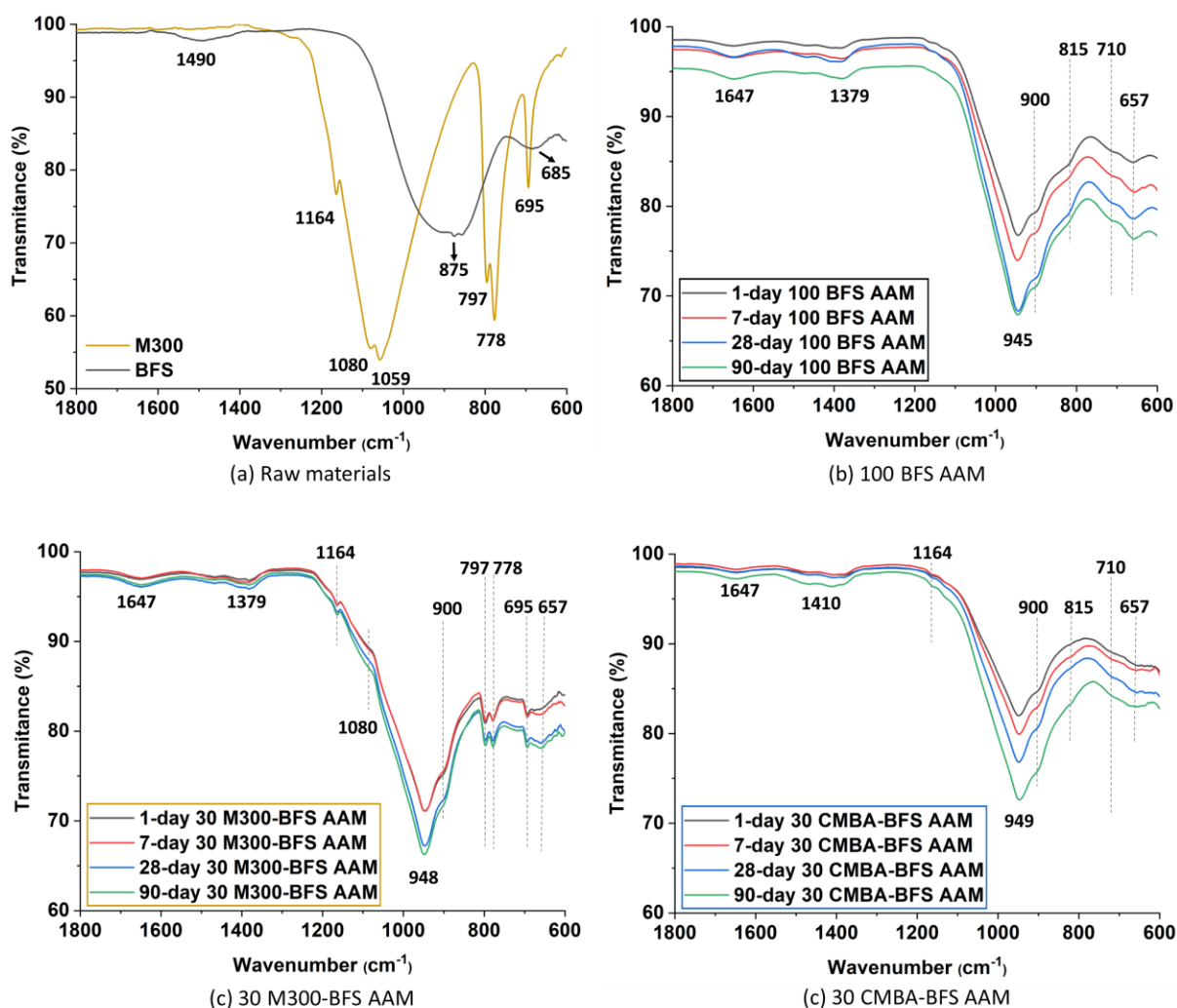


Figure 6.23 FTIR spectra of (a) BFS and M300, (b) 100 BFS AAM, (c) 30 M300-BFS AAM, (d) 30 CMBA-BFS AAM. The FTIR spectra of alkali-activated pastes are presented as a function of curing ages.

In the FTIR spectra of 30 CMBA-BFS AAM, 30 M300-BFS AAM, and 100 BFS AAM (Figure 6.23), the carbonate bands are in the region from 1300 to 1500  $\text{cm}^{-1}$  [343]. The carbonate bands within the same region were seen in the FTIR spectra of MBA and CMBA (Figure 6.10). In the spectrum of BFS, the small bands seen at 1490  $\text{cm}^{-1}$  [343], 875  $\text{cm}^{-1}$  [342], and 685  $\text{cm}^{-1}$  [359] represent the vibration of  $\text{CO}_3^{2-}$ . The weak bands at 1164  $\text{cm}^{-1}$  in the FTIR spectra of 30 CMBA-BFS AAM (Figure 6.23 (d)) can be attributed to the Si-O bond in quartz [342]. The quartz signal was also detected in the FTIR measurements of MBA and CMBA. The bands of quartz were also observed in the FTIR spectra of 30 M300-BFS AAM. In the FTIR spectra of M300, the bands

at  $1164\text{ cm}^{-1}$ ,  $1080\text{ cm}^{-1}$ ,  $1059\text{ cm}^{-1}$ ,  $797\text{ cm}^{-1}$ ,  $778\text{ cm}^{-1}$ , and  $693\text{ cm}^{-1}$  are characteristic vibrations of the Si-O bond in quartz [342].

The bands at  $1647\text{ cm}^{-1}$ ,  $900\text{ cm}^{-1}$ , and  $657\text{ cm}^{-1}$  were all detected in the FTIR measurements of 100 BFS AAM, 30 M300-BFS AAM, and 30 CMBA-BFS AAM. The band at  $1647\text{ cm}^{-1}$  is mainly caused by the bending vibration of the H-OH bond within the gel phases [350]. The bands at  $900\text{ cm}^{-1}$  and  $657\text{ cm}^{-1}$  can be assigned to the deformational vibrations of Si-O-Si in tobermorite [360]. The shoulder band located at  $900\text{ cm}^{-1}$  is due to the Si-O stretching vibrations, while the band at  $657\text{ cm}^{-1}$  is related to the Si-O-Si bending vibrations. The tobermorite band at  $657\text{ cm}^{-1}$  in 100 BFS AAM is sharper than that in 30 M300-BFS AAM and 30 CMBA-BFS AAM.

The shoulder bands at  $710\text{ cm}^{-1}$  and  $815\text{ cm}^{-1}$  were found in the FTIR spectra of 30 CMBA-BFS AAM and 100 BFS AAM but were not observed in the FTIR measurement of 30 M300-BFS AAM. These two shoulder bands observed in 30 CMBA-BFS AAM were not as evident as those in 100 BFS AAM. Given that these two shoulder bands only appeared after the alkali activation of BFS, the reaction products in alkali-activated BFS paste are responsible for the appearance of these two bands. The band at  $710\text{ cm}^{-1}$  corresponds to the bending of Al-O-Si bonds in the gel phases [361,362]. The shoulder band at  $815\text{ cm}^{-1}$  is typical for Si-O symmetric stretching vibrations [348].

BFS is a significant contributor to the formation of amorphous reaction products in 30 CMBA-BFS AAM and 30 M300-BFS AAM, as BFS accounts for 70 wt.% in the precursor and is more reactive than CMBA and M300. The BFS used in this work is highly amorphous. The changes in the molecular structure of the amorphous phases induced by the alkali activation of BFS can be detected by comparing the main bands of BFS and 100 BFS AAM in the FTIR spectra. The main band of BFS, which overlaps with the carbonate band (at  $875\text{ cm}^{-1}$ ), is broad and centered at around  $900\text{ cm}^{-1}$  (Figure 6.23 (a)). This band is associated with the asymmetric stretching vibration mode of Si-O-T bonds (T: tetrahedral Si or Al) [363]. Upon alkali activation of BFS, the main band was found at  $945\text{ cm}^{-1}$  in the FTIR spectra of 100 BFS AAM.

Compared with the FTIR spectra of 100 BFS AAM, the incorporation of CMBA or M300 in BFS-based AAM changed the position of the main band. As illustrated in Figure 6.23, the main band of 30 CMBA-BFS AAM, 30 M300-BFS AAM, and 100 BFS AAM appear at  $949\text{ cm}^{-1}$ ,  $948\text{ cm}^{-1}$ , and  $945\text{ cm}^{-1}$ , respectively. The main band of alkali-activated pastes (at around  $950\text{ cm}^{-1}$ ) can be assigned to the asymmetric stretching vibration of Si-O-T bonds (T: Si, Al, or  $\text{Na}^+$ ) in C-(N)-A-S-H gel (sodium-incorporated C-A-S-H gel), as well as the band at  $893\text{ cm}^{-1}$  [348–350,355]. These main bands did not change positions with the prolonging of curing time. However, their intensity increased from 1-day to 90-day samples, indicating that the C-(N)-A-S-H gel formed continuously.

The position of the Si-O-T stretching band reflects the extent of the polymerization degree of the gel formed in 30 CMBA-BFS AAM, 30 M300-BFS AAM, and 100 BFS AAM. The main band in 30 CMBA-BFS AAM appeared at the highest wavenumber, suggesting that the polymerization degree of the gel phases in 30 CMBA-BFS AAM is higher than 100 BFS AAM and 30 M300-BFS AAM [360]. The C-A-S-H gel formed due to the NaOH solution treatment of MBA and the pre-activation of CMBA may function as nuclei and promotes the growth and

polymerization of C-A-S-H gel in 30 CMBA-BFS AAM [357]. Besides, CMBA can provide silicate monomers for the formation of Si-O-Si bonds. The Si-O-T bond will also shift to a higher wavenumber with an increase in the percentage of the Si-O-Si bonds.

Apart from the polymerization degree, the final position of the Si-O-T band in 30 CMBA-BFS AAM, 30 M300-BFS AAM, and 100 BFS AAM is also influenced by the chemical composition of the gel phases, especially the Ca/Si molar ratio, Al/Si molar ratio, and the percentage of Na in the gel phases. When comparing the chemical composition of the gel phases, the Ca/Si and Al/Si molar ratios in 30 CMBA-BFS AAM are higher than in 100 BFS AAM and 30 M300-BFS AAM (see Table 6.3). The position of the Si-O-T bond shifts toward a higher wavenumber with decreasing Ca/Si molar ratio [360]. The substitution of Si with Al in the network will weaken the bond and shift the band to a lower wavenumber [364]. From this perspective, the main band of 30 CMBA-BFS AAM is expected to be positioned at a lower wavenumber. However, the Na/Si molar ratio is much higher in 100 BFS AAM and 30 M300-BFS AAM than in 30 CMBA-BFS AAM. The lower uptake of Na<sup>+</sup> in the Si-O-Si network of 30 CMBA-BFS AAM can cause a significant shift to a higher wavenumber [355]. As a result, the effects of the Ca/Si molar ratio and Al/Si molar ratio on the wavenumber position was compensated, and the main band of 30 CMBA-BFS AAM was positioned at a high wavenumber.

#### 6.3.4.4 Morphology of hardened alkali-activated pastes

The morphology of 90-day 30 CMBA-BFS AAM was observed under SEM to study the effect of CMBA on microstructure formation. Figure 6.24 shows the representative SEM-BSE images of 30 CMBA-BFS AAM. The SEM-BSE images of 90-day 100 BFS AAM and 30 M300-BFS AAM were also presented for comparison. In the BSE images of alkali-activated pastes (Figure 6.24), the pores filled with epoxy are black. The BFS, M300, and CMBA particles with irregular polygonal shapes are distributed throughout the gel phases. The gel phases generally show a darker grey color than the embedded particles, except for M300. The grey level of M300 is close to the gel phases. The BFS and M300 particles exhibit uniform grey values due to their homogeneous composition. Comparatively, the grey level of the CMBA particles varies over a wide range. Due to the heterogeneity in chemical compositions, the grey levels of different regions within a single CMBA particle are not necessarily the same. The CMBA particles can be brighter or darker than the BFS particles in the BSE images of 30 CMBA-BFS AAM.

The microstructure of 100 BFS AAM (Figure 6.24 (a)) observed at the magnification of 1500 is slightly denser than that of 30 M300-BFS AAM (Figure 6.24 (c)) and 30 CMBA-BFS AAM (Figure 6.24 (e)). The areas surrounding the BFS, M300, and CMBA particles were examined under the magnification of 4000. As shown in magnified BSE images, the reaction products formed rims around the partially reacted BFS particles. The BFS particles that had entirely reacted left regions with a darker greyscale value than the surrounding gel phases. These regions are usually in the shape of the original BFS particles (see Figure 6.24 (b)). Figure 6.24 (d) and (f) present a higher magnification view of the areas surrounding M300 and CMBA particles. These images indicate that a dense microstructure was formed around the M300 particles and CMBA particles.

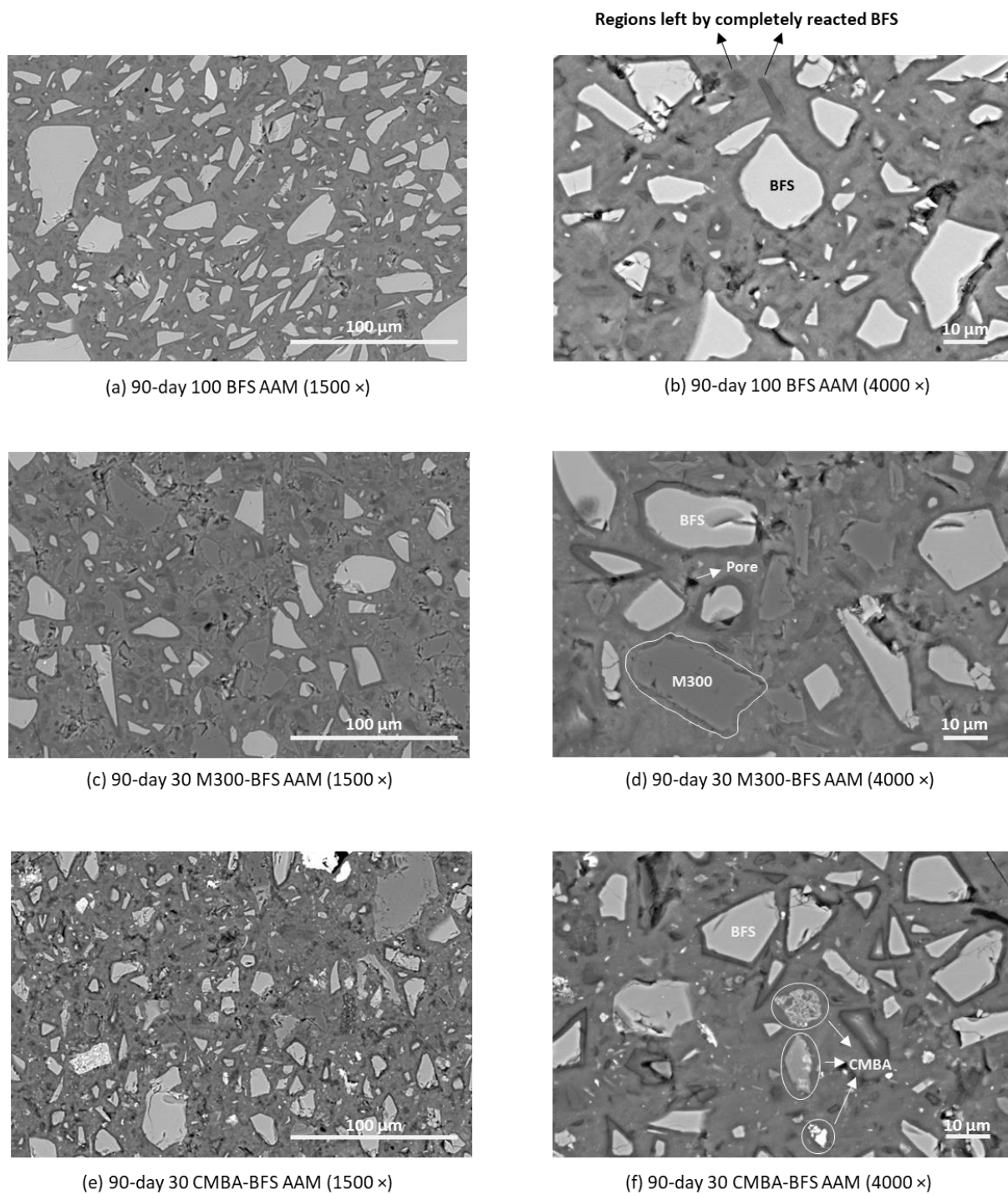
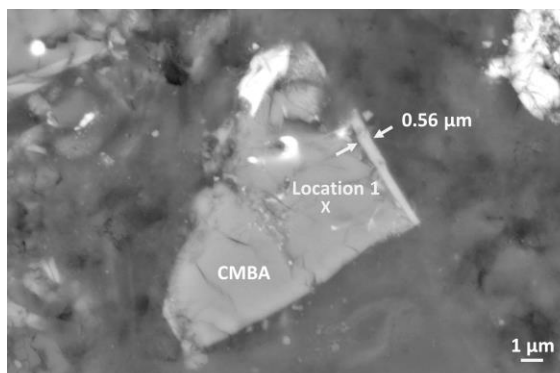


Figure 6.24 SEM-BSE images of 100 BFS AAM, 30 M300-BFS AAM, and 30 CMBA-BFS AAM paste samples at 90 days. The magnifications are 1500 (left images) and 4000 (right images).

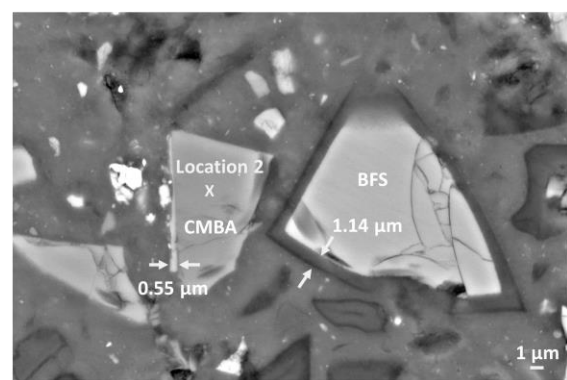


Figure 6.25 (a) and (b) illustrate two typical examples of partially reacted CMBA particles in 90-day 30 CMBA-BFS AAM. Layers of reaction products were found around the edges of these two CMBA particles (particle 1 and particle 2). The reaction product layers show a lighter grey color relative to the surrounding gel phases. The thickness of these reaction product layers is around  $0.55\ \mu\text{m}$ , which is about half the thickness of the reaction product rim of the BFS particle adjacent to particle 2. It is difficult to determine the chemical composition of the reaction product layers precipitated on particle 1 and particle 2 with SEM-EDS analysis. This is because the thickness of these reaction product layers is much smaller than the interaction volume between the radius of interaction volume between the electron beams and gel phases at 15 kV [315].

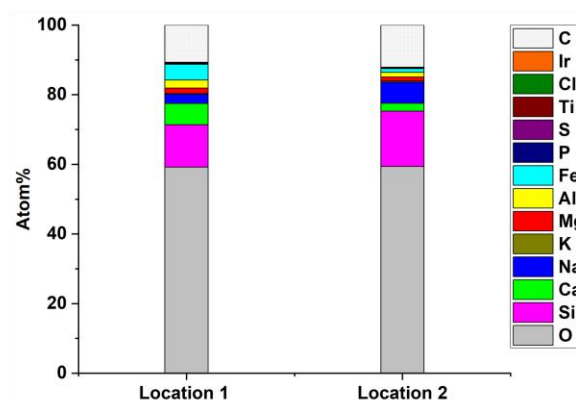
The reaction product layers were most likely formed due to the reaction of particle 1 and particle 2 in the pore solution of 30 CMBA-BFS AAM. However, the gel phases formed during the NaOH solution treatment of MBA and the pre-activation of CMBA may also precipitate reactive CMBA particles, such as particle 1 and particle 2. As discussed in section 6.3.1, the formation of C-A-S-H gel was detected in CMBA after the NaOH solution treatment of MBA. The pre-activation of CMBA could lead to the formation of C-A-S-H gel and N-A-S-H gel. During the curing process of 30 CMBA-BFS AAM, the ions dissolved from particle 1 and particle 2 may promote the growth of the gel initially precipitated on their surfaces, resulting in the formation of reaction product layers.



(a) Particle 1 of 90-day 30 CMBA-BFS AAM



(b) Particle 2 of 90-day 30 CMBA-BFS AAM



(c) Chemical compositions of the locations in particle 1 and particle 2 of 90-day 30 CMBA-BFS AAM

Figure 6.25 (a) and (b) SEM-BSE images of partially reacted CMBA particles in 90-day 30 CMBA-BFS AAM. (c) SEM-EDS spot analysis results of the locations labeled in particle 1 and particle 2.

The chemical compositions of particle 1 and particle 2 were measured to identify the phases incorporated in these two reactive CMBA particles. According to the SEM-EDS spot analysis (see Figure 6.25 (c)), the elements detected in location 1 of particle 1 and location 2 of particle 2 are mainly O, Si, Ca, Na, Al, Fe, and Mg. Considering that the glass particles are the primary resources of the reactive phase in MBA and CMBA, the chemical compositions measured in partially reacted CMBA particles (particle 1 and particle 2) were compared with the chemical composition of glass in MBA (see Chapter 5). The atomic percentages of Si, Ca, Na, Al, and Fe in partially reacted CMBA particles (particle 1 and particle 2) and glass particles were projected onto the ternary diagrams to visualize their relative contents. Figure 6.26 shows that the dots indicating the chemical composition of particle 1 and particle 2 are in the same areas of the ternary diagrams as the dots representing the chemical composition of the glass particles present in MBA. For the above reasons, the partially reacted CMBA particles (particle 1 and particle 2) in 90-day 30 CMBA-BFS AAM are mainly composed of glasses. This finding is consistent with the assumption made in Chapter 4 that the amorphous phase is the major reactive phase in MBA.

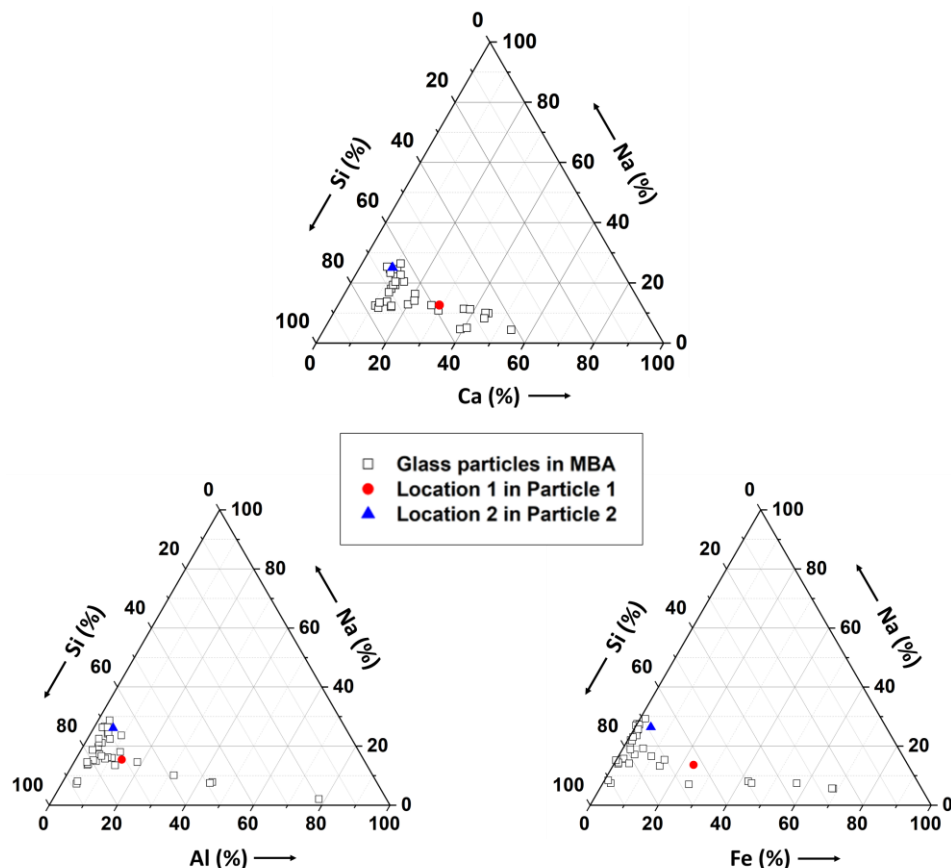


Figure 6.26 Comparison between the chemical compositions (atom %) of the glass in MBA and the chemical compositions measured at location 1 and location 2 (shown in Figure 6.25 (a) and (b)) in 90-day 30 CMBA-BFS AAM. The ternary diagrams are plotted according to the atomic percentages of the elements.

### 6.3.4.5 Chemical composition of the gel phases in alkali-activated pastes

The gel composition change induced by incorporating CMBA in BFS-based AAM was studied by comparing the gel phases formed in 90-day 30 CMBA-BFS AAM with those in 90-day 100 BFS AAM and 30 M300-BFS AAM. For each type of alkali-activated paste sample, the chemical composition of the gel phases was measured with SEM-EDS analysis at around 200 randomly selected locations in the region between unreacted particles. Figure 6.27 shows an example of the location (point 1) selected in the measurement of the gel phases.

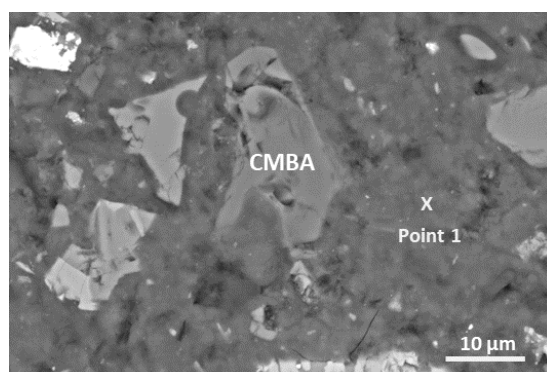


Figure 6.27 An example of the location selected for the measurement of the gel composition in SEM-EDS spot analysis. The sample is 90-day 30 CMBA-BFS AAM, and the magnification is 6000.

The gel compositions of 30 CMBA-BFS AAM were compared with that of 30 M300-BFS AAM and 100 BFS AAM by projecting all the measured compositions onto the ternary diagram, which graphically depicts the ratios of three elements as positions in an equilateral triangle. In Figure 6.28, the Al, Si, Ca, and Na atomic percentages are presented on an oxide basis and plotted in the  $\text{CaO} - \text{Al}_2\text{O}_3 - \text{SiO}_2$  and  $\text{Na}_2\text{O} - \text{Al}_2\text{O}_3 - \text{SiO}_2$  ternary diagrams after renormalization to 100 %.

Figure 6.28 shows that there is a significant overlap between the gel compositions of 30 CMBA-BFS AAM, 30 M300-BFS AAM, and 100 BFS AAM in the ternary diagrams. The dots representing the gel compositions are all located in the compositional region characterized by high  $\text{SiO}_2$  and  $\text{CaO}$  but low  $\text{Al}_2\text{O}_3$  and  $\text{Na}_2\text{O}$  percentages. This finding reveals that the C-(N)-A-S-H gel is dominant in these three AAM systems. The C-(N)-A-S-H gel, namely the C-A-S-H gel that incorporates sodium, is the main reaction product formed in Ca-rich AAM systems [207]. The dots indicating the gel compositions of 100 BFS AAM are closely clustered in the ternary diagrams. In contrast, the dots representing the gel compositions of 30 M300-BFS AAM and 30 CMBA-BFS AAM are spread over a wider area, especially the compositional region of lower  $\text{CaO}$  or  $\text{Na}_2\text{O}$ .

Apart from C-(N)-A-S-H gel, other types of gel may form in 30 CMBA-BFS AAM and 30 M300-BFS AAM. In the  $\text{CaO} - \text{Al}_2\text{O}_3 - \text{SiO}_2$  diagram (Figure 6.28 (a)), some dots, which correspond to the gel compositions of 30 CMBA-BFS AAM and 30 M300-BFS AAM, are located in the region where the  $\text{CaO}$  percentage is almost zero, suggesting the possible formation of N-A-S-H gel in these two AAM systems. However, the N-A-S-H gel was not detected in the FTIR analysis. The possible reason is that the amount of N-A-S-H gel formed in 30 CMBA-BFS AAM and 30 M300-



BFS AAM is too small to be detected. When a considerable amount of Ca is present in the pore solution of AAM due to the dissolution of BFS, the Si and Al tend to participate in the formation of C-A-S-H gel rather than N-A-S-H gel. The C-A-S-H gel is more stable than the N-A-S-H gel under highly alkaline conditions ( $\text{pH} > 12$ ) [350]. Besides, the Ca released by BFS can partially replace the Na in the N-A-S-H gel, resulting in the formation of (N,C)-A-S-H gel, also called calcium-modified N-A-S-H gel [365].

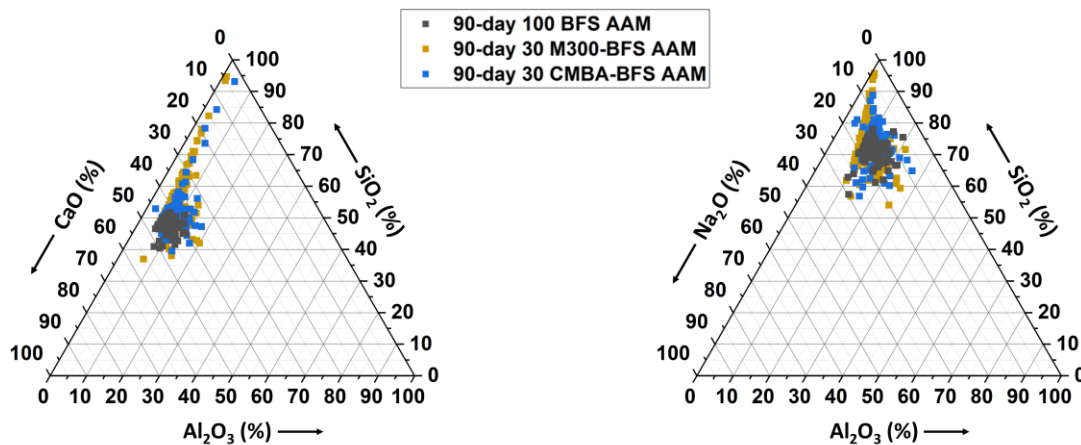


Figure 6.28 (a) CaO - Al<sub>2</sub>O<sub>3</sub> - SiO<sub>2</sub> and (b) Na<sub>2</sub>O - Al<sub>2</sub>O<sub>3</sub> - SiO<sub>2</sub> ternary diagrams comparing the main elements present in the gel phases 90-day 100 BFS AAM, 30 M300-BFS AAM, and 30 CMBA-BFS AAM. The diagrams are made using the atomic percentages obtained via SEM-EDS spot analysis. The ternary diagrams are plotted according to the atomic percentages of the oxides.

At some locations of the gel phases in 30 CMBA-BFS AAM and 30 M300-BFS AAM, sodium was rarely detected. Correspondingly, the dots representing their compositions approach the top vertex of the Na<sub>2</sub>O - Al<sub>2</sub>O<sub>3</sub> - SiO<sub>2</sub> ternary diagram at which the Na<sub>2</sub>O percentage is zero ((Figure 6.28 (b)). This observation implies the possibility of forming C-A-S-H gel without the inclusion of Na. This statement can be supported by the detection of tobermorite in the XRD analysis of 30 CMBA-BFS AAM and 30 M300-BFS AAM. In the case of 30 CMBA-BFS AAM, the C-A-S-H gel formed during the NaOH solution treatment of MBA and the pre-activation process of CMBA may function as nuclei and promote the formation of C-A-S-H gel [357].

The average atomic ratios are calculated for the gel matrix of the 90-day alkali-activated paste samples. As shown in Table 6.3, the differences in the Mg/Si and Al/Si atomic ratios are very small among the gel phases of 30 CMBA-BFS AAM, 100 BFS AAM, and 30 M300-BFS AAM. The Mg/Si atomic ratio is almost the same in the gel phases of 30 CMBA-BFS AAM, 100 BFS AAM, and 30 M300-BFS AAM (Table 6.3). The detection of Mg in the gel phases indicates the possible incorporation of Mg in the C-(N)-A-S-H gel. Since the diffusion of Mg from reacted BFS to the gel phases is difficult [366], the amount of Mg detected in the gel phases is also limited, resulting in a low Mg/Si atomic ratio (around 0.21). The Al/Si atomic ratio of the gel in 30 CMBA-BFS AAM is close to that in the gel of 100 BFS AAM. Compared with 30 M300-BFS AAM, the Al/Si atomic ratio of the gel in 30 CMBA-BFS AAM is slightly higher. This is because the dissolution of CMBA can provide Al for the formation of the gel phases.

Table 6.3 Atomic ratios of the elements present in the gel phases of 90-day 100 BFS AAM, 30 M300-BFS AAM, and 30 CMBA-BFS AAM.

Atomic ratio	100 BFS AAM		30 M300-BFS AAM		30 CMBA-BFS AAM	
	Average	Stdev	Average	Stdev	Average	Stdev
Ca/Si	0.91	0.06	0.73	0.12	0.77	0.11
Al/Si	0.32	0.08	0.29	0.08	0.33	0.08
Na/Si	0.44	0.08	0.47	0.1	0.39	0.08
Mg/Si	0.21	0.09	0.22	0.12	0.21	0.09

The incorporation of CMBA or M300 in BFS-based AAM mainly changed the Ca/Si and Na/Si atomic ratios of the gel phases (Table 6.3). The average Ca/Si atomic ratio of the gel in 100 BFS AAM is 0.91, close to the molar ratio of CaO/SiO<sub>2</sub> in the amorphous phase of BFS (see Chapter 4). Compared with 100 BFS AAM, the Ca/Si atomic ratio of the gel in 30 CMBA-BFS AAM and 30 M300-BFS AAM was lower. The gel in 30 CMBA-BFS AAM has a Ca/Si atomic ratio of 0.77, higher than that in 30 M300-BFS AAM. The higher Ca/Si atomic ratio of the gel in 30 CMBA-BFS AAM can be attributed to the higher reaction degree of BFS in 30 CMBA-BFS AAM than in 30 M300-BFS AAM (Figure 6.16). Besides, the amorphous phase of CMBA also contains CaO, which can be released upon the alkali-activation of CMBA.

The Na/Si atomic ratio of the gel in 30 M300-BFS AAM is the highest, followed by 100 BFS AAM and 30 CMBA-BFS AAM. The difference in the Na/Si atomic ratio among the gel phases of 90-day 100 BFS AAM, 30 M300-BFS AAM, and 30 CMBA-BFS AAM can be explained from the perspective of Ca content in AAM system. The low level of Ca in the binary system will stimulate the uptake of Al and Na in the C-(N-)A-S-H gels [349]. Compared with 30 M300-BFS AAM, the Al/Si atomic ratio of the gel in 30 CMBA-BFS AAM is higher, indicating that more Al was incorporated in the gel. As a result, the incorporation of Na in the gel of 30 CMBA-BFS AAM was less than that of 30 M300-BFS AAM. Instead of Al, the deficiency of Ca in the gel of 30 M300-BFS AAM was mainly compensated by the Na, resulting in a high Na/Si atomic ratio.

#### 6.3.4.6 Porosity of hardened alkali-activated pastes

The porosity of 90-day 30 CMBA-BFS AAM was compared with that of 90-day 100 BFS AAM and 30 M300-BFS AAM. As illustrated in Figure 6.29 (a), the total pore volume in 90-day 30 CMBA-BFS AAM is the largest, followed by 90-day 30 M300-BFS AAM and 100 BFS AAM. In the differential curve (Figure 6.29 (b)), the main peak of 90-day 30 CMBA-BFS AAM was observed at the same pore width as the peak of 90-day 100 BFS AAM. Only one peak was found in the differential curve of 90-day 100 BFS AAM. The corresponding critical pore width is 15 nm. The differential curve of 90-day 30 M300-BFS AAM follows the same trend as 90-day 100 BFS AAM, but its peak appears at a larger pore width (around 20 nm).

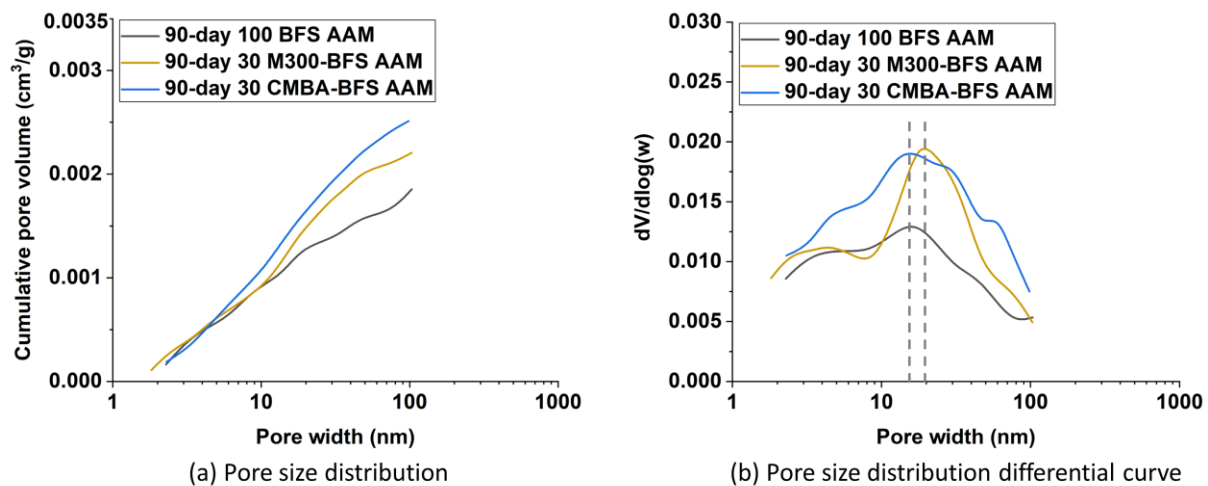


Figure 6.29 Pore size distribution of 100 BFS AAM, 30 M300-BFS AAM, and 30 CMBA-BFS AAM at 90 days, determined using the nitrogen adsorption method.

100 BFS AAM is made from 100 % BFS, while BFS only accounts for 70 wt.% in the precursor of 30 M300-BFS AAM and 30 CMBA-BFS AAM. Compared with 90-day 100 BFS AAM, the reaction products available to fill the pores are less in 90-day 30 CMBA-BFS AAM and 30 M300-BFS AAM, resulting in a larger porosity. Figure 6.29 (a) indicates that the porosity of 90-day 30 CMBA-BFS AAM is larger than 90-day 30 M300-BFS AAM. However, the reaction products formed in 90-day 30 CMBA-BFS AAM were more than that in 90-day 30 M300-BFS AAM, as the reaction degree of BFS in 90-day 30 CMBA-BFS AAM was higher (see section 6.3.4.1), and MBA participated into the formation of reaction products (see section 6.3.4.2 and section 6.3.4.4). The lower porosity in 90-day 30 CMBA-BFS AAM can be explained by the influences of densities of raw materials, reaction kinetics of alkali-activated pastes, and densities of reaction products.

- The amount of MBA used to prepare 30 CMBA-BFS AAM is the same as the amount of M300 used to prepare 30 M300-BFS AAM. However, the volume occupied by MBA in the pastes is smaller than that of M300 of the same mass because the density of MBA is larger than that of M300. As a result, the porosity of 30 CMBA-BFS AAM should be higher than 30 M300-BFS AAM at the beginning of the curing process.
- The calorimetric results indicate that at early ages, the reaction of BFS was delayed for a longer time in 30 CMBA-BFS AAM than in 30 M300-BFS AAM (Figure 6.15 (a)). Due to the delay of BFS reaction, fewer reaction products were formed after 7 days of curing, leading to a higher porosity in 7-day 30 CMBA-BFS AAM than 7-day 30 M300-BFS AAM. With the progress of reaction, the pores in the 7-day alkali-activated paste became smaller as the reaction products grew into the pore space. From 7 days to 90 days, more reaction products were formed in 30 CMBA-BFS AAM than in 30 M300-BFS AAM. However, the reaction products formed in 30 CMBA-BFS AAM during this period may not be able to reduce its porosity to smaller than that of 30 M300-BFS AAM.
- The hydrotalcite content also affects the porosity of BFS-based AAM. The density of hydrotalcite is lower than the gel formed in alkali-activated BFS paste [358]. Compared

with gel phases, the same amount of hydrotalcite by mass can fill a larger volume of pores [367]. The amount of hydrotalcite detected in 30 M300-BFS AAM is almost equal to that in 100 BFS AAM (see section 6.3.4.2). In comparison, much less hydrotalcite was formed in 30 CMBA-BFS AAM. The contribution of hydrotalcite to the porosity reduction was smaller in 30 CMBA-BFS AAM than in 30 M300-BFS AAM.

### 6.3.5 Strength development of hardened alkali-activated pastes

As shown in Figure 6.30, incorporating CMBA or M300 in BFS-based alkali-activated pastes reduced the compressive strength, especially at early ages. The 1-day compressive strength of 100 BFS AAM was 60 MPa. Relative to 100 BFS AAM, the 1-day compressive strength of 30 M300-BFS AAM and 30 CMBA-BFS AAM decreased by more than 30 %. At later ages, the reaction of BFS in the binary AAM system was enhanced due to the heterogeneous nucleation and dilution effect of M300 and CMBA (see section 6.3.4.1). After 90 days, the compressive strength of 30 CMBA-BFS AAM and 30 M300-BFS AAM was only around 10 % and 14 % lower than that of 90-day 100 BFS AAM, respectively.

Compared with 30 M300-BFS AAM, the 1-day and 7-day compressive strength of 30 CMBA-BFS AAM is lower. This is because the reaction of BFS was significantly delayed in 30 CMBA-BFS AAM during the first 7 days (see Figure 6.15 (a)). After 28 days, the compressive strength of 30 CMBA-BFS AAM increased to 110 MPa, exceeding the strength of 28-day 30 M300-BFS AAM. At 90 days, 30 CMBA-BFS AAM with a compressive strength of 116 MPa remained stronger than 30 M300-BFS AAM. The higher compressive strength of 30 CMBA-BFS AAM at later ages is mainly due to the formation of a larger amount of reaction products. The reaction degree of BFS in 90-day 30 CMBA-BFS AAM was higher than in 30 M300-BFS AAM. Besides, CMBA also reacted and contributed to the reaction product formation.

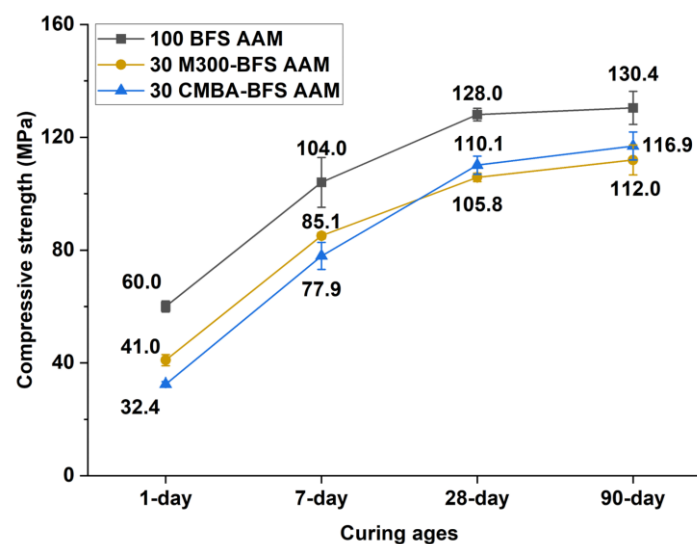


Figure 6.30 Compressive strength of 100 BFS AAM, 30 M300-BFS AAM, and 30 CMBA-BFS AAM as a function of curing ages.

## 6.4 Conclusions

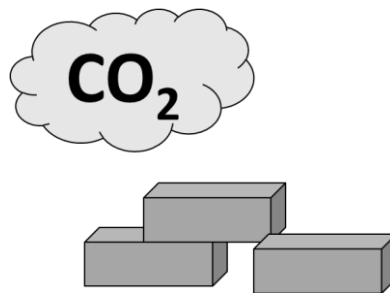
In this chapter, the use of *mechanically treated MSWI bottom ash (MBA)* as an alternative to Class F coal fly ash (FA) in the alkali-activated pastes prepared with blends of FA and blast furnace slag (BFS) was discussed. Compared with the alkali-activated BFS paste (100 BFS AAM), incorporating MBA in BFS-based alkali-activated pastes influenced the reaction of BFS and changed the reaction products and microstructure of alkali-activated pastes. The MBA added to BFS-based alkali-activated pastes participated in the formation of reaction products and contributed to strength development. The findings of this work are presented below:

- During the sample preparation process of alkali-activated CMBA-BFS pastes (CMBA-BFS AAM), the metallic Al content in MBA was reduced to zero after NaOH solution treatment of MBA. The formation of C-A-S-H gel was detected in *NaOH solution-treated MBA (CMBA)*. The 1-day pre-activation of CMBA could lead to the formation of C-A-S-H gel and N-A-S-H gel.
- The compressive strength of CMBA-BFS AAM was lower than that of 100 BFS AAM. For the same replacement level (from 10 to 30 wt.%), the 90-day compressive strength of CMBA-BFS AAM and the alkali-activated FA-BFS pastes (FA-BFS AAM) was almost equal.
- The incorporation of CMBA in BFS-based alkali-activated pastes delayed the reaction of BFS during the first 7 days but promoted the reaction of BFS at later ages. Compared with alkali-activated paste prepared with blends of 30 wt.% M300 and 70 wt.% BFS (30 M300-BFS AAM), the reaction of BFS was delayed for a longer time in alkali-activated paste prepared by replacing 30 wt.% BFS with MBA (30 CMBA-BFS AAM). After 90 days, the reaction degree of BFS in 30 CMBA-BFS AAM was higher than in 100 BFS AAM and 30 M300-BFS AAM.
- The crystalline reaction product, microcline, was only found in 30 CMBA-BFS AAM. The C-(N-)A-S-H gel was the primary amorphous reaction product in 30 CMBA-BFS AAM, 30 M300-BFS AAM, and 100 BFS AAM. The gel formed in 30 CMBA-BFS AAM had a polymerization degree higher than the gel of 100 BFS AAM and 30 M300-BFS AAM. The Ca/Si atomic ratio of the gel in 30 CMBA-BFS AAM and 30 M300-BFS AAM was similar, both lower than that in the gel of 100 BFS AAM. The Na/Si atomic ratio was the lowest in the gel of 30 CMBA-BFS AAM.
- More reaction products were formed in 30 CMBA-BFS AAM than in 30 M300-BFS AAM. However, the porosity of 90-day 30 CMBA-BFS AAM was higher than that of 90-day 30 M300-BFS AAM, as the pore volume in 30 CMBA-BFS AAM was larger than that of 30 M300-BFS AAM at early ages. This information explains the difference in the compressive strength of 30 CMBA-BFS AAM and 30 M300-BFS AAM.

# Chapter 7

---

## Environmental impacts of blended cement pastes and alkali-activated pastes prepared with mechanically treated MSWI bottom ash



### Highlights

- The blended cement pastes prepared by partially replacing Portland cement with *mechanically treated MSWI bottom ash (MBA)* have a lower environmental impact than Portland cement paste in every impact category. When comparing MBA and Portland cement, the contribution of MBA to the environmental impacts of blended cement pastes is minimal relative to that of Portland cement to plain cement paste.
- The alkali-activated pastes<sup>(1)</sup> prepared with blends of MBA and blast furnace slag have lower environmental impacts than Portland cement paste, except for the impact categories of human toxicity and ecotoxicity potential. Among all the ingredients, the activator is the most significant contributor to the environmental impacts of alkali-activated pastes.

---

<sup>(1)</sup> Alkali-activated paste, alkali-activated mortar, and alkali-activated concrete all belong to alkali-activated materials.

## 7.1 Introduction

The environmental impacts of the construction materials prepared with MSWI bottom ash as mineral additives are influenced by the treatments of MSWI bottom ash and the mix design (see Chapter 2). As stated in Chapter 1, reducing the carbon footprints of Portland cement-based construction materials is a primary motivation for using MSWI bottom ash as supplementary cementitious material (SCM) in blended cement or precursor for alkali-activated materials (AAM). In this chapter, a preliminary life cycle assessment (LCA) is performed to evaluate the environmental impacts of the blended cement pastes prepared using *mechanically treated MSWI bottom ash (MBA)* as SCM (WMBA CEM) and the alkali-activated pastes made from blends of MBA and blast furnace slag (CMBA-BFS AAM). The environmental impacts under consideration include global warming, abiotic resource depletion, ozone layer depletion, photochemical ozone creation, acidification of soil and water, eutrophication, human toxicity, and ecotoxicity [368].

The life cycle inventory (LCI) data of MBA is obtained by assessing the environmental impacts of the mechanical treatments of as-received MSWI bottom ash aggregates (see Chapter 3). The life cycle assessment is carried out for the mix design proposed in Chapter 5 and Chapter 6. As demonstrated in Chapter 5 and Chapter 6, MBA can be successfully used as an alternative to Class F coal fly ash (FA) for the application of SCM and AAM precursor, and paste samples with similar compressive strength can be obtained. During the sample preparation process, water treatment (see Chapter 5) and NaOH solution treatment (see Chapter 6) are performed on MBA to lower its metallic Al content. To improve the accuracy of the life cycle impact assessment (LCIA) results of WMBA CEM and CMBA-BFS AAM, the environmental impacts of the treatments of MBA are examined. In the end, the LCIA results of the MBA-containing blended cement pastes and alkali-activated pastes are compared with those of Portland cement paste and FA-containing blended cement pastes and alkali-activated pastes to determine which mix design is more environmentally friendly for paste production.

## 7.2 Methodology

The life cycle assessment of pastes was performed following the method described in ISO 14040 (2006) [180]. With this method, the LCA procedure consists of four phases: definition of goal and scope, inventory analysis, impact assessment, and interpretation of the results.

### 7.2.1 Definition of goal and scope

- *Goal*

The first goal of the life cycle assessment (LCA) is to assess the environmental impacts of WMBA CEM and CMBA-BFS AAM. The second goal is to identify the constituents with the most significant environmental impacts and find opportunities to reduce the environmental burdens of WMBA CEM and CMBA-BFS AAM.

- *Functional unit*

The environmental impacts of the pastes with different mix designs were calculated and compared on the basis of the functional unit, which is a quantified description of the functions



or performance characteristics of a product [369]. In this work, the functional unit was taken as 1 m<sup>3</sup> paste.

Table 7.1 provides information about the cement pastes and alkali-activated pastes evaluated in the life cycle assessment. It is worth noting that the water treatment or NaOH solution treatment was integrated into the sample preparation process of WMBA CEM and CMBA-BFS AAM, respectively. WMBA CEM was prepared with MBA and PC. The *water-treated MBA (WMBA)* is the solid obtained after the water treatment of MBA. The precursors used to prepare CMBA-BFS AAM are MBA and BFS. The *NaOH solution-treated MBA (CMBA)* is the solid resulting from the NaOH solution treatment of MBA. More detailed information about the cement pastes and alkali-activated pastes can be found in Chapter 5 and Chapter 6, respectively.

Table 7.1 Information about the cement pastes and alkali-activated pastes evaluated in LCA.

Names	Raw materials (wt.%)			
	CEM	BFS	MBA	FA
100 CEM	100	-	-	-
15 FA CEM	85	-	-	15
25 FA CEM	75	-	-	25
15 WMBA CEM*	85	-	15	-
25 WMBA CEM*	75	-	25	-
100 BFS	-	100	-	-
10 FA-BFS AAM	-	90	-	10
20 FA-BFS AAM	-	80	-	20
30 FA-BFS AAM	-	70	-	30
10 CMBA-BFS AAM**	-	90	10	-
20 CMBA-BFS AAM**	-	80	20	-
30 CMBA-BFS AAM**	-	70	30	-

\* The water treatment of MBA was integrated into the sample preparation process of WMBA CEM.

\*\*The NaOH solution treatment of MBA was integrated into the sample preparation process of CMBA-BFS AAM.

- *Scope*

According to EN 15804 (2012) [369], the life cycle of a building is divided into four stages: product stage, construction process stage, use stage, and end-of-life stage (in Figure 7.1). The LCA conducted in this work only covers the product stage in the life cycle (cradle to gate). The product stage includes raw material supply, transport, and manufacturing. Since the object of this work is to compare the environmental impacts of pastes prepared with different raw materials, the LCA only deals with the raw material supply in the product stage. The transportation and manufacturing in the product stage were assumed to be the same for all the cement and alkali-activated paste mixtures and thus were excluded from the LCA.

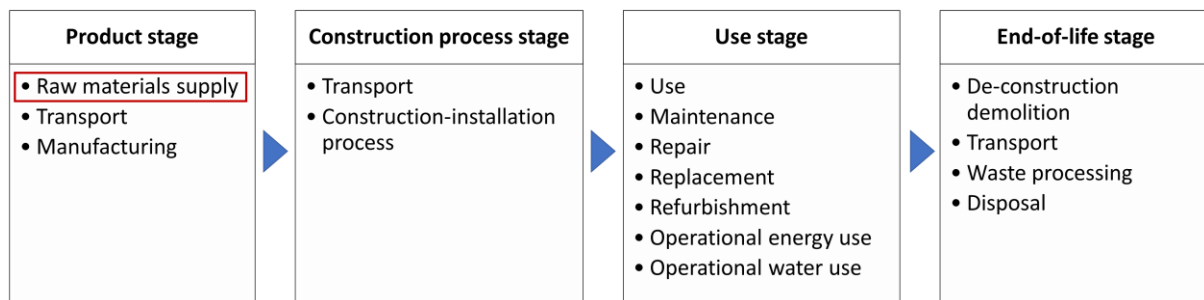


Figure 7.1 The four stages defined in the life cycle of a building [369].

### 7.2.2 Inventory analysis

The raw materials used for the paste sample preparation include MBA, Portland cement (CEM I 52.5 R), blast furnace slag, Class F Coal fly ash, NaOH pellets, sodium silicate solution (35 wt.% solid), and water. In terms of the data resources, the environmental impacts of MBA cannot be found in the current life cycle inventory (LCI) database. The LCI data of Portland cement (PC), BFS, and FA were taken from the environmental product declaration (EPD) provided by the suppliers, Heidelberg Cement, Eco2cem Benelux B.V., and Vliegasunie B.V., respectively. The LCI data of NaOH pellets and sodium silicate solution were provided by the database of NIBE [370]. The environmental impacts of water are assumed to be zero, as it is a kind of natural resource. The data collected for the environmental impacts of PC, BFS, FA, NaOH pellets, and sodium silicate solution are summarized in Table F 1 (see Appendix F).

As illustrated in Figure 7.2, MBA was obtained after the mechanical treatments of as-received MSWI bottom ash aggregates. As-received MSWI bottom ash aggregates can be considered as free of environmental burden [370] because it is the residue of the municipal solid waste incineration and the metal recovery process. The LCI data of MBA was obtained by assessing the environmental impacts of the mechanical treatment process [179]. Like other raw materials, the environmental impacts of MBA were also quantified using ten environmental impact categories and relevant impact indicators (Table 7.2), according to the CML-IA (baseline) impact method developed by the center of Environmental Science of Leiden [368].

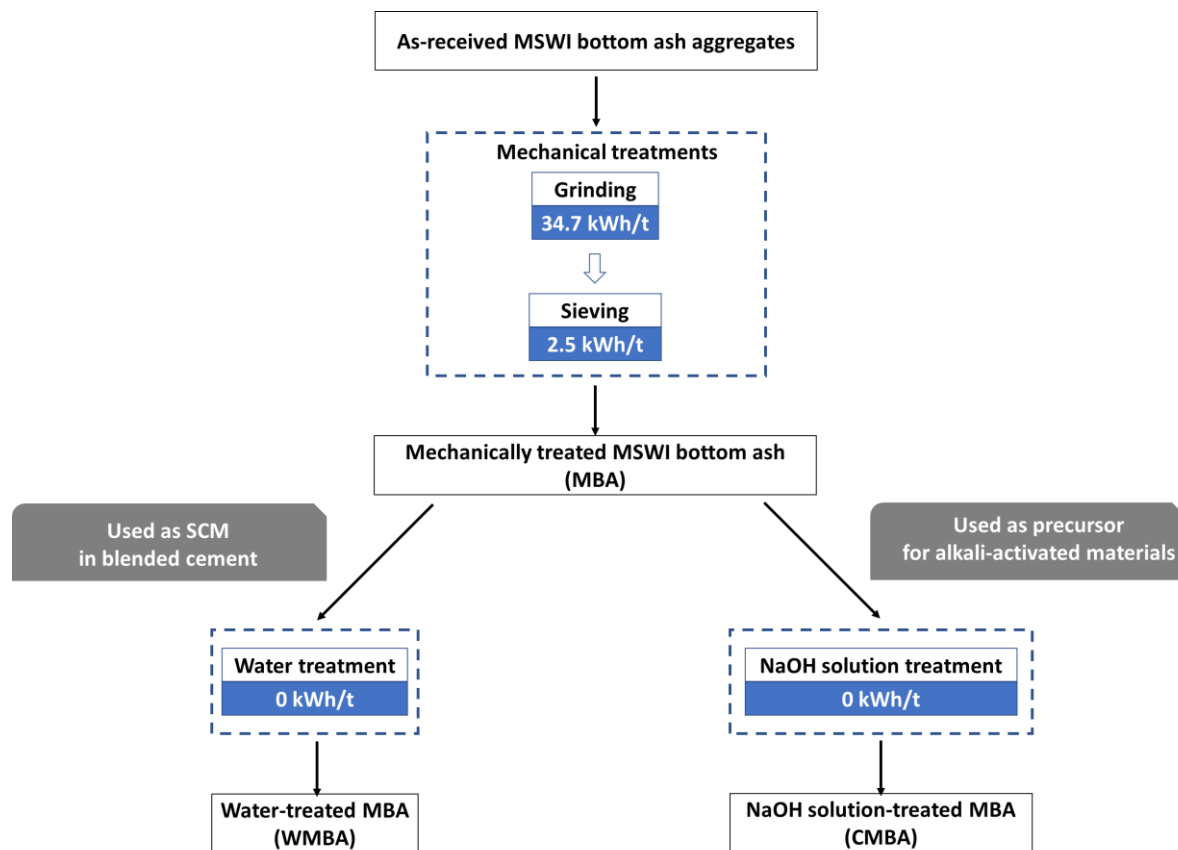


Figure 7.2 The energy consumption of the treatments conducted on as-received MSWI bottom ash aggregates and *mechanically treated MSWI bottom ash (MBA)*.

Table 7.2 The environmental impact categories and relevant impact indicators used in the CML-IA impact method [368] to quantify the environmental impacts in life cycle assessment.

Environmental impact categories	Impact indicators	Indicator abbreviations
Global warming	Global warming potential (100 years)	GWP
Abiotic resource depletion	Abiotic depletion potential-Elements Abiotic depletion potential--Fossil fuels	ADP-Elements ADP-fossil fuels
Ozone layer depletion	Ozone layer depletion potential	ODP
Photochemical ozone creation	Photochemical ozone creation potential	POCP
Acidification of soil and water	Acidification potential of soil and water	AP
Eutrophication	Eutrophication potential	EP
Human toxicity	Human toxicity potential	HTP
Ecotoxicity (freshwater)	Freshwater aquatic ecotoxicity potential	FAETP
Ecotoxicity (marine)	Marine aquatic ecotoxicity potential	MAETP
Ecotoxicity (terrestrial)	Terrestrial ecotoxicity potential	TETP

Table 7.3 Life cycle inventory data of Dutch wind power and the mechanical treatment process of as-received MSWI bottom ash aggregates. The full name of the environmental impact indicators can be found in Table 7.2.

Environmental impact indicators	Unit	Electricity (kWh): 100% wind power (NL) - low voltage (max 1kV) [370]	Mechanical treatments of 1 kg MSWI bottom ash aggregates (grinding and sieving)
GWP	kg CO <sub>2</sub> Equiv.	5.41E-02	2.01E-03
ADP-Elements	kg Sb Equiv.	3.24E-06	1.20E-07
ADP-Fossil fuels	kg Sb Equiv.	3.64E-04	1.35E-05
ODP	kg CFC 11 Equiv.	2.83E-09	1.05E-10
POCP	kg Ethene Equiv.	2.71E-05	1.01E-06
AP	kg SO <sub>2</sub> Equiv.	2.73E-04	1.02E-05
EP	kg PO <sub>4</sub> <sup>3-</sup> Equiv.	3.12E-05	1.16E-06
HTP	kg 1.4 DB Equiv.	6.71E-02	2.49E-03
FAETP		1.14E-03	4.24E-05
MAETP		3.38E+00	1.26E-01
TETP		3.16E-03	1.18E-04

The mechanical treatments consist of grinding and sieving (Figure 7.2). The grinding of as-received MSWI bottom ash aggregates is analogous to the methods of grinding Portland cement clinker. In terms of particle size, the  $D_{50}$  of MBA is 24  $\mu\text{m}$ , almost the same as that of CEM I 42.5N (23.4  $\mu\text{m}$ ) [371]. Therefore, the energy consumption of the grinding of as-received MSWI bottom ash is assumed to be 34.7 kWh/t, the same as that of the grinding employed in the production of Portland cement with 42.5 strength class [372]. The sieving process is also similar to that of the dynamic separator used in the mill plant of Portland cement [373]. Therefore, the energy consumption of the sieving process is taken to be 2.5 kWh/t [373].

The environmental impacts of the mechanical treatments of 1 kg as-received MSWI bottom ash were calculated using its energy consumption (0.0372 kWh/kg) times the environmental impacts of 1 kWh Dutch wind power provided by NIBE [370]. Wind power is widely used in the Netherlands, and its LCI data is shown in Table 7.3. The calculated LCI data of the mechanical treatments of 1 kg as-received MSWI bottom ash are presented in the same table.

As shown in Figure 7.2, when used as SCM and AAM precursor, MBA was further treated with water or NaOH solution to reduce its metallic Al content. The water treatment and NaOH solution treatment were performed at room temperature by manually immersing MBA in water and NaOH solution, respectively (see Chapter 5 and Chapter 6). Therefore, the energy consumption of water treatment and NaOH solution treatment can be negligible. The water treatment and NaOH solution treatment of MBA are considered as free of environmental burden.

### 7.2.3 Impact analysis

According to the CML-IA (baseline) impact method [368], ten environmental impact categories and relevant impact indicators (Table 7.2) were used to quantify the environmental impacts of 1 m<sup>3</sup> cement paste or alkali-activated paste. The equation used for the quantification of each environmental impact is  $C_{total} = \sum M_i \cdot C_i$ , where  $C_{total}$  represents the calculated impact indicator result of 1 m<sup>3</sup> paste,  $M_i$  is the mass of a certain kind of raw material used to prepare 1 m<sup>3</sup> paste, and  $C_i$  indicates the value of the impact indicator of a certain kind of raw material. Table 7.4 and Table 7.5 provide the mass of the raw materials used to prepare 1 m<sup>3</sup> cement paste and alkali-activated paste, respectively.

Table 7.4 Mass of the raw materials used to prepare 1 m<sup>3</sup> cement paste.

Sample names	PC	MBA	FA	H <sub>2</sub> O
	kg			
100 CEM	1401	-	-	561
15 FA CEM	1177	-	208	554
25 FA CEM	1030	-	343	549
15 WMBA CEM	1191	210	-	561
25 WMBA CEM	1051	350	-	561

Table 7.5 Mass of the raw materials used to prepare 1 m<sup>3</sup> alkali-activated paste.

Sample names	BFS	MBA	FA	Water glass solution	NaOH pellets	H <sub>2</sub> O
	kg					
100 BFS AAM	1507	-	-	271	69	335
10 FA-BFS AAM	1339	-	149	268	68	330
20 FA-BFS AAM	1176	-	294	264	68	326
30 FA-BFS AAM	1016	-	435	261	67	322
10 CMBA-BFS AAM	1351	150	-	270	69	333
20 CMBA-BFS AAM	1196	299	-	269	69	332
30 CMBA-BFS AAM	1042	447	-	268	68	331

It is worth noting that the LCIA results of pastes with different mix designs are comparable only when these paste samples have similar compressive strength [369]. The 90-day compressive strength of cement and alkali-activated paste samples is presented in Figure 7.3. Figure 7.3 (a) shows that the 90-day compressive strength of 15 WMBA CEM and 25 WMBA CEM is similar to the Portland cement paste (100 CEM). The WMBA CEM and FA CEM exhibited similar 90-day compressive strength when the same amount of MBA and FA was added to blended cement pastes. Figure 7.3 (b) indicates that the compressive strength of 10 CMBA-BFS AAM and 20 CMBA-BFS AAM is close to that of 100 BFS AAM. The compressive strength of 30 CMBA-BFS AAM is much lower than 100 BFS AAM but is within the same range as that of 100 CEM. The 90-day compressive strength of CMBA-BFS AAM and FA-BFS AAM are almost equal when the percentage of BFS replaced by MBA and FA (from 10 wt.% to 30 wt.%).

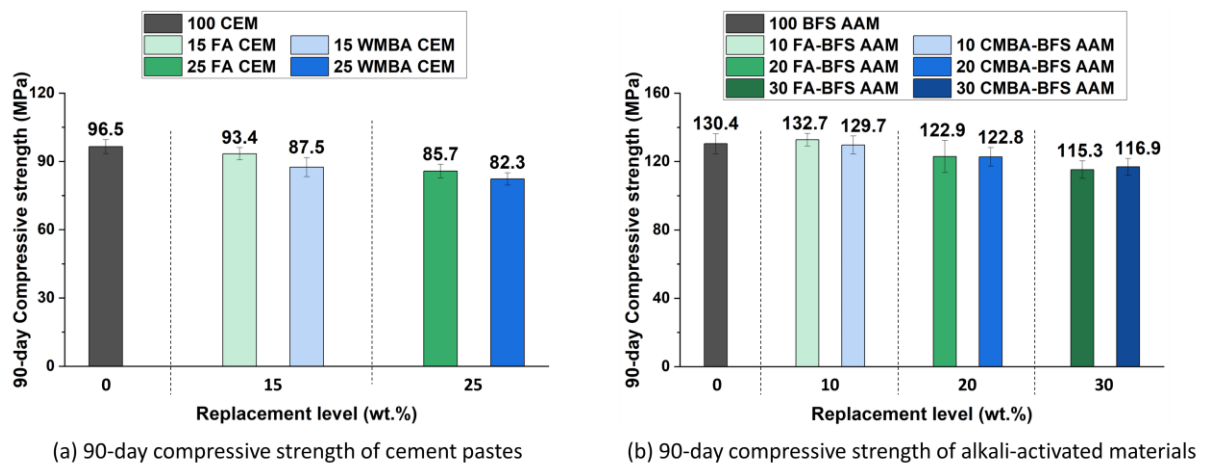


Figure 7.3 The 90-day compressive strength of cement and alkali-activated paste samples listed in Table 7.1.

## 7.3 Result interpretation

### 7.3.1 Environmental impacts of cement pastes

The environmental impacts of Portland cement blended with WMBA (WMBA CEM) were compared with that of the cement pastes with similar compressive strength, including 100 CEM and FA CEM. Figure 7.4 shows the LCIA results of cement pastes with different mix designs. As illustrated in Figure 7.4, WMBA CEM has a lower environmental impact than 100 CEM in every impact category. At the same replacement level (15 wt.% and 25 wt.%), WMBA CEM and FA CEM present similar results for all the environmental categories. The environmental benefits become more pronounced as the addition of MBA or FA in Portland cement paste increased from 15 wt.% to 25 wt.%.

Among all the constituents of blended cement pastes, PC is the most significant contributor in each impact category of WMBA CEM and FA CEM. The contribution of MBA or FA to the environmental impacts of blended cement pastes is almost negligible relative to that of PC. This is because MBA and FA are industrial by-products. Compared with PC, the environmental impacts of FA are much smaller (see Table F 1). As-received MSWI bottom ash aggregates are free of environmental burden. The environmental impacts of producing MBA via the mechanical treatments of as-received MSWI bottom ash are much smaller than the manufacturing of PC (see section 7.2.2). The large environmental impacts of PC are mainly caused by the calcination of raw ingredients to a temperature over 1000 °C for clinker production [32].

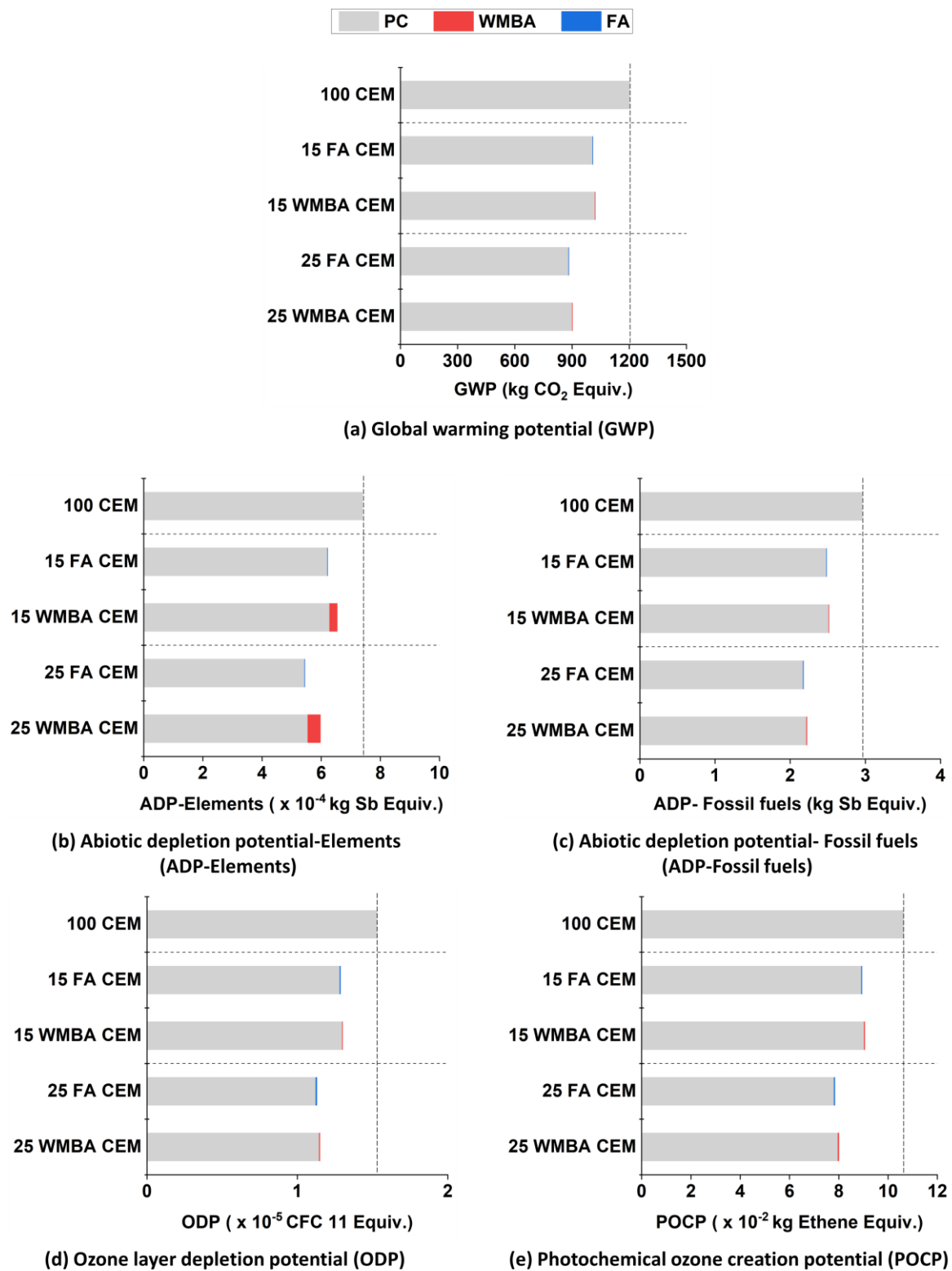


Figure 7.4 The life cycle impact analysis (LCIA) results showing the environmental impacts of 1 m<sup>3</sup> cement paste with different mix designs.



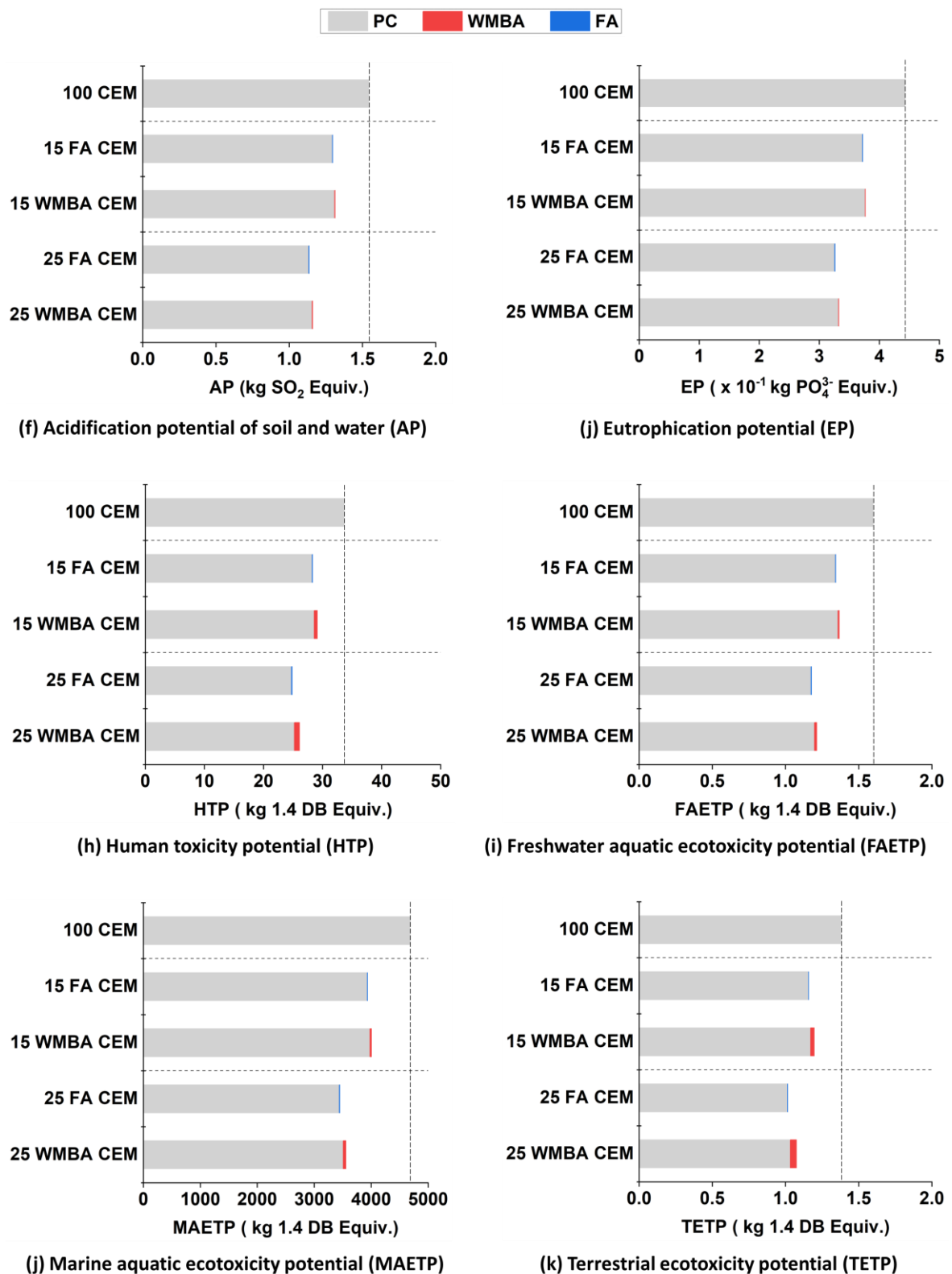


Figure 7.4 (Continued) the life cycle impact analysis (LCIA) results showing the environmental impacts of 1 m<sup>3</sup> cement paste with different mix designs.

### 7.3.2 Environmental impacts of alkali-activated pastes

Figure 7.5 demonstrates the LCIA results of the alkali-activated pastes with different mix designs. Considering that the environmental impacts can only be compared among the paste samples with similar compressive strength, the LCIA results of 10 CMBA-BFS AAM and 20 CMBA-BFS AAM are compared with those of 10 FA-BFS AAM, 20 FA-BFS AAM, and 100 BFS AAM. The environmental impacts of 30 CMBA-BFS AAM are comparable to those of 30 FA-BFS AAM and 100 CEM.

The environmental impacts of 10 CMBA-BFS AAM and 20 CMBA-BFS AAM are smaller than that of 100 BFS AAM in all impact categories. The discrepancy between the environmental impacts of CMBA-BFS AAM and 100 BFS AAM became larger when the addition of MBA increased from 10 wt.% to 20 wt.%. The environmental burdens of 100 BFS AAM are larger because the environmental impact of BFS is larger than that of MBA in every impact category (see Table 7.3 and Table F 1). For the CMBA-BFS AAM and FA-BFS AAM prepared with the same amount of MBA or FA (10 wt.% or 20 wt.%), their environmental impacts are almost equal. This is because MBA and FA have similar environmental footprints.

The LCIA results of 30 CMBA-BFS AAM are similar to that of 30 FA-BFS AAM. The environmental impact of 30 CMBA-BFS AAM is generally much lower than 100 CEM, except for the categories of human toxicity and ecotoxicity potential (HTP, FAETP, MAETP, and TETP). For all these toxicity categories, 30 CMBA-BFS AAM present higher impacts per functional unit when compared with 100 CEM. The higher toxicity potential of 30 CMBA-BFS AAM is due to the addition of NaOH pellets and sodium silicate solution. The environmental impacts of NaOH pellets and sodium silicate solution are much larger than the solid precursors in most of the impact categories, except for ADP-elements and MAETP. The NaOH pellets and sodium silicate solution are the ingredients of alkaline activator. It is recommended to reduce the environmental impacts of the alkaline activator to improve the sustainability of alkali-activated material. For example, alternative alkaline activators can be made from waste materials. The waste-derived activators have the potential to perform similarly to commercial activators [374].

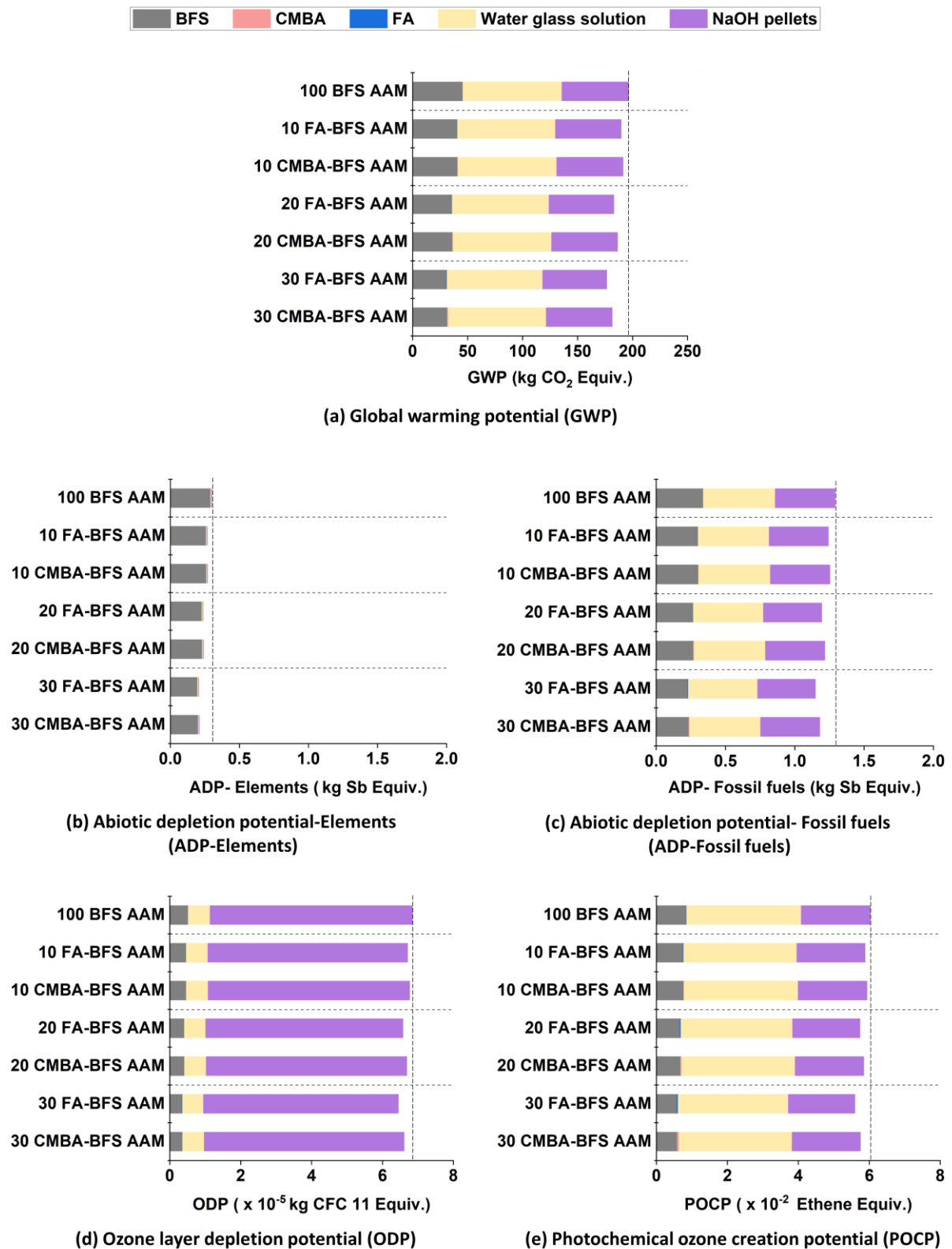


Figure 7.5 The life cycle impact analysis (LCIA) results showing the environmental impacts of 1 m<sup>3</sup> alkali-activated paste with different mix designs.

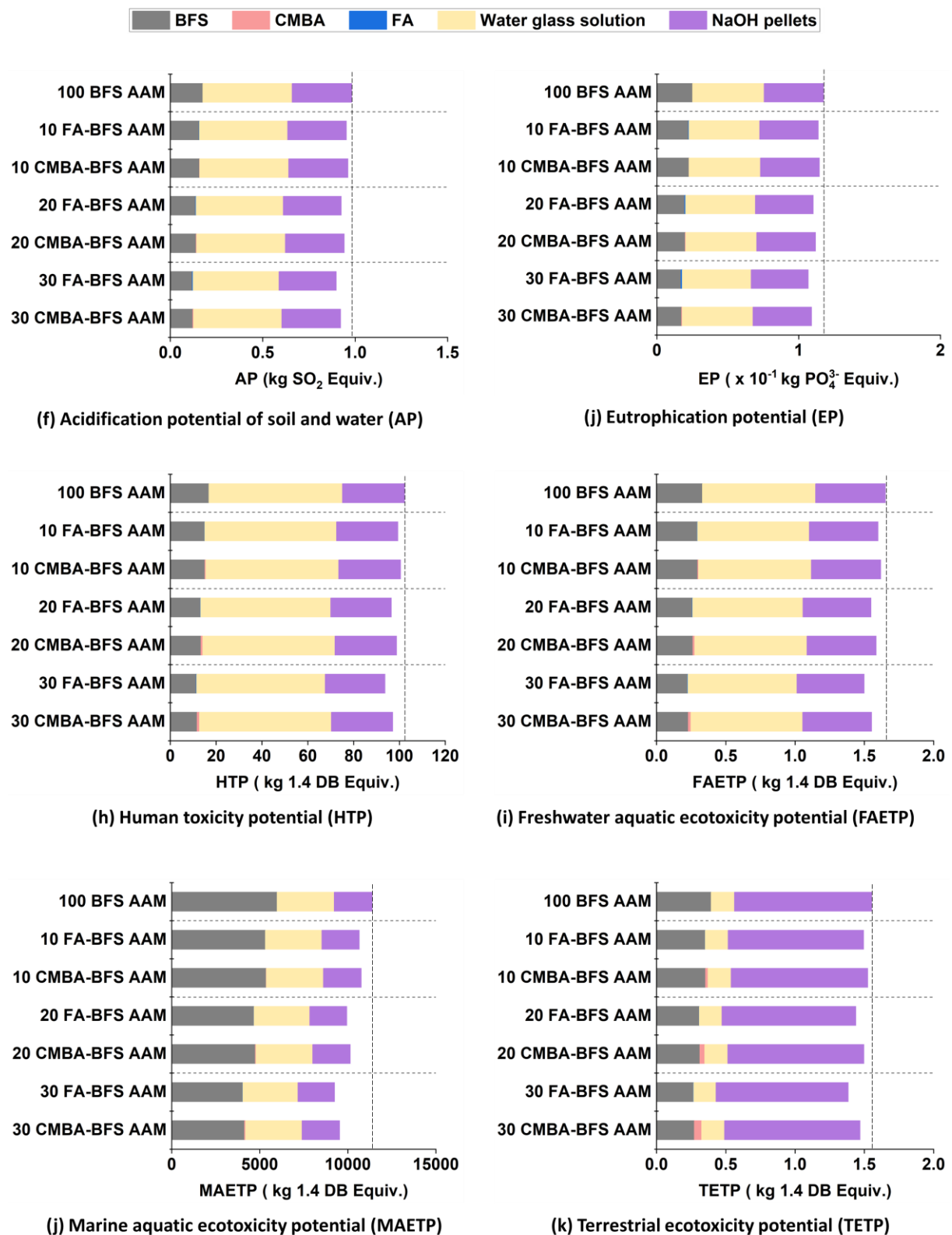


Figure 7.5 (Continued) the life cycle impact analysis (LCIA) results showing the environmental impacts of 1 m<sup>3</sup> alkali-activated paste with different mix designs.

## 7.4 Conclusions

In this chapter, the environmental impacts in the product stage were assessed for the blended cement pastes prepared by partially replacing Portland cement with *mechanically treated MSWI bottom ash* (WMBA CEM) and the alkali-activated pastes made from blends of BFS and MBA (CMBA-BFS AAM). The life cycle impact analysis (LCIA) results of WMBA CEM and CMBA-BFS AAM were also compared with those of the Portland cement paste (100 CEM), the Portland cement pastes blended with Class F coal fly ash (FA CEM), and alkali-activated FA-BFS pastes (FA-BFS AAM). The following conclusions and recommendations can be made:

- Using *mechanically treated MSWI bottom ash* (MBA) as an alternative to Class F coal fly ash (FA) brings little change to the environmental impacts of blended cement pastes and alkali-activated pastes. When the same amount of MBA and FA is blended with Portland cement, the results of calculated LCIA for WMBA CEM and FA CEM are almost equal. When the percentage of BFS replaced by MBA is the same as that of FA, the environmental impacts of CMBA-BFS AAM and FA-BFS AAM are similar.
- Compared with 100 CEM, the environmental impacts of WMBA CEM and FA CEM are smaller, indicating that the replacement of a portion of PC with MBA or FA to produce blended cement pastes is environmentally friendly. The contribution of MBA and FA to the environmental impacts of WMBA CEM and FA CEM is negligible relative to that of Portland cement (PC).
- The environmental impacts of alkali-activated paste prepared with 30 % of MBA (30 CMBA-BFS AAM) are smaller than that of 100 CEM, except for the impacts associated with human toxicity and ecotoxicity (HTP, FAETP, MAETP, and TETP). The higher toxicity potential of 30 CMBA-BFS AAM is caused by NaOH pellets and sodium silicate solution, the constituents that contribute the most to the environmental burdens of alkali-activated pastes. It is recommended to reduce the environmental burdens of alkali-activated pastes by using the activator derived from industrial by-products or wastes.

## 7.5 Limitations of this study

- In this study, the life cycle inventory (LCI) data of MBA was estimated by considering the energy consumed during the mechanical treatments of as-received MSWI bottom ash. The mechanical treatments consisting of grinding and sieving were assumed to be the same as those used in the industrial production of Portland cement. In order to improve the quality of the LCI data for MBA, it is necessary to upscale the lab-scale mechanical treatments to the industrial scale and perform the LCI analysis. This is because the parameters selected for the industrial-scale grinding of MSWI bottom ash aggregates can differ from the industrial parameter settings in the grinding of Portland cement clinker due to the differences in their hardness.
- Due to the lack of data, the life cycle assessment (LCA) performed in this work is limited to the raw material supply in the product stage. The transport and manufacturing in the product stage are assumed to be the same for the cement and AAM mixtures. This assumption is valid only when the transport distances of the raw materials and the sample

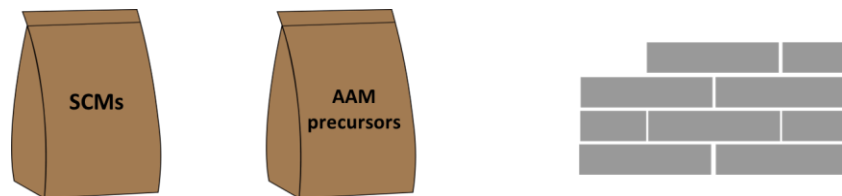
preparation methods are similar for cement pastes and alkali-activated pastes. Since the LCA only includes the product stage, the impacts of CMBA-BFS AAM and WMBA CEM may be underestimated in the categories of human toxicity and ecotoxicity potential. MBA contains leachable heavy metals and soluble salts, which may leach out at the use stage and the end-of-life stage of MBA-BFS AAM and WMBA CEM, increasing their toxicity potential.

- This work only performed the LCA at the paste level. The mix designs may have to be adjusted when the pastes are used in concretes. It is recommended to conduct a complete LCA (“cradle to grave”) at the concrete level. In addition to the compressive strength considered in this work, the durability and leaching test results also need to be considered when comparing the LCIA results of concretes. The concretes with superior durability usually have a longer service life, lowering the environmental impacts at the use stage. The durability of the concretes with CMBA-BFS AAM or WMBA CEM as binder can differ from that of the Portland cement concretes. The leaching of heavy metals and soluble salts from MBA hinders the recycling of demolition wastes, increasing the environmental burdens at the end-of-life stage.

# Chapter 8

---

## Retrospection, conclusions, contributions, and outlooks



*This chapter summarizes the work and main findings of this thesis and presents the scientific and engineering contribution of this research. Recommendations are given concerning the utilization of MSWI bottom ash as a mineral resource for construction materials.*



## 8.1 Retrospection

As discussed in Chapter 1, incineration with an effective air pollution control and energy recovery system is a sustainable solution for the disposal of municipal solid waste. However, municipal solid waste incineration (MSWI) discharges residues, among which bottom ash accounts for the largest proportion. The availability of MSWI bottom ash is in the range of massive cement production. Therefore, it is worth exploring the feasibility of using MSWI bottom ash as an ingredient of construction materials. In recent years, a lot of research has been conducted on the use of MSWI bottom ash as a mineral resource to develop blended cement pastes and alkali-activated pastes (see Chapter 2). This action can help to solve the environmental problems caused by the landfill of MSWI bottom ash, address the worldwide depletion of primary mineral sources, and provide a solution to future shortages of supplementary cementitious material (SCM) and precursor for alkali-activated materials (AAM).

The goal of this research is to develop the knowledge that can be used to guide the application of MSWI bottom ash as SCM and AAM precursor. Based on this knowledge, a strategy for using MSWI bottom ash produced in the Netherlands (4-11 mm) as a mineral resource for construction materials was proposed.

- In Chapter 3, the metallic Al embedded in as-received MSWI bottom ash particles was analyzed, with emphasis on the relationship between the particle size of bottom ash and its metallic Al content. Mechanical treatments consisting of grinding and sieving were selected and studied to reduce the particle size and the metallic Al content of as-received MSWI bottom ash.
- In Chapter 4, the link between the chemical composition of the reactive phases and the reactivity of *mechanically treated MSWI bottom ash (MBA)* was established. The leaching risk of contaminants from MBA to the environment was assessed. Based on this information, remarks about how to use MBA in blended cement pastes and alkali-activated pastes were made.
- In Chapter 5 and Chapter 6, the quality-upgrade treatments of MBA and the mix design of blended cement pastes and alkali-activated pastes were proposed according to the remarks made in Chapter 4. Water treatment and NaOH solution treatment were included in the sample preparation process of blended cement pastes and alkali-activated pastes, respectively, to lower the metallic Al content in MBA. Water treatment and NaOH solution treatment were both performed at room temperature. The extent to which these quality-upgrade treatments can reduce the metallic Al content in MBA was discussed. The acceptable metallic Al content in MSWI bottom ash as SCM and AAM precursor was determined. The chemical reactions that occurred during these quality-upgrade treatments of MBA were analyzed. The reaction of treated MBA in blended cement pastes and alkali-activated pastes was investigated to examine its contribution to microstructure formation and strength development.
- In Chapter 7, the environmental impacts of pastes prepared with MSWI bottom ash SCM and AAM precursor were assessed with the aim of evaluating whether it is

environmentally beneficial to use MSWI bottom ash as a mineral resource for construction materials.

## 8.2 Conclusions

The findings of this research are summarized as follows:

1. *Mechanical treatments dramatically reduce the metallic Al content and particle size of as-received MSWI bottom ash. The effectiveness of mechanical treatments in reducing metallic Al content is strongly influenced by the distribution of metallic Al in MSWI bottom ash particles.*

Most metallic Al removed by mechanical treatment comes from the 0.5-1.6 mm size fraction. The metallic Al embedded in MSWI bottom ash particles smaller than 0.5 mm is difficult to remove with mechanical treatments because they are in the same size range as the mineral particles after grinding. Comparatively, during the grinding process, metallic Al incorporated in coarse MSWI bottom ash particles is more likely to be pressed into plate-shaped scraps with sizes larger than the mineral particles (see *Chapter 3*).

1. *The reactivity of MBA as SCM and AAM precursor is found similar to that of Class F coal fly ash (FA), but much smaller than that of blast furnace slag (BFS). The reactivity of MBA as SCM and AAM precursor is determined by the content and the chemical composition of its amorphous phase.*

The amorphous phase of MBA has a chemical composition within the same range as the amorphous phase of FA. Moreover, the content of the amorphous phase in MBA is close to that of the amorphous phase in FA. Compared with BFS, MBA has less amorphous phase. The CaO/SiO<sub>2</sub> mass ratio of the amorphous phase in MBA is lower than that of the amorphous phase in BFS. The amorphous phase with a lower CaO/SiO<sub>2</sub> mass ratio tends to have a less depolymerized and disordered structure and is thus less reactive under alkaline conditions (see *Chapter 4*).

2. *The factors that influence the utilization of MBA in blended cement pastes and alkali-activated pastes include its reactivity, leaching potential, and metallic Al content.*

Given that the reactivity of MBA is similar to that of FA, the mix design of MBA as SCM and AAM precursor can benefit from the experience with FA reported in the literature. The leaching of Sb and sulfate from MBA is above the upper limits set by the Dutch government. The dosage of MBA in blended cement pastes and alkali-activated paste should not exceed 50 wt.% to prevent the environmental risks of contaminant leaching from the pastes into the environment. The metallic Al content in MBA may not exceed 0.02 wt.% for the application of SCM to prevent the formation of expansive cracks in blended cement pastes. Prior to the application as AAM precursor, the metallic Al content in MBA needs to be reduced to zero to avoid volume expansion of alkali-activated pastes (see *Chapters 4-6*).

3. *Thermodynamic modeling is a very useful tool to guide the mix design when MBA is used as AAM precursor.*

The chemical and mineralogical compositions of MBA are within the same ranges as the compositions of MSWI bottom ash reported in the literature. The phase assemblages of alkali-activated MBA paste predicted by thermodynamic modeling are in good agreement with the experimental results of previous researchers. The modeling results indicate that if the  $\text{Na}_2\text{O}$  content in the activator is higher than 5 wt.%, some of the Si released by MBA will be present in the pore solution rather than forming stable reaction products with the Na provided by the activator. This modeling result can give a rough guide to the mix design. When MBA is used to prepare alkali-activated pastes, the  $\text{Na}_2\text{O}$  content in the activator may not exceed 5 wt.% to ensure that all the Si released by MBA is incorporated into the reaction products. If the  $\text{Na}_2\text{O}$  content in the activator is designed to be higher than 5 wt.%, it is better to blend MBA with Ca- or Al-enriched precursors to prepare AAM, such as blast furnace slag, to consume the Si dissolved from MBA (see Chapter 4).

*4. The water treatment proposed in this work is effective in lowering the metallic Al content of MBA at room temperature. At the same replacement level, the compressive strength of WMBA blended Portland cement pastes is close to that of FA blended Portland cement pastes.*

After water treatment of MBA, the residual metallic Al content in WMBA is around 0.02 wt.%. Water treatment of MBA only slightly changes the mineralogical compositions by increasing the content of amorphous phase and calcite. When water treatment is combined with the sample preparation process, the replacement level of MBA in blended cement pastes can reach up to 25 wt.% without forming cracks caused by hydrogen gas release (see Chapter 5).

*5. The metallic Al embedded in MBA can be completely oxidized at room temperature with the NaOH solution treatment proposed in this work. The compressive strength of alkali-activated CMBA-BFS pastes is almost equal to that of alkali-activated FA-BFS pastes when the amount of MBA and FA used in sample preparation is the same.*

MBA reacts during the NaOH solution treatment, resulting in slight dissolution of the amorphous phase and formation of a trace amount of C-A-S-H gel. When NaOH solution treatment is part of the mixture preparation process, the highest achievable dosage of MBA in alkali-activated pastes is 30 wt.%. If the dosage of MBA exceeds 30 wt.%, the amount of solution required for the NaOH solution treatment of MBA is more than that can be taken from the activator used for the preparation of alkali-activated CMBA-BFS pastes (see Chapter 6).

*6. Adding MBA in Portland cement paste and alkali-activated BFS paste changes the reaction product and microstructure formation. The reaction products of WMBA and CMBA contribute to the strength development of blended cement pastes and alkali-activated pastes, respectively.*

Although blending WMBA with Portland cement delays clinker hydration on the first day, the hydration of clinker is enhanced at later ages. The sulfate dissolved from MBA during water treatment promotes ettringite formation in 1-day WMBA blended Portland cement pastes. The reaction of WMBA consumes portlandite, resulting in the formation of sodicgedrite and

amorphous phase. The Ca/Si atomic ratio of the C-S-H gel formed in WMBA blended Portland cement pastes is smaller than that of the C-S-H gel generated in Portland cement paste (see Chapter 5).

The reaction of BFS in the alkali-activated CMBA-BFS pastes is delayed during the first 7 days but is enhanced at later ages. Microcline is the newly formed crystalline reaction product after adding CMBA in alkali-activated BFS. Blending CMBA with BFS increased the polymerization degree of the gel phases formed in alkali-activated pastes. The Ca/Si atomic ratio and the Na/Si atomic ratio of the gel in alkali-activated CMBA-BFS pastes are lower than the ratios of the gel in alkali-activated BFS paste (see Chapter 6).

*7. Using MBA as a mineral resource to prepare blended cement pastes and alkali-activated pastes is environmentally beneficial, especially for the reduction of CO<sub>2</sub> emission.*

The partial replacement of Portland cement with MBA can reduce the environmental footprints of Portland cement paste in every impact category, including global warming, abiotic resource depletion, ozone layer depletion, photochemical ozone creation, acidification of soil and water, eutrophication, human toxicity, and ecotoxicity (see Chapter 7).

Compared with Portland cement paste, alkali-activated pastes prepared with blends of MBA and blast furnace slag have lower environmental impacts, except for the impact categories of human toxicity and ecotoxicity potential. Among all the ingredients, the activator is the most significant contributor to the environmental impacts of alkali-activated pastes (see Chapter 7).

### 8.3 Contributions of this research to science and engineering

The contributions of this research to science and the application of MSWI bottom ash as SCM and AAM precursor are summarized as follows:

*1. This research deepens the understanding of the reaction of MSWI bottom ash as SCM and AAM precursor. The knowledge developed in this work can help to stimulate the application of MSWI bottom ash as mineral resources in construction materials.*

The chemical and mineralogical compositions of the MSWI bottom ash studied in this research are within the same range as the compositions of the MSWI bottom ash reported in the literature. The knowledge developed in this work, including the distribution of metallic Al embedded in MSWI bottom ash particles, the chemical properties of the amorphous phase of MSWI bottom ash, and the reaction of MSWI bottom ash in blended cement pastes and alkali-activated pastes, can be used to stimulate the application of MSWI bottom ash produced in other regions.

*2. This study proposed a solution for the quality upgrade of MSWI bottom ash (4-11 mm) produced in the Netherlands, making it suitable as an alternative to Class F coal fly ash for the application of supplementary cementitious material and precursor for alkali-activated materials.*

The mechanical treatments, water treatment, and NaOH solution treatment proposed in this work are effective in reducing the metallic Al content of MSWI bottom ash and have the potential to be up-scaled to commercial plant-scale treatments. During mechanical treatments of as-received MSWI bottom ash, grinding is performed at low speed and finished within a short time. The energy consumption and cost of proposed mechanical treatments are relatively low. The water treatment and NaOH solution treatment have very low environmental impacts, as they are performed at room temperature and no wastewater is discharged from these treatments.

*3. This work demonstrated how to develop blended cement pastes and alkali-activated pastes with MSWI bottom ash by considering the chemical and physical properties of as-received MSWI bottom ash. The strategy employed in this work is also applicable to the development of construction materials by using MSWI bottom ash produced in other regions as SCM and AAM precursor.*

In this research, the method used to develop blended cement pastes and alkali-activated pastes with MSWI bottom ash includes the following five steps:

- **Step 1** Characterization of as-received MSWI bottom ash to identify the issues that hinder the application of MSWI bottom ash as SCM or AAM precursor (see *Chapter 3*).
- **Step 2.** Selection of appropriate treatments to improve the quality of as-received MSWI bottom ash and make treated MSWI bottom ash meet the requirements for use as SCM and AAM precursor (see *Chapters 3-6*).
- **Step 3.** Mix design according to the reactivity and leaching potential of treated MSWI bottom ash and targeted compressive strength of blended cement pastes and alkali-activated pastes (see *Chapters 4-6*).
- **Step 4.** Assessment of the environmental impacts of the construction materials prepared with MSWI bottom ash as SCM and AAM precursor (see *Chapter 7*).

## 8.4 Outlooks

*Mix design of blended cement pastes and alkali-activated pastes with MSWI bottom ash as SCM and AAM precursor*

Thermodynamic modeling is a powerful tool to simulate the reaction products and pore solution of the pastes prepared with MSWI bottom ash as SCM and AAM precursor (see Chapter 4). The simulation results can be used as a reference to guide the mix design when MSWI bottom ash is used to prepare blended cement pastes and alkali-activated pastes. With the help of modeling, it takes a shorter time to find a desirable mix design. In this way, the efficiency of developing new construction materials with MSWI bottom ash can be greatly improved.

It is worth noting that the accuracy of the modeling results is determined by the ideal solid solution model used for the simulation of the gel phases. Given that the composition of the amorphous phase in MSWI bottom ash is within the same range as Class F coal fly ash (see

Chapter 4), it is recommended to extend the N(C)ASH<sub>ss</sub> model proposed for Class F coal fly ash and improve its accuracy in predicting the reaction products of alkali-activated MSWI bottom ash. The experimental study of the solid phase evolution of alkali-activated MSWI bottom ash pastes is required to validate the simulated solid phase evolution. Considering the wide variety of the MSWI bottom ash produced in the world, it is recommended to study the ones with representative chemical and mineralogical compositions. The compositional range for the MSWI bottom ash produced worldwide can be found in Chapter 2.

#### *Industrial application of MSWI bottom ash as SCM and AAM precursor*

The prerequisite for using a high dosage of MSWI bottom ash in blended cement pastes and alkali-activated pastes is to improve the quality of MSWI bottom ash through quality-upgrade treatments. However, a high dosage of MSWI bottom ash should not be realized at the expense of unexpected damage to the environment. The risk of excessive heavy metal leaching and high cost of quality-upgrade treatments discourage the construction industry from using MSWI bottom ash as SCM or AAM precursor. Considering the rapid growth rate of global MSWI bottom ash production, it is necessary to invest time and energy in developing environmentally friendly and economical plant-scale treatment techniques.

It is recommended to build a database about the chemical and physical properties of MSWI bottom ash produced in the world. Based on this database, a classification system can be made according to the qualities of MSWI bottom ash. The classification system of cement can be used as a reference for classifying MSWI bottom ash. Establishing a database can help promote the commercial application of MSWI bottom ash in concrete.

This research shows that the addition of MSWI bottom ash in blended cement pastes and alkali-activated pastes changes the reaction production and microstructure (see Chapter 5 and Chapter 6). It is necessary to investigate whether these changes have any impact on the long-term performance of the pastes. It is important to study the fresh properties, long-term performance, durability, leaching potential, and environmental impacts of concrete products prepared with MSWI bottom ash. This information is critical for the formulation of the design codes when MSWI bottom ash is used as an ingredient of concrete. Once the legal guidelines are established, the widespread industrial application of MSWI bottom ash as a mineral resource for construction materials will be possible.

#### *Environmental impacts of constructions containing MSWI bottom ash*

It is important to keep track of the leaching of heavy metals over the life cycle of constructions containing MSWI bottom ash. The concrete elements that contain MSWI bottom ash should be registered. In this case, at the stage of demolition, it is possible to distinguish and separate the concretes made from MSWI bottom ash. The demolished concrete elements with MSWI bottom ash as an ingredient should not mix with other demolition wastes to avoid contamination of heavy metals. The recycling of the demolition waste containing MSWI bottom ash is another important topic from the perspective of minimizing environmental impacts.

---

## *Appendixes*

---



## Appendix A

Table A 1 Mineralogical compositions of weathered MSWI bottom ash determined by QXRD analysis.

Mineral Types	Minerals (wt.%)	Particle size (mm) of weathered MSWI bottom ash											
		< 0.6 [115]		0 - 8 [375]	8 - 30 [375]	≤ 4 [110]	4 - 12 [82]	Unknown [70]	Not separated [17]	0 - 2 [112]	Unknown [125]	0 - 8 [81]	
		Thailand		UK		The Netherlands			Germany	Spain	Canada	Belgium	
SiO <sub>2</sub>	Quartz	13.5	22.6	7.2	7.6	12.5	5.4	14.4	9.4	10.9	4.7	12	21
	Cristobalite	-	-	-	-	-	-	-	0.3	-	-	0.6	1.1
FeO <sub>x</sub>	Hematite	0.8	1.5	-	-	3.8	0.4	0.9	1.8	0.9	1.6	1	2.4
	Magnetite	1.8	2.9	-	-	8.9	0.2	-	1.8	1.7	-	2.5	0.8
	Wustite	-	-	-	-	1.5	-	-	0.6	-	-	0.6	-
	Magnesioferrite	-	-	0.9	0.7	-	-	-	-	-	-	-	-
Silicates	Melilite group												
	Melilite	-	-	2.1	1.2	4.7	2	-	2.1	-	-	-	-
	Gehlenite	-	11.3	-	-	-	-	2.2	-	-	-	4.5	0.7
	Feldspar group												
	Alkali Feldspar	-	-	-	-	-	-	-	-	-	-	1.8	2.2
	Sanidine	-	-	1.1	2.0	-	-	-	-	-	-	-	-
	Microcline	3.5	3.3	-	-	-	-	-	-	1.4	-	-	-
	Albite	4.5	1.2	3.0	6.7	-	4.3	-	-	2.3	-	-	-
	Plagioclase Feldspar	-	-	-	-	5.7	-	-	1.7	-	5.1	-	-
	Anorthite	-	-	-	-	-	-	0.6	-	-	-	-	-
	Pyroxene group												

	Pyroxene	-	-	-	-	4.2	-	-	-	-	-	1	-
	Diopside	-	-	-	-	-	1.8	-	1.4	-	-	-	-
	Wollastonite	-	-	-	-	-	-	-	-	-	-	1.8	1.6
	Augite	-	-	-	-	-	-	-	1.1	-	-	-	-
	Clinopyroxene	-	-	-	-	-	-	9.3	-	-	-	-	-
	Other silicates												
	Mullite	12.1	-	-	-	-	-	-	-	-	-	-	-
	Mg-chloritoid	2.3	-	-	-	-	-	-	-	-	-	--	-
	Margarite	-	-	0.3	1.3	-	-	-	-	-	-	-	-
	Muscovite	-	-	-	-	-	-	-	2.8	0.9	-	-	-
	Zeolite	-	-	-	-	0.1	-	-	-	-	-	-	-
	Chabazite	-	-	-	-	-	-	-	0.8	-	-	-	-
	Amphibole	-	-	-	-	-	-	-	3.7	-	-	-	-
Carbonates	Calcite	2.7	-	0.9	0.8	13.5	2.9	3.4	4.7	11.4	22.7	7.5	1.9
	Dolomite	-	-	-	-	-	1.2	-	-	-	-	-	-
	Potassium carbonate	-	-	-	-	-	-	-	2.1	-	-	-	-
Sulfates	Ettringite	-	-	-	-	0.2	-	-	6.5	-	-	-	-
	Gypsum	-	-	-	-	0.2	-	-	-	-	-	0.7	0.4
	Anhydrite	-	-	-	-	-	-	-	1.7	-	4.2	0.3	4.1
	Vishnevite	-	-	0.3	0.8	-	-	-	-	-	-	-	-
	Rozenite	-	-	-	0.8	-	-	-	-	-	-	-	-
	Alunite	-	-	-	-	-	-	-	0.7	-	-	-	-
	Baryte	-	-	-	-	-	-	-	0.2	-	-	-	-
Chloride Salts	Halite	-	-	-	-	0.8	0.5	-	-	-	2.4	-	-
Phosphates	Apatite	-	-	-	-	6.5	-	-	-	1.1	-	-	7.7
Non-ferrous metal oxides	Corundum	-	-	-	-	-	-	-	4.4	-	-	-	-
	Periclase	-	-	-	-	-	-	-	0.5	-	-	-	-
	Rutile	-	-	-	-	1.3	-	-	0.9	-	2.2	-	-
Hydroxides	Hydrocalumite	-	-	-	-	-	-	-	15.4	6.7	-	-	-
	Hydroxilapatite	-	-	-	-	-	-	-	-	2.1	-	-	-

	Rosenhahnite	-	-	-	-	-	-	-	1.5	-	-	-	-
	Gibbsite	-	-	-	-	-	-	-	0.4	-	-	-	-
	Lepidocrocite	-	-	-	-	-	-	-	0.6	-	-	-	-
	Tobermorite	-	-	-	-	-	-	-	0.6	-	-	-	-
Sulfides	Covellite	-	-	-	-	-	-	-	0.8	-	-	-	-
Other minerals	Hercynite	-	-	-	-	-	-	-	0.8	-	-	-	-
	Graphite	-	-	1.7	2.4	-	-	-	-	-	-	-	-
	Silicon	-	-	-	-	-	-	-	0.3	-	-	-	-
Amorphous		58.8	59.3	81.3	75.4	36.1	81.2	69.2	30.8	60.1	57.1	65	56

Table A 2 Summary of the studies reporting utilization of MSWI bottom ash as supplementary cementitious materials.

Origin	Particle size of used MSWI bottom ash ( $\mu\text{m}$ ) and plant-scale treatments	Lab-scale treatments and remaining metallic Al content (wt.%)	SiO <sub>2</sub>	CaO	Binder		Water to binder ratio	Mix ratio	Curing conditions	Measured specimen size (mm)	Compressive strength at max. replacement (MPa)	References
			wt.% from XRF		MSWI bottom ash (Max. wt.%)	Other binders						
Belgium	< 250 (as - received: fresh 0 - 2 mm, 2 - 6 mm, 6 - 15 mm)	Ball milled + water treated+ dried (105 °C)	32.1 - 56.6	14.47 - 22.70	25	Portland cement (CEM I 52.5 N)	0.5	1:3 (M)	N	40 × 40 × 160	28d: decreased compared with reference mortar	[56]
Belgium	< 142 D <sub>50</sub> = 10 (as - received: 2 - 6 mm)	Ball milled + sieved Metallic Al: 0.19	43.9	18.4	20	Portland cement (CEM I 52.5R)	0.48 (OPC concrete) 0.46 (BA blended concrete) (superplasticizer)	C	20 ± 2 °C, 95 ± 5 % RH	150 × 150 × 150	2d and 7d: close to reference concrete 28d and 91d: higher than reference concrete	[149]
Canada	Average: 9.3	Milled Metallic Al: 0.06	28.64	22.91	20	Portland cement	Paste (pressurized compact molding): 0.15 Concrete (dry cast): 0.35	P C	100% RH	Cylindrical paste: 15 (diameter) × 30 (height) Concrete: 100 × 76 × 31	Paste: 76.51 <sup>90d</sup> (88.3 % of reference OPC) Concrete: 32.02 <sup>90d</sup> (18.4 % higher than reference OPC concrete)	[125]
China	< 45	Ball milled	59.59	7.58	50	Portland cement (PII 52.5)	N	M	20 ± 1 °C, > 95 % RH	40 × 40 × 160	10.1 <sup>3d</sup> , 29.2 <sup>28d</sup> (decreased 54.7 % and 44.5 % compared with OPC mortar)	[27]
China	< 150 Average: 30	Ball milled, Alkali treated + water washed Metallic Al: 0	25.89	32.47	20	Portland cement	0.484 (superplasticizer)	1:2.75 (M)	Lime water immersion	50 × 50 × 50	90d: close to reference mortar	[130]
China	< 154 Average: around 10	Milled	53.8	14.30	50	Portland cement Class 42.5	N	P	20 ± 2 °C, > 90 ± 5 % RH	40 × 40 × 160	28d: dramatic decrease compared with reference paste	[153]
China	< 180	Ball milled	48.41	14.78	30	Portland cement Class 42.5	0.5	1:3 (M) 0.5:1.86:3.78 (C)	20 ± 2 °C, > 95 % RH	40 × 40 × 160	24.4 <sup>28d</sup> (decreased compared with reference mortar)	[376]
China	D <sub>50</sub> = 10-40 (as-received: 5 - 10 mm)	Ball milled	51.18	15.47	20	Portland cement	0.484	1:2.75 (M)	Ambient (23 °C)	40 × 40 × 40	28d: decreased 10 - 20 % compared with OPC mortar 90d: close to OPC mortar	[28]
China	D <sub>50</sub> = 10	Ball milled	53.76	14.25	30	Portland cement Class 42.5	0.5	1:3 (M)	20 ± 2 °C, saturated lime water	40 × 40 × 160	28d: around 40	[152]
Italy	D <sub>50</sub> = 3	Microsphere milled (wet ground,	53.41	13.25	30	Portland cement	0.5 (superplasticizer)	C	95 % RH	100 × 100 × 100	64.5 <sup>28d</sup> (1.6 % higher than OPC concrete)	[30]

		solid/water ratio of 1:1)				(CEM I 52.5 R)					90d and 180d: higher than OPC concrete	
Italy	D <sub>50</sub> = 3.5	wet ground (solid content in the slurry: 44 %)	61.9	15.9	30	Portland cement	0.43 (superplasticizer)	C	20 °C, moist curing	100 × 100 × 100	87 <sup>180d</sup> (around 20 % higher than OPC concrete)	[151]
Netherlands	< 63 (as - received: < 2 mm)	Ball milled + thermally treated (550 °C, 750 °C) Metallic Al: < 0.2	35.98	19.34	30	Portland cement (CEM I 52.5 R)	N	1:3 (M)	Water immersion	40 × 40 × 160	51 <sup>28d</sup> (15 % reduction compared to reference mortar)	[53]
Netherlands	D <sub>50</sub> = 39 (as - received material: < 3 mm)	Milled	50.7	12.9	5	Portland cement (CEM I 52.5 R and CEM I 42.5 N)	0.5	1:3 (M)	N	40 × 40 × 160	28d: decreased 7-11 % compared with reference mortar	[103]
Portugal	Average: 39	N	51.84	22.99	40	Portland cement (CEM I 42.5 R) and coal fly ash	0.72 (water reducer)	C	20 ± 2 °C, 50 ± 5 % RH	150 × 150 × 150	Decreased compared with reference concrete	[49]
Slovenia	< 90 (as - received: 1 to 200 mm)	Ball milled	24	39	40	Portland cement (CEM I 42.5 R)	0.5	1:3 (M)	22 ± 2 °C, 100% RH	40 × 40 × 160	28d: decreased compared with OPC mortar	[150]
Taiwan	< 75	Thermal treated (1400 °C, vitrification) + Ball milled	25.6	26.1	40	Portland cement (type I)	0.38	P	25 °C, > 98 % RH	Rectangular	21 <sup>7d</sup> , 38 <sup>28d</sup> , 50 <sup>90d</sup> (decreased 42 %, 19 %, and 10 %, respectively, compared with OPC)	[16]
Taiwan	< 75	Thermal treated (1400 °C, vitrification) + Ball milled	25.6	26.1	40	Portland cement (type I)	0.38	P	25 °C, > 98 % RH	50 × 50 × 50	From 1d till 90d: 10 to 42 % decline compared with OPC	[154]
Taiwan	D <sub>90</sub> < 21 (as - received 5 - 10 mm)	Water washed + acid washed + thermally treated (1100 °C) + ball milled	38.14 (raw) 86.46 (treated)	43.27 (raw) 6.14 (treated)	15 vol.% (volume percentage)	15 vol.% rice husk ash (treated at 550, 700, 900 °C) + 70 vol. % Portland cement (type I)	0.21 (superplasticizer)	P	25 ± 2 °C, water	50 × 50 × 50	28d: 35.92-42.11 (decreased by 25.6 % to 12.8 %)	[132]
Thailand	< 45 D <sub>50</sub> = 5.15	Ball milled	15.8	38.1	40	Portland cement	0.484 (superplasticizer)	1:2.75 (M)	Saturated limewater	50 × 50 × 50	29.3 <sup>7d</sup> 35.7 <sup>28d</sup>	[176]

US	< 90 (as - received: < 50 mm)	Ball milled Metallic Al: 0.03 %	N	N	30	Portland cement (type I)	> 0.5	P	21 ± 1 °C, 70 ± 3 % RH	Cylinder: 100 (diameter) × 50 (height)	15.1 <sup>28d</sup> (decreased 46.6 % compared with OPC)	[377]
----	-------------------------------------	---------------------------------------	---	---	----	--------------------------------	-------	---	---------------------------	--	--	-------

N: no information

D<sub>50</sub>: Mean particle size, RH: Relative humidity, P: Paste, M: Mortar (cement: sand), C: Concrete (cement: sand: aggregate), d: day

Table A 3 Summary of studies reporting utilization of MSWI bottom ash as precursor for alkali-activated materials.

Alkali-activated materials prepared using MSWI bottom ash as precursor													
Origin	Information of used MSWI bottom ash and plant-scale treatments	Lab-scale treatments and metallic Al content (wt.%)	SiO <sub>2</sub>	Al <sub>2</sub> O <sub>3</sub>	CaO	Binder	Activators		Mix ratio	Curing conditions	Measured specimen size (mm)	Compressive strength (MPa)	References
			wt.% from XRF			MSWI bottom ash (%)							
China	Metallic Al content: 1.92 wt.%	Water washed + ball milled + NaOH solution treated (3 h) or calcinated (1050 °C)	51.82	14.18	16.44	100	Na <sub>2</sub> SiO <sub>3</sub> solution + NaOH solution	0.6 (liquid to binder ratio)	1:3 (M)	20 ± 2 °C, 95 % RH	40 × 40 × 160	Original: 0 <sup>3d</sup> 2.4 <sup>28d</sup>	[131]
												After NaOH treatment: 1.9 <sup>3d</sup> 8.4 <sup>28d</sup> 10.3 <sup>60d</sup>	
												After calcination: 3.8 <sup>3d</sup> 10.4 <sup>28d</sup> 13.3 <sup>60d</sup>	
Portugal	D <sub>50</sub> = 45 µm Contains metallic Al (percentage unknown)	Ball milled Metallic Al: 0.44 (defoamed before casting)	51.84	5.00	23.00	100	Na <sub>2</sub> SiO <sub>3</sub> solution or NaOH solution	0.65 (liquid to binder ratio) (2% water reducer)	1:3 (M)	70 °C (1d) then 20 ± 3 °C, 50 % RH	40 × 40 × 160	90d NaOH activated samples: 6 - 7	[156]
												90d Na <sub>2</sub> SiO <sub>3</sub> activated samples: 1 - 4	



Portugal	D <sub>50</sub> = 45 µm Contains metallic Al (percentage unknown)	Ball milled Metallic Al: 0.44 (15 min mixing time + 45 min defoamed before casting)	51.84	5.00	23.00	100	NaOH solution (10M)	0.65 (water reducer)	1:3 (M)	18 °C, 65 % RH (1d) or 70 °C (1d) or 70 °C (2d) or 90 °C (1d) then 20 °C, 60 % RH	40 × 40 × 160	112d: 15 - 30  90d flexural strength: 2 - 4	[155]
Singapore	D <sub>50</sub> < 20 µm (Fresh) Contains metallic Al (percentage unknown)	105°C 24 h	32.75	8.57	29.06	100	NaOH solution+ Na <sub>2</sub> SiO <sub>3</sub> solution	0.6 or 0.75 or 0.9 (liquid to solid ratio)	P	75 °C (3d)	50 × 50 × 50	3d: 0.95 - 2.82	[170]
Singapore	< 75 µm (Fresh)	Ball milled + sieved (only use the glass fraction)	67.64	1.76	9.81	100	NaOH solution (14 M) + Na <sub>2</sub> SiO <sub>3</sub> solution Mass ratio: 1:2	0.5 (liquid to solid ratio)	P	75 °C, 98 % RH – 3d	50 × 50 × 50	30.0 <sup>3d</sup>	[165]
Singapore	Glass fraction: < 75 µm, D <sub>50</sub> = 16.9 µm	Manual separation + magnet separation + ball milled	68.04-69.05 Glass fraction:	1.71-1.96 Glass fraction	9.59-10.42 Glass fraction	Glass fraction + non-ferrous fraction	NaOH solution (8 M) + Na <sub>2</sub> SiO <sub>3</sub> solution SiO <sub>2</sub> /Na <sub>2</sub> O ratio = 1.57)	0.5 (solution to solid)	P	75 °C 3d, 98 % RH	50 × 50 × 50	3d: 4.0 - 31.7	[168]
	Non-ferrous fraction: < 150 µm, D <sub>50</sub> = 22.7 µm (> 1.18 mm fraction)		30.5-40.2 Non-ferrous fraction	8.87-10 Non-ferrous fraction	24.16-30.1 Non-ferrous fraction								
	Fresh, original < 1 dm Contains metallic Al (percentage unknown)												
Spain	< 80 µm (Weathered 3 months) Contains metallic Al (percentage unknown)	Sieved + crushed (Jaw) + milled (disc mill)	45.44	10.38	17.55	100	Na <sub>2</sub> SiO <sub>3</sub> solution+ NaOH solution Mass ratio 4:1	1 (liquid to solid ratio)	P	25 ± 1 °C 95 ± 5 % RH (demold after 3 days)	25 × 25 × 25	28d: 4 - 7	[29]

Spain	< 80 μm (As-received: 8 - 30 mm) Weathered (2 - 3 months) Contains metallic Al (percentage unknown)	Crushed + milled Contains metallic Al (percentage unknown)	52.08	6.35	20.72	100	Na <sub>2</sub> SiO <sub>3</sub> solution+ NaOH solution Mass ratio: 4:1	0.8 (liquid to solid mass ratio)	P	25 ± 1 °C > 95 ± 5 % RH	25 × 25 × 25 Demoulded after 3 days	28d(max.): 22.8	[102]	
UK	< 200 μm (weathered , as received < 14 mm) Contains metallic Al (percentage unknown)	Milled (hammer + ball) + thermally treated (800 °C)	36.2	8.48	20.20	90	Hydrated lime (10 wt.% of dry mix)	0.5 0.2 (water to solid ratio)	P	Condition 1: 20 °C, 98 % RH (3d), then demold Condition 2: 20 °C, 98 % RH (7d) + lime water immersion (21d)	20 (diameter) × 40	7d: 0.5 - 12.7 28d: 1.1 - 14.7	[76]	
UK	< 200 μm (weathered , original < 14 mm) Contains metallic Al (percentage unknown)	Hammer milled + ball milled + thermally treated (600, 700, 800, 880 °C)	36.2	8.48	29.20	100	Hydrated lime	0.5 (water to solid ratio)	P	Demold after 3 days	20 (diameter) × 40	28d: 0.5 - 3	[57]	
AAM prepared with MSWI bottom ash and other industrial by-products as precursor														
Origin	Information of used MSWI bottom ash and plant-scale treatments	Lab-scale treatment and metallic Al content (wt.%)	SiO <sub>2</sub>	Al <sub>2</sub> O <sub>3</sub>	CaO	Binder		Activators		Mix ratio	Curing condition	Analyzed specimen size (mm)	compressive strength (MPa) and Curing age (days)	References
			wt.% from XRF			MSWI botto m ash	Others							
China	D <sub>50</sub> = 47 μm Contains metallic Al (percentage unknown)	Ground + sieved + NaOH defoamed	53.82	14.18	14.44	60	BFS	NaOH + Na <sub>2</sub> SiO <sub>3</sub>	0.6 (liquid to binder ratio)	1:3 (M)	Sealed, 20 ± 2 °C, > 95 % RH	40 × 40 × 160	53.7 <sup>28d</sup> 56.3 <sup>60d</sup>	[172]
China	Contains metallic Al (percentage unknown)	Ball milled Alkali-treated	53.82	14.18	14.44	60	BFS	NaOH + Na <sub>2</sub> SiO <sub>3</sub> (NaOH pellets percentage in the activator: 0 - 16.9 wt.%)	0.5	1:3 (M)	20 ± 2 °C, > 95 % RH	40 × 40 × 160	28d: 4.7 - 47.4 60d: 5.2 - 50.6	[173]

China	D <sub>50</sub> = 47 µm Contains metallic Al (percentage unknown)	Sieving + NaOH defoaming	53.8	14.2	14.4	60	BFS	NaOH + Na <sub>2</sub> SiO <sub>3</sub> (SiO <sub>2</sub> /Na <sub>2</sub> O molar ratio: 0 - 1.14)	0.5 (liquid to binder ratio)	1:3 (M)	20 ± 2 °C, > 95 % RH	40 × 40 × 160	Max: 49.6 <sup>28d</sup> , 53.4 <sup>60d</sup>	[157]
China	Metallic Al content: 1.92 wt. %	Water washed + ball milled + calcinated (700 °C) + NaOH treatment (3h)	51.82	14.18	16.44	60	BFS	Na <sub>2</sub> SiO <sub>3</sub> + NaOH	0.6 (liquid to binder ratio)	1:3 (M)	20 ± 2 °C, 95 % RH	40 × 40 × 160	40.6 <sup>28d</sup> 45.4 <sup>60d</sup>	[131]
China	D <sub>50</sub> = 18.44 µm (original: < 2.36 mm)	Sieved + oven dried + ball milled Metallic Al content: 0.048	37.72	8.46	21.6	0-80	Waste glass	NaOH	0.4 - 0.8 (liquid to solid ratio)	P	Steam curing, 80 °C	50 (diameter) × 100	28-day: 0.86 - 21	[91]
China	D <sub>50</sub> = 49 µm	Dried + ball milled	53.82	14.18	14.44	60	BFS	NaOH Or Na <sub>2</sub> SiO <sub>3</sub> Or Na <sub>2</sub> SiO <sub>3</sub> + NaOH	0.5 (liquid to solid ratio)	1:3 (M)	20 ± 2 °C, > 95 % RH	40 × 40 × 160	NaOH activated: 28d: 0.8 - 25.7 60d: 1.2 - 29.4 Na <sub>2</sub> SiO <sub>3</sub> activated: 3d: 5.6 - 8.4 28d: 7.5 - 12.2 60d: 8.2 - 14.4 Na <sub>2</sub> SiO <sub>3</sub> + NaOH activated: 28d: 34.7 - 43.1 60d: 38.6 - 48.2	[174]
Singapore	< 150 µm Contains metallic Al (percentage unknown)	Oven dried + ball milled	29.7	7.77	26.35	7.5-17.5	Metakaolin	Na <sub>2</sub> SiO <sub>3</sub> + NaOH	1.36 (activator to metakaolin mass ratio)	P	28 ± 3 °C 84 ± 10 % RH	50 × 50 × 50	3d: 5.5 - 10.9	[175]

Spain	< 80 $\mu\text{m}$ (weathered , 8-30 mm)	Crushed + milled	52.08	6.35	20.72	90-98	PAVAL® (second ary aluminu m recyclin g by- product )	$\text{Na}_2\text{SiO}_3 + \text{NaOH}$ ( $\text{Na}_2\text{O}$ respect to the total solid: 5.2 %, 5.8 %; $\text{SiO}_2/\text{Na}_2\text{O}$ molar ratio: 2.3, 2.5)	0.6	P	$25 \pm 1$ °C, $95 \pm 5$ % RH (demold after 3 days)	$25 \times 25 \times 25$	28d: 11 - 26	[177]
Thailand	< 45 $\mu\text{m}$ $D_{50} = 5.15$ $\mu\text{m}$	Ball milled	15.8	0.9	38.1	0-40	Coal Fly ash	$\text{NaOH}$ (10M) + $\text{Na}_2\text{SiO}_3$ (mass ratio: 1:1)	0.65 (liquid to binder ratio)	1:2.75 (M)	60 °C for 2days, then in controlled room at 25 °C, 50 % RH	$50 \times 50 \times 50$	9.2 <sup>7d</sup> 10.6 <sup>28d</sup>	[176]

$D_{50}$ : Mean particle size, RH: Relative humidity, M: Mortar, P: Paste, d: day

## Appendix B

Table B 1 Chemical compositions of different size fractions of as-received MSWI bottom ash (determined by XRF).

Compounds (wt.%)	< 0.063 mm	0.063 - 0.125 mm	0.125 - 0.25 mm	0.25 - 0.5 mm	0.5 - 1.6 mm
SiO <sub>2</sub>	42.31	48.86	51.57	52.71	53.17
CaO	14.42	12.67	12.77	13.25	13.63
Al <sub>2</sub> O <sub>3</sub>	12.44	11.66	11.26	10.60	9.83
Fe <sub>2</sub> O <sub>3</sub>	9.81	8.78	8.79	9.08	9.58
Na <sub>2</sub> O	2.91	3.24	3.70	4.26	4.80
K <sub>2</sub> O	0.88	0.86	0.84	0.85	0.83
SO <sub>3</sub>	1.64	1.04	0.82	0.65	0.42
Cl	0.36	0.30	0.28	0.22	0.19
P <sub>2</sub> O <sub>5</sub>	1.04	1.06	1.06	1.04	0.94
MgO	2.27	2.15	2.28	2.43	2.56
ZnO	0.74	0.64	0.58	0.58	0.54
CuO	0.47	0.39	0.39	0.34	0.42
TiO <sub>2</sub>	1.01	0.96	1.03	1.05	1.13
MnO	0.28	0.20	0.18	0.20	0.19
PbO	0.11	0.09	0.10	0.11	0.08
Cr <sub>2</sub> O <sub>3</sub>	0.08	0.07	0.08	0.09	0.08
BaO	0.05	0.05	0.06	0.06	0.05
NiO	0.04	0.03	0.03	0.03	0.02
SrO	0.05	0.04	0.04	0.04	0.04
SnO <sub>2</sub>	0.02	0.01	0.01	0.01	0.02
LOI <sub>550</sub>	9.04	6.87	4.1	2.38	1.42
Sum	100	100	100	100	100

Table B 2 Quantitative X-ray Diffraction analysis results for different size fractions of MSWI bottom ash.

Phases (wt.%)	< 0.063 mm	0.063 - 0.125 mm	0.125 - 0.25 mm	0.25 - 0.5 mm	0.5 - 1.6 mm
Quartz	11.5	16.7	17.3	15.3	12.1
Cristobalite	0.4	0.5	0.4	0.5	0.2
Magnetite	1.1	1.0	0.9	0.9	1.0
Hematite	0.5	0.5	0.5	0.4	0.4
Wustite	0.2	0.3	0.3	0.2	0.3
Gehlenite	2.6	2.5	2.7	3.2	3.7
Albite	0.8	1.4	2.0	2.1	3.0
Orthopyroxene	1.7	1.0	0.6	-	1.0
Diopside	2.7	2.9	3.6	4.1	5.8
Wollastonite	3.5	2.1	2.6	2.1	2.2
Calcite	6.1	3.8	2.6	1.3	1.3
Anhydrite	1.3	0.4	0.1	0.2	-
Halite	0.2	0.4	0.5	0.3	0.3
Whitlockite	1.1	0.5	0.9	0.5	0.7
Phosphammite	1.2	1.3	1.1	0.9	0.5
Corundum	0.5	0.6	0.6	0.8	1.3
Goethite	0.5	0.6	0.4	0.3	0.2
Gibbsite	0.3	0.5	0.5	0.4	0.5
Aluminum	-	-	0.1	0.1	0.2
Iron	0.1	0.1	0.1	0.1	0.1
Amorphous phase	63.7	63.2	62.3	66.3	65.2
Sum	100	100	100	100	100

## Appendix C

In Chapter 4, thermodynamic modeling was used to predict the reaction products that could form after the alkali activation of *mechanically treated MSWI bottom ash (MBA)*, Class F coal fly ash (FA), or blast furnace slag (BFS). According to thermodynamic modeling, the gel phases formed in alkali-activated MBA paste will be C-(N-)A-S-H gel and N-(C-)A-S-H gel. The gel phase generated upon the alkali activation of BFS is C-(N-)A-S-H gel. The N-(C-)A-S-H gel is the amorphous reaction product formed in alkali-activated FA paste. The chemical composition of the gel formed in alkali-activated MBA paste is compared with that of the gel formed in alkali-activated BFS paste and alkali-activated FA paste, respectively. Detailed information is presented in the following sections.

### Predicted C-(N-)A-S-H gel

In thermodynamic calculation, the chemistry of the C-(N-)A-S-H was simulated by the sublattice solid solution. The changes in the solid solution reflect the structure and composition changes of the C-(N-)A-S-H gel. Figure C 1 (a) and (b) provide information about the end-members chosen within the CNASH\_ss model to define the C-(N-)A-S-H gel in alkali-activated BFS paste and alkali-activated MBA paste.

As illustrated in Figure C 1 (a), the solid solution used to describe the chemistry of the C-(N-)A-S-H gel in alkali-activated BFS paste consists of eight end-members. The molar percentages of the C-A-S-H end-members (5CA, INFCA) and the C-S-H end member (T5C) in the solid solution model decreased with increasing Na<sub>2</sub>O content in the activator. Meanwhile, the molar percentages of C-N-A-S-H end-members (INFCNA and 5CNA) increased in the solid solution model. The C-N-A-S-H end-members have a higher Na content than the C-A-S-H and C-S-H end-members. This composition change in the solid solution indicates that the Na content of C-(N-)A-S-H gel in alkali-activated BFS paste would increase after increasing the Na<sub>2</sub>O content in the activator.

For alkali-activated MBA paste (see Figure C 1 (b)), the C-N-S-H end-member (INFCN) was the dominant component of the solid solution used for the description of the C-(N-)A-S-H gel. The INFCN has a Ca/Si molar ratio of 0.67 (see Table 4.1). This value is lower than most end-members selected in the solid solution that represents the chemical composition of the C-(N-)A-S-H gel in alkali-activated BFS paste. Accordingly, the Ca/Si molar ratio of the C-(N-)A-S-H gel in alkali-activated MBA paste could be much lower than that in alkali-activated BFS paste. The lower Ca/Si in the C-(N-)A-S-H gel of alkali-activated MBA paste can be attributed to the lower CaO content in the amorphous phase of MBA (Table 4.8).

Apart from the C-N-S-H end-member (INFCN), the solid solution used to describe the C-(N-)A-S-H gel of alkali-activated MBA paste also includes C-A-S-H end-members (INFCA, 5CA) and C-N-A-S-H end-member (INFCNA). The total amount of these Al-bearing constituents in the solid solution was predicted to be less than 10 mol%, and their molar percentages decreased with the increase in Na<sub>2</sub>O content. In the case of alkali-activated BFS paste, much more Al-bearing end-members (54 to 67 mol %) were included in the solid solution to simulate the C-(N-)A-S-H gel. This forecast suggests that the C-(N-)A-S-H gel formed in alkali-activated MBA paste would incorporate much less Al than that in alkali-activated BFS paste. The low Al content in



the C-(N-)A-S-H gel of alkali-activated MBA paste could be explained by the low  $\text{Al}_2\text{O}_3$  content (7.9 wt.%) in the amorphous phase of MBA.

In addition, as predicted by the modeling, the total amount of the C-S-H end-members in the solid solution would not exceed 15 mol% for the C-(N-)A-S-H gel of alkali-activated MBA paste. At the same  $\text{Na}_2\text{O}$  wt.%, the molar percentages of the C-S-H end-members in the solid solution representing the C-(N-)A-S-H gel in alkali-activated MBA paste was forecast to be much lower relative to alkali-activated BFS paste (Figure C 1 (a) and (b)). For alkali-activated MBA paste, the molar percentages of the C-S-H end-members in the solid solution decreased with the increase of  $\text{Na}_2\text{O}$  content. The C-S-H end-members (T2C, T5C, TobH) selected in the solid solution model to define the C-(N-)A-S-H gel were derived from the downscaled CSH3Tmodel [210]. The C-S-H end-members defined in the CSH3T model have a Ca/Si ratio between 0.67 and 1.5.

According to Zhu et al. [162], the chemical structure of the C-S-H gel formed in alkali-activated MSWI bottom ash paste was similar to that detected in 10-month Portland cement paste. Although the C-S-H endmembers belonging to the CSHQ model were selected in the database, these endmembers were chosen by the model for the simulation of the C-(N-)A-S-H gel in alkali-activated MBA paste. The CSHQ model [195,210] is usually used in the thermodynamic modeling of Portland cement [210]. The Ca/Si ratio of the C-S-H gel described in the CSHQ model ranges from 0.67 to 2.25 [210]. A possible explanation for this prediction could be that the amorphous phase of MBA has much less CaO than cement clinker [99], resulting in a lower Ca/Si ratio of the C-S-H gel. In comparison, the CaO content (determined by XRF) in the MSWI bottom ash used by Zhu et al. [162] was almost two times that in MBA. The C-S-H gel synthesized by Zhu et al. [162] could have a higher Ca/Si ratio and thus was more similar to the C-S-H gel of Portland cement.

#### *Predicted N-(C-)A-S-H gel*

The compositions of the solid solution used for the description of the chemistry of the N-(C-)A-S-H gel in alkali-activated FA paste and alkali-activated MBA paste are shown in Figure C 1 (c) and (d). The solid solution representing the N-(C-)A-S-H gel in alkali-activated MBA paste was predicted to mainly consist of the N-A-S-H end-members. The N-A-S-H end-members were also expected to be the main components of the N-(C-)A-S-H gel formed after the alkali activation of FA. These modeling results about the solid solution suggest that the N-(C-)A-S-H gel in alkali-activated MBA paste and alkali-activated FA paste could be similar in chemical structure and composition. This prediction is consistent with the experimental results reported by Zhu et al. [162,163]. In their research, the aluminate silicate gel found in alkali-activated MSWI bottom ash paste had a chemical structure similar to that found in the 180-day alkali-activated Class F coal fly ash.

In addition to the N-A-S-H end-members, the N-C-A-S-H end-members were also included in the solid solution model to consider the uptake of Ca by N-A-S-H gel in alkali-activated MBA paste and alkali-activated FA paste. Compared with alkali-activated FA paste, the proportions of these Ca-bearing end-members selected to model the N-(C-)A-S-H gel in alkali-activated MBA paste were smaller. For alkali-activated MBA paste, the Ca-bearing end-members in the solid solution decreased from around 20 mol% to zero when increasing the  $\text{Na}_2\text{O}$  content from

2 to 10 wt.% in the activator. For alkali-activated FA paste, the total amount of N-C-A-S-H end-members in the solid solution was in the range of 15 to 40 mol %. The prediction about the Ca-bearing end-members indicates that the Ca content of the N-(C-)A-S-H gel in alkali-activated MBA paste would be lower than that in alkali-activated FA paste.

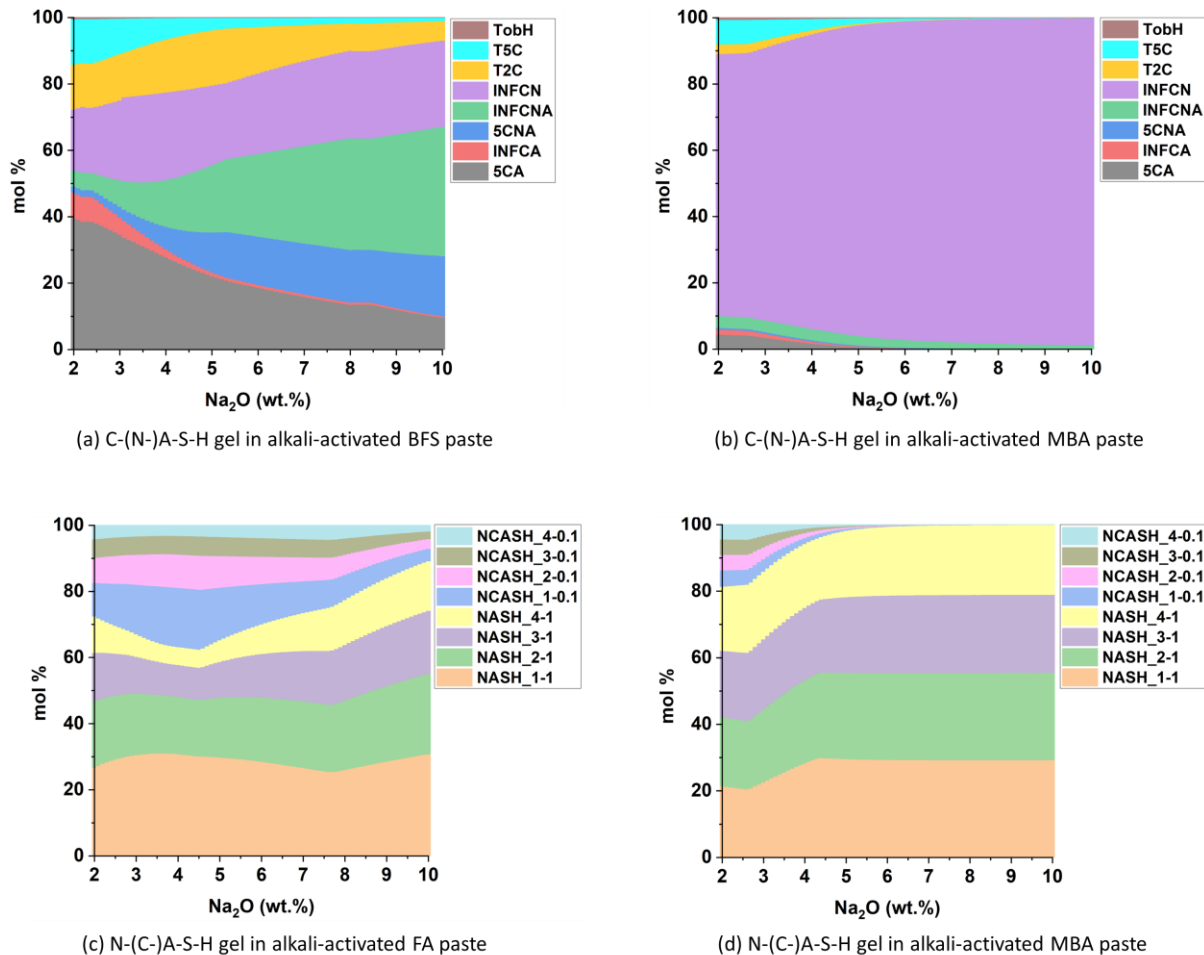


Figure C 1 (a) and (b) Molar percentages of the end-members in the solid solution used for the description of the C-(N-)A-S-H gel predicted in alkali-activated MBA paste and alkali-activated BFS paste. (c) and (d) Molar percentages of the end-members in the solid solution used for the description of the N-(C-)A-S-H gel predicted in alkali-activated MBA paste and alkali-activated FA paste. These end-members were defined in the N(C)ASH<sub>ss</sub> model [209] and C(N)ASH<sub>ss</sub> model [207]. Detailed information about these end-members can be found in Table 4.1 and Table 4.3. The data is presented as a function of the Na<sub>2</sub>O content in the activator. The percentage of Na<sub>2</sub>O is with respect to the mass of the precursor.

## Appendix D

Table D 1 Mineralogical composition of 100CEM at different curing ages, determined by QXRD.

Phases (wt.%)	100 CEM			
	1-day	7-day	28-day	90-day
Alite ( $C_3S$ )	11	3	2.4	0.9
Belite( $C_2S$ )	10.1	9.7	8.3	5.3
$C_3A$ cubic	0.6	0.5	0.4	0.2
$C_3A$ orthorombic	0.7	0.3	0.1	0
$C_4AF$	3.3	2.7	2.5	2.4
Calcite	0.2	0.2	0.2	0.5
Mayenite	0.8	0.3	0	0
Bassanite	1.8	2	2	2
Quartz	0.2	0.2	0.2	0.2
Cristobalite	0.5	0.5	0.5	0.5
Arcanite	0.2	0	0	0
Periclase	0.8	0.5	0.5	0.4
Monocarbonate	0	0	2.3	2.6
Portlandite	14.8	17.6	17.7	17.8
Monosulfate (AFm)	0.1	0.2	0.2	0.5
Ettringite (AFt)	3.6	2	2	2.1
Amorphous phase	51.3	60.3	60.7	64.6
Sum	100	100	100	100

Table D 2 Mineralogical composition of 25 M300 CEM at different curing ages, determined by QXRD.

Phases (wt.%)	25 M300 CEM			
	1-day	7-day	28-day	90-day
Alite ( $C_3S$ )	8	0.6	0	0
Belite( $C_2S$ )	8.9	7.8	4.6	1.8
$C_3A$ orthorombic	1.4	0.1	0.1	0
$C_4AF$	3.1	1.5	0.9	0.9
Calcite	0.8	0.2	0.2	0.3
Mayenite	1	0.7	0.7	0.7
Bassanite	1.2	1.6	1.1	0.7
Quartz	25.4	23.3	23.3	23.3
Cristobalite	0.5	0.4	0.3	0.3
Arcanite	0	0	0	0
Periclase	0.4	0.5	0.3	0.3
Monocarbonate	0.0	0.0	1.7	1.9
Portlandite	14.2	15.7	15.8	15.8
Monosulfate (AFm)	0.1	0.4	0.5	0.8
Ettringite (AFt)	4.3	2.4	1.9	1.5
Amorphous phase	30.7	44.8	48.6	51.7
Sum	100.0	100.0	100.0	100.0

Table D 3 Mineralogical composition of 25 WMBA CEM at different curing ages, determined by QXRD.

Phases (wt.%)	25 WMBA CEM			
	1-day	7-day	28-day	90-day
Alite (C <sub>3</sub> S)	7.6	0.5	0	0
Belite(C <sub>2</sub> S)	9.1	8.3	4.9	4.4
C <sub>3</sub> A <sub>cubic</sub>	0.3	0	0	0
C <sub>3</sub> A <sub>orthorombic</sub>	0.6	0.2	0.2	0.2
C <sub>4</sub> AF	3.4	0	0	0
Calcite	0.4	0.4	0.5	0.2
Mayenite	1.5	0.8	0.3	0
Bassanite	0.4	0.3	0.0	0.0
Quartz	3.0	3.0	3.0	2.9
Cristobalite	0.2	0.2	0.2	0.2
Arcanite	0	0	0	0
Periclase	0.8	0.5	0.3	0.2
Portlandite	11.8	14.4	12.3	13.4
Ettringite (AFt)	6.0	3.0	2.7	3.3
Sodicgedrite	0.0	0.2	0.3	0.5
Magnetite	0.4	0.3	0.2	0.2
Hematite	0.3	0.1	0.1	0.1
Gehlenite	1.1	1.1	1.1	1
Orthopyroxene	0.4	0.1	0	0
Diopside	1	0.9	0.9	0.9
Wollastonite	1.4	1.4	1.4	1.4
Amorphous phase	50.3	64.3	71.6	71.1
Sum	100	100	100	100

## Appendix E

Table E 1 Mineralogical composition of 100 BFS AAM at different curing ages, determined by QXRD.

Phases (wt.%)	100 BFS AAM			
	1-day	7-day	28-day	90-day
Tobermorite	1.7	2.2	2.8	2.9
Hydrotalcite	0.7	1.0	1.6	1.8
Brucite	-	-	0.4	0.5
Bornite	-	0.1	0.1	0.1
Nickel titanium	-	0.1	0.1	0.1
Amorphous phase	97.6	96.6	95.0	94.6
Sum	100.0	100.0	100.0	100.0

Table E 2 Mineralogical composition of 30 M300-BFS AAM at different curing ages, determined by QXRD.

Phases (wt.%)	30 M300-BFS AAM			
	1-day	7-day	28-day	90-day
Tobermorite	-	-	0.5	1.6
Hydrotalcite	0.7	1.5	2.1	2.1
Brucite	-	-	0.1	0.1
Quartz	27.2	27.2	27.2	27.2
Nickel titanium	-	-	0.1	0.1
Amorphous phase	72.1	71.3	70.0	68.9
Sum	100.0	100.0	100.0	100.0

Table E 3 Mineralogical composition of 30 CMBA-BFS AAM at different curing ages, determined by QXRD.

Phases (wt.%)	30 CMBA-BFS AAM			
	1-day	7-day	28-day	90-day
Tobermorite	1.4	2.1	2.1	2.8
Hydrotalcite	0.3	0.5	0.9	1.2
Microcline	1.1	1.6	1.8	1.9
Quartz	2.8	2.8	2.7	2.3
Cristobalite	0.3	0.3	0.2	0.2
Magnetite	0.3	0.3	0.3	0.3
Hematite	0.2	0.2	0.2	0.2
Gehlenite	1.5	1.5	1.5	1.5
Diopside	1.5	1.4	1.3	1.0
Wollastonite	1.6	1.6	1.6	1.6
Calcite	0.5	0.5	0.5	0.5
Amorphous phase	88.5	87.2	86.9	86.5
Sum	100.0	100.0	100.0	100.0

## Appendix F

Table F 1 Life cycle inventory data of the raw materials used for the preparation of cement pastes and alkali-activated pastes.

Environmental impact indicators*	Unit	CEM I 52.5 R (PC) [ENCI / Heidelberg Cement] [370]	Blast furnace slag (BFS) [Eco <sub>2</sub> cem] [378]	Class F Coal fly ash (FA) [Vliegassunie] [370]	NaOH pellets [370]	Sodium silicate solution (35 wt.% solid) [370]
GWP	kg CO <sub>2</sub> Equiv.	8.57E-01	3.03E-02	1.33E-03	8.73E-01	3.33E-01
ADP-Elements	kg Sb Equiv.	5.28E-07	1.94E-04	1.26E-09	2.66E-05	2.51E-05
ADP-Fossil fuels	kg Sb Equiv.	2.11E-03	2.26E-04	8.42E-06	6.23E-03	1.91E-03
ODP	kg CFC 11 Equiv.	1.09E-08	3.47E-09	1.94E-10	8.23E-07	2.27E-08
POCP	kg Ethene Equiv.	7.58E-05	5.68E-06	7.72E-07	2.81E-04	1.19E-04
AP	kg SO <sub>2</sub> Equiv.	1.10E-03	1.17E-04	9.57E-06	4.64E-03	1.78E-03
EP	kg PO <sub>4</sub> <sup>3-</sup> Equiv.	3.16E-04	1.67E-05	2.11E-06	6.04E-04	1.86E-04
HTP	kg 1.4 DB Equiv.	2.40E-02	1.12E-02	3.40E-04	3.91E-01	2.15E-01
FAETP		1.14E-03	2.20E-04	7.98E-06	7.26E-03	3.01E-03
MAETP		3.34E+00	3.97E+00	2.48E-02	3.11E+01	1.20E+01
TETP		9.83E-04	2.62E-04	5.13E-06	1.43E-02	6.17E-04

\*The full names of the impact indicators: global warming potential (GWP, 100 years), abiotic depletion potential (including ADP-Elements and ADP-fossil fuels), ozone layer depletion potential (ODP), photochemical ozone creation potential (POCP), acidification potential of soil and water (AP), eutrophication potential (EP), human toxicity potential (HTP), freshwater aquatic ecotoxicity potential (FAETP), marine aquatic ecotoxicity potential (MAETP), and terrestrial ecotoxicity potential (TETP).

# References

---

- [1] S. Kaza, L. Yao, P. Bhada-Tata, F. Van Woerden, What a waste 2.0: a global snapshot of solid waste management to 2050, The World Bank, 2018.
- [2] D.M.-C. Chen, B.L. Bodirsky, T. Krueger, A. Mishra, A. Popp, The world's growing municipal solid waste: trends and impacts, *Environ. Res. Lett.* 15 (2020) 74021. <https://doi.org/10.1088/1748-9326/ab8659>.
- [3] N. Ferronato, V. Torretta, Waste Mismanagement in Developing Countries: A Review of Global Issues, *Int. J. Environ. Res. Public Heal.* 16 (2019). <https://doi.org/10.3390/ijerph16061060>.
- [4] S.-Y. Pan, M.A. Du, I.-T. Huang, I.-H. Liu, E.-E. Chang, P.-C. Chiang, Strategies on implementation of waste-to-energy (WTE) supply chain for circular economy system: a review, *J. Clean. Prod.* 108 (2015) 409–421. <https://doi.org/10.1016/j.jclepro.2015.06.124>.
- [5] A. Tozlu, E. Özahi, A. Abuşoğlu, Waste to energy technologies for municipal solid waste management in Gaziantep, *Renew. Sustain. Energy Rev.* 54 (2016) 809–815. <https://doi.org/10.1016/J.RSER.2015.10.097>.
- [6] R. Bunge, R.B.- Removal, Treatment, U. of Waste, undefined 2015, R. Bunge, R.B.- Removal, Treatment, U. of Waste, undefined 2015, Recovery of metals from waste incinerator bottom ash, Hochschule Für Tech. Rapperswil Rapperswil. Available Online [https://www.umtec.ch/Fileadmin/User\\_upload/Umtec\\_Hsr\\_Ch/Dokumente/News/1504\\_Metals\\_from\\_MWIBA\\_R.\\_Bunge.Pdf](https://www.umtec.ch/Fileadmin/User_upload/Umtec_Hsr_Ch/Dokumente/News/1504_Metals_from_MWIBA_R._Bunge.Pdf) (Accessed 16 May 2019). (2015). <https://vbsa.ch/wp-content/uploads/2016/07/Studie-Bunge-Internetversion.pdf>.
- [7] M.H. Kim, H.B. Song, Y. Song, I.T. Jeong, J.W. Kim, Evaluation of food waste disposal options in terms of global warming and energy recovery: Korea, *Int. J. Energy Environ. Eng.* 2013 41. 4 (2013) 1–12. <https://doi.org/10.1186/2251-6832-4-1>.
- [8] Municipal waste statistics - Statistics Explained, (n.d.). [https://ec.europa.eu/eurostat/statistics-explained/index.php?title=Municipal\\_waste\\_statistics#Municipal\\_waste\\_generation](https://ec.europa.eu/eurostat/statistics-explained/index.php?title=Municipal_waste_statistics#Municipal_waste_generation).
- [9] National Bureau of Statistics, (n.d.). <https://data.stats.gov.cn/easyquery.htm?cn=E0103>.
- [10] M. Li, J. Xiang, S. Hu, L. Sun, S. Su, P. Li, X. Sun, Characterization of solid residues from municipal solid waste incinerator, *Fuel* 83 (2004) 1397–1405.
- [11] T. Sabbas, A. Poletti, R. Pomi, T. Astrup, O.H.-W. management, undefined 2003, Management of municipal solid waste incineration residues, Elsevier. (n.d.). [https://www.sciencedirect.com/science/article/pii/S0956053X02001617?casa\\_token=1qYc-l3ytcIAAAAA:UV\\_Oiy3yHttcZohyok2gFGw-5A80GFgeumto\\_Aig6fd1Dx2uRKldneWHp\\_eaZHM1evTdy0HHYv0](https://www.sciencedirect.com/science/article/pii/S0956053X02001617?casa_token=1qYc-l3ytcIAAAAA:UV_Oiy3yHttcZohyok2gFGw-5A80GFgeumto_Aig6fd1Dx2uRKldneWHp_eaZHM1evTdy0HHYv0).
- [12] Z. Phua, A. Giannis, Z.L. Dong, G. Lisak, W.J. Ng, Characteristics of incineration ash for sustainable treatment and reutilization, *Environ. Sci. Pollut. Res.* 26 (2019) 16974–16997. <https://doi.org/10.1007/s11356-019-05217-8>.



- [13] A.U. Zaman, Comparative study of municipal solid waste treatment technologies using life cycle assessment method, *Int. J. Environ. Sci. Technol.* 7 (2010) 225–234. <https://doi.org/10.1007/BF03326132>.
- [14] M. Margallo, M.B.M. Taddei, A. Hernández-Pellón, R. Aldaco, Á. Irabien, Environmental sustainability assessment of the management of municipal solid waste incineration residues: A review of the current situation, *Clean Technol. Environ. Policy.* 17 (2015) 1333–1353. <https://doi.org/10.1007/s10098-015-0961-6>.
- [15] J.M. Chimenos, M. Segarra, M.A. Fernandez, F. Espiell, Characterization of the bottom ash in municipal solid waste incinerator, *J. Hazard. Mater. A.* 64 (1999) 211–222.
- [16] K.L. Lin, D.F. Lin, Hydration characteristics of municipal solid waste incinerator bottom ash slag as a pozzolanic material for use in cement, *Cem. Concr. Compos.* 28 (2006) 817–823. <https://doi.org/10.1016/j.cemconcomp.2006.03.003>.
- [17] A.P. Bayuseno, W.W. Schmahl, Understanding the chemical and mineralogical properties of the inorganic portion of MSWI bottom ash, *Waste Manag.* 30 (2010) 1509–1520. <https://doi.org/10.1016/j.wasman.2010.03.010>.
- [18] T. Prior, D. Giurco, G. Mudd, L. Mason, J. Behrisch, Resource depletion, peak minerals and the implications for sustainable resource management, *Glob. Environ. Chang.* 22 (2012) 577–587. <https://doi.org/https://doi.org/10.1016/j.gloenvcha.2011.08.009>.
- [19] Y.M. Li, X.Q. Wu, L.J. Wang, R.Q. Li, T.Y. Huang, X.Q. Wen, Comparative study on utilization of different types of municipal solid waste incineration bottom ash for clinker sintering, *J. Mater. Cycles Waste Manag.* 22 (2020) 1828–1843. <https://doi.org/10.1007/s10163-020-01067-6>.
- [20] Z. Zhang, J. Wang, L. Liu, J. Ma, B. Shen, Preparation of additive-free glass-ceramics from MSW incineration bottom ash and coal fly ash, *Constr. Build. Mater.* 254 (2020). <https://doi.org/10.1016/j.conbuildmat.2020.119345>.
- [21] P. Appendino, M. Ferraris, I. Matekovits, M. Salvo, Production of glass-ceramic bodies from the bottom ashes of municipal solid waste incinerators, *J. Eur. Ceram. Soc.* 24 (2004) 803–810. [https://doi.org/10.1016/S0955-2219\(03\)00264-4](https://doi.org/10.1016/S0955-2219(03)00264-4).
- [22] R.C.C. Monteiro, S.J.G. Alendouro, F.M.L.F.-J. of Non ..., undefined 2006, Development and properties of a glass made from MSWI bottom ash, Elsevier. (n.d.). [https://www.sciencedirect.com/science/article/pii/S0022309305007817?casa\\_token=PsI8j7l1rlgAAAAA:zVFv00Wtfvpra78Hi0BpU0fSkvRrO2OqN1ddht5MQYfvjQWu34v6xq2dwg\\_7\\_zAofCd6T5q3BmI](https://www.sciencedirect.com/science/article/pii/S0022309305007817?casa_token=PsI8j7l1rlgAAAAA:zVFv00Wtfvpra78Hi0BpU0fSkvRrO2OqN1ddht5MQYfvjQWu34v6xq2dwg_7_zAofCd6T5q3BmI).
- [23] E. Rambaldi, L. Esposito, F. Andreola, L. Barbieri, I. Lancellotti, I. Vassura, The recycling of MSWI bottom ash in silicate based ceramic, *Ceram. Int.* 36 (2010) 2469–2476. <https://doi.org/10.1016/J.CERAMINT.2010.08.005>.
- [24] R. Taurino, A. Karamanov, R.R.-J. of the European ..., undefined 2017, New ceramic materials from MSWI bottom ash obtained by an innovative microwave-assisted sintering process, Elsevier. (n.d.). [https://www.sciencedirect.com/science/article/pii/S0955221916304320?casa\\_token=ZtaE3a0mNu4AAA:uJYa4uyVvFq30H52girrE4FCm0hubjQYYims9YTAIGcqvN7cRix7B8ZNRcBqM2T7eCzowqbc](https://www.sciencedirect.com/science/article/pii/S0955221916304320?casa_token=ZtaE3a0mNu4AAA:uJYa4uyVvFq30H52girrE4FCm0hubjQYYims9YTAIGcqvN7cRix7B8ZNRcBqM2T7eCzowqbc).
- [25] I. Vegas, J.A. Ibañez, J.T.S. José, A. Urzelai, Construction demolition wastes, Waelz slag and MSWI

- bottom ash: A comparative technical analysis as material for road construction, *Waste Manag.* 28 (2008) 565–574. <https://doi.org/10.1016/j.wasman.2007.01.016>.
- [26] J. Pera, L. Coutaz, J. Ambroise, M. Chababbet, USE OF INCINERATOR BOTTOM ASH IN CONCRETE, *Cem. Concr. Res.* 27 (1997).
- [27] X.G. Li, Y. Lv, B.G. Ma, Q. Bin Chen, X.B. Yin, S.W. Jian, Utilization of municipal solid waste incineration bottom ash in blended cement, *J. Clean. Prod.* 32 (2012) 96–100. <https://doi.org/10.1016/j.jclepro.2012.03.038>.
- [28] P. Tang, W. Chen, D. Xuan, Y. Zuo, C.S. Poon, Investigation of cementitious properties of different constituents in municipal solid waste incineration bottom ash as supplementary cementitious materials, *J. Clean. Prod.* 258 (2020). <https://doi.org/10.1016/j.jclepro.2020.120675>.
- [29] À. Maldonado-Alameda, J. Giro-Paloma, A. Alfocea-Roig, J. Formosa, J.M. Chimenos, Municipal solid waste incineration bottom ash as sole precursor in the alkali-activated binder formulation, *Appl. Sci.* 10 (2020). <https://doi.org/10.3390/APP10124129>.
- [30] L. Bertolini, M. Carsana, D. Cassago, A.Q. Curzio, M. Collepardi, MSWI ashes as mineral additions in concrete, *Cem. Concr. Res.* 34 (2004) 1899–1906. <https://doi.org/10.1016/j.cemconres.2004.02.001>.
- [31] K.A. Clavier, B. Watts, Y. Liu, C.C. Ferraro, T.G. Townsend, Risk and performance assessment of cement made using municipal solid waste incinerator bottom ash as a cement kiln feed, *Resour. Conserv. Recycl.* 146 (2019) 270–279. <https://doi.org/10.1016/j.resconrec.2019.03.047>.
- [32] R.M. Andrew, Global CO<sub>2</sub> emissions from cement production, *Earth Syst. Sci. Data.* 10 (2018) 195–217.
- [33] Cement Industry Energy and CO<sub>2</sub> performance “Getting the Numbers Right,” (n.d.). <http://docs.wbcsd.org/2009/06/CementIndustryEnergyAndCO2Performance.pdf#:~:text=The WBCSD Cement Sustainability Initiative> “Getting the Numbers, industry is monitoring and addressing its emission trends.
- [34] B.C. McLellan, R.P. Williams, J. Lay, A. Van Riessen, G.D. Corder, Costs and carbon emissions for geopolymer pastes in comparison to ordinary portland cement, *J. Clean. Prod.* 19 (2011) 1080–1090.
- [35] G. Habert, C. Ouellet-Plamondon, Recent update on the environmental impact of geopolymers, *RILEM Tech. Lett.* 1 (2016) 17–23.
- [36] G. Habert, J.B.D. De Lacaillerie, N. Roussel, An environmental evaluation of geopolymer based concrete production: reviewing current research trends, *J. Clean. Prod.* 19 (2011) 1229–1238.
- [37] G. Habert, A method for allocation according to the economic behaviour in the EU-ETS for by-products used in cement industry, *Int. J. Life Cycle Assess.* 18 (2013) 113–126.
- [38] M. Weil, K. Dombrowski, A. Buchwald, Life-cycle analysis of geopolymers, in: *Geopolymers*, Elsevier, 2009: pp. 194–210.
- [39] T.S. Ng, Y.L. Voo, S.J. Foster, Sustainability with ultra-high performance and geopolymer concrete construction, in: *Innov. Mater. Tech. Concr. Constr.*, Springer, 2012: pp. 81–100.

- [40] T. Stengel, D. Heinz, J. Reger, Life cycle assessment of geopolymer concrete--what is the environmental benefit, in: *Proceeding 24th Bienn. Conf. Concr. Inst. Aust.*, 2009.
- [41] P. den Heede, N. De Belie, Environmental impact and life cycle assessment (LCA) of traditional and 'green' concretes: Literature review and theoretical calculations, *Cem. Concr. Compos.* 34 (2012) 431–442.
- [42] A. Heath, K. Paine, M. McManus, Minimising the global warming potential of clay based geopolymers, *J. Clean. Prod.* 78 (2014) 75–83.
- [43] J.L. Provis, Alkali-activated materials, *Cem. Concr. Res.* 114 (2018) 40–48. <https://doi.org/https://doi.org/10.1016/j.cemconres.2017.02.009>.
- [44] J.L. Provis, J.S.J. Van Deventer, Alkali activated materials: state-of-the-art report, RILEM TC 224-AAM, Springer Science & Business Media, 2013.
- [45] Cement technology Roadmap 2009 Carbon emission reductions up to 2025, (n.d.). <https://www.wbcds.org/contentwbc/download/4586/61682/1>.
- [46] Technology Roadmap Low-Carbon Transition in the Cement Industry, (n.d.). <https://www.wbcds.org/contentwbc/download/4586/61682/1>.
- [47] A. Maldonado-Alameda, J. Giro-Paloma, A. Svobodova-Sedlackova, J. Formosa, J.M. Chimenos, Municipal solid waste incineration bottom ash as alkali-activated cement precursor depending on particle size, *J. Clean. Prod.* 242 (2020). <https://doi.org/10.1016/j.jclepro.2019.118443>.
- [48] N. Saikia, G. Cornelis, G. Mertens, J. Elsen, K. Van Balen, T. Van Gerven, C. Vandecasteele, Assessment of Pb-slag, MSWI bottom ash and boiler and fly ash for using as a fine aggregate in cement mortar, *J. Hazard. Mater.* 154 (2008) 766–777. <https://doi.org/10.1016/j.jhazmat.2007.10.093>.
- [49] B. Simões, P.R. da Silva, R. V Silva, Y. Avila, J.A. Forero, Ternary mixes of self-compacting concrete with fly ash and municipal solid waste incinerator bottom ash, *Appl. Sci.* 11 (2021) 1–17. <https://doi.org/10.3390/app11010107>.
- [50] P. Filippini, A. Polettini, R. Pomi, P. Sirini, Physical and mechanical properties of cement-based products containing incineration bottom ash, *Waste Manag.* 23 (2003) 145–156. [https://doi.org/10.1016/S0956-053X\(02\)00041-7](https://doi.org/10.1016/S0956-053X(02)00041-7).
- [51] A.M. Joseph, S. Matthys, N. De Belie, Reactivity of Municipal Solid Waste Incineration Ashes as a Supplementary Cementitious Material, in: *15th Int. Congr. Chem. Cem., ICCC*, 2019.
- [52] B. Verbinnen, P. Billen, J. Van Caneghem, C. Vandecasteele, Recycling of MSWI Bottom Ash: A Review of Chemical Barriers, Engineering Applications and Treatment Technologies, *Waste and Biomass Valorization*. 8 (2017) 1453–1466. <https://doi.org/10.1007/s12649-016-9704-0>.
- [53] P. Tang, M.V.A. Florea, P. Spiesz, H.J.H. Brouwers, Application of thermally activated municipal solid waste incineration (MSWI) bottom ash fines as binder substitute, *Cem. Concr. Compos.* 70 (2016) 194–205. <https://doi.org/10.1016/j.cemconcomp.2016.03.015>.
- [54] B. Chen, M.B. van Zijl, A. Keulen, G. Ye, Thermal Treatment on MSWI Bottom Ash for the Utilisation in

- Alkali Activated Materials, *KnE Eng.* (2020). <https://doi.org/10.18502/keg.v5i4.6792>.
- [55] D. Xuan, C.S. Poon, Removal of metallic Al and Al/Zn alloys in MSWI bottom ash by alkaline treatment, *J. Hazard. Mater.* 344 (2018) 73–80. <https://doi.org/10.1016/j.jhazmat.2017.10.002>.
- [56] A. Mary Joseph, R. Snellings, P. Nielsen, S. Matthys, N. De Belie, A.M. Joseph, R. Snellings, P. Nielsen, S. Matthys, N. De Belie, Pre-treatment and utilisation of municipal solid waste incineration bottom ashes towards a circular economy, *Constr. Build. Mater.* 260 (2020) 120485. <https://doi.org/10.1016/j.conbuildmat.2020.120485>.
- [57] X.C. Qiao, M. Tyrer, C.S. Poon, C.R. Cheeseman, Characterization of alkali-activated thermally treated incinerator bottom ash, *Waste Manag.* 28 (2008) 1955–1962. <https://doi.org/10.1016/j.wasman.2007.09.007>.
- [58] A.C. Bourtsalas, Review of WTE ash utilization processes under development in northwest Europe, in: 2012.
- [59] W. de Vries, ADR: The use of Advanced Dry Recovery in recycling fine moist granular materials, (2017). <https://www.narcis.nl/publication/RecordID/oai:tudelft.nl:uuid%3Ac3c8578d-fd2c-493f-b4c5-79e63bc6d70c>.
- [60] C. Vandecasteele, G. Wauters, S. Arickx, M. Jaspers, T. Van Gerven, Integrated municipal solid waste treatment using a grate furnace incinerator: The Indaver case, *Waste Manag.* 27 (2007) 1366–1375. <https://doi.org/10.1016/j.wasman.2006.08.005>.
- [61] C. Speiser, T. Baumann, R. Niessner, Morphological and chemical characterization of calcium-hydrate phases formed in alteration processes of deposited municipal solid waste incinerator bottom ash, *Environ. Sci. Technol.* 34 (2000) 5030–5037. <https://doi.org/10.1021/es990739c>.
- [62] A. Saffarzadeh, T. Shimaoka, Y. Wei, K.H. Gardner, C.N. Musselman, Impacts of natural weathering on the transformation/neoformation processes in landfilled MSWI bottom ash: A geoenvironmental perspective, *Waste Manag.* 31 (2011) 2440–2454. <https://doi.org/10.1016/j.wasman.2011.07.017>.
- [63] A. Saffarzadeh, N. Arumugam, T. Shimaoka, Aluminum and aluminum alloys in municipal solid waste incineration (MSWI) bottom ash: A potential source for the production of hydrogen gas, *Int. J. Hydrogen Energy.* 41 (2016) 820–831. <https://doi.org/10.1016/j.ijhydene.2015.11.059>.
- [64] J. Yao, W.B. Li, Q. Kong, F. Xia, D.S. Shen, Effect of weathering on the mobility of zinc in municipal solid waste incinerator bottom ash, *Fuel.* 93 (2012) 99–104. <https://doi.org/10.1016/j.fuel.2011.11.026>.
- [65] J.M. Chimenos, A.I. Fernández, R. Nadal, F. Espiell, Short-term natural weathering of MSWI bottom ash, *J. Hazard. Mater.* 79 (2000) 287–299. [https://doi.org/https://doi.org/10.1016/S0304-3894\(00\)00270-3](https://doi.org/https://doi.org/10.1016/S0304-3894(00)00270-3).
- [66] J.A. Meima, R.N.J.C.-A. Geochemistry, undefined 1999, The leaching of trace elements from municipal solid waste incinerator bottom ash at different stages of weathering, Elsevier. (n.d.). [https://www.sciencedirect.com/science/article/pii/S088329279800047X?casa\\_token=KjPWFhjBSu8AAA:AAA:Fs48Uooo5sTFLiXeh5G5kBRGBJAXY0BpRMgt3rR-14UeqeJb\\_plmFeyxAkiCDr2yIOceCHZhnaK](https://www.sciencedirect.com/science/article/pii/S088329279800047X?casa_token=KjPWFhjBSu8AAA:AAA:Fs48Uooo5sTFLiXeh5G5kBRGBJAXY0BpRMgt3rR-14UeqeJb_plmFeyxAkiCDr2yIOceCHZhnaK).
- [67] M. Šyc, F.G. Simon, J. Hykš, R. Braga, L. Biganzoli, G. Costa, V. Funari, M. Grosso, Metal recovery from incineration bottom ash: State-of-the-art and recent developments, *J. Hazard. Mater.* 393 (2020)

122433. <https://doi.org/10.1016/j.jhazmat.2020.122433>.
- [68] Q. Alam, M.V.A. Florea, K. Schollbach, H.J.H. Brouwers, A two-stage treatment for Municipal Solid Waste Incineration (MSWI) bottom ash to remove agglomerated fine particles and leachable contaminants, *Waste Manag.* 67 (2017) 181–192. <https://doi.org/10.1016/j.wasman.2017.05.029>.
- [69] Q. Alam, A. Lazaro, K. Schollbach, H.J.H. Brouwers, Chemical speciation, distribution and leaching behavior of chlorides from municipal solid waste incineration bottom ash, *Chemosphere*. 241 (2020). <https://doi.org/10.1016/j.chemosphere.2019.124985>.
- [70] G. Flesoura, B. Garcia-Banos, J.M. Catala-Civera, J. Vleugels, Y. Pontikes, In-situ measurements of high-temperature dielectric properties of municipal solid waste incinerator bottom ash, *Ceram. Int.* 45 (2019) 18751–18759. <https://doi.org/10.1016/j.ceramint.2019.06.101>.
- [71] L. De Windt, D. Dabo, S. Lidelöw, R. Badreddine, A. Lagerkvist, L. De Windt, D. Dabo, S. Lidelöw, R. Badreddine, A. Lagerkvist, MSWI bottom ash used as basement at two pilot-scale roads: Comparison of leachate chemistry and reactive transport modeling, *Waste Manag.* 31 (2011) 267–280. <https://doi.org/https://doi.org/10.1016/j.wasman.2010.06.002>.
- [72] N.H. Le, A. Razakamanantsoa, M.L. Nguyen, V.T. Phan, P.L. Dao, D.H. Nguyen, Evaluation of physicochemical and hydromechanical properties of MSWI bottom ash for road construction, *Waste Manag.* 80 (2018) 168–174. <https://doi.org/10.1016/j.wasman.2018.09.007>.
- [73] C.R. Cheeseman, S.M. Da Rocha, C. Sollars, S. Bethanis, A.R. Boccaccini, Ceramic processing of incinerator bottom ash, *Waste Manag.* 23 (2003) 907–916. [https://doi.org/10.1016/S0956-053X\(03\)00039-4](https://doi.org/10.1016/S0956-053X(03)00039-4).
- [74] X.C. Qiao, B.R. Ng, M. Tyrer, C.S. Poon, C.R. Cheeseman, Production of lightweight concrete using incinerator bottom ash, *Constr. Build. Mater.* 22 (2008) 473–480. <https://doi.org/10.1016/j.conbuildmat.2006.11.013>.
- [75] S. Bethanis, C.R. Cheeseman, C.J. Sollars, Effect of sintering temperature on the properties and leaching of incinerator bottom ash, *Waste Manag. Res.* 22 (2004) 255–264. <https://doi.org/10.1177/0734242X04045426>.
- [76] X.C. Qiao, M. Tyrer, C.S. Poon, C.R. Cheeseman, Novel cementitious materials produced from incinerator bottom ash, *Resour. Conserv. Recycl.* 52 (2008) 496–510. <https://doi.org/10.1016/j.resconrec.2007.06.003>.
- [77] L. Biganzoli, A. Ilyas, M. van Praagh, K.M. Persson, M. Grosso, Aluminium recovery vs. hydrogen production as resource recovery options for fine MSWI bottom ash fraction, *Waste Manag.* 33 (2013) 1174–1181. <https://doi.org/10.1016/j.wasman.2013.01.037>.
- [78] K. Rübner, F. Haamkens, O. Linde, Use of municipal solid waste incinerator bottom ash as aggregate in concrete, *Q. J. Eng. Geol. Hydrogeol.* 41 (2008) 459–464. <https://doi.org/10.1144/1470-9236/07-036>.
- [79] J. Giro-Paloma, A. Maldonado-Alameda, J. Formosa, L. Barbieri, J.M. Chimenos, I. Lancellotti, Geopolymers based on the valorization of Municipal Solid Waste Incineration residues, in: *IOP Conf. Ser. Mater. Sci. Eng.*, Institute of Physics Publishing, 2017. <https://doi.org/10.1088/1757-899X/251/1/012125>.

- [80] M. Izquierdo, Á. López-Soler, E.V. Ramonich, M. Barra, X. Querol, Characterisation of bottom ash from municipal solid waste incineration in Catalonia, *J. Chem. Technol. Biotechnol.* 77 (2002) 576–583. <https://doi.org/10.1002/jctb.605>.
- [81] R.M. Santos, G. Mertens, M. Salman, Ö. Cizer, T. Van Gerven, Comparative study of ageing, heat treatment and accelerated carbonation for stabilization of municipal solid waste incineration bottom ash in view of reducing regulated heavy metal/metalloid leaching, *J. Environ. Manage.* 128 (2013) 807–821. <https://doi.org/10.1016/j.jenvman.2013.06.033>.
- [82] Q. Alam, Y. Hendrix, L. Thijs, A. Lazaro, K. Schollbach, H.J.H. Brouwers, Novel low temperature synthesis of sodium silicate and ordered mesoporous silica from incineration bottom ash, *J. Clean. Prod.* 211 (2019) 874–883. <https://doi.org/10.1016/j.jclepro.2018.11.173>.
- [83] E. Allegrini, A. Maresca, M.E. Olsson, M.S. Holtze, A. Boldrin, T.F. Astrup, Quantification of the resource recovery potential of municipal solid waste incineration bottom ashes, *Waste Manag.* 34 (2014) 1627–1636. <https://doi.org/10.1016/j.wasman.2014.05.003>.
- [84] A. Keulen, A. Van Zomeren, P. Harpe, W. Aarnink, H.A.E. Simons, H.J.H. Brouwers, High performance of treated and washed MSWI bottom ash granulates as natural aggregate replacement within earth-moist concrete, *Waste Manag.* 49 (2016) 83–95. <https://doi.org/10.1016/j.wasman.2016.01.010>.
- [85] W. de Vries, P. Rem, P.B.-P. of the ISWA international, undefined 2009, ADR: A new method for dry classification, *Vivis.De.* (n.d.). [https://www.vivis.de/wp-content/uploads/WM4/2014\\_WM\\_329\\_344\\_de\\_Vries\\_Rem\\_Berkhout.pdf](https://www.vivis.de/wp-content/uploads/WM4/2014_WM_329_344_de_Vries_Rem_Berkhout.pdf).
- [86] M. Gori, B. Bergfeldt, G. Pfrang-Stotz, J. Reichelt, P. Sirini, Effect of short-term natural weathering on MSWI and wood waste bottom ash leaching behaviour, *J. Hazard. Mater.* 189 (2011) 435–443. <https://doi.org/10.1016/j.jhazmat.2011.02.045>.
- [87] J.M. Chimenos, A.I. Fernández, L. Miralles, M. Segarra, F. Espiell, Short-term natural weathering of MSWI bottom ash as a function of particle size, *Waste Manag.* 23 (2003) 887–895. [https://doi.org/10.1016/S0956-053X\(03\)00074-6](https://doi.org/10.1016/S0956-053X(03)00074-6).
- [88] C. Speiser, T. Baumann, R. Niessner, Characterization of municipal solid waste incineration (MSWI) bottom ash by scanning electron microscopy and quantitative energy dispersive X-ray microanalysis (SEM/EDX), *Fresenius. J. Anal. Chem.* 370 (2001) 752–759.
- [89] N. Saikia, G. Mertens, K. Van Balen, J. Elsen, T. Van Gerven, C. Vandecasteele, Pre-treatment of municipal solid waste incineration (MSWI) bottom ash for utilisation in cement mortar, *Constr. Build. Mater.* 96 (2015) 76–85. <https://doi.org/10.1016/j.conbuildmat.2015.07.185>.
- [90] G. Zhen, X. Lu, Y. Zhao, J. Niu, X. Chai, L. Su, Y.Y. Li, Y. Liu, J. Du, T. Hojo, Y. Hu, Characterization of controlled low-strength material obtained from dewatered sludge and refuse incineration bottom ash: Mechanical and microstructural perspectives, *J. Environ. Manage.* 129 (2013) 183–189. <https://doi.org/10.1016/j.jenvman.2013.07.008>.
- [91] D. Xuan, P. Tang, C.S. Poon, MSWIBA-based cellular alkali-activated concrete incorporating waste glass powder, *Cem. Concr. Compos.* 95 (2019) 128–136. <https://doi.org/10.1016/j.cemconcomp.2018.10.018>.
- [92] K. Yan, H. Sun, F. Gao, D. Ge, L. You, Assessment and mechanism analysis of municipal solid waste

- incineration bottom ash as aggregate in cement stabilized macadam, *J. Clean. Prod.* 244 (2020). <https://doi.org/10.1016/j.jclepro.2019.118750>.
- [93] G. Aouad, J.L. Crovisier, D. Damidot, P. Stille, E. Hutchens, J. Mutterer, J.M. Meyer, V.A. Geoffroy, Interactions between municipal solid waste incinerator bottom ash and bacteria (*Pseudomonas aeruginosa*), *Sci. Total Environ.* 393 (2008) 385–393. <https://doi.org/10.1016/j.scitotenv.2008.01.017>.
- [94] M. Antoun, F. Becquart, N. Gerges, G. Aouad, The use of calcium sulfo-aluminate cement as an alternative to Portland Cement for the recycling of municipal solid waste incineration bottom ash in mortar, *Waste Manag. Res.* 38 (2020) 868–875. <https://doi.org/10.1177/0734242X20925170>.
- [95] X. Gao, B. Yuan, Q.L. Yu, H.J.H. Brouwers, Characterization and application of municipal solid waste incineration (MSWI) bottom ash and waste granite powder in alkali activated slag, *J. Clean. Prod.* 164 (2017) 410–419. <https://doi.org/10.1016/j.jclepro.2017.06.218>.
- [96] V. Caprai, Treatment and Valorization of Municipal Solid Waste Incineration Bottom Ash, (n.d.).
- [97] T. Hemalatha, A. Ramaswamy, A review on fly ash characteristics – Towards promoting high volume utilization in developing sustainable concrete, *J. Clean. Prod.* 147 (2017) 546–559. <https://doi.org/https://doi.org/10.1016/j.jclepro.2017.01.114>.
- [98] E. Özbay, M. Erdemir, H.İ. Durmuş, Utilization and efficiency of ground granulated blast furnace slag on concrete properties – A review, *Constr. Build. Mater.* 105 (2016) 423–434. <https://doi.org/https://doi.org/10.1016/j.conbuildmat.2015.12.153>.
- [99] P. Hewlett, M. Liska, Lea's chemistry of cement and concrete, Butterworth-Heinemann, 2019.
- [100] NEN Connect - NEN-EN 196-1:2016 en, (n.d.). <https://connect.nen.nl/Standard/Detail/219352?compid=10037&collectionId=0>.
- [101] P.J. Nixon, C.L. Page, Pore solution chemistry and alkali aggregate reaction, *Spec. Publ.* 100 (1987) 1833–1862.
- [102] A. Maldonado-Alameda, J. Giro-Paloma, J. Mañosa, J. Formosa, J.M. Chimenos, Alkali-activated binders based on the coarse fraction of municipal solid waste incineration bottom ash, *Boletín La Soc. Española Cerámica y Vidr.* (2021). <https://doi.org/https://doi.org/10.1016/j.bsecv.2020.12.002>.
- [103] E. Loginova, K. Schollbach, M. Proskurnin, H.J.H. Brouwers, Municipal solid waste incineration bottom ash fines: Transformation into a minor additional constituent for cements, *Resour. Conserv. Recycl.* 166 (2021). <https://doi.org/10.1016/j.resconrec.2020.105354>.
- [104] J.A. Meima, A. Van Zomeren, R.N.J. Comans, Complexation of Cu with dissolved organic carbon in municipal solid waste incinerator bottom ash leachates, *Environ. Sci. Technol.* 33 (1999) 1424–1429. <https://doi.org/10.1021/es971113u>.
- [105] S. Olsson, J.W.J. Van Schaik, J.P. Gustafsson, D.B. Kleja, P.A.W. Van Hees, Copper(II) binding to dissolved organic matter fractions in municipal solid waste incinerator bottom ash leachate, *Environ. Sci. Technol.* 41 (2007) 4286–4291. <https://doi.org/10.1021/es062954g>.
- [106] O. Heiri, A.F. Lotter, G. Lemcke, Loss on ignition as a method for estimating organic and carbonate



- content in sediments: reproducibility and comparability of results, *J. Paleolimnol.* 25 (2001) 101–110.
- [107] J. Ribeiro, T.F. Silva, J.G. Mendonça Filho, D. Flores, Fly ash from coal combustion – An environmental source of organic compounds, *Appl. Geochemistry*. 44 (2014) 103–110. <https://doi.org/https://doi.org/10.1016/j.apgeochem.2013.06.014>.
- [108] C. Zevenbergen, L.P. Van Reeuwijk, J.P. Bradley, R.N.J. Comans, R.D. Schuiling, Weathering of MSWI bottom ash with emphasis on the glassy constituents, *J. Geochemical Explor.* 62 (1998) 293–298.
- [109] P. Freyssinet, P. Piantone, M. Azaroual, Y. Itard, B. Clozel-Leloup, D. Guyonnet, J.C. Baubron, Chemical changes and leachate mass balance of municipal solid waste bottom ash submitted to weathering, *Waste Manag.* 22 (2002) 159–172. [https://doi.org/10.1016/S0956-053X\(01\)00065-4](https://doi.org/10.1016/S0956-053X(01)00065-4).
- [110] Q. Alam, K. Schollbach, C. van Hoek, S. van der Laan, T. de Wolf, H.J.H. Brouwers, In-depth mineralogical quantification of MSWI bottom ash phases and their association with potentially toxic elements, *Waste Manag.* 87 (2019) 1–12. <https://doi.org/10.1016/j.wasman.2019.01.031>.
- [111] Y. Wei, T. Shimaoka, A. Saffarzadeh, F. Takahashi, Alteration of municipal solid waste incineration bottom ash focusing on the evolution of iron-rich constituents, *Waste Manag.* 31 (2011) 1992–2000. <https://doi.org/10.1016/j.wasman.2011.04.021>.
- [112] R. del Valle-Zermeño, J. Gómez-Manrique, J. Giro-Paloma, J. Formosa, J.M. Chimenos, Material characterization of the MSWI bottom ash as a function of particle size. Effects of glass recycling over time, *Sci. Total Environ.* 581–582 (2017) 897–905. <https://doi.org/10.1016/j.scitotenv.2017.01.047>.
- [113] P. Piantone, F. Bodéan, L. Chatelet-Snidaro, Mineralogical study of secondary mineral phases from weathered MSWI bottom ash: Implications for the modelling and trapping of heavy metals, *Appl. Geochemistry*. 19 (2004) 1891–1904. <https://doi.org/10.1016/j.apgeochem.2004.05.006>.
- [114] Z. Jing, X. Ran, F. Jin, E.H. Ishida, Hydrothermal solidification of municipal solid waste incineration bottom ash with slag addition, *Waste Manag.* 30 (2010) 1521–1527. <https://doi.org/10.1016/j.wasman.2010.03.024>.
- [115] M. Wyrzykowski, S. Ghourchian, S. Sinthupinyo, N. Chitvoranund, T. Chintana, P. Lura, Internal curing of high performance mortars with bottom ash, *Cem. Concr. Compos.* 71 (2016) 1–9. <https://doi.org/10.1016/j.cemconcomp.2016.04.009>.
- [116] K. Inkaew, A. Saffarzadeh, T. Shimaoka, Modeling the formation of the quench product in municipal solid waste incineration (MSWI) bottom ash, *Waste Manag.* 52 (2016) 159–168. <https://doi.org/10.1016/j.wasman.2016.03.019>.
- [117] J. Yu, L. Sun, J. Xiang, L. Jin, S. Hu, S. Su, J. Qiu, Physical and chemical characterization of ashes from a municipal solid waste incinerator in China, *Waste Manag. Res.* 31 (2013) 663–673. <https://doi.org/10.1177/0734242X13485793>.
- [118] P.R. Kowalski, M. Kasina, M. Michalik, Metallic Elements Occurrences in the Municipal Waste Incineration Bottom Ash, in: *Energy Procedia*, Elsevier Ltd, 2017: pp. 56–62. <https://doi.org/10.1016/j.egypro.2017.08.060>.
- [119] J.A. Meima, R.N.J. Comans, Geochemical modeling of weathering reactions in municipal solid waste

- incinerator bottom ash, *Environ. Sci. Technol.* 31 (1997) 1269–1276.  
<https://doi.org/10.1021/ES9603158>.
- [120] J. Yao, Z. Qiu, Q. Kong, L. Chen, H. Zhu, Y. Long, D. Shen, Migration of Cu, Zn and Cr through municipal solid waste incinerator bottom ash layer in the simulated landfill, *Ecol. Eng.* 102 (2017) 577–582.  
<https://doi.org/10.1016/j.ecoleng.2017.02.063>.
- [121] S.S. Alterary, N.H. Marei, Fly ash properties, characterization, and applications: A review, *J. King Saud Univ. - Sci.* 33 (2021) 101536. <https://doi.org/https://doi.org/10.1016/j.jksus.2021.101536>.
- [122] F. Puertas, Escorias de alto horno: composición y comportamiento hidráulico, *Mater. Construcción.* 43 (1993) 37–48.
- [123] I. Garcia-Lodeiro, A. Palomo, A. Fernández-Jiménez, 3 - Crucial insights on the mix design of alkali-activated cement-based binders, in: F. Pacheco-Torgal, J.A. Labrincha, C. Leonelli, A. Palomo, P.B.T.-H. of A.-A.C. Chindaprasirt *Mortars and Concretes* (Eds.), Woodhead Publishing, Oxford, 2015: pp. 49–73.  
<https://doi.org/https://doi.org/10.1533/9781782422884.1.49>.
- [124] J.L. Provis, J.S.J. Van Deventer, *Geopolymers: structures, processing, properties and industrial applications*, Elsevier, 2009.
- [125] S. Zhang, Z. Ghouleh, Z. He, L. Hu, Y. Shao, Use of municipal solid waste incineration bottom ash as a supplementary cementitious material in dry-cast concrete, *Constr. Build. Mater.* 266 (2021).  
<https://doi.org/10.1016/j.conbuildmat.2020.120890>.
- [126] B. Chen, Y. Sun, L. Jacquemin, ... S.Z.-2nd R.S., undefined 2019, Pre-Treatments Of MSWI Bottom Ash For The Application As Supplementary Cementitious Material In Blended Cement Paste, *Pure.Tudelft.Nl.* 1 (2019) 187–193.  
[http://pure.tudelft.nl/ws/files/57003844/25\\_Chen\\_2019\\_Pre\\_treatments\\_of\\_MSWI\\_bottom\\_ash\\_for\\_the\\_application\\_as\\_supplementary\\_cementitious\\_material.pdf](http://pure.tudelft.nl/ws/files/57003844/25_Chen_2019_Pre_treatments_of_MSWI_bottom_ash_for_the_application_as_supplementary_cementitious_material.pdf).
- [127] Y. Sun, Investigation on the potential application of MSWI bottom ash as substitute material in Portland cement concrete, (2018). <https://repository.tudelft.nl/islandora/object/uuid%3A95a5fe81-5842-40da-9647-66cd8b36a062>.
- [128] Y. SUN, B. CHEN, S. ZHANG, K. BLOM, M. LUKOVIĆ, G. YE, INVESTIGATION ON THE POTENTIAL APPLICATION OF MSWI BOTTOM ASH AS CEMENT SUBSTITUTES, (n.d.). [https://slag-valorisation-symposium.eu/2019/downloads/Yubo Sun - Proceedings of the 6th International Slag Valorisation Symposium.pdf](https://slag-valorisation-symposium.eu/2019/downloads/Yubo%20Sun%20-%20Proceedings%20of%20the%206th%20International%20Slag%20Valorisation%20Symposium.pdf).
- [129] G. Mathews, F. Moazeni, R. Smolinski, Treatment of reclaimed municipal solid waste incinerator sands using alkaline treatments with mechanical agitation, *J. Mater. Cycles Waste Manag.* 22 (2020) 1630–1638. <https://doi.org/10.1007/s10163-020-01053-y>.
- [130] Y. Liu, K.S. Sidhu, Z. Chen, E.H. Yang, Alkali-treated incineration bottom ash as supplementary cementitious materials, *Constr. Build. Mater.* 179 (2018) 371–378.  
<https://doi.org/10.1016/j.conbuildmat.2018.05.231>.
- [131] G. Huang, K. Yang, L. Chen, Z. Lu, Y. Sun, X. Zhang, Y. Feng, Y. Ji, Z. Xu, Use of pretreatment to prevent expansion and foaming in high-performance MSWI bottom ash alkali-activated mortars, *Constr. Build. Mater.* 245 (2020). <https://doi.org/10.1016/j.conbuildmat.2020.118471>.

- [132] F.C. Lo, S.L. Lo, M.G. Lee, Effect of partially replacing ordinary Portland cement with municipal solid waste incinerator ashes and rice husk ashes on pervious concrete quality, *Environ. Sci. Pollut. Res.* 27 (2020) 23742–23760. <https://doi.org/10.1007/S11356-020-08796-Z>.
- [133] M. Ferraris, M. Salvo, A. Ventrella, L. Buzzi, M. Veglia, Use of vitrified MSWI bottom ashes for concrete production, *Waste Manag.* 29 (2009) 1041–1047. <https://doi.org/10.1016/j.wasman.2008.07.014>.
- [134] Y. Xiao, M. Oorsprong, Y. Yang, J.H.L. Voncken, Vitrification of bottom ash from a municipal solid waste incinerator, *Waste Manag.* 28 (2008) 1020–1026. <https://doi.org/https://doi.org/10.1016/j.wasman.2007.02.034>.
- [135] W.L. Troxler, S.K. Goh, L.W.R. Dicks, Treatment of pesticide-contaminated soils with thermal desorption technologies, *Air Waste.* 43 (1993) 1610–1617.
- [136] A. Van Zomeren, R.N.J. Comans, Contribution of natural organic matter to copper leaching from municipal solid waste incinerator bottom ash, *Environ. Sci. Technol.* 38 (2004) 3927–3932. <https://doi.org/10.1021/es035266v>.
- [137] P. Stabile, M. Bello, M. Petrelli, E. Paris, M.R. Carroll, Vitrification treatment of municipal solid waste bottom ash, *Waste Manag.* 95 (2019) 250–258. <https://doi.org/https://doi.org/10.1016/j.wasman.2019.06.021>.
- [138] A.M. Joseph, Processed bottom ash based sustainable binders for concrete, (2021). <http://hdl.handle.net/1854/LU-8694932>.
- [139] Standard Test Methods for Measuring the Reactivity of Supplementary Cementitious Materials by Isothermal Calorimetry and Bound Water Measurements, (n.d.). <https://www.astm.org/c1897-20.html>.
- [140] X. Li, R. Snellings, M. Antoni, N.M. Alderete, M. Ben Haha, S. Bishnoi, Ö. Cizer, M. Cyr, K. De Weerd, Y. Dhandapani, Reactivity tests for supplementary cementitious materials: RILEM TC 267-TRM phase 1, *Mater. Struct.* 51 (2018) 1–14.
- [141] S. Donatello, M. Tyrer, C.R. Cheeseman, Comparison of test methods to assess pozzolanic activity, *Cem. Concr. Compos.* 32 (2010) 121–127. <https://doi.org/https://doi.org/10.1016/j.cemconcomp.2009.10.008>.
- [142] K. Scrivener, R. Snellings, B. Lothenbach, A practical guide to microstructural analysis of cementitious materials, Crc Press, 2018.
- [143] Z. Chen, E.H. Yang, Early age hydration of blended cement with different size fractions of municipal solid waste incineration bottom ash, *Constr. Build. Mater.* 156 (2017) 880–890. <https://doi.org/10.1016/j.conbuildmat.2017.09.063>.
- [144] H.F.W. Taylor, Cement chemistry, Thomas Telford London, 1997.
- [145] A. Quennoz, Hydration of C3A with calcium sulfate alone and in the presence of calcium silicate, (2011). <https://infoscience.epfl.ch/record/164029>.
- [146] M. Yousuf, A. Mollah, R.K. Vempati, T.C. Lin, D.L. Cocke, The interfacial chemistry of solidification/stabilization of metals in cement and pozzolanic material systems, *Waste Manag.* 15

- (1995) 137–148. [https://doi.org/10.1016/0956-053X\(95\)00013-P](https://doi.org/10.1016/0956-053X(95)00013-P).
- [147] J.F. Young, Y. JF, A discussion of the interactions between hydrating calcium silicates and set-modifying admixtures, (1978).
- [148] G. Arliguie, J.P. Ollivier, J. Grandet, Etude de l'effet retardateur du zinc sur l'hydratation de la pate de ciment Portland, *Cem. Concr. Res.* 12 (1982) 79–86.
- [149] N.M. Alderete, A.M. Joseph, P. Van den Heede, S. Matthys, N. De Belie, Effective and sustainable use of municipal solid waste incineration bottom ash in concrete regarding strength and durability, *Resour. Conserv. Recycl.* 167 (2021). <https://doi.org/10.1016/j.resconrec.2020.105356>.
- [150] B. Jurič, L. Hanžič, R. Ilić, N. Samec, Utilization of municipal solid waste bottom ash and recycled aggregate in concrete, *Waste Manag.* 26 (2006) 1436–1442. <https://doi.org/10.1016/j.wasman.2005.10.016>.
- [151] M. Carsana, M. Gastaldi, F. Lollini, E. Redaelli, L. Bertolini, Improving durability of reinforced concrete structures by recycling wet-ground MSWI bottom ash, *Mater. Corros.* 67 (2016) 573–582. <https://doi.org/10.1002/maco.201608881>.
- [152] Z. Yang, S. Tian, L. Liu, X. Wang, Z. Zhang, Recycling ground MSWI bottom ash in cement composites: Long-term environmental impacts, *Waste Manag.* 78 (2018) 841–848. <https://doi.org/10.1016/j.wasman.2018.07.002>.
- [153] Z. Yang, R. Ji, L. Liu, X. Wang, Z. Zhang, Recycling of municipal solid waste incineration by-product for cement composites preparation, *Constr. Build. Mater.* 162 (2018) 794–801. <https://doi.org/10.1016/j.conbuildmat.2017.12.081>.
- [154] K.L. Lin, W.C. Chang, D.F. Lin, Pozzolan characteristics of pulverized incinerator bottom ash slag, *Constr. Build. Mater.* 22 (2008) 324–329. <https://doi.org/10.1016/j.conbuildmat.2006.08.012>.
- [155] S. Casanova, R. V Silva, J. de Brito, M.F.C. Pereira, Mortars with alkali-activated municipal solid waste incinerator bottom ash and fine recycled aggregates, *J. Clean. Prod.* 289 (2021). <https://doi.org/10.1016/j.jclepro.2020.125707>.
- [156] R. Carvalho, R. V Silva, J. de Brito, M.F.C. Pereira, Alkali activation of bottom ash from municipal solid waste incineration: Optimization of NaOH- and Na 2SiO3-based activators, *J. Clean. Prod.* 291 (2021). <https://doi.org/10.1016/j.jclepro.2021.125930>.
- [157] G. Huang, Y. Ji, J. Li, L. Zhang, X. Liu, B. Liu, Effect of activated silica on polymerization mechanism and strength development of MSWI bottom ash alkali-activated mortars, *Constr. Build. Mater.* 201 (2019) 90–99. <https://doi.org/10.1016/j.conbuildmat.2018.12.125>.
- [158] I. Lancellotti, C. Ponzoni, L. Barbieri, C. Leonelli, Alkali activation processes for incinerator residues management, *Waste Manag.* 33 (2013) 1740–1749. <https://doi.org/10.1016/j.wasman.2013.04.013>.
- [159] Y. Ma, Microstructure and Engineering Properties of Alkali Activated Fly Ash-as an environment friendly alternative to Portland cement, (2013).
- [160] C. Ruiz-Santaquiteria, A. Fernández-Jiménez, A. Palomo, Quantitative determination of reactive SiO<sub>2</sub>

- and Al<sub>2</sub>O<sub>3</sub> in aluminosilicate materials, in: Proc. XIII Int. Congr. Chem. Cem. Madrid, Spain, 2011.
- [161] P. Duxson, S.W. Mallicoat, G.C. Lukey, W.M. Kriven, J.S.J. van Deventer, The effect of alkali and Si/Al ratio on the development of mechanical properties of metakaolin-based geopolymers, *Colloids Surfaces A Physicochem. Eng. Asp.* 292 (2007) 8–20. <https://doi.org/10.1016/j.colsurfa.2006.05.044>.
- [162] W. Zhu, X. Chen, L.J. Struble, E.H. Yang, Characterization of calcium-containing phases in alkali-activated municipal solid waste incineration bottom ash binder through chemical extraction and deconvoluted Fourier transform infrared spectra, *J. Clean. Prod.* 192 (2018) 782–789. <https://doi.org/10.1016/j.jclepro.2018.05.049>.
- [163] W. Zhu, X. Chen, L.J. Struble, E.H. Yang, Quantitative characterization of aluminosilicate gels in alkali-activated incineration bottom ash through sequential chemical extractions and deconvoluted nuclear magnetic resonance spectra, *Cem. Concr. Compos.* 99 (2019) 175–180. <https://doi.org/10.1016/j.cemconcomp.2019.03.014>.
- [164] M. Criado, A. Fernández-Jiménez, A. Palomo, I. Sobrados, J. Sanz, Effect of the SiO<sub>2</sub>/Na<sub>2</sub>O ratio on the alkali activation of fly ash. Part II: <sup>29</sup>Si MAS-NMR Survey, *Microporous Mesoporous Mater.* 109 (2008) 525–534.
- [165] W. Zhu, X. Chen, A. Zhao, L.J. Struble, E.H. Yang, Synthesis of high strength binders from alkali activation of glass materials from municipal solid waste incineration bottom ash, *J. Clean. Prod.* 212 (2019) 261–269. <https://doi.org/10.1016/j.jclepro.2018.11.295>.
- [166] C.W. Sinton, W.C. LaCourse, Experimental survey of the chemical durability of commercial soda-lime-silicate glasses, *Mater. Res. Bull.* 36 (2001) 2471–2479.
- [167] R. Redden, N. Neithalath, Microstructure, strength, and moisture stability of alkali activated glass powder-based binders, *Cem. Concr. Compos.* 45 (2014) 46–56. <https://doi.org/https://doi.org/10.1016/j.cemconcomp.2013.09.011>.
- [168] W. Zhu, P.J. Teoh, Y. Liu, Z. Chen, E.H. Yang, Strategic utilization of municipal solid waste incineration bottom ash for the synthesis of lightweight aerated alkali-activated materials, *J. Clean. Prod.* 235 (2019) 603–612. <https://doi.org/10.1016/j.jclepro.2019.06.286>.
- [169] I. Lancellotti, M. Cannio, F. Bollino, M. Catauro, L. Barbieri, C. Leonelli, Geopolymers: An option for the valorization of incinerator bottom ash derived “end of waste,” *Ceram. Int.* 41 (2015) 2116–2123. <https://doi.org/10.1016/j.ceramint.2014.10.008>.
- [170] Z. Chen, Y. Liu, W. Zhu, E.H. Yang, Incinerator bottom ash (IBA) aerated geopolymer, *Constr. Build. Mater.* 112 (2016) 1025–1031. <https://doi.org/10.1016/j.conbuildmat.2016.02.164>.
- [171] P. Apostoli, S. Giusti, D. Bartoli, A. Perico, P. Bavazzano, L. Alessio, Multiple exposure to arsenic, antimony, and other elements in art glass manufacturing, *Am. J. Ind. Med.* 34 (1998) 65–72. <https://onlinelibrary.wiley.com/doi/epdf/10.1002/%28SICI%291097-0274%28199807%2934%3A1%3C65%3A%3AAID-AJIM9%3E3.0.CO%3B2-P>.
- [172] G. Huang, Y. Ji, L. Zhang, J. Li, Z. Hou, The influence of curing methods on the strength of MSWI bottom ash-based alkali-activated mortars: The role of leaching of OH<sup>−</sup> and free alkali, *Constr. Build. Mater.* 186 (2018) 978–985. <https://doi.org/10.1016/j.conbuildmat.2018.07.224>.

- [173] G. Huang, K. Yang, Y. Sun, Z. Lu, X. Zhang, L. Zuo, Y. Feng, R. Qian, Y. Qi, Y. Ji, Z. Xu, Influence of NaOH content on the alkali conversion mechanism in MSWI bottom ash alkali-activated mortars, *Constr. Build. Mater.* 248 (2020). <https://doi.org/10.1016/j.conbuildmat.2020.118582>.
- [174] L. Jin, G. Huang, Y. Li, X. Zhang, Y. Ji, Z. Xu, Positive influence of liquid sodium silicate on the setting time, polymerization, and strength development mechanism of mswi bottom ash alkali-activated mortars, *Materials (Basel)*. 14 (2021). <https://doi.org/10.3390/ma14081927>.
- [175] W. Zhu, X.H. Rao, Y. Liu, E.H. Yang, Lightweight aerated metakaolin-based geopolymer incorporating municipal solid waste incineration bottom ash as gas-forming agent, *J. Clean. Prod.* 177 (2018) 775–781. <https://doi.org/10.1016/j.jclepro.2017.12.267>.
- [176] A. Wongsas, K. Boonserm, C. Waisurasingha, V. Sata, P. Chindaprasirt, Use of municipal solid waste incinerator (MSWI) bottom ash in high calcium fly ash geopolymer matrix, *J. Clean. Prod.* 148 (2017) 49–59. <https://doi.org/10.1016/j.jclepro.2017.01.147>.
- [177] A. Maldonado-Alameda, J. Mañosa, J. Giro-Paloma, J. Formosa, J.M. Chimenos, Alkali-activated binders using bottom ash from waste-to-energy plants and aluminium recycling waste, *Appl. Sci.* 11 (2021). <https://doi.org/10.3390/app11093840>.
- [178] G. Huang, L. Yuan, Y. Ji, B. Liu, Z. Xu, Cooperative action and compatibility between Portland cement and MSWI bottom ash alkali-activated double gel system materials, *Constr. Build. Mater.* 209 (2019) 445–453. <https://doi.org/10.1016/j.conbuildmat.2019.03.141>.
- [179] D. Torelli, Use of waste material in AAM concrete: application in circular economy, Swiss Federal Institute of Technology Zurich, 2020.
- [180] NEN Connect - ISO 14040:2006 en, (n.d.). <https://connect.nen.nl/Standard/Detail/107792?compId=10037&collectionId=0>.
- [181] P.M.F. van de Wouw, E. Loginova, M.V.A. Florea, H.J.H. Brouwers, Compositional modelling and crushing behaviour of MSWI bottom ash material classes, *Waste Manag.* 101 (2020) 268–282. <https://doi.org/10.1016/j.wasman.2019.10.013>.
- [182] Soil Quality Degree [WWW Document], 2015, (n.d.). <https://wetten.overheid.nl/BWBR0022929/2015-07-01>.
- [183] NEN Connect - NEN-EN 1744-7:2012 en, (n.d.). <https://connect.nen.nl/Standard/Detail/169013?compId=10037&collectionId=0>.
- [184] N. Doebelin, R. Kleeberg, Profex: a graphical user interface for the Rietveld refinement program BGMN., *J. Appl. Crystallogr.* 48 (2015) 1573–1580. <https://doi.org/10.1107/S1600576715014685>.
- [185] L. Muchova, E. Bakker, P. Rem, Precious metals in municipal solid waste incineration bottom ash, *Water, Air, Soil Pollut. Focus*. 9 (2009) 107–116. <https://doi.org/10.1007/s11267-008-9191-9>.
- [186] P.C. Rem, C. De Vries, L.A. Van Kooy, P. Bevilacqua, M.A. Reuter, The Amsterdam pilot on bottom ash, in: *Miner. Eng.*, 2004: pp. 363–365. <https://doi.org/10.1016/j.mineng.2003.11.009>.
- [187] N. Otsu, A Threshold Selection Method from Gray-Level Histograms, *IEEE Trans. Syst. Man. Cybern.* 9

- (1979) 62–66. <https://doi.org/10.1109/TSMC.1979.4310076>.
- [188] Y. Hu, M.C.M. Bakker, P.G. de Heij, Recovery and distribution of incinerated aluminum packaging waste, *Waste Manag.* 31 (2011) 2422–2430. <https://doi.org/10.1016/j.wasman.2011.07.021>.
- [189] S. Eggen, K. Sandaunet, L. Kolbeinsen, A. Kvithyld, Recycling of Aluminium from Mixed Household Waste, *Miner. Met. Mater. Ser.* (2020) 1091–1100. [https://doi.org/10.1007/978-3-030-36408-3\\_148](https://doi.org/10.1007/978-3-030-36408-3_148).
- [190] J.R. Davis, *Corrosion of aluminum and aluminum alloys*, Asm International, 1999.
- [191] R.T. Chancey, P. Stutzman, M.C.G. Juenger, D.W. Fowler, Comprehensive phase characterization of crystalline and amorphous phases of a Class F fly ash, *Cem. Concr. Res.* 40 (2010) 146–156. <https://doi.org/https://doi.org/10.1016/j.cemconres.2009.08.029>.
- [192] S.C. Pal, A. Mukherjee, S.R. Pathak, Investigation of hydraulic activity of ground granulated blast furnace slag in concrete, *Cem. Concr. Res.* 33 (2003) 1481–1486. [https://doi.org/https://doi.org/10.1016/S0008-8846\(03\)00062-0](https://doi.org/https://doi.org/10.1016/S0008-8846(03)00062-0).
- [193] J.L. Provis, S.A. Bernal, Geopolymers and related alkali-activated materials, *Annu. Rev. Mater. Res.* 44 (2014) 299–327.
- [194] P. Duxson, A. Fernández-Jiménez, J.L. Provis, G.C. Lukey, A. Palomo, J.S.J. van Deventer, Geopolymer technology: the current state of the art, *J. Mater. Sci.* 42 (2007) 2917–2933. <https://doi.org/10.1007/s10853-006-0637-z>.
- [195] B. Lothenbach, D.A. Kulik, T. Matschei, M. Balonis, L. Baquerizo, B. Dilnesa, G.D. Miron, R.J. Myers, Cemdata18: A chemical thermodynamic database for hydrated Portland cements and alkali-activated materials, *Cem. Concr. Res.* 115 (2019) 472–506. <https://doi.org/https://doi.org/10.1016/j.cemconres.2018.04.018>.
- [196] R.J. Myers, S.A. Bernal, J.L. Provis, Phase diagrams for alkali-activated slag binders, *Cem. Concr. Res.* 95 (2017) 30–38. <https://doi.org/https://doi.org/10.1016/j.cemconres.2017.02.006>.
- [197] R. Xiao, X. Jiang, M. Zhang, P. Polaczyk, B. Huang, Analytical investigation of phase assemblages of alkali-activated materials in CaO-SiO<sub>2</sub>-Al<sub>2</sub>O<sub>3</sub> systems: The management of reaction products and designing of precursors, *Mater. Des.* 194 (2020) 108975. <https://doi.org/https://doi.org/10.1016/j.matdes.2020.108975>.
- [198] NEN Connect - NEN-EN 15167-1:2006 en, (n.d.). <https://connect.nen.nl/Standard/Detail/109308?compId=10037&collectionId=0>.
- [199] NEN Connect - NEN-EN 1744-1:2009+A1:2012 en, (n.d.). <https://connect.nen.nl/Standard/Detail/178537?compId=10037&collectionId=0>.
- [200] S. Zhang, A. Keulen, K. Arbi, G. Ye, Waste glass as partial mineral precursor in alkali-activated slag/fly ash system, *Cem. Concr. Res.* 102 (2017) 29–40. <https://doi.org/https://doi.org/10.1016/j.cemconres.2017.08.012>.
- [201] NEN Connect - NEN-EN 196-2:2013 en, (n.d.). <https://connect.nen.nl/Standard/Detail/184482?compId=10037&collectionId=0>.



- [202] R. Snellings, Solution-controlled dissolution of supplementary cementitious material glasses at pH 13: the effect of solution composition on glass dissolution rates, *J. Am. Ceram. Soc.* 96 (2013) 2467–2475.
- [203] A. Schöler, F. Winnefeld, M. Ben Haha, B. Lothenbach, The effect of glass composition on the reactivity of synthetic glasses, *J. Am. Ceram. Soc.* 100 (2017) 2553–2567.
- [204] Y. Zuo, M. Nedeljković, G. Ye, Pore solution composition of alkali-activated slag/fly ash pastes, *Cem. Concr. Res.* 115 (2019) 230–250.
- [205] T. Wagner, D.A. Kulik, F.F. Hingerl, S. V Dmytrieva, GEM-Selektor geochemical modeling package: TSolMod library and data interface for multicomponent phase models, *Can. Mineral.* 50 (2012) 1173–1195.
- [206] D.A. Kulik, T. Wagner, S. V Dmytrieva, G. Kosakowski, F.F. Hingerl, K. V Chudnenko, U.R. Berner, GEM-Selektor geochemical modeling package: revised algorithm and GEMS3K numerical kernel for coupled simulation codes, *Comput. Geosci.* 17 (2013) 1–24.
- [207] R.J. Myers, S.A. Bernal, J.L. Provis, A thermodynamic model for C-(N-)A-S-H gel: CNASH\_ss. Derivation and validation, *Cem. Concr. Res.* 66 (2014) 27–47.  
<https://doi.org/https://doi.org/10.1016/j.cemconres.2014.07.005>.
- [208] R.J. Myers, B. Lothenbach, S.A. Bernal, J.L. Provis, Thermodynamic modelling of alkali-activated slag cements, *Appl. Geochemistry.* 61 (2015) 233–247.  
<https://doi.org/https://doi.org/10.1016/j.apgeochem.2015.06.006>.
- [209] Y. Zuo, Experimental Study and Numerical Simulation of the Reaction Process and Microstructure Formation of Alkali-Activated Materials, Delft University of Technology, 2019.
- [210] D.A. Kulik, Improving the structural consistency of C-S-H solid solution thermodynamic models, *Cem. Concr. Res.* 41 (2011) 477–495. <https://doi.org/https://doi.org/10.1016/j.cemconres.2011.01.012>.
- [211] NEN Connect - NEN-EN 12457-4:2002 en, (n.d.).  
<https://connect.nen.nl/Standard/Detail/82471?compId=10037&collectionId=0>.
- [212] “Soil Quality Decree,” 2015. [Online]. Available:  
[http://wetten.overheid.nl/BWBR0023085/BijlageA/geldigheidsdatum\\_09-10-2015.](http://wetten.overheid.nl/BWBR0023085/BijlageA/geldigheidsdatum_09-10-2015.), (n.d.).
- [213] E. Loginova, D.S. Volkov, P.M.F. van de Wouw, M.V.A. Florea, H.J.H. Brouwers, Detailed characterization of particle size fractions of municipal solid waste incineration bottom ash, *J. Clean. Prod.* 207 (2019) 866–874. <https://doi.org/https://doi.org/10.1016/j.jclepro.2018.10.022>.
- [214] U. Müller, K. Rübner, The microstructure of concrete made with municipal waste incinerator bottom ash as an aggregate component, *Cem. Concr. Res.* 36 (2006) 1434–1443.  
<https://doi.org/10.1016/j.cemconres.2006.03.023>.
- [215] NEN Connect - NEN-EN 206:2014+A2:2021 en, (n.d.).  
<https://connect.nen.nl/Standard/Detail/3650677?compId=10037&collectionId=0>.
- [216] T.P. Seward III, T. Vascott, High temperature glass melt property database for process modeling, Wiley-American Ceramic Society, 2005.

- [217] D. Glosser, P. Suraneni, O.B. Isgor, W.J. Weiss, Using glass content to determine the reactivity of fly ash for thermodynamic calculations, *Cem. Concr. Compos.* 115 (2021) 103849. <https://doi.org/https://doi.org/10.1016/j.cemconcomp.2020.103849>.
- [218] Z. Sun, A. Vollpracht, One year geopolymerisation of sodium silicate activated fly ash and metakaolin geopolymers, *Cem. Concr. Compos.* 95 (2019) 98–110. <https://doi.org/https://doi.org/10.1016/j.cemconcomp.2018.10.014>.
- [219] A. Schöler, B. Lothenbach, F. Winnefeld, M. Zajac, Hydration of quaternary Portland cement blends containing blast-furnace slag, siliceous fly ash and limestone powder, *Cem. Concr. Compos.* 55 (2015) 374–382. <https://doi.org/https://doi.org/10.1016/j.cemconcomp.2014.10.001>.
- [220] G.V.P. Bhagath Singh, K.V.L. Subramaniam, Quantitative XRD study of amorphous phase in alkali activated low calcium siliceous fly ash, *Constr. Build. Mater.* 124 (2016) 139–147. <https://doi.org/https://doi.org/10.1016/j.conbuildmat.2016.07.081>.
- [221] C.R. Ward, D. French, Determination of glass content and estimation of glass composition in fly ash using quantitative X-ray diffractometry, *Fuel*. 85 (2006) 2268–2277. <https://doi.org/https://doi.org/10.1016/j.fuel.2005.12.026>.
- [222] Y. Jin, W. Feng, D. Zheng, Z. Dong, H. Cui, Structure refinement of fly ash in connection with its reactivity in geopolymerization, *Waste Manag.* 118 (2020) 350–359. <https://doi.org/https://doi.org/10.1016/j.wasman.2020.08.049>.
- [223] G.B. Singh, K. V Subramaniam, Characterization of Indian fly ashes using different experimental techniques, *Indian Concr. J.* 92 (2018) 10–23.
- [224] B. Valentim, A. Guedes, D. Flores, C.R. Ward, J.C. Hower, Variations in fly ash composition with sampling location: Case study from a Portuguese power plant, (2010).
- [225] S. Chithiraputhiran, N. Neithalath, Isothermal reaction kinetics and temperature dependence of alkali activation of slag, fly ash and their blends, *Constr. Build. Mater.* 45 (2013) 233–242.
- [226] J.J. Thomas, A.J. Allen, H.M. Jennings, Density and water content of nanoscale solid C–S–H formed in alkali-activated slag (AAS) paste and implications for chemical shrinkage, *Cem. Concr. Res.* 42 (2012) 377–383.
- [227] K. Gong, C.E. White, Impact of chemical variability of ground granulated blast-furnace slag on the phase formation in alkali-activated slag pastes, *Cem. Concr. Res.* 89 (2016) 310–319.
- [228] H. Ye, A. Radlińska, Quantitative analysis of phase assemblage and chemical shrinkage of alkali-activated slag, *J. Adv. Concr. Technol.* 14 (2016) 245–260.
- [229] N. Marjanović, M. Komljenović, Z. Baščarević, V. Nikolić, R. Petrović, Physical–mechanical and microstructural properties of alkali-activated fly ash–blast furnace slag blends, *Ceram. Int.* 41 (2015) 1421–1435.
- [230] R. Cao, S. Zhang, N. Banthia, Y. Zhang, Z. Zhang, Interpreting the early-age reaction process of alkali-activated slag by using combined embedded ultrasonic measurement, thermal analysis, XRD, FTIR and SEM, *Compos. Part B Eng.* 186 (2020) 107840.

- [231] Z. Sun, A. Vollpracht, Isothermal calorimetry and in-situ XRD study of the NaOH activated fly ash, metakaolin and slag, *Cem. Concr. Res.* 103 (2018) 110–122.
- [232] F. Puertas, B. González-Fonteboa, I. González-Taboada, M.M. Alonso, M. Torres-Carrasco, G. Rojo, F. Martínez-Abella, Alkali-activated slag concrete: Fresh and hardened behaviour, *Cem. Concr. Compos.* 85 (2018) 22–31.
- [233] M. Chi, Effects of dosage of alkali-activated solution and curing conditions on the properties and durability of alkali-activated slag concrete, *Constr. Build. Mater.* 35 (2012) 240–245.
- [234] O. Mikhailova, A. del Campo, P. Rovnanik, J.F. Fernández, M. Torres-Carrasco, In situ characterization of main reaction products in alkali-activated slag materials by Confocal Raman Microscopy, *Cem. Concr. Compos.* 99 (2019) 32–39.
- [235] Y. Zuo, M. Nedeljković, G. Ye, Coupled thermodynamic modelling and experimental study of sodium hydroxide activated slag, *Constr. Build. Mater.* 188 (2018) 262–279.
- [236] S. Puligilla, P. Mondal, Role of slag in microstructural development and hardening of fly ash-slag geopolymer, *Cem. Concr. Res.* 43 (2013) 70–80.
- [237] W. Liu, T. Aldahri, C. Xu, C. Li, S. Rohani, Synthesis of sole gismondine-type zeolite from blast furnace slag during CO<sub>2</sub> mineralization process, *J. Environ. Chem. Eng.* 9 (2021) 104652.
- [238] X. Gao, Q.L. Yu, H.J.H. Brouwers, Reaction kinetics, gel character and strength of ambient temperature cured alkali activated slag–fly ash blends, *Constr. Build. Mater.* 80 (2015) 105–115.
- [239] A. Font, L. Soriano, S.M. de Moraes Pinheiro, M.M. Tashima, J. Monzó, M.V. Borrachero, J. Payá, Design and properties of 100% waste-based ternary alkali-activated mortars: Blast furnace slag, olive-stone biomass ash and rice husk ash, *J. Clean. Prod.* 243 (2020) 118568.
- [240] G.M. Kim, J.G. Jang, F. Naeem, H.-K. Lee, Heavy metal leaching, CO<sub>2</sub> uptake and mechanical characteristics of carbonated porous concrete with alkali-activated slag and bottom ash, *Int. J. Concr. Struct. Mater.* 9 (2015) 283–294.
- [241] M. Ben Haha, G. Le Saout, F. Winnefeld, B. Lothenbach, Influence of activator type on hydration kinetics, hydrate assemblage and microstructural development of alkali activated blast-furnace slags, *Cem. Concr. Res.* 41 (2011) 301–310.
- [242] A. Keulen, A. Van Zomeren, J.J. Dijkstra, Leaching of monolithic and granular alkali activated slag-fly ash materials, as a function of the mixture design, *Waste Manag.* 78 (2018) 497–508.
- [243] D. Ravikumar, N. Neithalath, Reaction kinetics in sodium silicate powder and liquid activated slag binders evaluated using isothermal calorimetry, *Thermochim. Acta.* 546 (2012) 32–43.
- [244] F. Puertas, M. Palacios, H. Manzano, J.S. Dolado, A. Rico, J. Rodríguez, A model for the CASH gel formed in alkali-activated slag cements, *J. Eur. Ceram. Soc.* 31 (2011) 2043–2056.
- [245] S. Ramanathan, M. Croly, P. Suraneni, Comparison of the effects that supplementary cementitious materials replacement levels have on cementitious paste properties, *Cem. Concr. Compos.* 112 (2020) 103678.

- [246] I.G. Lodeiro, N. Cristelo, A. Palomo, A. Fernández-Jiménez, Use of industrial by-products as alkaline cement activators, *Constr. Build. Mater.* 253 (2020) 119000.
- [247] P. Suraneni, J. Weiss, Examining the pozzolanicity of supplementary cementitious materials using isothermal calorimetry and thermogravimetric analysis, *Cem. Concr. Compos.* 83 (2017) 273–278.
- [248] M. Askarian, Z. Tao, B. Samali, G. Adam, R. Shuaibu, Mix composition and characterisation of one-part geopolymers with different activators, *Constr. Build. Mater.* 225 (2019) 526–537.
- [249] J. Aliques-Granero, M.T. Tognonvi, A. Tagnit-Hamou, Durability study of AAMs: Sulfate attack resistance, *Constr. Build. Mater.* 229 (2019) 117100.
- [250] M. Kamath, S. Prashant, M. Kumar, Micro-characterisation of alkali activated paste with fly ash-GGBS-metakaolin binder system with ambient setting characteristics, *Constr. Build. Mater.* 277 (2021) 122323.
- [251] S. Park, H.N. Yoon, J. Seo, H.-K. Lee, J.G. Jang, Structural evolution of binder gel in alkali-activated cements exposed to electrically accelerated leaching conditions, *J. Hazard. Mater.* 387 (2020) 121825.
- [252] Y.J. Zhang, L. Kang, L.C. Liu, Alkali-activated cements for photocatalytic degradation of organic dyes, in: *Handb. Alkali-Activated Cem. Mortars Concr.*, Elsevier, 2015: pp. 729–775.
- [253] J. Wang, T. Huang, L. Han, F. Xie, Z. Liu, D. Wang, Optimization of alkali-activated concrete based on the characteristics of binder systems, *Constr. Build. Mater.* 300 (2021) 123952.
- [254] Y. Wang, R. Chen, J. Hu, Z. Zhang, H. Huang, Y. Ma, J. Wei, Z. Zhang, S. Yin, H. Wang, others, Surface characteristics and electrochemical behaviors of passive reinforcing steel in alkali-activated slag, *Corros. Sci.* 190 (2021) 109657.
- [255] A. Nićs, N.A. Eren, A. Çevik, Effects of nanosilica and steel fibers on the impact resistance of slag based self-compacting alkali-activated concrete, *Ceram. Int.* (2021).
- [256] O.M. Abdulkareem, A. Ben Fraj, M. Bouasker, L. Khouchaf, A. Khelidj, Microstructural investigation of slag-blended UHPC: The effects of slag content and chemical/thermal activation, *Constr. Build. Mater.* 292 (2021) 123455.
- [257] N.T.A. Júnior, V.M.E. Lima, S.M. Torres, P.E.A. Basto, A.A.M. Neto, Experimental investigation of mix design for high-strength alkali-activated slag concrete, *Constr. Build. Mater.* 291 (2021) 123387.
- [258] Y. Tian, C. Yang, S. Yuan, H. Yuan, K. Yang, L. Yu, M. Zhang, X. Zhu, Understanding the rheological properties of alkali-activated slag pastes from the cohesion and friction interactions, *Constr. Build. Mater.* 291 (2021) 123311.
- [259] M. Teymouri, K. Behfarnia, A. Shabani, Mix design effects on the durability of alkali-activated slag concrete in a hydrochloric acid environment, *Sustainability.* 13 (2021) 8096.
- [260] R. Cai, H. Ye, Clinkerless ultra-high strength concrete based on alkali-activated slag at high temperatures, *Cem. Concr. Res.* 145 (2021) 106465.

- [261] S. Marathe, I.R. Mithanthaya, R.Y. Shenoy, Durability and microstructure studies on Slag-Fly Ash-Glass powder based alkali activated pavement quality concrete mixes, *Constr. Build. Mater.* 287 (2021) 123047.
- [262] F. Moodi, S. Norouzi, P. Dashti, Mechanical properties and durability of alkali-activated slag repair mortars containing silica fume against freeze-thaw cycles and salt scaling attack, *Adv. Concr. Constr.* 11 (2021) 493–505.
- [263] H. Geng, Q. Xu, S.B. Duraman, Q. Li, Effect of Rheology of Fresh Paste on the Pore Structure and Properties of Pervious Concrete Based on the High Fluidity Alkali-Activated Slag, *Crystals*. 11 (2021) 593.
- [264] G. Fang, Q. Wang, M. Zhang, Micromechanical analysis of interfacial transition zone in alkali-activated fly ash-slag concrete, *Cem. Concr. Compos.* 119 (2021) 103990.
- [265] K. Kondepudi, K.V.L. Subramaniam, Formulation of alkali-activated fly ash-slag binders for 3D concrete printing, *Cem. Concr. Compos.* 119 (2021) 103983.
- [266] L. Mengasini, M. Mavroulidou, M.J. Gunn, Alkali-activated concrete mixes with ground granulated blast furnace slag and paper sludge ash in seawater environments, *Sustain. Chem. Pharm.* 20 (2021) 100380.
- [267] J. Huang, C. Zou, D. Sun, B. Yang, J. Yan, Effect of recycled fine aggregates on alkali-activated slag concrete properties, in: *Structures*, 2021: pp. 89–99.
- [268] A. Alzaza, K. Ohenoja, M. Illikainen, One-part alkali-activated blast furnace slag for sustainable construction at subzero temperatures, *Constr. Build. Mater.* 276 (2021) 122026.
- [269] Z. Li, T. Lu, Y. Chen, B. Wu, G. Ye, Prediction of the autogenous shrinkage and microcracking of alkali-activated slag and fly ash concrete, *Cem. Concr. Compos.* 117 (2021) 103913.
- [270] J. Lei, W.W. Law, E.-H. Yang, Effect of calcium hydroxide on the alkali-silica reaction of alkali-activated slag mortars activated by sodium hydroxide, *Constr. Build. Mater.* 272 (2021) 121868.
- [271] Y. Du, J. Wang, C. Shi, H.-J. Hwang, N. Li, Flexural behavior of alkali-activated slag-based concrete beams, *Eng. Struct.* 229 (2021) 111644.
- [272] S. Uppalapati, L. Vandewalle, Ö. Cizer, Monitoring the setting process of alkali-activated slag-fly ash cements with ultrasonic P-wave velocity, *Constr. Build. Mater.* 271 (2021) 121592.
- [273] S. Rajaei, P. Shoaie, M. Shariati, F. Ameri, H.R. Musaei, B. Behforouz, J. de Brito, Rubberized alkali-activated slag mortar reinforced with polypropylene fibres for application in lightweight thermal insulating materials, *Constr. Build. Mater.* 270 (2021) 121430.
- [274] G.F. Huseien, A.R.M. Sam, R. Alyousef, Texture, morphology and strength performance of self-compacting alkali-activated concrete: Role of fly ash as GBFS replacement, *Constr. Build. Mater.* 270 (2021) 121368.
- [275] B.H. Tekle, K. Holschemacher, P. Löber, B. Heiden, Mechanical Behavior and Frost-Resistance of Alkali-Activated Cement Concrete with Blended Binder at Ambient Curing Condition, *Buildings*. 11 (2021) 52.

- [276] X. Wei, D. Li, F. Ming, C. Yang, L. Chen, Y. Liu, Influence of low-temperature curing on the mechanical strength, hydration process, and microstructure of alkali-activated fly ash and ground granulated blast furnace slag mortar, *Constr. Build. Mater.* 269 (2021) 121811.
- [277] A.M. Humad, J.L. Provis, K. Habermehl-Cwirzen, M. Rajczakowska, A. Cwirzen, Creep and Long-Term Properties of Alkali-Activated Swedish-Slag Concrete, *J. Mater. Civ. Eng.* 33 (2021) 4020475.
- [278] X. Zhou, Y. Zeng, P. Chen, Z. Jiao, W. Zheng, Mechanical properties of basalt and polypropylene fibre-reinforced alkali-activated slag concrete, *Constr. Build. Mater.* 269 (2021) 121284.
- [279] M.N.N. Khan, A.K. Saha, P.K. Sarker, Evaluation of the ASR of waste glass fine aggregate in alkali activated concrete by concrete prism tests, *Constr. Build. Mater.* 266 (2021) 121121.
- [280] S. Kucharczyk, M. Sitarz, M. Zajac, J. Deja, The effect of CaO/SiO<sub>2</sub> molar ratio of CaO-Al<sub>2</sub>O<sub>3</sub>-SiO<sub>2</sub> glasses on their structure and reactivity in alkali activated system, *Spectrochim. Acta Part A Mol. Biomol. Spectrosc.* 194 (2018) 163–171. <https://doi.org/10.1016/j.saa.2018.01.018>.
- [281] P. Durdziński, R. Snellings, C.F. Dunant, M. Ben Haha, K.L. Scrivener, Fly ash as an assemblage of model Ca--Mg--Na-aluminosilicate glasses, *Cem. Concr. Res.* 78 (2015) 263–272.
- [282] I. Garcia-Lodeiro, E. Aparicio-Rebollo, A. Fernández-Jimenez, A. Palomo, Effect of calcium on the alkaline activation of aluminosilicate glass, *Ceram. Int.* 42 (2016) 7697–7707. <https://doi.org/https://doi.org/10.1016/j.ceramint.2016.01.184>.
- [283] I. Garcia-Lodeiro, A. Fernández-Jimenez, P. Pena, A. Palomo, Alkaline activation of synthetic aluminosilicate glass, *Ceram. Int.* 40 (2014) 5547–5558. <https://doi.org/https://doi.org/10.1016/j.ceramint.2013.10.146>.
- [284] F. Pacheco-Torgal, J. Castro-Gomes, S. Jalali, Alkali-activated binders: A review. Part 2. About materials and binders manufacture, *Constr. Build. Mater.* 22 (2008) 1315–1322.
- [285] R.A. Fletcher, K.J.D. MacKenzie, C.L. Nicholson, S. Shimada, The composition range of aluminosilicate geopolymers, *J. Eur. Ceram. Soc.* 25 (2005) 1471–1477.
- [286] A. Fernández-Jiménez, A. Palomo, Characterisation of fly ashes. Potential reactivity as alkaline cements☆, *Fuel*. 82 (2003) 2259–2265.
- [287] H. Wang, H. Li, F. Yan, Synthesis and mechanical properties of metakaolinite-based geopolymer, *Colloids Surfaces A Physicochem. Eng. Asp.* 268 (2005) 1–6.
- [288] C. Ruiz Santa Quiteria Gómez, *Materias primas alternativas para el desarrollo de nuevos cementos: activación alcalina de vidrios silicoaluminosos*, (2013).
- [289] J. Petrovic, G. Thomas, *Reaction of Aluminum with Water to Produce Hydrogen-2010 Update*, 2011.
- [290] K.C. Newlands, M. Foss, T. Matchei, J. Skibsted, D.E. Macphee, Early stage dissolution characteristics of aluminosilicate glasses with blast furnace slag-and fly-ash-like compositions, *J. Am. Ceram. Soc.* 100 (2017) 1941–1955.

- [291] S. Song, H.M. Jennings, Pore solution chemistry of alkali-activated ground granulated blast-furnace slag11This paper was originally submitted to Advanced Cement Based Materials. The paper was received at the Editorial Office of Cement and Concrete Research on 12 November 1998 an, Cem. Concr. Res. 29 (1999) 159–170. [https://doi.org/https://doi.org/10.1016/S0008-8846\(98\)00212-9](https://doi.org/https://doi.org/10.1016/S0008-8846(98)00212-9).
- [292] P. Duxson, J.L. Provis, G.C. Lukey, S.W. Mallicoat, W.M. Kriven, J.S.J. van Deventer, Understanding the relationship between geopolymers composition, microstructure and mechanical properties, Colloids Surfaces A Physicochem. Eng. Asp. 269 (2005) 47–58. <https://doi.org/https://doi.org/10.1016/j.colsurfa.2005.06.060>.
- [293] X. Dou, F. Ren, M.Q. Nguyen, A. Ahamed, K. Yin, W.P. Chan, V.W.C. Chang, Review of MSWI bottom ash utilization from perspectives of collective characterization, treatment and existing application, Renew. Sustain. Energy Rev. 79 (2017) 24–38. <https://doi.org/10.1016/j.rser.2017.05.044>.
- [294] V.O. Özçelik, C.E. White, Nanoscale charge-balancing mechanism in alkali-substituted calcium--silicate--hydrate gels, J. Phys. Chem. Lett. 7 (2016) 5266–5272.
- [295] M. Criado, A. Fernández-Jiménez, A.G. De La Torre, M.A.G. Aranda, A. Palomo, An XRD study of the effect of the SiO<sub>2</sub>/Na<sub>2</sub>O ratio on the alkali activation of fly ash, Cem. Concr. Res. 37 (2007) 671–679.
- [296] M. Tella, G.S. Pokrovski, Antimony (III) complexing with O-bearing organic ligands in aqueous solution: An X-ray absorption fine structure spectroscopy and solubility study, Geochim. Cosmochim. Acta. 73 (2009) 268–290.
- [297] M. Tella, G.S. Pokrovski, Stability and structure of pentavalent antimony complexes with aqueous organic ligands, Chem. Geol. 292 (2012) 57–68.
- [298] M. Tella, G.S. Pokrovski, Antimony (V) complexing with O-bearing organic ligands in aqueous solution: an X-ray absorption fine structure spectroscopy and potentiometric study, Mineral. Mag. 72 (2008) 205–209.
- [299] S. Steely, D. Amarasinghe, B. Xing, An investigation of inorganic antimony species and antimony associated with soil humic acid molar mass fractions in contaminated soils, Environ. Pollut. 148 (2007) 590–598.
- [300] G. Ceriotti, D. Amarasinghe, A study of antimony complexed to soil-derived humic acids and inorganic antimony species along a Massachusetts highway, Microchem. J. 91 (2009) 85–93.
- [301] B. Verbinnen, J. Van Caneghem, P. Billen, C. Vandecasteele, Long Term Leaching Behavior of Antimony from MSWI Bottom Ash: Influence of Mineral Additives and of Organic Acids, Waste and Biomass Valorization. 8 (2017) 2545–2552. <https://doi.org/10.1007/s12649-016-9796-6>.
- [302] K. Andersson, B. Allard, M. Bengtsson, B. Magnusson, Chemical composition of cement pore solutions, Cem. Concr. Res. 19 (1989) 327–332. [https://doi.org/https://doi.org/10.1016/0008-8846\(89\)90022-7](https://doi.org/https://doi.org/10.1016/0008-8846(89)90022-7).
- [303] G. Cornelis, T. Van Gerven, R. Snellings, B. Verbinnen, J. Elsen, C. Vandecasteele, Stability of pyrochlores in alkaline matrices: Solubility of calcium antimonate, Appl. Geochemistry. 26 (2011) 809–817. <https://doi.org/https://doi.org/10.1016/j.apgeochem.2011.02.002>.
- [304] B. Guo, B. Liu, J. Yang, S. Zhang, The mechanisms of heavy metal immobilization by cementitious material treatments and thermal treatments: A review, J. Environ. Manage. 193 (2017) 410–422.

- <https://doi.org/https://doi.org/10.1016/j.jenvman.2017.02.026>.
- [305] M. Irannajad, H. Kamran Haghighi, Removal of Heavy Metals from Polluted Solutions by Zeolitic Adsorbents: a Review, *Environ. Process.* 8 (2021) 7–35. <https://doi.org/10.1007/s40710-020-00476-x>.
- [306] J. Zhang, J.L. Provis, D. Feng, J.S.J. van Deventer, Geopolymers for immobilization of Cr<sup>6+</sup>, Cd<sup>2+</sup>, and Pb<sup>2+</sup>, *J. Hazard. Mater.* 157 (2008) 587–598. <https://doi.org/https://doi.org/10.1016/j.jhazmat.2008.01.053>.
- [307] J. Deja, Immobilization of Cr<sup>6+</sup>, Cd<sup>2+</sup>, Zn<sup>2+</sup> and Pb<sup>2+</sup> in alkali-activated slag binders, *Cem. Concr. Res.* 32 (2002) 1971–1979. [https://doi.org/https://doi.org/10.1016/S0008-8846\(02\)00904-3](https://doi.org/https://doi.org/10.1016/S0008-8846(02)00904-3).
- [308] P.K. Mehta, P.J.M. Monteiro, *Concrete: microstructure, properties, and materials*, McGraw-Hill Education, 2014.
- [309] Z.T. Yao, X.S. Ji, P.K. Sarker, J.H. Tang, L.Q. Ge, M.S. Xia, Y.Q. Xi, A comprehensive review on the applications of coal fly ash, *Earth-Science Rev.* 141 (2015) 105–121. <https://doi.org/https://doi.org/10.1016/j.earscirev.2014.11.016>.
- [310] G.W. Zack, W.E. Rogers, S.A. Latt, Automatic measurement of sister chromatid exchange frequency., *J. Histochem. Cytochem.* 25 (1977) 741–753. <https://doi.org/10.1177/25.7.70454>.
- [311] B. Schmid, J. Schindelin, A. Cardona, M. Longair, M. Heisenberg, A high-level 3D visualization API for Java and ImageJ, *BMC Bioinformatics.* 11 (2010) 274. <https://doi.org/10.1186/1471-2105-11-274>.
- [312] R.S. Barneyback, S. Diamond, Expression and analysis of pore fluids from hardened cement pastes and mortars, *Cem. Concr. Res.* 11 (1981) 279–285. [https://doi.org/https://doi.org/10.1016/0008-8846\(81\)90069-7](https://doi.org/https://doi.org/10.1016/0008-8846(81)90069-7).
- [313] Standard Practice for Measuring Hydration Kinetics of Hydraulic Cementitious Mixtures Using Isothermal Calorimetry, (n.d.). <https://www.astm.org/c1679-17.html>.
- [314] B. Lothenbach, K. Scrivener, R.D.H.- Cement, concrete research, undefined 2011, Supplementary cementitious materials, Elsevier. (n.d.). [https://www.sciencedirect.com/science/article/pii/S0008884610002632?casa\\_token=H-ZjVtXhiZWAAAAA:7eVhZD-xDz1XIFAOUYdeT1dfsYcQYLLN2whdcVYEFsiUblMbv3HepFOmKVZ7-rjtgnkqSrJWEU](https://www.sciencedirect.com/science/article/pii/S0008884610002632?casa_token=H-ZjVtXhiZWAAAAA:7eVhZD-xDz1XIFAOUYdeT1dfsYcQYLLN2whdcVYEFsiUblMbv3HepFOmKVZ7-rjtgnkqSrJWEU).
- [315] J.E. Rossen, K.L. Scrivener, Optimization of SEM-EDS to determine the C--A--S--H composition in matured cement paste samples, *Mater. Charact.* 123 (2017) 294–306.
- [316] E.P. Barrett, L.G. Joyner, P.P. Halenda, The determination of pore volume and area distributions in porous substances. I. Computations from nitrogen isotherms, *J. Am. Chem. Soc.* 73 (1951) 373–380.
- [317] 827 pH lab; 230 V, EU with Primatrode, (n.d.). [https://www.metrohm.com/content/metrohm/en\\_nl/products/2/8270/28270114.html](https://www.metrohm.com/content/metrohm/en_nl/products/2/8270/28270114.html).
- [318] H.-T. Teng, T.-Y. Lee, Y.-K. Chen, H.-W. Wang, G. Cao, Effect of Al(OH)<sub>3</sub> on the hydrogen generation of aluminum–water system, *J. Power Sources.* 219 (2012) 16–21. <https://doi.org/https://doi.org/10.1016/j.jpowsour.2012.06.077>.



- [319] X. Chen, Z. Zhao, M. Hao, D. Wang, Research of hydrogen generation by the reaction of Al-based materials with water, *J. Power Sources*. 222 (2013) 188–195. <https://doi.org/https://doi.org/10.1016/j.jpowsour.2012.08.078>.
- [320] J.P. Hamilton, C.G. Pantano, S.L. Brantley, Dissolution of albite glass and crystal, *Geochim. Cosmochim. Acta*. 64 (2000) 2603–2615. [https://doi.org/https://doi.org/10.1016/S0016-7037\(00\)00388-4](https://doi.org/https://doi.org/10.1016/S0016-7037(00)00388-4).
- [321] C.A. Macris, R.C. Newton, J. Wykes, R. Pan, C.E. Manning, Diopside, enstatite and forsterite solubilities in H<sub>2</sub>O and H<sub>2</sub>O-NaCl solutions at lower crustal and upper mantle conditions, *Geochim. Cosmochim. Acta*. 279 (2020) 119–142. <https://doi.org/https://doi.org/10.1016/j.gca.2020.03.035>.
- [322] A. Stefánsson, Dissolution of primary minerals of basalt in natural waters: I. Calculation of mineral solubilities from 0°C to 350°C, *Chem. Geol.* 172 (2001) 225–250. [https://doi.org/https://doi.org/10.1016/S0009-2541\(00\)00263-1](https://doi.org/https://doi.org/10.1016/S0009-2541(00)00263-1).
- [323] Q.Y. Chen, C.D. Hills, M. Tyrer, I. Slipper, H.G. Shen, A. Brough, Characterisation of products of tricalcium silicate hydration in the presence of heavy metals, *J. Hazard. Mater.* 147 (2007) 817–825. <https://doi.org/https://doi.org/10.1016/j.jhazmat.2007.01.136>.
- [324] J.F. Young, A review of the mechanisms of set-retardation in portland cement pastes containing organic admixtures, *Cem. Concr. Res.* 2 (1972) 415–433. [https://doi.org/https://doi.org/10.1016/0008-8846\(72\)90057-9](https://doi.org/https://doi.org/10.1016/0008-8846(72)90057-9).
- [325] D. Jansen, F. Goetz-Neunhoffer, C. Stabler, J. Neubauer, A remastered external standard method applied to the quantification of early OPC hydration, *Cem. Concr. Res.* 41 (2011) 602–608. <https://doi.org/https://doi.org/10.1016/j.cemconres.2011.03.004>.
- [326] P. Lawrence, M. Cyr, E. Ringot, Mineral admixtures in mortars: Effect of inert materials on short-term hydration, *Cem. Concr. Res.* 33 (2003) 1939–1947. [https://doi.org/https://doi.org/10.1016/S0008-8846\(03\)00183-2](https://doi.org/https://doi.org/10.1016/S0008-8846(03)00183-2).
- [327] E. Berodier, K. Scrivener, Understanding the Filler Effect on the Nucleation and Growth of C-S-H, *J. Am. Ceram. Soc.* 97 (2014) 3764–3773.
- [328] D.P. Bentz, P.-C. Aitcin, The hidden meaning of water-cement ratio, *Concr. Int.* 30 (2008) 51–54.
- [329] J.W. Bullard, H.M. Jennings, R.A. Livingston, A. Nonat, G.W. Scherer, J.S. Schweitzer, K.L. Scrivener, J.J. Thomas, Mechanisms of cement hydration, *Cem. Concr. Res.* 41 (2011) 1208–1223. <https://doi.org/https://doi.org/10.1016/j.cemconres.2010.09.011>.
- [330] K.L. Scrivener, T. Füllmann, E. Gallucci, G. Walenta, E. Bermejo, Quantitative study of Portland cement hydration by X-ray diffraction/Rietveld analysis and independent methods, *Cem. Concr. Res.* 34 (2004) 1541–1547. <https://doi.org/https://doi.org/10.1016/j.cemconres.2004.04.014>.
- [331] B. Lothenbach, G. Le Saout, E. Gallucci, K. Scrivener, Influence of limestone on the hydration of Portland cements, *Cem. Concr. Res.* 38 (2008) 848–860. <https://doi.org/https://doi.org/10.1016/j.cemconres.2008.01.002>.
- [332] G. Le Saoût, B. Lothenbach, A. Hori, T. Higuchi, F. Winnefeld, Hydration of Portland cement with additions of calcium sulfoaluminates, *Cem. Concr. Res.* 43 (2013) 81–94. <https://doi.org/https://doi.org/10.1016/j.cemconres.2012.10.011>.

- [333] D.P. Bentz, S. Remond, Incorporation of fly ash into a 3-D cement hydration microstructure model, US Department of Commerce, Technology Administration, National Institute of ..., 1997.
- [334] S. Mindess, J.F. Young, D. Darwin, Concrete Prentice-Hall, Englewood Cliffs, NJ. 481 (1981).
- [335] A.M. Neville, Properties of concrete, Pitman, 1973.
- [336] M. Nedeljković, Z. Li, G. Ye, Setting, Strength, and Autogenous Shrinkage of Alkali-Activated Fly Ash and Slag Pastes: Effect of Slag Content, *Mater. .* 11 (2018). <https://doi.org/10.3390/ma11112121>.
- [337] B. Sun, Y. Sun, G. Ye, G. De Schutter, A mix design methodology of slag and fly ash-based alkali-activated paste, *Cem. Concr. Compos.* 126 (2022) 104368. <https://doi.org/https://doi.org/10.1016/j.cemconcomp.2021.104368>.
- [338] S. Roels, J. Elsen, J. Carmeliet, H. Hens, Characterisation of pore structure by combining mercury porosimetry and micrography, *Mater. Struct.* 34 (2001) 76–82. <https://doi.org/10.1007/BF02481555>.
- [339] G. Ye, Experimental study and numerical simulation of the development of the microstructure and permeability of cementitious materials, (2003).
- [340] F. Chayes, Petrographic modal analysis : an elementary statistical appraisal, Wiley , New York, 1956.
- [341] J.M.S. Prewitt, M.L. Mendelsohn, THE ANALYSIS OF CELL IMAGES\*, *Ann. N. Y. Acad. Sci.* 128 (1966) 1035–1053. <https://doi.org/https://doi.org/10.1111/j.1749-6632.1965.tb11715.x>.
- [342] F.B. Reig, J.V.G. Adelantado, M.C.M. Moya Moreno, FTIR quantitative analysis of calcium carbonate (calcite) and silica (quartz) mixtures using the constant ratio method. Application to geological samples, *Talanta*. 58 (2002) 811–821. [https://doi.org/https://doi.org/10.1016/S0039-9140\(02\)00372-7](https://doi.org/https://doi.org/10.1016/S0039-9140(02)00372-7).
- [343] C.K. Huang, P.F. Kerr, Infrared study of the carbonate minerals, *Am. Mineral.* 45 (1960) 311–324.
- [344] M.R. Filgueiras, G. La Torre, L.L. Hench, Solution effects on the surface reactions of a bioactive glass, *J. Biomed. Mater. Res.* 27 (1993) 445–453. <https://doi.org/https://doi.org/10.1002/jbm.820270405>.
- [345] M. Torres-Carrasco, A. Palomo, F. Puertas, Sodium silicate solutions from dissolution of glass wastes. Statistical analysis, (2014).
- [346] J.L. Bass, G.L. Turner, Anion Distributions in Sodium Silicate Solutions. Characterization by <sup>29</sup>Si NMR and Infrared Spectroscopies, and Vapor Phase Osmometry, *J. Phys. Chem. B.* 101 (1997) 10638–10644. <https://doi.org/10.1021/jp9715282>.
- [347] H. Xu, J.S.J. Van Deventer, The geopolymerisation of alumino-silicate minerals, *Int. J. Miner. Process.* 59 (2000) 247–266. [https://doi.org/https://doi.org/10.1016/S0301-7516\(99\)00074-5](https://doi.org/https://doi.org/10.1016/S0301-7516(99)00074-5).
- [348] I. García Lodeiro, A. Fernández-Jimenez, A. Palomo, D.E. Macphee, Effect on fresh C-S-H gels of the simultaneous addition of alkali and aluminium, *Cem. Concr. Res.* 40 (2010) 27–32. <https://doi.org/https://doi.org/10.1016/j.cemconres.2009.08.004>.
- [349] B. Walkley, R. San Nicolas, M.-A. Sani, G.J. Rees, J. V Hanna, J.S.J. van Deventer, J.L. Provis, Phase

- evolution of C-(N)-ASH/NASH gel blends investigated via alkali-activation of synthetic calcium aluminosilicate precursors, *Cem. Concr. Res.* 89 (2016) 120–135.
- [350] I. Garcia-Lodeiro, A. Palomo, A. Fernández-Jiménez, D.E. Macphee, Compatibility studies between NASH and CASH gels. Study in the ternary diagram  $\text{Na}_2\text{O}-\text{CaO}-\text{Al}_2\text{O}_3-\text{SiO}_2-\text{H}_2\text{O}$ , *Cem. Concr. Res.* 41 (2011) 923–931.
- [351] M. Król, J. Minkiewicz, W. Mozgawa, IR spectroscopy studies of zeolites in geopolymeric materials derived from kaolinite, *J. Mol. Struct.* 1126 (2016) 200–206.  
<https://doi.org/https://doi.org/10.1016/j.molstruc.2016.02.027>.
- [352] M.I.M. Alzeer, H. Nguyen, C. Cheeseman, P. Kinnunen, Alkali-activation of synthetic aluminosilicate glass with basaltic composition, *Front. Chem.* 9 (2021).
- [353] C.A. Rees, Mechanisms and kinetics of gel formation in geopolymers, (2007).
- [354] A. Fernández-Jiménez, A. Palomo, Mid-infrared spectroscopic studies of alkali-activated fly ash structure, *Microporous Mesoporous Mater.* 86 (2005) 207–214.
- [355] J.R. Sweet, W.B. White, Study of sodium silicate glasses and liquids by infrared reflectance spectroscopy, *Phys. Chem. Glas.* 10 (1969) 246.
- [356] J.L. Provis, J.S.J. Van Deventer, Geopolymerisation kinetics. 2. Reaction kinetic modelling, *Chem. Eng. Sci.* 62 (2007) 2318–2329.
- [357] S. Puligilla, X. Chen, P. Mondal, Does synthesized CSH seed promote nucleation in alkali activated fly ash-slag geopolymer binder?, *Mater. Struct.* 52 (2019) 1–13.
- [358] M. Ben Haha, B. Lothenbach, G. Le Saout, F. Winnefeld, Influence of slag chemistry on the hydration of alkali-activated blast-furnace slag — Part I: Effect of  $\text{MgO}$ , *Cem. Concr. Res.* 41 (2011) 955–963.  
<https://doi.org/https://doi.org/10.1016/j.cemconres.2011.05.002>.
- [359] A. Fernández-Jiménez, F. Puertas, Effect of activator mix on the hydration and strength behaviour of alkali-activated slag cements, *Adv. Cem. Res.* 15 (2003) 129–136.  
<https://doi.org/10.1680/adcr.2003.15.3.129>.
- [360] P. Yu, R.J. Kirkpatrick, B. Poe, P.F. McMillan, X. Cong, Structure of calcium silicate hydrate (C-S-H): Near-, Mid-, and Far-infrared spectroscopy, *J. Am. Ceram. Soc.* 82 (1999) 742–748.
- [361] M. Sitarz, M. Handke, W. Mozgawa, Identification of silicoxygen rings in  $\text{SiO}_2$  based on IR spectra, *Spectrochim. Acta Part A Mol. Biomol. Spectrosc.* 56 (2000) 1819–1823.
- [362] M. Sitarz, M. Handke, W. Mozgawa, E. Galuskin, I. Galuskina, The non-ring cations influence on silicoxygen ring vibrations, *J. Mol. Struct.* 555 (2000) 357–362.  
[https://doi.org/https://doi.org/10.1016/S0022-2860\(00\)00621-9](https://doi.org/https://doi.org/10.1016/S0022-2860(00)00621-9).
- [363] V. STUBIČAN, R. ROY, Infrared Spectra of Layer-Structure Silicates, *J. Am. Ceram. Soc.* 44 (1961) 625–627. <https://doi.org/https://doi.org/10.1111/j.1151-2916.1961.tb11670.x>.
- [364] E. Kapeluszna, Ł. Kotwica, A. Różycka, Ł. Gołek, Incorporation of Al in C-A-S-H gels with various Ca/Si

- and Al/Si ratio: Microstructural and structural characteristics with DTA/TG, XRD, FTIR and TEM analysis, *Constr. Build. Mater.* 155 (2017) 643–653.  
<https://doi.org/https://doi.org/10.1016/j.conbuildmat.2017.08.091>.
- [365] I. García-Lodeiro, A. Fernández-Jiménez, A. Palomo, D.E. Macphee, Effect of calcium additions on N–A–S–H cementitious gels, *J. Am. Ceram. Soc.* 93 (2010) 1934–1940.
- [366] M. Nedeljković, Carbonation mechanism of alkali-activated fly ash and slag materials: In view of long-term performance predictions, (2019).
- [367] M. Ben Haha, B. Lothenbach, G. Le Saout, F. Winnefeld, Influence of slag chemistry on the hydration of alkali-activated blast-furnace slag — Part II: Effect of Al<sub>2</sub>O<sub>3</sub>, *Cem. Concr. Res.* 42 (2012) 74–83.  
<https://doi.org/https://doi.org/10.1016/j.cemconres.2011.08.005>.
- [368] R. Heijungs, J.B. Guinée, G. Huppes, Impact categories for natural resources and land use: survey and analysis of existing and proposed methods in the context of environmental life cycle assessment, (1997).
- [369] NEN Connect - NEN-EN 15804:2012+A2:2019 en, (n.d.).  
<https://connect.nen.nl/Standard/Detail/3621354?compId=10037&collectionId=0>.
- [370] NIBE EPD, (n.d.). <https://www.nibe-sustainability-experts.com/en/epd-tool>.
- [371] M.V.A. Florea, Z. Ning, H.J.H. Brouwers, Activation of liberated concrete fines and their application in mortars, *Constr. Build. Mater.* 50 (2014) 1–12.  
<https://doi.org/https://doi.org/10.1016/j.conbuildmat.2013.09.012>.
- [372] D. Song, J. Yang, B. Chen, T. Hayat, A. Alsaedi, Life-cycle environmental impact analysis of a typical cement production chain, *Appl. Energy.* 164 (2016) 916–923.  
<https://doi.org/https://doi.org/10.1016/j.apenergy.2015.09.003>.
- [373] V. Ghalandari, A. Iranmanesh, Energy and exergy analyses for a cement ball mill of a new generation cement plant and optimizing grinding process: A case study, *Adv. Powder Technol.* 31 (2020) 1796–1810. <https://doi.org/https://doi.org/10.1016/j.apert.2020.02.013>.
- [374] M.F. Alnahhal, T. Kim, A. Hajimohammadi, Waste-derived activators for alkali-activated materials: A review, *Cem. Concr. Compos.* 118 (2021) 103980.  
<https://doi.org/https://doi.org/10.1016/j.cemconcomp.2021.103980>.
- [375] K.A. Paine, R.K. Dhir, V.P.A. Doran, Incinerator Bottom Ash: Engineering and Environmental Properties as a Cement Bound Paving Material, *Int. J. Pavement Eng.* 3 (2002) 43–52.  
<https://doi.org/10.1080/10298430290023458>.
- [376] Y. Cheng, Y. Dong, J. Diao, G. Zhang, C. Chen, D. Wu, MSWI bottom ash application to resist sulfate attack on concrete, *Appl. Sci.* 9 (2019). <https://doi.org/10.3390/app9235091>.
- [377] J. Kim, J. An, B.H. Nam, K.M. Tasneem, Investigation on the side effects of municipal solid waste incineration ashes when used as mineral addition in cement-based material, *Road Mater. Pavement Des.* 17 (2016) 345–364. <https://doi.org/10.1080/14680629.2015.1083463>.

- [378] Ecocem Benelux B.V. - Eco2cem GGBS - Milieu Relevante Product Informatie, (n.d.).  
<https://www.mrpi.nl/epd/ecocem-benelux-b-v-eco2cem-ggbs/>.

# Acknowledgements

---

From 2012 to 2023, this decade is like a dream for me. I evolved from a bachelor to a master, and then to a doctor. If I go back to 2012, I ask myself, “Do you want to be a doctor?” The answer would be, “I am not sure.” But if I ask myself, “Do you want to explore the world, meet different people, and get to know yourself by pursuing Ph.D.?” The answer would be, “Why not? That sounds great!”.

I am very happy that I can finish my Ph.D. in 2023. First of all, I would like to acknowledge the China Scholarship Council (CSC) and Mineralz B.V. for their financial support of the work presented in this dissertation. I would also like to take this opportunity to acknowledge all the people who have helped and supported me over these years.

I would like to pay tribute to my promoter Prof. Klaas van Breugel. I am proud to be your student. I admire your serious and rigorous work ethic. You set such an amazing example for all of us. Under your guidance, I get to know the beauty of science and the art of scientific writing. The comments and feedback I received from you are among the best gifts I have ever received. I will always keep them in mind.

I would like to express my deepest appreciation to my co-promoter Dr. Guang Ye. I feel very lucky to have you as my mentor. I feel very honored to be a member of the CMMB research group. Thanks a lot for your guidance, support and help over these years. Thank you for always helping me get out of my comfort zone and guiding me to do better in my research area. Your constructive feedback gives more motivation to explore new possibilities. Your trust in me gives me more confidence to overcome difficulties. The Chinese food you and your wife (Ms. Lei Zhang) shared with us makes us feel at home and more energetic at work.

I would also like to extend my sincere thanks to all the other committee members: the chairperson, Prof.dr. H.M. Jonkers, Prof.dr. L.M. Ottosen, Prof.dr. N. Štirmer, Prof.dr. Y. Zhang, Dr.ir. G.M.H. Meesters, and Prof.dr.ir. E. Schlangen. I very much appreciate your efforts in evaluating my thesis. Thank you for helping me complete this journey.

Special thanks are given to the mentors of my master’s thesis, Prof. Bart Blanpain, Dr. Yiannis Pontikes, and Dr. Silvana Onisei from KU Leuven, for guiding me into the world of waste recycling and alkali-activated materials.

It is a fantastic experience to work in Microlab. I am very grateful to Prof. Erik Schlangen for creating a perfect working environment for all the researchers in Microlab. The continued support and help you provided to us are invaluable. Prof.dr. H.M. Jonkers, our discussion on sustainability and life cycle assessments gives me a lot of inspiration. Thank you so much! I also wish to thank Dr. Oguzhan Copuroglu for your advice and support for my SEM tests. I really get a lot of useful information by taking the CMC course. Many thanks to Dr. Branko Šavija and Dr. Mladena Luković for all the inspiring conversation and lectures. Thanks also to Dr. Dessi Koleva for all the knowledge and experiences you shared with us during the CSC<sup>2</sup>I course.

I must thank the technical staff at Microlab. Without your kind support and hard work, I will never be able to accomplish so much experimental work.

Maiko, thank you for always being there to support me and my experiments. You are such a nice person with a golden heart. I will never forget the words you sent to me: *“The main purpose of life is not measured in achievements, but on how many memories and friends you collected — Maiko van Leeuwen”*. I would like to say, “You are one of the best memories and friends I collected during my stay at TU Delft”.

Ton, you are my “Superman”. I cannot imagine how I can survive from all the crushing and grinding work without your help. You are always full of energy and power. Working with you brings me so much joy.

John, thank you so much for your professional advice on my experiments. I am glad to receive your greeting every time you say “Ní hǎo, nǚ hái” (“hello, girl” in English). I know sometimes it means “Good morning! or good afternoon!”, and sometimes it means “How are you?”. You are such a nice person. I feel very happy to work with you.

Arjan, thank you for your “Magic power”. Your “eagle eyes” and “golden hands” dramatically increase the efficiency of my experimental work. You are an excellent “photographer”. I really like the pictures you took for my samples. Thanks a lot for your patience and support. Bedankt, Meneer Arjan!

I also had a great pleasure of working with the technical staff in other labs of TU Delft. Ruud, I gratefully acknowledge your help with my XRD and XRF samples. I must also thank Wim and Ellen for your kind support for my CT scan. Ron, thank you for your support with my XRF tests and other experiments at the initial stage of my research. Dr. Nijemeisland and Durga thanks a lot for your kind assistance with my FTIR tests. Paul and Kees, thank you for helping me solve issues with the setups used for the volume stability test.

I would also like to extend my deepest gratitude to the researchers/engineers outside TU Delft. Meneer Rob Bleijerveld, thanks for your interest in my research topic. You have been so supportive throughout my doctoral study. Marc Brito van Zijl, many thanks for all the very nice discussions and your help in my experimental works. Thank you, Dr. Arno Keulen, for all the excellent work you did for MSWI bottom ash aggregates, which provided a solid foundation for my research. Thanks for your valuable insights into the recycling of MSWI bottom ash and the help you gave me at the beginning of my doctoral study. Thanks should also go to Dr. Nicola Döbelin, who provided strong support for my QXRD analysis.

I am honored to have opportunities to collaborate with so many talented professors and researchers. I would like to thank Prof. dr. Mirja Illikainen and Dr. Priyadharshini Perumal from the University of Oulu for your support and encouragement. I am also very lucky that I can collaborate with Dr. Hua Dong, Dr. Yibing Zuo, Dr. Zhenming Li, Dr. Shizhe Zhang, Jiayi Chen, Fernando França de Mendonça Filho, Luiz Miranda de Lima, Yubo Sun, Xuhui Liang, Yun Chen, and Clarissa L. Justino de Lima. Many thanks for your support and all the very nice exchange of ideas. Special thanks to Dr. Marija Nedeljković and Patrick Holthuizen for all your kind support during these years. Marija, I feel super lucky to have you with me on this journey.

Patrick, thank you for helping me with the Dutch translation of my thesis. Thank you very much for all the informative talks.

I am very grateful to my officemates, Hua, Shizhe, and Zhiyuan, for your kind support. We almost meet every working day during these years. You three bring me so much joy and warmth. I also would like to thank my previous officemates: Albina and Ana. I will never forget the time we spent together.

My gratitude also extends to my other colleagues from Microlab: Dr. Xiujiao Qiu, Guilherme da Silva Munhoz, Irving Flores Beltran, Chen Liu, Yu Zeng, Hu Shi, Farnaz Aghabeyk, Haoming Wu, Ivana Mariam Paul, Xinrui Zhang, Dr. Xingliang Yao, Dr. Yidong Gan, Dr. Yu Zhang, Dr. Yu Chen, Dr. Yading Xu, Dr. Ze Chang, Shan He, Zhi Wan, Jinbao Xie, Minfei Liang, Stefan Chaves Figueiredo, Claudia Romero Rodriguez, Bart Hendrix, Dr. Yask Kulshreshtha, Anne Linde van Overmeir, Dr. Emanuele Rossi, Dr. Marija Krstic, Dr. Ana Mafalda Matos, Renee Mors, Jeanette van de Bos, Ameya Kamat, Ali Ghaderiaram. Together we learn from each other, help each other, and support each other. Thank you!

I gratefully acknowledge Bei Wu, Hao Huang, Xuliang Hou, Dr. Zhuqing Yu, Dr. Wejuan Lyu, Dr. Shi Xu, Dr. Yong Zhang, Dr. Xu Ma, Dr. Peng Gao, Dr. Xiaowei Ouyang, Dr. Zhiwei Qian, Dr. Tianshi Lu, Dr. Zhipei Chen, Dr. Hongzhi Zhang, Dr. Leyang Lyu, Prof. Jian Zhou, Jiahua Liu, Dr. Yuguang Yang, Dr. Bin Hu, Dr. Fengqiao Zhang, for your valuable advice and supports. I can always learn a lot from you.

Many thanks to the secretary team of 3MD: Jaap, Jacqueline, Iris, Sandra, and Claire. Thanks for always being there to help us. Your supports give me a sense of belonging. Thank you for all your dedication.

Last but definitely not least, I would like to express my deepest gratitude to my parents, family, and friends. Thank you, my dearest 爸爸 and 妈妈. Without your unconditional support and love, I do not think I could have made it this far. Thank you for always trusting me more than myself. Thank you for always taking care of my emotions. Thank you for treating your daughter as your best friend. From now on, you will no longer need to worry about the study of your daughter. Very happy, right? I also want to thank my family, especially my 爷爷 and 奶奶, for your love. Many thanks to my best friends (also my sisters). Thank you for growing up with me. I would also like to thank all the friends I meet in the Netherlands and Belgium. Trust me, I will never forget your names.

Best wishes for our future!

Boyu Chen

Delft, Feb, 2023



# Curriculum vitae

---

## Personal information

Name: Boyu CHEN (陈泊羽)

Date of birth: 8<sup>th</sup> March 1991

Place of birth: Jingdezhen, Jiangxi Province, China

Email: Chen\_Boyu@hotmail.com

## Education background

Dec. 2022 - Present

Post-doc Researcher

Faculty of Civil Engineering and Geoscience

Delft University of Technology

The Netherlands

Sep. 2017-Nov. 2022

Phd candidate

Faculty of Civil Engineering and Geoscience

Delft University of Technology

The Netherlands

Sep 2012 – Jun 2015

MSc student

Depart of Materials Engineering

KU Leuven

Belgium

Sep 2008 – Jun 2012

BSc student

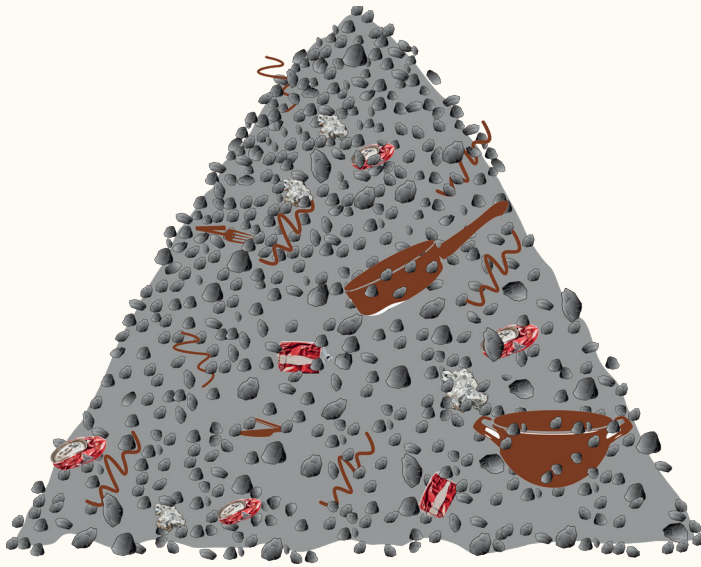
Jingdezhen Ceramic Institute

School of Materials Science and Engineering

China



Not wastes !  
But renewable resources !



 **TU**Delft

